Spatial Localization of Cartilage Degradation Using Electromechanical Surface Spectroscopy With Variable Wavelength and Frequency

by

Scott I. Berkenblit

S.M., Electrical Engineering and Computer Science, M.I.T. (1990)
S.B., Electrical Engineering, M.I.T. (1986)
S.B., Mathematics, M.I.T. (1986)

Submitted to the Harvard-M.I.T.
Division of Health Sciences and Technology
in Partial Fulfillment of the Requirements
for the Degree of

Doctor of Philosophy

at the

Massachusetts Institute of Technology
June, 1996

Signature of Author _____
Harvard-M.I.T. Division of Health Sciences and Technology
May 28, 1996

Certified by _____
Alan J. Grodzinsky, Sc.D.
Professor of Electrical, Mechanical, and Bioengineering
Thesis Supervisor

Accepted by _____
Martha L. Gray, Ph.D.
Associate Professor of Electrical Engineering
Chairman, Department Committee on Graduate Students

Spatial Localization of Cartilage Degradation Using Electromechanical Surface Spectroscopy With Variable Wavelength and Frequency

by

Scott I. Berkenblit

Submitted to the Harvard-M.I.T. Division of Health Sciences and Technology
on May 28, 1996 in Partial Fulfillment of the Requirements
for the Degree of Doctor of Philosophy

Abstract

This work focuses on developing a new technology for nondestructively measuring electrical and mechanical properties of articular cartilage via electrodes placed on the tissue surface. The long-term goal of this work is to enable detection of early stages of cartilage degradation (e.g., in osteoarthritis) based on the sensitivity of cartilage electromechanical properties to loss of highly charged aggrecan molecules from the tissue. Ultimately, this technique could enable early *in vivo* detection of cartilage degradation via arthroscopy.

Theoretical analysis has suggested that an electric current applied to the articular surface of cartilage will give rise to a mechanical current-generated stress within the bulk of the tissue, via electrokinetic mechanisms, measurable at the surface. Based on this principle, an *electrokinetic surface probe* was developed, containing silver/silver chloride electrodes for applying current to the cartilage surface and an overlying piezoelectric polymer film sensor for measuring the resulting stress. Small sinusoidal currents applied to disks of bovine articular cartilage produced sinusoidal surface stresses at the same frequency. The frequency response was found to agree well with a theoretical poroelastic model. Titration of intratissue pH resulted in changes in stress amplitude and phase which paralleled known changes in tissue fixed charge density, with the stress amplitude reaching a minimum near the isoelectric pH of the tissue.

Because the depth to which current penetrates into the tissue is proportional to the imposed spatial wavelength (twice the electrode spacing), it was hypothesized that measurements using multiple wavelengths could enable detection of partial-thickness degradation, as occurs in early osteoarthritis. Thus, a multiple-wavelength probe was developed and tested with full-thickness plugs of calf cartilage. A model system was also developed for producing nonuniform loss of aggrecan, using trypsin, as a model for cartilage degradative changes. Histological and biochemical analysis confirmed that trypsin exposure resulted in progressive loss of aggrecan, proceeding inward from the articular surface. Enzymatic

extraction of aggrecan using this model resulted in a relatively greater attenuation of the stress measured using a short-wavelength excitation, in which current remained confined to the degraded region, as compared to long-wavelength excitation, in which current could penetrate the underlying normal tissue as well. These results support the use of wavelength- and frequency-scanning surface spectroscopy for spatially imaging focal regions of cartilage degradation.

Thesis Supervisor:

Alan J. Grodzinsky, Sc.D. ..... Professor of Electrical, Mechanical and Bioengineering
Massachusetts Institute of Technology

Thesis Committee:

Eliot H. Frank, Ph.D. ..... Research Engineer, Center for Biomedical Engineering
Massachusetts Institute of Technology

Roger D. Kamm, Ph.D. ..... Professor of Mechanical Engineering
Massachusetts Institute of Technology

Myron Spector, Ph.D. ..... Director of Orthopaedic Research
Brigham and Womens Hospital
Lecturer in Mechanical Engineering, M.I.T.

Acknowledgments

What can I say about Alan J. Grodzinsky that has not already been said in somebody else's thesis acknowledgments? How about this: he's a great guy, for a viola player... Seriously, though, Al has been a terrific mentor and role model in numerous ways. His ability to communicate equally well with engineers, biochemists, and even orthopods is inspiring and reflects the truly interdisciplinary nature of doing clinically relevant research on cartilage biomechanics. Also, he demonstrated, by example, the critical importance of both good coffee and good beer in doing high-quality research.

To the rest of my thesis committee—Roger Kamm, Myron Spector, and Eliot Frank—I am grateful for their insightful, helpful, and provocative comments and suggestions during the course of this work.

Linda Bragman and Eliot Frank (there's that name again) are not usually mentioned in the same paragraph, but they share the distinction of being indispensable to the running of the Continuum Electromechanics Group. The lab would be a bleak place, indeed, without Linda's stewardship as financial manager, social coordinator, and mild-mannered receptionist. Eliot's intuitive understanding of How Things Work is truly impressive, and I've probably learned more hard-core hands-on engineering by watching him fix things in the lab (from hardware to software to chart recorder transmissions) than in any course I've taken at M.I.T.

Minerva García has been my sometime partner-in-crime, having helped plan and carry out a number of devious schemes including the RectoMagnetoGraph advertisement, the "radio in the ceiling," and the kidnaping and ransom of Al's mug (it was *her* idea). Unfortunately, we never did figure out a good way to hack Martha...

Tom Quinn is a complex and multifaceted individual, whose very presence keeps the lab, or at least our office, from ever being a boring place, particularly during the thesis crunch of the past two months. What I've discovered about Tom is that behind the crude Western Canadian facade there lies a sensitive, caring young man whose dedication to scientific inquiry is surpassed only by his passion for guitar rock. If the post-doc in Switzerland doesn't work out, he can always tour with Slash and the Snakepit.

Larry Bonassar finished his thesis last year, but he still spends a lot of time hanging around the lab, mainly trying to bum cookies from Minerva. I am grateful to Larry for many things, from providing weekly *L.A. Law* plot summaries, to giving me useful advice on where to live in Baltimore, to sharing some memorable evenings consuming copious amounts of fried alligator bits and large Abitas during those wild ORS forays into the French Quarter.

Marc Levenston, our resident FEM expert, was masochistic enough to modify his

finite element code, on extremely short notice, to model the surface probe geometry (or at least a radially symmetric approximation thereof). I would also like to thank Marc for his useful advice on how to approach one's final committee meeting and thesis defense, the details of which advice I dare not divulge in this context, as I still hope to graduate.

I would like also to acknowledge the other "probesters" in the lab, eclectic and accomplished bunch that they are. Steve Treppo is already moving the probe project onward in interesting new directions. Dave Bombard developed the first "hand held" version of the probe, then wisely decided to punt engineering altogether to become a ski bum in Colorado. Dr. Evan Salant is now long gone from the lab, but his reputation lives on; while most of us only dream about appearing in full-page ads in both the *New England Journal of Medicine* and *JAMA,* Evan has lived that dream, serving as an Army National Guard poster child.

Amid the vast sea of humanity that is the HST administration, four individuals deserve special mention for having helped me on numerous occasions (usually having to do with straightening out my registration problems or canceling items on my M.I.T. bill): Keiko Oh, the only person in the world who understands how HST finances work (and whom I first met 14 years ago, as she was my freshman adviser at M.I.T.); Ron Smith, the only person in the world who understands how both the M.I.T. and Harvard registration systems work; Patty Cunningham, HST's rep at the MEC; and the late Gloria McAvenia, whose untimely passing has undoubtedly been felt by all HST students.

Although I received no funding from the Harvard M.D.-Ph.D. program, I have definitely benefited from my association with the program. In particular, it has been gratifying to be able to commiserate with other students who were also going through the constant struggle of trying to forge some semblance of unity and cohesion out of two completely different, and often antithetical, educational programs. Also, I first met Gail at an M.D.-Ph.D. retreat.

I am grateful to the Johns Hopkins Department of Orthopaedic Surgery for luring me away from Boston, after having spent 14 years here, to spend the next five years of my training in Baltimore. Maybe I'll come back to New England for my fellowship. . .

Being involved in various musical groups at M.I.T. has helped keep me sane during my ten-year grad/med school career. I have been privileged to work with many fine student musicians, too numerous to mention individually. My most significant musical experiences have involved that unique organization known as the M.I.T. Concert Band, particularly the tour of Iceland in January, 1993. More recently, the *Brass Rats* (otherwise known as the *Boltzmann Brass,* the *International World Festival Brass Quintet in Casual Attire,* and several other guises), a quintessential M.I.T. brass quintet, has been my sole musical outlet.

Gail Benson has been a constant source of love, support, ice cream, and back rubs during these past five and a half years. I just hope that I can do as good a job of being there

for her when she is finishing her thesis.

Finally, I am eternally grateful to my parents for their love, nagging, and support (moral, financial, and otherwise), even when they weren't quite sure how all these abbreviations with which I have been associated (MIT/HMS/HST/MEMP/MD-PhD. . .) fit together, or what they all stand for.

This work was supported, in part, by National Science Foundation Grant BCS-9111401 and Veteran's Administration Grant V525P-1743. I'd like to think it was money well spent.

"Education is. . . hanging around until you've got the hang of it."
—*Robert Frost*

"Don't undertake a project unless it is manifestly important and nearly impossible." —*Edwin H. Land*

"Sometimes a scream is better than a thesis." —*Albert Einstein*

Contents

List of Figures

List of Tables

List of Symbols

AC	articular cartilage
ANOVA	analysis of variance
CS	chondroitin sulfate
DMB	dimethylmethylene blue
ECM	extracellular matrix
EDTA	[ethylenedinitrilo]tetraacetic acid
FCD	fixed charge density
GAG	glycosaminoglycan
HA	hyaluronan (hyaluronic acid)
IEP	isoelectric pH
KS	keratan sulfate
NEM	*N*-ethylmaleimide
OA	osteoarthritis
PG	proteoglycan
PMMA	poly[methyl methacrylate]
PMSF	phenylmethylsulfonyl fluoride
PVDF	polyvinylidene fluoride
RHT	ruthenium hexaammine trichloride
THD	total harmonic distortion

A	area of sensor electrode subjected to stress
A'	total metallized area of sensor electrode
b_{ij}	phenomenological coefficients; $[b_{ij}] = [k_{ij}]^{-1}$
C	channel capacitance of piezoelectric sensor

$\bar{c}_{\pm}$	cation/anion concentration within tissue
c_b	cation and anion concentration in bath
D	diffusion coefficient
d_t	piezoelectric strain constant
F	Faraday's constant, = 9.6487×10^4 Coul/mol
f	temporal frequency, Hz
G	Lamé elastic coefficient (shear modulus) of solid matrix
H_A	equilibrium modulus, = $2G + \lambda_L$
I	electrical current
$\vec{J}$	electrical current density
J_n	Fourier coefficient of nth spatial mode
j	$\sqrt{-1}$
k	spatial wavenumber, = $2\pi/\lambda$
k_{11}	short-circuit Darcy hydraulic permeability
k_{12}, k_{21}	electrokinetic coupling coefficients ($k_{12} = k_{21}$ by Onsager reciprocity)
k_{22}	electrical conductivity (with no fluid flow)
k_c	$k_{12}k_{21}/k_{11}k_{22}$
k_e	electrokinetic coefficient, = k_{21}/k_{22}
k_s	$\omega b_{11}/H_A\phi_0$
ℓ^*	characteristic length
M	number of electrode pairs
n	$1 - 2\nu$
P	fluid pressure (per unit total area)
Q	electrical charge on electrode
r	$k_s\xi^*(1 + n)$
s	electrode spacing (center-to-center)

T_{zz}	normal stress
T_{yz}	shear stress
t	time
$\vec{U}$	relative fluid velocity, = $\vec{v}_f - \vec{v}_s$
$\vec{u}$	solid matrix displacement
$\bar{u}_{\pm}$	ionic mobility of cations/anions within tissue
V	electrical voltage
$\vec{v}_f, \vec{v}_s$	fluid, solid velocity
w	electrode width
Y	spatial period in y-direction
Z	electrical impedance
z	depth into tissue
$z_{\pm}$	valence of cations/anions
α_0	solid volume fraction, = $(1 - \phi_0)/\phi_0$
γ	$k(\delta + z)$
Δ	mechanical diffusion depth, = $\sqrt{H_A k_{11} \phi_0 / \omega}$
δ	cartilage thickness
δ_{ij}	Krönecker delta function, = 1 if $i = j$, 0 otherwise
ϵ	dielectric coefficient
$\vec{\vec{\epsilon}}$	small-strain tensor
Λ	$\sqrt{1 - jk_s/k}$
Λ_{eq}	equivalent conductance of binary electrolyte
λ	spatial wavelength, = $2\pi/k$
λ_L	Lamé elastic coefficient of solid matrix
ν	Poisson's ratio

ξ^*	normalization length
ρ_m	fixed charge density of tissue matrix
σ	mechanical stress; electrical conductivity
$\vec{\vec{\sigma}}$	solid stress tensor
Φ	electrical potential
Φ_J	Laplacian potential, = $k_{21}P - k_{22}\Phi$
ϕ_0	porosity (void fraction), = $1/(1+\alpha_0)$
ω	angular frequency, = $2\pi f$

Chapter I

Introduction

1.1 Articular Cartilage

1.1.1 Structure and Function

Articular cartilage (AC) is the dense connective tissue which lines the articulating surfaces of synovial joints and acts as a load-bearing, shock-absorbing, wear-resistant material. Although adult cartilage has neither innervation nor a blood or lymphatic supply, it is a metabolically active tissue. The tissue's sparse population of cells (chondrocytes), comprising less than 10% of the tissue volume [34], is responsible for the synthesis and continual turnover of the complex extracellular matrix (Figure 1.1).

The extracellular matrix of cartilage is highly hydrated, with water comprising 60–80% of the wet weight of the tissue [161]. Of the dry weight of cartilage, 50–70% consists of collagen [142,153], predominantly in a cross-linked fibrillar network containing approximately 95% type II collagen, with smaller amounts of types IX and XI associated with the network as well [59]. In contrast to type I collagen, the main protein constituent of most other connective tissues (e.g., dermis, tendon, ligament, bone) [36], type II collagen has a much higher content of hydroxylysine residues [229], which form the trivalent pyridinoline (hydroxypyridinium) cross-linking groups that hold the network together [59]. Type IX collagen is thought to mediate interactions between type II fibrils and matrix proteoglycans [36,59], while type XI may be involved in regulating the diameter or growth of the fibrils [36]. Several other types of collagen (including V, VI, and X) are also found in small amounts in cartilage, localized to specific regions of the matrix [59]. The collagen content of cartilage is approximately constant with depth into the tissue [142,161].

Most of the remainder of the dry weight of the tissue is comprised of proteoglycan (PG) molecules, predominantly the large aggregating proteoglycan species known as *ag-*

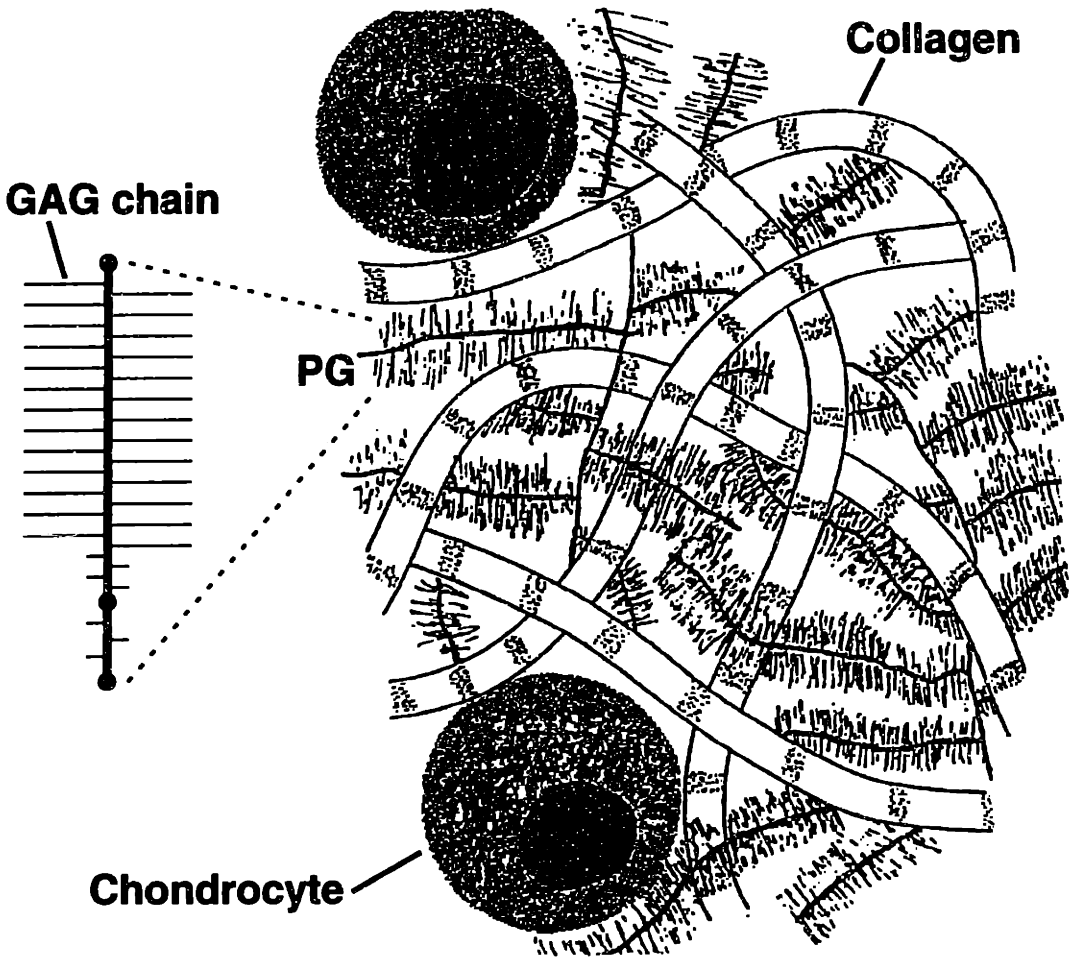

Figure 1.1: Schematic illustration of the structure of articular cartilage, showing cells (chondrocytes), collagen fibrils, and proteoglycan (PG) aggregates with their constituent glycosaminoglycan (GAG) chains bound to the core protein.

grecan. Like all proteoglycans, aggrecan subunits (or monomers)[1] contain a core protein to which long-chain polysaccharides (glycosaminoglycans, or GAGs) are attached [101], radiating outward from the core (Figures 1.1,1.2). Each aggrecan molecule contains 100–150 GAG chains [95,101], consisting of three different types of sulfated GAGs: two structural isomers of *chondroitin sulfate* (CS), which together account for 55–90% of the GAG content of the tissue [153], and *keratan sulfate* (KS). The core protein contains three globular domains (denoted G1–G3), a short linear region to which most of the KS residues are bound, and a much longer CS-rich region of variable length (Figure 1.2). In addition to the GAG chains, a number of *N*-linked and *O*-linked oligosaccharides are also bound to the core protein [95]. Most of the aggrecan subunits in normal cartilage are non-covalently bound to long chains of hyaluronic acid (hyaluronan, or HA), a non-sulfated GAG, to form huge proteoglycan aggregates having molecular weights on the order of 10^8 Da [95]. The specific interaction of HA with the N-terminal binding region of the core protein is stabilized by a 39 kDa *link protein* [94,98]. At physiological pH, the carboxyl and sulfate residues on the CS and KS chains are highly ionized, while the collagen fibrils have no net charge [25,161]. PG aggregate formation acts to immobilize these anionic groups within the matrix, giving the tissue a high negative *fixed charge density,* approximately 5.3 mEq/gm dry weight in normal human femoral head cartilage [39]. To maintain electroneutrality, there is a slight excess of mobile positive ions within the interstitial fluid. Although cartilage is electrically neutral, however, it has a high swelling pressure arising from electrostatic repulsion between the fixed anionic groups; macroscopically, this phenomenon manifests itself as a Donnan osmotic swelling force [56,89,239]. In contrast to collagen content, the PG content of cartilage varies with depth into the tissue, with the highest concentration in the middle region and the lowest concentration at the articular surface [70,143,202,228].

In addition to aggrecan, cartilage contains several smaller proteoglycan species as well as a variety of other noncollagenous proteins, glycoproteins, and lipids. While several

[1] Although aggrecan subunits are often referred to as "monomers" in the literature, they do not polymerize in the classical sense; rather than reacting with each other to form larger structures, they form *aggregates* in which many subunits are individually bound to a single hyaluronic acid chain.

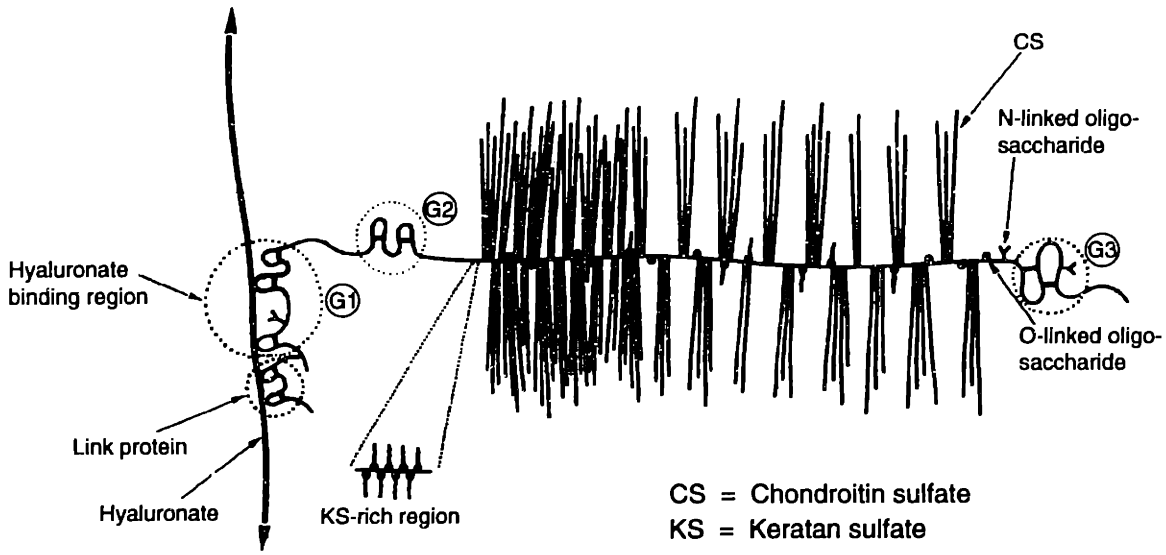

Figure 1.2: Schematic illustration of aggrecan subunit structure, showing GAG chains (CS and KS) attached to the core protein between the G2 and G3 globular domains, *N*-linked and *O*-linked oligosaccharides, and link protein-stabilized interaction of the G1 domain with hyaluronate (adapted from [101]).

of these molecules are unique to cartilage, others, including the glycoprotein *fibronectin* and the small proteoglycans *decorin* and *biglycan,* are ubiquitous among connective tissues [101]. Although the functions of these noncollagenous macromolecules have not been completely characterized, they are believed to be involved in extracellular matrix assembly and in mediating cell-matrix interactions.

1.1.2 Mechanical Behavior

For the purposes of engineering analysis and modeling, articular cartilage may be considered to be a composite material composed of a fibrous mesh (collagen) embedded in a highly hydrated gel of proteoglycans. The high cross-link content of the collagen network is primarily responsible for the tissue's strength in tension, while the high swelling pressure of the PGs enables cartilage to resist compressive loading. There is considerable experimental data to support this model. In a variety of *in vitro* experimental systems, for example, enzymatic extraction of cartilage PGs has been shown to produce a marked decrease in

the tissue's equilibrium compressive modulus [33,96,128,226] with little or no change in tensile stiffness or strength [33,128,217]; conversely, selective digestion of collagen has been found to predominantly affect the tissue's tensile properties [128].

The dynamic rheological behavior of cartilage is the result of interactions between the solid matrix components and the interstitial fluid. Although initial attempts at modeling cartilage mechanics treated the tissue as a viscoelastic solid [100,190], cartilage is more accurately modeled as a *poroelastic* medium; i.e., a fluid-saturated porous material in which viscous effects are predominantly due to frictional interactions between the fluid and solid phases [168]. Historically, the theory of poroelasticity has been developed in the context of geophysics, with applications to consolidation and wave propagation in moist soil [16–18,74], and later extended to describe the mechanics of porous rock [205]. More recent poroelastic models have been developed using a mixture-theory approach [85,129], in which material properties and constitutive relations are derived separately for the fluid and solid phases. Based on this approach, a detailed *biphasic theory* describing the poroelastic behavior of cartilage was developed by Mow and co-workers [150,179,180]. The biphasic composition of cartilage is also responsible for its "weeping bearing" behavior, which is thought to provide the articulating surfaces with the very low coefficient of friction necessary for normal synovial joint function [167].

1.1.3 Electrokinetic Transduction

During the past two decades, investigators have found that electromechanical interactions play a significant role in the physiology of articular cartilage. When the tissue is compressed *in vitro,* for example, mechanical-to-electrical transduction occurs, resulting in measurable electrical potentials [8,90,146]. Although a variety of mechanisms were postulated to account for this behavior, the mechanism is now known to be an *electrokinetic* effect. The arrangement of fixed negative charge groups and an excess of mobile counterions in the interstitial fluid gives rise to the formation of an *electrical double layer* at the interface between the solid matrix and the aqueous phase [171]. Several types of electrokinetic transduction

phenomena in cartilage, including both mechanical-to-electrical (streaming potential) and electrical-to-mechanical (current-generated stress) effects, result from interactions between the electrical double layer and fluid flow [87].

Streaming Potential

Mechanical deformation of the hydrated extracellular matrix of cartilage causes a flow of interstitial fluid relative to the fixed charge groups of the solid matrix. Fluid convection of entrained counterions separates these ions from the oppositely charged matrix macromolecules, giving rise to a voltage gradient, or *streaming potential,* in the direction of fluid flow [66,90,136]. This phenomenon was observed in a series of experiments [64] using cylindrical disks of adult bovine femoropatellar groove cartilage that were uniaxially compressed between two silver chloride electrodes. A small-amplitude sinusoidal compression ($\sim$1% strain) superimposed on a 10–20% static offset compression produced a sinusoidal potential at the same frequency (in the 0.001–20 Hz range), whose amplitude and phase varied with frequency in a manner consistent with an electrokinetic mechanism [65,136]. Mechanically generated streaming potentials have also been studied as an important phenomenon in cortical bone [92,194,214,215,218].[2]

Current-Generated Stress

More recently, a converse electrokinetic phenomenon has been observed in cartilage: *current-generated stress* [65]. Application of an electric current across a cartilage specimen in uniaxial compression (Figure 1.3) exerts an *electrophoretic* force on the negatively charged solid matrix and an opposite directed force on the mobile cations, producing *electroosmotic* flow of interstitial fluid. Together, these two coupled effects produce a deformation within the matrix and a bulk mechanical stress, measurable at the surface

[2]Although electromechanical transduction in bone was originally ascribed to a *piezoelectric* mechanism (i.e., electrical polarization resulting from mechanical deformation of a solid with an asymmetric crystal structure) [76], later studies showed that under physiologically moist conditions, electrokinetic effects are the dominant mechanism for this phenomenon [6,123,185].

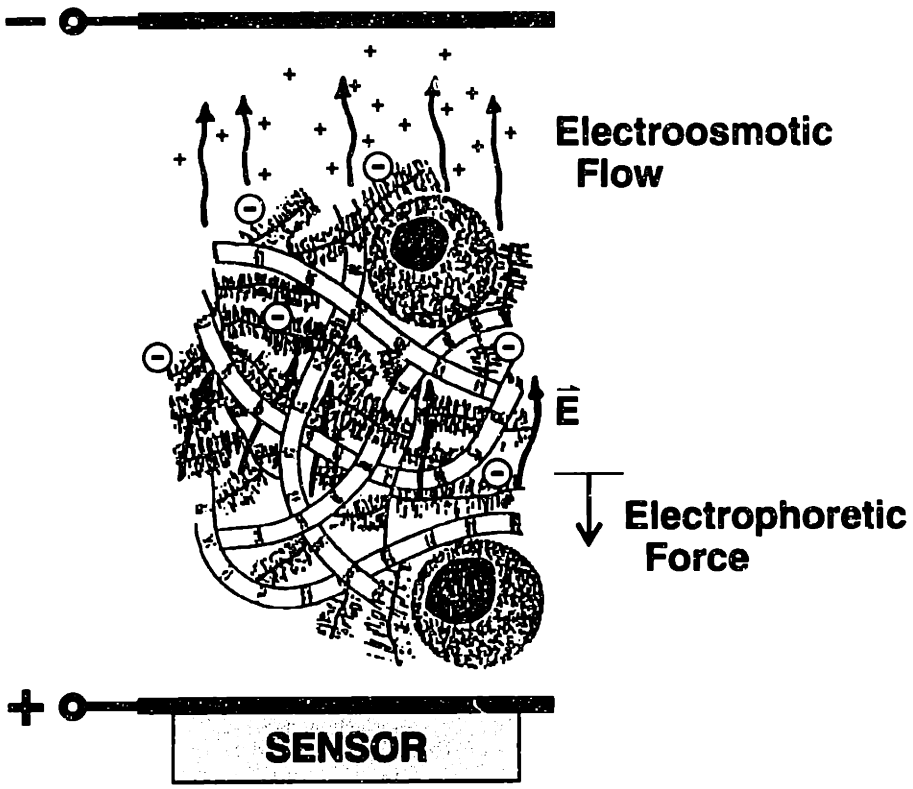

Figure 1.3: Mechanism of current-generated stress (electrical-to-mechanical transduction) in cartilage in a uniaxial geometry. Current injection produces coupled electrophoretic motion of the solid matrix (toward the anode) and opposite electroosmotic fluid flow, resulting in a mechanical stress which can be detected by an overlying stress sensor.

by an overlying stress sensor (Figure 1.3). The mechanism of current-generated stress is similar to electrical-to-mechanical energy conversion observed previously in type I collagen fibers [250] and membranes [91] immersed in an aqueous electrolyte solution. This phenomenon is also physically analogous to gel electrophoresis, with the collagen network in cartilage serving the analogous function of the polyacrylamide gel.

Origin of Electrokinetic Effects in Cartilage

A one-dimensional continuum model of electrokinetic transduction in cartilage has been developed [63,65]. The dynamic amplitude and phase of both streaming potential and current-generated stress have been successfully modeled by combining the phenomenological, macroscopic, linear equations of non-equilibrium thermodynamics for electrokinetic

coupling in isotropic media [49] with the linear biphasic theory [179,180] that relates stress, strain, and fluid flow in cartilage. The model has been found to correlate well with experimental measurements of dynamic stiffness, streaming potential, and current-generated stress made in uniaxial compression [65]. The application of continuum electromechanical concepts, as developed by J. R. Melcher [171], to both cartilage and synthetic polymer gels is discussed further in Reference [15].

The molecular mechanisms that underlie analogous electrokinetic phenomena have been characterized and theoretically modeled in a variety of colloidal and polymeric gel systems [140,187]. The molecular constituents responsible for electrokinetic phenomena in cartilage have been studied by examining the dependence of compression-induced streaming potentials on bath pH and ionic strength [64,136]. These studies confirmed that at physiological pH, the charged proteoglycan molecules are the predominant source of the potentials; hence, the transduction response is seated in the fixed charge groups of the cartilage extracellular matrix. Measuring changes in tissue properties resulting from loss of these charge groups, as occurs in degenerative conditions such osteoarthritis (described in the next section), could provide a sensitive means of quantitatively assessing the functional mechanical state and biochemical composition of degenerated tissue.

1.2 Osteoarthritis

Osteoarthritis (OA), or *degenerative joint disease,* is a heterogeneous disease of uncertain etiology characterized by progressive loss of articular cartilage, particularly from weight-bearing joints. The pathology of cartilage degeneration has been recognized for at least 250 years [109], and skeletal evidence of the disease has been found in human remains dating back to the Neanderthal era [124]. The most common human joint disorder, OA is also a major, if not the *the* major, cause of disability in the United States [61]. OA has the highest morbidity of any human illness [20], mainly because of its high prevalence: an estimated 61 million Americans between the ages of 18 and 79 have radiologic evidence of the disease [107]. The economic impact of the disease is considerable as well; in 1988, the

total costs associated with OA in the U.S. amounted to $54.6 billion, or 43% of the total cost of all musculoskeletal conditions [198].

1.2.1 Pathology

Historically, OA has been viewed as a "wear and tear" disease of the joints, and cartilage degeneration resembling OA has been successfully induced in a variety of animal models (reviewed in [237]) by imposing excessive and/or abnormal joint loading forces. A more current view of the pathogenesis of OA is that some (as yet unkown) primary insult results in the release of degradative enzymes, particularly the metalloproteinases *collagenase* and *stromelysin* [197], which degrade components of the extracellular matrix. The chondrocytes initially increase their biosynthetic activity in an attempt to repair the damage, but eventually they fail, leading to erosion of cartilage from the articular surface [176]. Thus, the pathology of OA results from the combination of excess degradation and abnormal repair.

The gross pathological changes seen in osteoarthritic cartilage include surface fibrillation, fissure formation, and erosion, eventually with full-thickness loss of cartilage and "eburnation" of the exposed subchondral bone [176]. Reactive changes, including sclerosis, pseudocyst formation, and growth of osteophytes (bone spurs) at the joint margins, occur in the underlying bone. Synovitis is common and may be histologically indistiguishable from the inflammation of rheumatoid arthritis [82,141,204]. Calcification of cartilage in OA has also been observed [52,204] and may be causally related to the synovial inflammation.

1.2.2 Biochemical Changes

The gross morphological changes described above appear relatively late in the course of the disease and are preceded by distinct biochemical changes in the affected cartilage, as first described by Hirsch some 50 years ago [103]. These changes occur throughout the affected joint [169,177,208,241] and have been detected in tissue that still appeared grossly normal [39,127,169,208,243].

It has been widely reported that the PG content of osteoarthritic cartilage is substan-

tially lower than normal [21,22,103- 105,116,154,163,241], as determined by biochemical analysis of the sulfated GAG content of the tissue. The degree of loss has been shown to correlate well with the severity of the disease, as assessed by a histological-histochemical grading system [154]. Histologic staining of osteoarthritic tissue has demonstrated that the PG loss is *nonuniform* with depth into the tissue, beginning at the articular surface and proceeding progressively inward [21,103,118,170]. The PGs which remain in osteoarthritic cartilage are characterized by a number of qualitative abnormalities, including decreased aggregate formation [29,116,169,177], decreased size of both PG aggregates [29,151,240] and aggrecan subunits [22,115,116], and increased extractability from the tissue [26,151,169,233]. These changes support the hypothesis that in OA the matrix PGs are cleaved, presumably by proteolytic enzymes, at multiple cleavage sites [145,216]. Furthermore, the PGs of osteoarthritic cartilage have a higher than normal ratio of chondroitin sulfate to keratan sulfate [22,169,233] and thus resemble the PGs of immature cartilage, reflecting the increased *de novo* synthesis of aggrecan by the chondrocytes in an attempt to repair the tissue damage.

Despite the decreased content of intact PG aggregates, which are responsible for maintaining the highly hydrated state of normal cartilage, osteoarthritic tissue has a *higher* water content than normal [22,39,93,115,155,169,222,241]. This is thought to result from damage to the collagen network (prior to gross fibrillation), which normally opposes the high swelling forces developed by the PGs [160,162,241]. The changes in water content and GAG content in OA are opposite to those found in normal cartilage with increasing age [93,242]; thus, OA does not appear to be simply an inevitable by-product of the aging process. The net result of a *decreased* PG content and *increased* water content in osteoarthritic cartilage is a decrease in the fixed charge density, with concomitant changes in the material properties of the tissue, including decreased compressive [7,103,105,127,208,222], tensile [208,222], and shear [135,222] moduli. As with the biochemical changes seen in early OA, these biomechanical alterations have been observed in cartilage that appeared grossly normal [7,127,135,208].

There is some evidence that the early degenerative changes of OA may be reversible [20,195], and it has been hypothesized that a "threshold" exists beyond which the process becomes irreversible [195]. Recent *in vitro* studies using a rabbit model [238,248] have suggested that cleavage of the collagen network may be the threshold event. Thus, detection of the earliest biochemical changes in OA, while the disease process is still reversible, could potentially lead to improved treatment. However, at present there exist neither a good method for detecting and monitoring the early stages of degeneration nor an effective disease-modifying treatment for OA.

1.2.3 Treatment

The methods currently available for therapy of osteoarthritis (physical therapy, medication, and surgery) are palliative, serving to alleviate symptoms and improve patients' mobility without actually altering progression of the disease process. At present the only approved drugs for treating OA are nonspecific analgesic and/or antiinflammatory agents [176], some of which may actually exacerbate the disease process by inhibiting GAG synthesis [189]. Several putative "chondroprotective" agents, including GAG polysulfate (Arteparon) and GAG-peptide complex (Rumalon), have been developed and investigated, but more definitive trials using standardized, validated assessment techniques will be needed to establish their efficacy [234]. A more recent approach to antiarthritic therapy has been to develop drugs that inhibit, by various means, the actions of matrix metalloproteinases [244], in the hope that inhibition of these degradative enzymes could slow or even reverse progression of OA. However, a major obstacle to the development of effective antiarthritic drugs has been the lack of a good *in vivo* tool for monitoring disease progression (particularly in the early stages of the disease) and thus assessing the efficacy of treatment, in either human patients or animal models of the disease [234].

Surgical management of OA includes both arthroscopic and open surgical procedures (reviewed in [35]), ranging from debridement of the affected joints to total joint arthroplasty. Total knee replacement provides significant benefits to the patient (reduction

of pain and improved joint range of motion), but at a cost of approximately $30,000 per procedure [97]. Arthroscopic debridement is a much less invasive procedure, with a correspondingly lower associated morbidity [4]. However, while short-term outcomes of this procedure are generally favorable [201], the long-term benefits are much less clear [37]. Earlier diagnosis of OA, coupled with effective disease-modifying drug therapy, could greatly reduce the need for surgical intervention.

1.3 Diagnosis of Oseoarthritis

At present, the diagnosis of OA is typically made on the basis of the patient's medical history, findings on physical examination, laboratory tests (to rule out rheumatoid arthritis and related diseases), and radiography [3]. Typical physical findings include pain, inflammation, stiffness, crepitus, and limited range of motion of the affected joints. A number of investigators are working on developing a variety of new physical and biochemical techniques for detecting osteoarthritic degeneration. While some of these techniques reveal changes resulting from loss of cartilage thickness and thus are only capable of detecting relatively late-stage disease, other techniques have the potential to enable diagnosis of OA at much earlier stages than is currently possible.

1.3.1 Imaging

Radiography

The plain-film x-ray remains the "gold standard" in the diagnosis of OA, even though the changes detectable by x-ray are limited to late, probably irreversible lesions and the correlation between radiographic findings and disease progression is inconsistent [1,28]. Radiographic evidence of the disease includes reactive bony changes and joint space narrowing, an indirect indicator of cartilage loss [235]. *Double-contrast arthrography,* a radiographic technique in which a water-soluble contrast medium and air are introduced into the joint as contrast agents [38,73], provides improved localization of focal cartilage

defects [235] but is technically more difficult to perform (since it requires precise positioning of the x-ray beam) and is less accurate than techniques such as scintigraphy [235] or arthroscopy [120] at indicating disease severity.

Magnetic Resonance Imaging

Since magnetic resonance imaging (MRI) allows visualization of soft tissues, including cartilage, its potential as an alternative imaging modality for diagnosis of OA has been studied in both animal models [191,209] and human subjects [42,113]. Although MRI using the standard *spin echo* protocol has been found to be a more sensitive indicator of disease severity than radiography, showing changes earlier in the course of the disease [42,191,209], the findings are limited to gross morphological changes such as loss of cartilage thickness. Alternative imaging sequences, however, have also been investigated *in vivo* and found to reveal quantitative changes in signal intensity corresponding to PG loss from osteoarthritic joints [131]. More recently, a *contrast-enhanced* MRI technique has been developed [75,134] which could enable improved noninvasive determination of tissue composition. A paramagnetic, cationic contrast agent (such as free Mn^{2+} ions) introduced into the tissue *in vitro* binds to matrix GAG chains, producing an enhanced MRI signal whose intensity varies with tissue GAG content. Although such a technique could ultimately lead to an *in vivo* method for early diagnosis of OA, several obstacles remain, including toxicity of the contrast agents used at present [134]. Nuclear magnetic resonance (NMR) spectroscopy techniques have also been developed which allow quantitative determination of tissue GAG and collagen content [138,139]; however, these techniques have not yet been adapted for *in vivo* imaging applications.

Sonography

Ultrasound imaging (sonography) has been used to measure cartilage thickness in human knees; qualitative changes in surface and internal characteristics of osteoarthritic tissue have also been detected [2,166]. A recent advance is the development of a high-frequency

ultrasound imaging instrument for intra-articular use during arthroscopy [181]. However, although the echogenic properties of the tissue change in response to even subtle morphological changes, no correlation has been found between sonic velocity in cartilage and biochemical *composition* of the tissue [181]. Thus, the ability of this technique to detect *early* degenerative changes may be limited.

Scintigraphy

Radionuclide scanning (scintigraphy) techniques, using bone-specific agents such as technetium-99m labelled diphosphonates, have been adapted for use in the diagnosis of OA. The effectiveness of this approach, however, is inconclusive; while some studies have found that scintigraphic changes precede radiographic abnormalities in joints of the hand [112,164], other investigators have reported that scintigraphy is less sensitive than radiography at detecting early degenerative changes in the knee [55]. The ability of scintigraphy to predict subsequent disease progression has been assessed in the knee joint [50]; while the technique has a very high negative predictive value, the positive predictive value was only 39%. A recently synthesized radiopharmaceutical, [^{75}Se] bis[β-(N, N, N-trimethylamino)ethyl]selenide diiodide ([^{75}Se] BISTAES), has been shown to preferentially concentrate in cartilage when administered systemically to guinea pigs [251] and thus has the potential to become a clinically useful cartilage-specific imaging agent.

1.3.2 Biochemical Markers

Since the earliest changes in OA are biochemical, there has been considerable interest in identifying biochemical markers of cartilage degradation and quantitatively relating the levels of these markers in various bodily fluids to the degree of disease progression. Immunological methods have been developed for identifying keratan sulfate (KS) epitopes in serum [41,236], and elevated serum KS levels have been detected in OA patients. Elevated levels of PG degradation products [132] and pyridinoline cross-links (as a cartilage-specific marker of collagen degradation) [19,219] have been found in the urine of OA patients as

well. However, doubts have ben raised about the utility of such generalized marker levels as a means of diagnosing OA or monitoring disease progression [27] because of the high variability of normal levels and the fact that serum or urinary levels of biochemical markers provide a systemic, rather than localized, measurement of joint involvement. Measurement of KS [40], other PG degradation products [144], and peptide markers of type II collagen turnover [225] in joint fluid may overcome some of these problems by providing a more localized indication of specific joint disease. However, interpretation of these results is complicated by the fact that even low-grade synovial inflammation can significantly alter the rate of clearance of these markers from the joint fluid [182].

1.3.3 Arthroscopy

Over the past 30 years, arthroscopy has become an important technique in the diagnosis and therapy of OA, particularly in disease affecting the knee [4]. In this procedure, a 4 mm diameter arthroscope tube with a powerful light source is inserted into the joint capsule, allowing direct visualization of the joint surface, ligaments, and menisci. Diagnostic and surgical instruments are inserted through a separate incision and manipulated under visual control. Because the complication rate and morbidity associated with the procedure are so low, arthroscopy is increasingly being performed on joints that are only minimally symptomatic [119], before pathological changes are evident by other techniques such as radiography [28,62,147]. The recent advent of a 1.8 mm diameter *needle arthroscope* has the potential to transform arthroscopic examination from a hospital-based procedure to a routine office procedure, although the needle arthroscope is somewhat less sensitive than the full-size device in assessing degenerative changes in joint cartilage [114].

During a diagnostic arthroscopic examination of the knee, the examiner typically inspects the AC surface for gross changes (such as fibrillation) and palpates the patellar AC with a blunt probe to subjectively assess the degree of softening ("grade I chondromalacia") due to increased water content and decreased PG content [230]. Dashefsky [48] has developed an experimental instrument, consisting of a mechanical indenter attached to a

miniature pressure transducer, for quantitatively measuring cartilage compliance during arthroscopy. Among a group of 107 human knees with "patellofemoral symptoms and signs" that were tested with the device, more than 90% were evaluated as "soft"; over half of these knees, however, showed no visually observable changes in the articular surface. More recently, Kiviranta *et al.* [130], using an arthroscopic indenter instrumented with strain gauges [148], detected 30–40% decreases in cartilage stiffness in the patellar cartilage of patients with chondromalacia as well as more subtle changes throughout the knee joint, even in cartilage that appeared grossly normal. These results suggest that visual inspection of the joint surface during arthroscopy may not be sufficient to detect early osteoarthritic degeneration and that quantitative diagnostic tools capable of measuring physical properties of cartilage are needed.

1.3.4 Noninvasive Mechanical Testing

Several noninvasive mechanical techniques have been investigated as possible methods for diagnosing osteoarthritis. For example, Chu *et al.* [43] used a pair of microphones applied to the skin overlying the knee joint to record the acoustical signals produced in the joint during active flexion and extension of the knee. In contrast to normal and rheumatoid knees, the signals recorded from patients with known osteoarthritis had a much broader power spectrum, with significant energy throughout the entire audible range (60–20,000 Hz).

Other investigators have used accelerometers attached to the knee to measure vibration signals during active or passive joint motion, a technique termed "vibration arthrography" or "vibroarthrography" [165,178,203]. Recent improvements in sensor technology [178,203] have enabled these measurements to be made with a single miniature piezoresistive accelerometer mounted over the patella. In contrast to normal joints, which exhibit a smooth signal with occasional "patellar clicks" [165], knees with osteoarthritis or chondromalacia exhibit an irregular response, with significantly greater mean power in the 100–500 Hz range [203].

Mechanical impact testing has also been investigated as a means of detecting carti-

lage degeneration in human knee joints [200]. An impact is applied to the heel of a subject using a hammer instrumented with a force transducer; an accelerometer mounted either on the tibial tuberosity, medial femoral condyle, or iliac crest records the resulting oscillatory acceleration. In a small experimental series, patients with known osteoarthritis were found to have a significantly higher peak acceleration for a given applied force as compared with normal subjects, with a smaller difference in damping coefficient as well [200]. These differences were attributed to a decreased shock absorbing capability of the degenerated joints. With impact testing as well as acoustic and vibrational signal analysis, the differences between normal and osteoarthritic joints depend on gross changes in the degenerated joints, such as loss of cartilage thickness. It is not clear how early in the disease process these techniques would be capable of distinguishing diseased tissue from normal.

1.3.5 Mechanical and Electromechanical Measurements

As discussed in Section 1.2.2, osteoarthritic cartilage is significantly softer (i.e., less resistant to compressive loading) than normal tissue, due to loss of the charged proteoglycan molecules from the matrix. Because electrokinetic transduction in cartilage (Section 1.1.3) also depends critically on the presence of these charge groups, the magnitude of electrokinetic effects is sensitive to changes in the matrix fixed charge density. A number of *in vitro* studies have demonstrated that enzymatic degradation of cartilage PGs, as a model for osteoarthritic degeneration, results in a reduction in dynamic stiffness as well as a relatively greater reduction in streaming potential amplitude [66,136,175]. An animal model, in which OA-like degenerative changes developed in rabbit knees following meniscectomy, showed similar changes [105]. More recently, using an *in vivo* model for cartilage degradation, Bonassar *et al* [24] found that intra-articular injection of stromelysin into rabbit joints resulted in loss of aggrecan from the cartilage surface, producing a significant decrease in electrokinetic coefficient but little or no change in tissue mechanical properties (equilibrium modulus, dynamic stiffness, and hydraulic permeability). Thus, measurement of electrokinetic properties has been shown to provide a more sensitive indicator of molecular-level

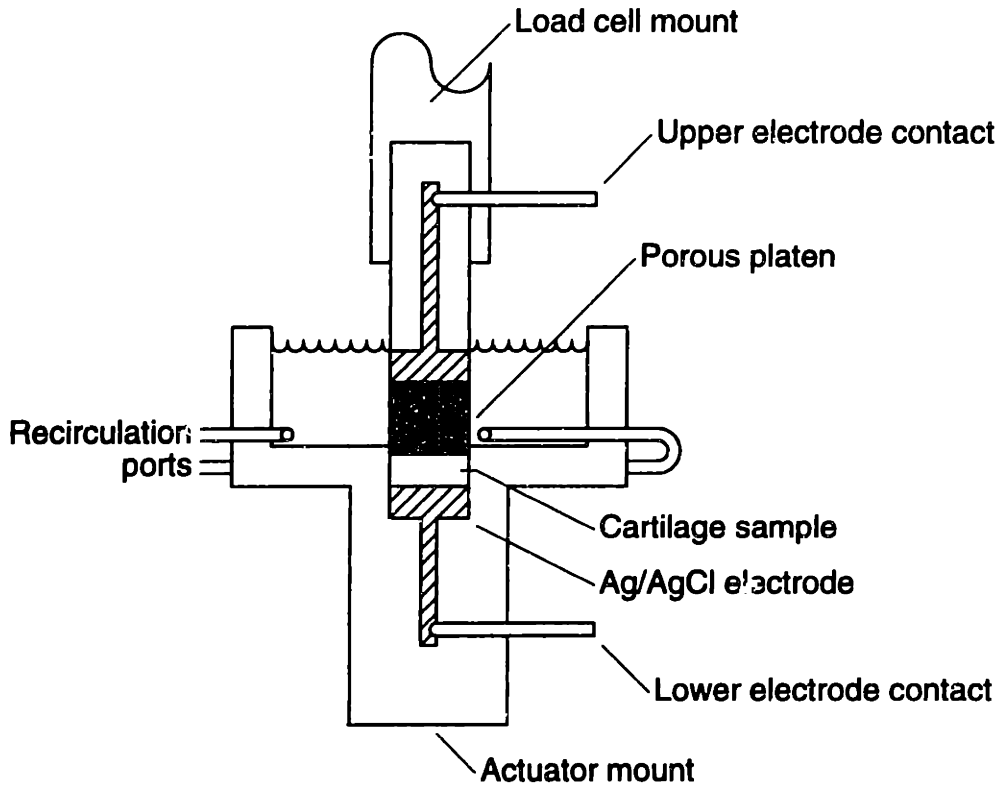

Figure 1.4: Schematic illustration of chamber used for uniaxial measurement of streaming potential and current-generated stress in cartilage. This apparatus requires that a cartilage disk be excised and placed between two electrodes, precluding its use in intact joints.

degradative changes than purely mechanical tests.

Previous measurements of current-generated stress and streaming potential in cartilage [63,64,66] have utilized a *uniaxial* configuration (Figure 1.4), in which it was necessary to access two opposite surfaces of an excised cartilage disk. Theoretical analysis [210,211], however, suggested that current-generated stress in cartilage could also be detected via measurements made with an electrode array applied to the articular surface of intact cartilage. This technique of *electromechanical surface spectroscopy,* described in the next section, provides a method of nondestructively measuring functional electromechanical properties of cartilage on intact joints via a surface probe. The development of such a technique, which could ultimately be incorporated into an arthroscopic instrument, is the goal of this thesis work.

1.4 Repair of Focal Cartilage Defects

A variety of pathologic conditions, including osteoarthritis, trauma to the joint, and diseases such as osteochondritis dissecans, can produce focal defects in the articular surface. Because of the avascular nature of the tissue, partial-thickness defects do not heal significantly, as inflammatory cells cannot reach the tissue. Full-thickness defects (down to subchondral bone) tend to heal with the production of fibrocartilage (containing predominantly type I collagen), which is mechanically inferior to noamrl articular cartilage in bearing the joint loading forces [152]. In recent years, there has been interest, and some progress, in developing techniques for improving the healing of cartilage defects with the production of functional repair tissue. For exampie, autografts of periosteum, the cambium layer of which contains mesenchymal cells capable of differentiating into chondrocytes, have been used in both a rabbit model [184] and a limited number of human subjects (reviewed in [207]), producing repair tissue which grossly, histologically, and biochemically resembled normal articular cartilage. An alternative approach has been to implant cultured chondrocytes, suspended in either a type I collagen sponge [9,30] or a biodegradable synthetic polymer gel [72,174], in some cases with added growth factors [9]. In a recent clinical trial [30], autologous chondrocyte transplantation produced good-to-excellent clinical results in 14 out of 16 patients with focal defects on the femoral condyle; the results were less satisfactory with OA-like lesions of the patella.

In rabbit models and, in some cases, by biopsy of human subjects, the quality of the repair tissue has typically been assessed by comparing the gross tissue morphology, a semiquantitative assessment of the histology, and the biochemical composition (including GAG and type II collagen content) with that of normal or control tissue. The few studies in which the mechanical behavior of repair tissue was assessed [84,174], however, revealed that the repair tissue was more compliant and more permeable than native cartilage; thus, the *functional* behavior of the repair tissue may be different from that of normal cartilage. Measuring electrokinetic phenomena such as current-generated stress in the repair tissue could provide a more quantitative functional assessment of the status of the tissue; compar-

ing the response with that of adjacent normal tissue would provide an internal control for the measurements. Thus, surface spectroscopy could provide a means of nondestructively monitoring the progress of the healing process and assessing the quality of the repair tissue produced by these new therapies.

1.5 Surface Spectroscopy

1.5.1 Introduction: Imposed ω-k Sensing

The term *surface spectroscopy* will be used in this document to refer to a series of related techniques for measuring electrical or electromechanical properties of a material by applying a spatially and temporally periodic sinusoidal signal, typically via an interdigitated electrode array, to a single surface of the material and simultaneously recording an electrical or mechanical response at the same surface. This method is denoted "spectroscopy," by analogy to measurement and imaging techniques such as *impedance spectroscopy* [149], because it involves measurements made over a range (spectrum) of imposed frequencies (both temporal and spatial). This definition includes the method of *interdigital dielectrometry,* described in Section 1.5.2, in which dielectric properties of a material are estimated from surface electrical measurements, as well as *electromechanical surface spectroscopy,* discussed in Section 1.5.3, which provides the theoretical basis for the work described in this thesis. The general technique has also been termed "imposed ω-k sensing" [173,254] because the medium is excited at a specified temporal (angular) frequency, ω, by an electrode structure having a spatial period $\lambda = 2\pi/k$ (determined by the electrode geometry) and hence a dominant wavenumber k. The technique has also been described as "intimate sensing" [254] because the measurements reflect local material properties within a short distance of the electrode structure.

The imposed ω-k approach has several advantages over classical methods of measuring dielectric or electromechanical properties, in which the material under test is placed between a pair of plane-parallel electrodes. First, because the excitation is coupled to the

medium from a single surface, measurements can be made nondestructively, an important requirement for *in vivo* measurement of cartilage properties. Second, because the electric fields generated by the electrodes are quasistatic and periodic along the surface, they tend to decay exponentially into the material, with a penetration depth on the order of $\lambda/5$ to $\lambda/3$ [245,254]. Thus, different depths of the material may be tested by varying the imposed spatial wavelength, and spatial homogeneities in material properties can be detected by making surface measurements using a series of imposed spatial wavelengths. In contrast, parallel-plate dielectrometry provides a measure of material properties *averaged* over the entire sample thickness. Finally, modern microfabrication techniques enable the excitation electrodes, sensing electrodes, and associated circuitry to be integrated on a single chip.

1.5.2 Interdigital Dielectrometry and Magnetometry

A microelectronic device has been developed for measuring the low-frequency complex dielectric constant (complex permittivity) of materials via interdigitated surface electrodes [220,224]. The silicon "microdielectrometer" chip, measuring less than 2×2 mm, contains two interdigitated electrodes (Figure 1.5): one, the *driven gate,* is connected to an external excitation, while the other, the *floating gate,* extends over the channel region of a depletion-mode n-channel metal-oxide-semiconductor field-effect transistor (MOSFET) on the chip. A layer of silicon dioxide insulates the electrodes from the silicon substrate, so that the electrical connection between the driven and floating gates is primarily through the sample material, which is placed in contact with the electrode array. Applying a sinusoidal voltage, v_D, to the driven gate causes a time-varying current to flow through the sample to the floating gate, producing a time-varying voltage, v_F, at the floating gate which modulates the FET channel conductance. Since the complex transfer function relating the floating gate voltage (as measured by the FET) to the driving voltage depends on the real and imaginary parts of the dielectric constant (ϵ' and ϵ'', respectively), these values can be determined by comparing the measured amplitude and phase with a set of calibration curves. Applications of microdielectrometry include monitoring the curing of epoxy resins [221,224], measure-

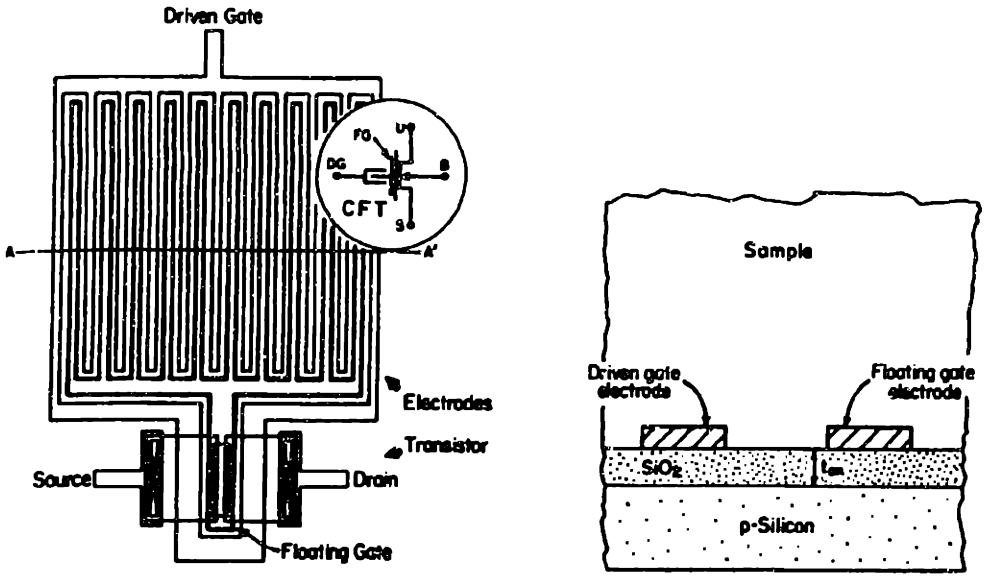

Figure 1.5: Top view (left) and cross-section (right) of the sensor portion of the microdielectrometer chip, showing the interdigitated "driven" and "floating" gate electrodes, insulating oxide layer, and silicon substrate (from [224]).

ment of relative humidity of air (by coating the chip with a thin film of polyethylene oxide, a polymer whose dielectric properties vary with moisture content) [77], monitoring moisture adsorption into transformer pressboard [245], measurement of spatial inhomogeneities in ice [117], and robotic proximity and feature sensing [81].

An analogous magnetic device, termed a *meandering wire magnetometer,* has been designed for measuring properties of conducting and magnetic media [83,172]. With this type of sensor, a sinusoidal current, i_1, having temporal frequency ω, is applied to a "meandering" primary winding (driver) placed on or near the surface of the material being tested. The geometry of this winding determines the imposed spatial wavelength (and hence, since the system is magnetoquasistatic, the penetration depth). The resulting sinusoidal voltage, v_2, across the terminals of a parallel secondary winding (sensor) is measured; material properties, including magnetic permeability and electrical conductivity, are determined from the magnitude and phase of the transinductance, $v_2/j\omega i_1$. Potential applications of meandering-wire magnetometry include noninvasive monitoring of magnetization and conduction properties of materials during manufacture, measurement of properties of thin

magnetizable films (e.g., in magnetic memories), and proximity sensing [172].

A continuum model of the quasistatic electric field interactions in interdigital dielectrometry has been developed [254]. The dielectric properties of a linear medium can be represented by a complex *surface capacitance density,* defined as the complex ratio of the normal displacement field at the electrode-medium interface to the interfacial potential. The material properties may vary in a direction perpendicular to the plane of the electrodes but are assumed to be uniform within any plane parallel to the electrodes. Given an arbitrary surface capacitance density, which is a function of the imposed frequency and wavelength, the model predicts the complex transfer relation between the driven and floating electrodes as a function of the electrode geometry and the continuum parameters of the medium. Analysis of the electrostatic field problem requires solution of a mixed boundary value problem, since the potential is constrained at the electrode surfaces but merely required to be continuous across the surface in the inter-electrode regions. Because the length of the electrodes is much greater than their width, the resulting fields are approximately two-dimensional, simplifying the analysis. Numerical solutions have been obtained for three different configurations: a semi-infinite half-space with uniform complex permittivity, a semi-infinite uniform medium with a surface charge density at the electrode interface, and a finite-thickness layer of uniform permittivity. Given a series of measurements (transfer function gain and phase), various material properties, including layer thickness, permittivity, and surface conductivity, can be determined by applying parameter estimation techniques using the appropriate geometric model. This approach has been used to measure the thickness of particle sedimentation layers and plasma-deposited thin films, the complex permittivity of transformer oil and oil-impregnated paper, and the surface conductivity resulting from water adsorption on a silicon substrate [252]. The technique has also been incorporated into a device for measuring the moisture content of transformer oil [253] as a means of averting potentially disastrous and costly transformer failure resulting from electrical breakdown of the normally insulating oil.

Multiple-Wavelength Sensing

The dielectrometry devices described above are capable of making measurements over a wide range of temporal frequencies (0.005 Hz to 10 kHz) but at a single spatial wavelength, determined by the geometry of the interdigitated electrode array. Theoretical analysis [246] has demonstrated the feasibility of using *multiple-wavelength* measurements to determine spatially nonuniform permittivity profiles in materials. Recently, a device has been developed [245] that allows measurements to be made simultaneously at three different wavelengths, corresponding to three different penetration depths into the material. The sensor contains three sets of interdigitated etched copper electrodes, with imposed spatial wavelengths of 1 mm, 2.5 mm, and 5 mm, on a flexible polymer film substrate. Although the three arrays share a common drive signal, the sensor electrodes are electrically shielded from each other by guarded shield electrodes. This device was used to measure the time course of adsorption of moisture into vacuum-dehydrated oil-free transformer pressboard ($\sim$1 mm thick). As moisture diffused into the material (from the surface opposite the sensor), the long-wavelength sensor was the first to detect a change in permittivity, as indicated by changes in the gain and phase of the voltage transfer function. The shortest wavelength sensor did not detect a change in moisture content until approximately five hours later, when the moisture had diffused far enough into the board to affect the dielectric properties close to the electrode surface. From the data, the diffusion time constant and diffusivity could be estimated. The ability of the sensor to detect the transient spatial variation in moisture content supports the utility of multiple-wavelength ω-k sensing for localizing spatial inhomogeneities in dielectric properties within a medium.

1.5.3 Electromechanical Surface Spectroscopy

In addition to measuring purely electrical or magnetic material properties, the imposed ω-k technique can also be used to study *electromechanical* transduction effects in materials. For example, the technique has been used to probe double-layer transduction at a polarized mercury-electrolyte interface [255]. An interdigitated electrode structure in the electrolyte

solution applies a sinusoidal standing-wave voltage with imposed ω and k, producing a periodic shear surface force density at the interface. Motion of the interface alters the double-layer charge distribution, generating an electric field within the electrolyte which is detected by interdigitated sensor electrodes. The response depends on the electrical and mechanical parameters of the interface, including the equilibrium surface elasticity and surface charge density, which can be estimated by comparing experimental measurements with a continuum electromechanical model of the system.

Mechanical-to-electrical transduction in charged collagen membranes has also been investigated using an imposed ω-k approach [88]. Applying a standing wave of mechanical displacement (via an array of pistons capped with latex membranes and driven by a loudspeaker) to a membrane suspended in an aqueous electrolyte solution induced a trans-membrane potential having the same frequency and wavelength. As predicted by a continuum electrohydrodynamic model of the system, resonance of the electrical response was found to occur at certain frequencies, reflecting the interaction between membrane elasticity and bulk fluid inertia (coupled by fluid viscous stresses). The resonance frequency varied with system geometry, membrane tension, and bath pH in a manner consistent with an electrokinetic phenomenon.

1.5.4 Electromechanically Coupled Poroelastic Medium

The surface spectroscopic technique which forms the basis for the cartilage surface probe described in this thesis relies on making direct measurements of the mechanical surface stresses generated by an applied electric current (Figure 1.6). Sachs [210,211] has modeled the fields, forces, and flows generated within an electromechanically coupled poroelastic medium, such as cartilage (see Section 1.1.3), in response to a periodic electric current applied to the surface. The model predicts the two-dimensional distribution of current density, horizontal and vertical displacement and velocity, pressure, and electrical potential throughout the medium resulting from an applied sinusoidal current with imposed ω and k; superposition of modal solutions can be used to obtain the response to more general

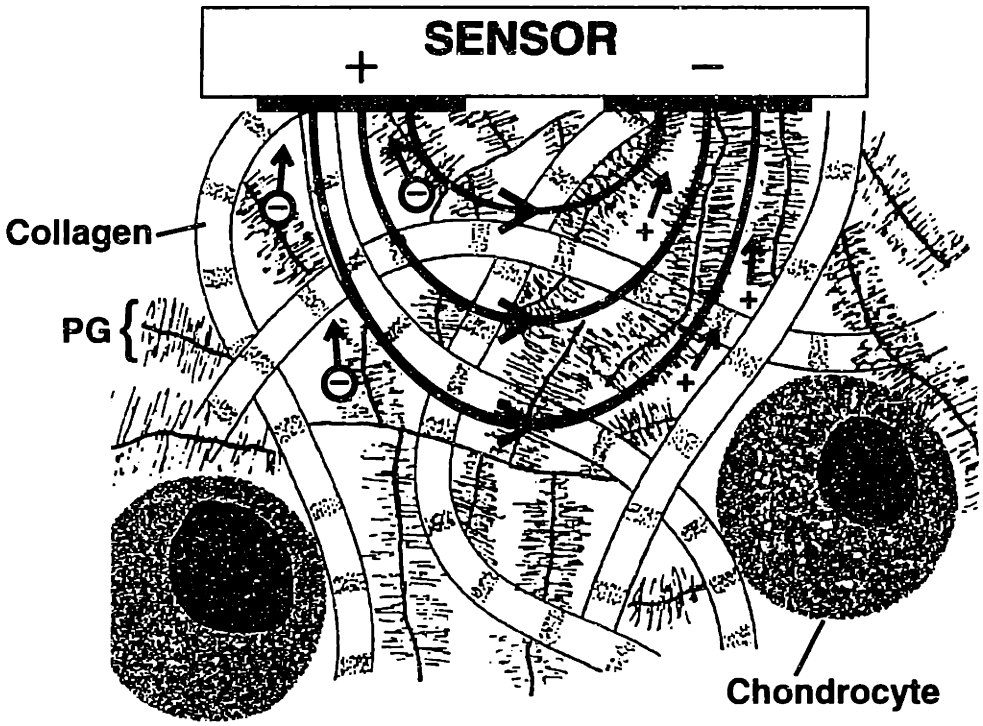

Figure 1.6: Mechanism of current-generated stress (electrical-to-mechanical transduction) in cartilage produced by surface electrodes. As in Figure 1.3, current injection (heavy arrows) produces coupled electrophoretic motion of the negatively charged solid matrix and opposite electroosmotic fluid flow (due to an excess of cations in the interstitial fluid), resulting in a mechanical stress which can be detected at the surface by an overlying stress sensor.

periodic time- and space-dependent excitations. The distributions resulting from both an ideal sinusoidal excitation as well as from a finite electrode array were analyzed, with qualitatively similar results for the current distribution. Analysis of the latter case requires solution of a mixed boundary value problem, as in the continuum model of dielectrometry. The converse problem of determining the electrical streaming potential resulting from an imposed sinusoidal mechanical displacement at the cartilage surface has also been analyzed [210,212].

Figure 1.7 shows the theoretical distribution of current density within a cartilage specimen produced by a two-electrode surface array, the simplest possible electrode configuration. The model predicts a complicated distribution of mechanical stress within the

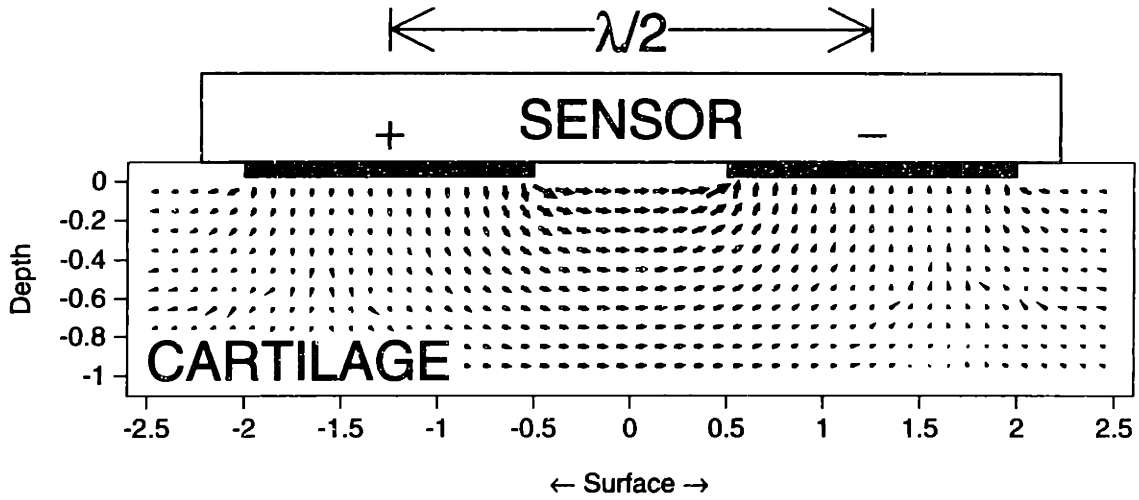

Figure 1.7: Theoretical distribution of current density produced by a two-electrode surface array, determined by solving Laplace's equation, $\nabla^2 \vec{J} = \vec{0}$, with the appropriate boundary conditions. Arrows indicate direction and relative amplitude of current density. The penetration depth depends on the effective spatial wavelength.

bulk of the tissue. However, the normal stress at the surface has the same spatial periodicity as the current excitation (but is temporally out of phase). This result suggests that current-generated stress can be assessed by simultaneously measuring the normal mechanical stress exerted on the electrodes in response to an applied current. For this purpose, the cartilage surface probe utilizes a piezoelectric stress sensor, as described in Section A.1.

Wavelength and Penetration Depth

The depth to which the current penetrates into the medium is proportional to the effective spatial wavelength, which is equal to twice the center-to-center distance between adjacent electrodes. The separation between the edges of adjacent electrodes is an independent parameter; a separation equal to $\lambda/4$ has been found to be satisfactory for interdigital dielectrometry [254]. By changing the imposed spatial wavelength, various depths of the medium can theoretically be "probed." One strategy for obtaining multiple-wavelength capability with a single device is to use an array of *independently addressable* electrodes. This

approach is illustrated in Figures 1.8 and 1.9 with an array of 12 evenly spaced electrodes. In a *short-wavelength* configuration (Figure 1.8), the electrode polarity alternates from each electrode to the adjacent electrode; since penetration depth is a fraction of the spatial wavelength, a measurement made with a probe using this configuration would only reflect material properties just below the surface. In a *long-wavelength* configuration (Figure 1.9), the outer four electrodes on each side are driven by opposite polarity, while the middle four electrodes are allowed to electrically "float." With this configuration, the current density distribution resembles the distribution produced by the two-electrode array (Figure 1.7), with full-thickness penetration into the sample. Measurements made using this configuration would therefore reflect bulk material properties of the entire thickness. Intermediate wavelengths are also obtainable by a suitable choice of polarity for each electrode. Analogous techniques have been used to obtain variable-wavelength capability with interdigital dielectrometry [81,117,173] and magnetometry [172].

Thus, theoretical analysis suggests the feasibility of nondestructively measuring current-generated stress in cartilage using a surface probe. A prototype device has been developed, consisting of photofabricated excitation electrodes for applying electric currents to the cartilage surface and a piezoelectric sensor for detecting the resulting stress. The development, characterization, and testing of the probe are described in the following chapters.

1.6 Objectives and Overview

The main objective of the work described in this thesis is the development of an *electrokinetic surface probe* capable of applying small electric currents to the cartilage surface and simultaneously measuring the resulting current-generated stress. Since the electromechanical transduction mechanisms in AC are highly sensitive to changes in PG content, this device could provide a means of assessing the functional biomechanical state and biochemical composition of the tissue. Comparison of measurements made over a range of imposed wavelengths and frequencies with the poroelastic model [211] could enable

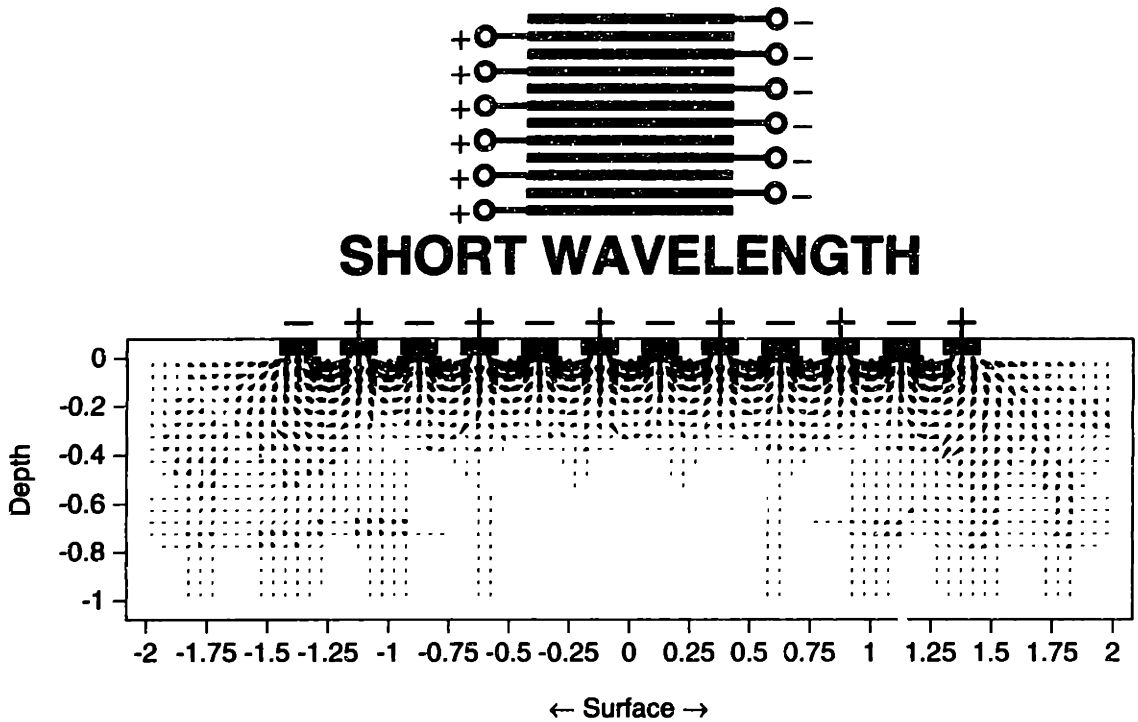

Figure 1.8: Electrode polarity (top) and relative current density distribution corresponding to an array of 12 evenly spaced electrodes configured for short-wavelength excitation. Penetration depth is only a small fraction of the thickness of the layer.

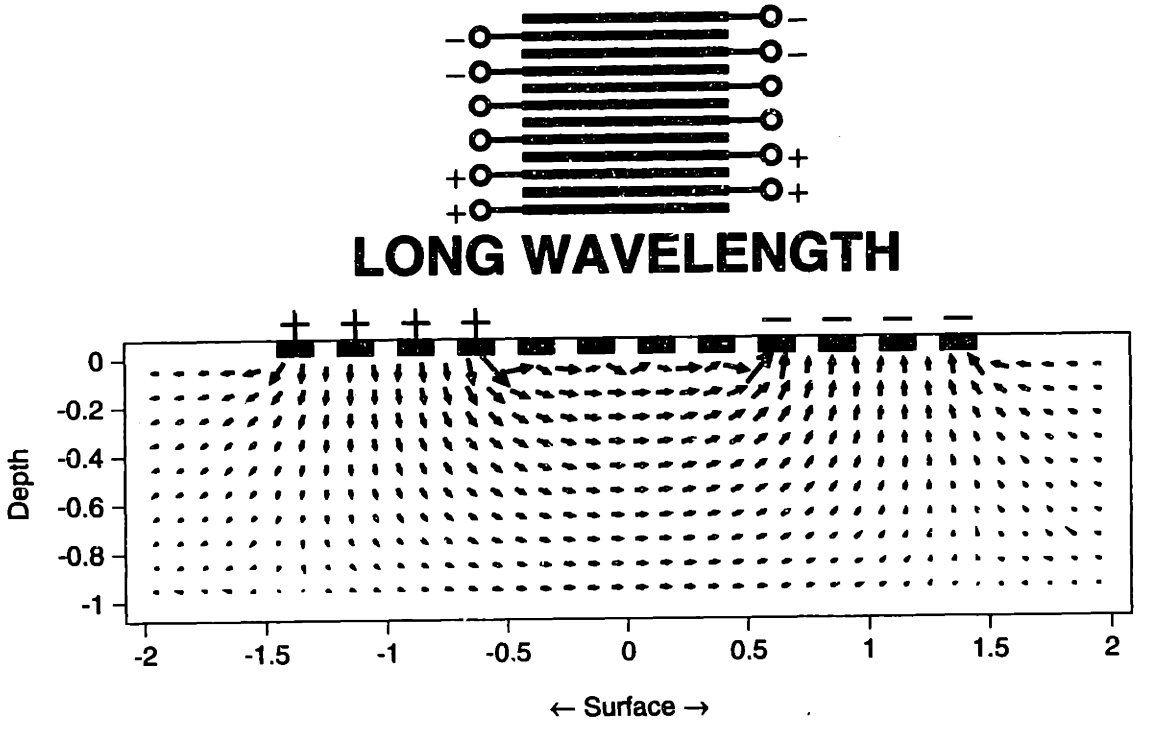

Figure 1.9: Electrode polarity (top) and relative current density distribution corresponding to an array of 12 evenly spaced electrodes configured for long-wavelength excitation. Full-thickness penetration into the tissue is achieved; compare Figure 1.7.

estimation of bulk material properties from the surface measurements. Furthermore, since the penetration depth of current into the tissue depends on the spatial wavelength, variable-wavelength surface spectroscopy can be used to spatially localize regions of nonuniform cartilage degradation.

1.6.1 Applications of Surface Probe Technology

There are several potential applications of the surface probe technology. First, it provides a means of nondestructively monitoring disease progression in animal models of OA, particularly at the earliest stages of the disease, thus providing a way to quantitatively assess the effectiveness of specific putative pharmacological or physical interventions in modifying the early biochemical changes of OA. Ultimately, the device could be incorporated into a clinical instrument for diagnosing cartilage degeneration in intact joints during arthroscopy, allowing the disease to be detected at a much earlier stage than is currently possible. In joints with regions of grossly evident OA (e.g., in "unicompartmental" OA of the knee), the probe could be used to assess the cartilage in the remainder of the joint, which may be functionally abnormal despite normal radiological and clinical appearance [183]. By providing a *quantitative* assessment of the state of the tissue, in contrast to the qualitative grading systems typically used at present [186], the probe could enable more accurate prediction of the prognosis for a particular patient.

In addition, the surface probe could provide a more quantitative means of assessing the *functional* biochemical and biomechanical status of repair tissue in the various techniques under development for treating focal cartilage defects [9,30,72,174,184]. The normal cartilage adjacent to the repair site could serve as an internal control for such measurements, reducing the uncertainty due to patient-to-patient variability. Finally, the device could be used to assess cartilage properties during open surgical procedures as well. For example, during hip hemiarthroplasty (for osteonecrosis of the femoral head), glass hemispheres of graded diameters are placed into the acetabulum (hip socket) in order to determine the optimal size of the femoral head prosthesis [5]; instrumenting these glass hemispheres with

an array of surface probes could provide a quantitative assessment of the condition of the acetabular cartilage, which might enable improved prediction of the long-range outcome of the joint replacement procedure.

1.6.2 Outline of Results Presented

The present work has focused on developing the technology using a controlled, *in vitro* experimental system. Chapter II (a version of which appears as Reference [14]) describes the construction and calibration of a prototype two-electrode probe as well as the results of preliminary experiments using disks of adult bovine cartilage. These experiments established the ability of the probe to detect changes in bulk electromechanical properties of cartilage resulting from several types of induced chemical modification (titration of intratissue pH and enzymatic extraction of cartilage PGs). This work is an extension of preliminary studies reported previously [68,69,213].

Chapter III (a version of which also appears as Reference [13]) presents the results of a study involving *multiple-wavelength* spectroscopy. A model system for nonuniform cartilage degeneration is described, in which surface digestion of cartilage-bone plugs with trypsin results in nonuniform PG loss, as a model for the biochemical changes characteristic of early OA. A version of the probe having independently addressable electrodes (and thus multiple-wavelength capability) was developed and tested with calf cartilage-bone plugs digested with trypsin using this protocol in order to test the hypothesis that sequential measurements at various wavelengths and frequencies could enable *spatial localization* of focal regions of cartilage degeneration.

In Chapter IV, mathematical simulations based on the poroelastic model of Sachs [210,211], modified to account for the actual geometry of the probe electrodes, are presented. The predictions of the theoretical model are compared with probe measurements of surface stress as a function of frequency, wavelength, and tissue thickness. Chapter V presents the results of a study in which the probe was used to measure the electrical impedance of cartilage specimens of various thicknesses; these results are compared

with the predictions of the theoretical model. Finally, Chapter VI summarizes the results and suggests some directions for future research.

Further details of the probe fabrication protocol and experimental techniques are contained in Appendices A and B, respectively. Appendices C and D contain supplemental data pertaining to the results presented in Chapters II and III, including additional results pertaining to the surface trypsin digestion model. Appendix E summarizes the mathematical model of Sachs and the method of solution used for simulation, while Appendices F and G contain additional results related to the simulations and impedance measurements presented in Chapters IV and V, respectively.

Chapter II

Detection of Chemically-Induced Modification of Cartilage Fixed Charge Density using Electromechanical Surface Spectroscopy

2.1 Summary

[1] We have constructed an *electrokinetic surface probe* capable of applying small sinusoidal currents to the surface of articular cartilage and measuring the resulting *current-generated stress* with a piezoelectric sensor. Using the probe, we have characterized the electromechanical response of excised disks of normal and chemically modified adult bovine femoropatellar groove cartilage. The measured stress amplitude was proportional to the applied current density and inversely proportional to the excitation frequency, consistent with a poroelastic model. As a function of bath pH, the stress amplitude exhibited a minimum in the range pH 2.4–2.8 and the phase underwent an abrupt 180° transition in the same range, consistent with an electrokinetic mechanism as the origin of the current-generated mechanical stress. Digestion of the tissue with trypsin resulted in a progressive loss of highly charged proteoglycan molecules from the tissue, with a concomitant decrease in the measured stress amplitude. These results support the feasibility of surface measurements as a means of assessing electromechanical transduction in cartilage and of detecting subtle molecular-level degradative changes in the extracellular matrix. This technique of surface spectroscopy provides a new means of nondestructively measuring the material properties of cartilage on intact joints and detecting degradative changes such as those seen in the earliest stages of osteoarthritis.

[1] A version of this chapter appears as Reference [14]. Supplemental data pertaining to the experiments described in this chapter are found in Appendix C.

2.2 Introduction

Articular cartilage (AC) is the dense connective tissue that lines the articulating surfaces of synovial joints and acts as a load-bearing, shock-absorbing, wear-resistant material. Although adult cartilage has neither innervation nor a blood supply, it is a metabolically active tissue. The tissue's sparse population of cells (chondrocytes) is responsible for the synthesis and continual turnover of the extracellular matrix (ECM), which is composed principally of a hydrated collagen fibril network enmeshed in a gel of highly charged proteoglycan molecules [34]. The osmotically swollen ECM (20–30% of tissue wet weight) and the tissue's high water content (70–80% of wet weight) enable normal cartilage to resist complex biomechanical loading forces *in vivo*.

The proteoglycan (PG) molecules of cartilage (called aggrecan, $M_r \sim 2 \times 10^6$) are composed of long glycosaminoglycan (GAG) chains (chondroitin sulfate and keratan sulfate) covalently bound to a protein core [101]. In normal cartilage, most of the PG molecules are non-covalently associated with long chain hyaluronic acid (hyaluronan) and link protein molecules to form PG aggregates with molecular weights on the order of 10^8 Da [95]. At physiological pH, the high density of ionized fixed charge groups (COO^-, SO_3^-) on the GAG chains of PGs is responsible for the electrostatic swelling pressure that enables cartilaginous tissues to resist compressive loads [161]. The collagen network, on the other hand, enables cartilage to resist tensile and shear loads and also resists and confines the natural swelling tendency of the enmeshed PG gel [161].

2.2.1 Electrokinetic Transduction

During the past two decades, investigators have found that electromechanical interactions play a significant role in the physiology of connective tissues. When cartilage is compressed, mechanical-to-electrical transduction occurs, resulting in measurable electrical potentials [8,90,146]. The mechanism for this phenomenon has been shown to be a "streaming" or electrokinetic effect: mechanical deformation of the cartilage ECM causes a flow of interstitial fluid and entrained counterions relative to the fixed charge groups

of the matrix. Fluid convection of counterions separates these ions from the oppositely charged matrix macromolecules, giving rise to a voltage gradient or "streaming potential" in the direction of fluid flow [66,90,136]. This phenomenon was observed in a series of experiments [64] using cylindrical disks of adult bovine femoropatellar groove cartilage that were uniaxially compressed between two silver chloride electrodes. A small-amplitude sinusoidal compression (~1% strain) superimposed on a 10–20% static offset compression produced a sinusoidal potential at the same frequency (in the 0.001-20 Hz range), whose amplitude and phase varied with frequency in a manner consistent with an electrokinetic mechanism [65,136]. Mechanically generated streaming potentials have also been studied as an important phenomenon in cortical bone [92,194,214,218].

More recently, a converse electrokinetic phenomenon has been observed in cartilage: *current-generated stress* [64]. Application of a sinusoidal electric current density across a cartilage disk in uniaxial compression exerts an electrophoretic force on the negatively charged matrix and an opposite force on the mobile counterions resulting in electroosmotic flow of tissue fluid; this combination produces a deformation within the matrix and a mechanical stress measurable at the tissue surface. The stress amplitude and phase have been successfully modeled [65] by combining linear electrokinetic coupling laws [49] with the biphasic theory [180] that relates stress, strain, and fluid flow in cartilage. The molecular constituents responsible for electrokinetic phenomena in cartilage have been studied by examining the dependence of compression-induced streaming potentials on bath pH and ionic strength [64,136]. At physiological pH, the proteoglycan molecules were found to be the predominant source of the potentials; hence, the transduction response is seated in the charge groups of the extracellular matrix. The molecular mechanisms that underlie electrokinetic phenomena have been characterized and theoretically modeled in a variety of colloidal and polymeric gel systems [140,187].

2.2.2 Cartilage Degeneration

Osteoarthritis (OA) is a heterogeneous disease of uncertain etiology characterized by progressive loss of articular cartilage, particularly from weight-bearing joints [176]. The earliest and most important biochemical features, which precede gross pathological changes, include nonuniform loss of proteoglycan molecules with an associated increase in tissue water content and, ultimately, fibrillation of the tissue's collagen network [153,161]. Degradative enzymes, including the metalloproteinases collagenase and stromelysin, have been implicated in the pathogenesis of the matrix damage [197]. Loss of PG decreases the ability of the cartilage to withstand compressive loading and thus makes the tissue softer and more susceptible to further wear and fibrillation [126]. Hence, early loss of PG should be detectable by measurement of tissue material properties well before visible signs of cartilage degeneration are present. To test this hypothesis, Dashefsky [48] used a mechanical indenter attached to a miniature force transducer to qualitatively assess cartilage compliance during arthroscopy; of 90 knees whose cartilage was evaluated as being "soft," more than half showed no observable changes in the articular surface.

Since streaming potential and other electrokinetic effects are directly proportional to PG charge density, early osteoarthritic degeneration should be detectable by electrokinetic measurements as well. This hypothesis was tested by Hoch *et al.* [105], who compared early biochemical, mechanical, and electromechanical changes in the knee joint cartilage of ambulating rabbits as a function of time after medial meniscectomy, a well established surgical model for OA-like cartilage degradation [177,223]. Early focal loss of PG was consistently found in medial tibial plateau cartilage, with an associated decrease in the streaming potential measured from cartilage plugs removed from the same joint surface. In an *in vitro* model for cartilage degeneration, Frank *et al.* [66] found that enzymatic extraction of PG from disks of bovine femoropatellar groove cartilage resulted in a decrease in dynamic stiffness and a significantly greater relative reduction in streaming potential. Thus, electrokinetic measurements may provide a more sensitive indicator of molecular-level cartilage degeneration than purely mechanical tests.

2.2.3 Surface Spectroscopy

Previous measurements of current-generated stress and streaming potential utilized a uniaxial configuration, in which it was necessary to access two opposite surfaces of an excised cartilage disk. Theoretical analysis [211], however, suggested that a spatially periodic standing wave of current applied to a *single* surface of an electromechanically coupled poroelastic medium such as cartilage could also produce a bulk mechanical stress, measurable at the surface (Figure 2.1). The three-dimensional current-generated stress distribution within the bulk of the tissue is complex but is related to that of the current density; the normal stress at the surface has the same spatial periodicity as the current excitation but is temporally out of phase. (For further details, Sachs and Grodzinsky [211] describe the spatial distribution of matrix displacement, fluid velocity, hydrostatic pressure, and electric and stress fields produced by an idealized spatially sinusoidal current applied to the surface of a charged, isotropic, homogeneous poroelastic layer of finite thickness, in the limit where the length of each surface electrode is much greater than its width). The surface spectroscopic approach has been motivated in part by recent advances in interdigitated-electrode sensor technology and dielectric materials characterization [224,252,254]. In classical dielectric spectroscopy, dielectric measurements made over a wide frequency range are used to infer properties about a homogeneous medium placed between two electrodes. It has now been found that surface excitations, applied by an interdigital electrode structure with an imposed spatial wavelength (determined by the electrode geometry) and temporal frequency, can also yield information about bulk material properties of dielectric materials [254].

The surface spectroscopic approach, with variable imposed spatial wavelength and temporal frequency, offers several distinct advantages. First, surface electrodes may be used to make measurements on cartilage *nondestructively.* Second, the technique introduces microstructural spatial sensitivity into such measurements [254]. Because of the Laplacian nature of the electric fields in the medium, short wavelength (λ) excitations (Figure 2.1B) at the surface decay within a short distance from the electrodes into the bulk ($\leq \lambda/3$), while longer wavelength excitations generate fields that penetrate proportionally further

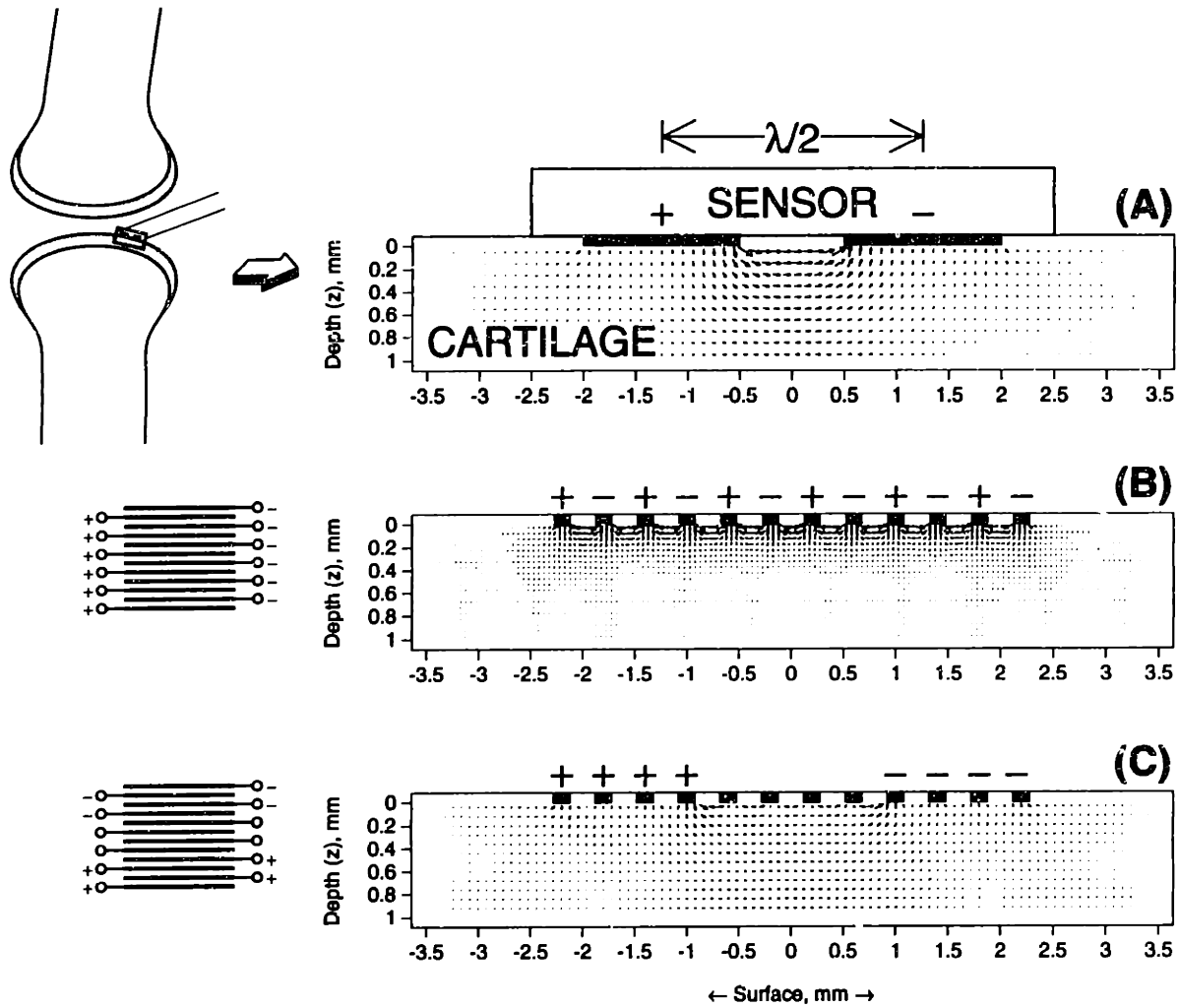

Figure 2.1: **A:** Theoretical distribution of current density within the bulk of a cartilage specimen produced by a two-electrode array applied to the cartilage surface, determined by solving the vector Laplace equation $\nabla^2 \vec{J} = \vec{0}$ [211] subject to the appropriate boundary conditions (no tangential electric field component at the perfectly conducting electrode surface and no normal field component at the perfectly insulating AC-bone interface, the surface not in contact with the electrodes, or the lateral edges). Arrows indicate direction and relative amplitude of current density. The penetration depth increases with the effective spatial wavelength, which is equal to twice the electrode separation. **B:** Electrode polarity (left) and relative current density distribution corresponding to a 12-electrode array configured for short-wavelength excitation. Penetration depth is only a small fraction of the thickness of the sample. **C:** Electrode polarity (left) and relative current density distribution corresponding to a 12-electrode array configured for long-wavelength excitation. Full-thickness penetration into the tissue is achieved; note the qualitative similarity to the distribution in **A.**

into the medium (Figure 2.1C). Hence, this approach is capable of resolving differences between surface properties and those deeper within the material and of probing spatial nonuniformities in the bulk. Parameter estimation techniques have been used to infer thickness, complex bulk permittivity, and other surface and bulk continuum properties of dielectric materials using this surface measurement technique [252].

The goal of the present work is to apply this approach in the context of *electro-mechanical surface spectroscopy* of articular cartilage. We have constructed a prototype *electrokinetic surface probe* capable of applying small-amplitude sinusoidal currents to the cartilage surface and measuring the resulting current-generated stress. In this paper, we report (1) measurement of current-generated stress in cartilage using the surface probe, (2) the relation between the measured stress and the amplitude and frequency of the applied current, and (3) the sensitivity of current-generated stress to PG changes caused by chemical modification or enzymatic extraction. Ultimately, this approach could be incorporated into a diagnostic instrument for making *in vivo* measurements at the time of arthroscopy.

2.3 Methods

2.3.1 Probe Construction

[2] The prototype electrokinetic probe is a 250 μm thick multilaminated structure (Figure 2.2) consisting of a pair of 25.4 μm thick silver-silver chloride excitation electrodes for applying current to the cartilage surface and a piezoelectric stress transducer, electrically isolated from the excitation electrodes, to measure the resulting mechanical stress. Electrical isolation is provided by a 25.4 μm thick piece of Mylar polyester film with a thin metal ground plane on one surface, insulated from the sensor by a second sheet of 25.4 μm nonmetallized Mylar. The stress sensor consists of 52 μm thick polyvinylidene fluoride (PVDF) film (AMP Inc. Piezo Film Sensors[3], Valley Forge, PA), a piezoelectric polymer that develops an electrical

[2]Further details of the fabrication methods described here appear in Appendix A.

[3]Formerly manufactured by Atochem North America, and prior to that by Pennwalt Corp. as Kynar Piezo Film

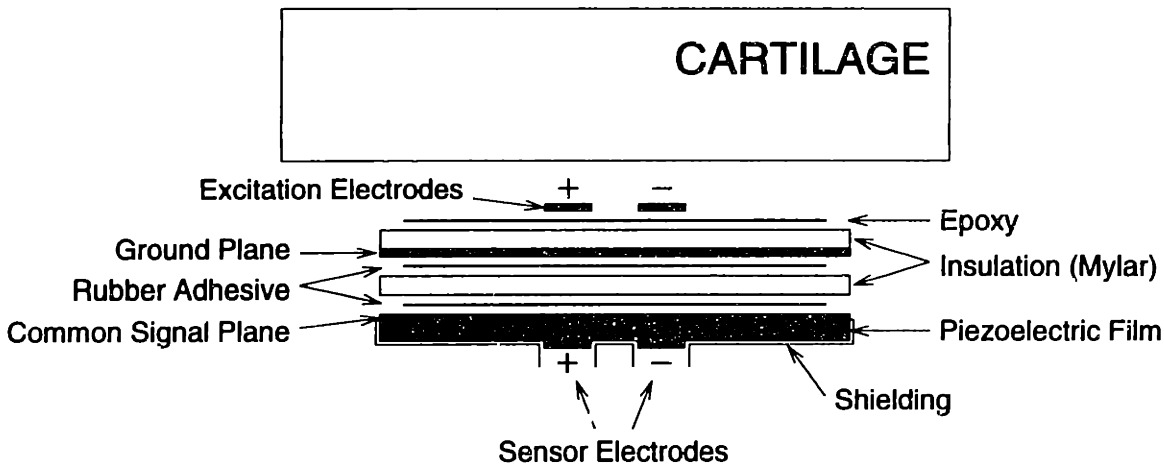

Figure 2.2: Cross section of electrokinetic surface probe, showing excitation electrodes (top) and piezoelectric stress sensor (bottom). Intermediate layers and shielding serve to electrically isolate the sensor output from the excitation electrodes.

charge proportional to an applied compressive or tensile stress, with thin (300 nm) vacuum-deposited Ni-Cu metallization on both sides. Although significant shear stresses may be generated as well, they are *not* transduced by the PVDF film [32]. The active area of each excitation electrode is a 1.5 × 4.0 mm rectangle, with 1 mm space between; the sensor electrode metallization pattern on the PVDF film has the same geometry and is spatially aligned with the excitation electrodes. A sinusoidal current imposed at the excitation electrodes produces a spatial standing wave of current density (Figure 2.1A), which induces a similar standing wave of mechanical stress within the cartilage. This current-generated stress is sensed by the piezoelectric film, producing a sinusoidal output voltage at the sensor electrodes (relative to the common signal plane on the opposite surface of the PVDF). The sensor output electrodes were further shielded from the current-injecting electrodes by copper tape to minimize stray capacitive coupling, as indicated in Figure 2.2. The center-to-center electrode separation (half spatial wavelength) in Figure 2.1A imposes a dominant spatial wavelength of 5 mm, allowing penetration of current to be on the order of the cartilage thickness; with narrower, more closely spaced electrodes, the current would be confined to the superficial region (Figure 2.1B).

A layer of silver sheet was bonded to the upper Mylar film using urethane epoxy

(Tycel 7000/7200, Liofil Co., Cary, NC[4]), while the other layers were bonded using 38 μm phenolic rubber adhesive (Plymaster 212, Norwood Industries, Frazer, PA). The excitation and sensor electrodes were etched from the silver layer and PVDF metallization, respectively, using standard photofabrication techniques. Both surfaces were coated with a light-sensitive photoresist compound (KPR Photoresist, KTI Chemicals, Sunnyvale, CA) and then baked at 80°C for 10 min to harden the photoresist. To prevent breakdown of the resist image during etching, it was found necessary to gently abrade the silver surface and then to acidify the surface by immersion in 15% nitric acid prior to coating with photoresist. The resist-coated probe was placed between two negative-image masks of the desired electrode pattern and exposed to ultraviolet light for 15 min, selectively cross-linking the photoresist polymer. The unexposed (non-cross-linked) regions of photoresist were removed by immersing the probe in a xylene-based developer solution (KPR Developer, KTI) for 60 sec, leaving an etchant-resistant stencil of the electrode pattern on both surfaces. Both the silver and the PVDF metallization were etched with a 55% w/v solution of ferric nitrate heated to 45°C; complete etching required 10–12 minutes for the silver but only several seconds for the PVDF metallization. The remaining photoresist image was softened with a stripping compound (Kepro Circuit Systems, Fenton, MO) and removed with a cotton-tipped swab. A chloride layer of 1000 mA-sec/cm^2 was then deposited on each excitation electrode by mounting the probe in the testing chamber (described below) with a bath of 0.1 *M* NaCl at pH 4 and separately passing a DC current (100 μA for 10 min) between each electrode and a platinum anode suspended in the bath.

2.3.2 Experimental Setup

[5] For testing, the probe was mounted in a cylindrical poly[methyl methacrylate] (PMMA) chamber, shown schematically in Figure 2.3A, with a 35 ml bath reservoir and terminals for making external connections to the input and output circuitry. Full-thickness articular carti-

[4]Formerly manufactured by Lord Corp., Erie, PA

[5]Further details of the methods described here appear in Appendix B.

lage disks, 800 μm thick and 7 mm in diameter, were harvested from the the femoropatellar groove of adult bovine knee joints (City Packing, Boston, MA) as previously described [64]. Each 7 mm disk was cored from a 9.5 mm diameter disk, leaving an annular ring that was used as a control for biochemical assays. Cartilage disks were placed in the chamber with the articular surface in contact with the probe and the other surface in contact with a porous polyethylene platen mounted on a hollow stainless steel shaft, as used previously in studies of soft-tissue swelling [57]. The chamber and porous platen assembly were mounted in a servo-controlled Dynastat mechanical spectrometer (IMASS, Hingham, MA) as described previously [64] and held in unconfined compression at a constant offset stress of 50 kPa to ensure good contact between the sample and the probe electrodes. The bath was continuously recirculated using a peristaltic roller pump and maintained at 20 ± 0.5°C by means of a proportional temperature controller. Previous experiments using living tissue at 37°C have shown that similar electrokinetic phenomena occur under physiologic conditions [102].

Sinusoidal currents were generated by a bipolar operational amplifier (Kepco, Flushing, NY), configured as a current source and driven by a computer-controlled programmable frequency synthesizer (Rockland Systems, West Nyack, NY). Current amplitudes of up to 62 μA (corresponding to a nominal current density of 10 A/m^2 at the surface of the stimulating electrodes) were used, at frequencies from 0.025 to 1 Hz. The output of each piezoelectric sensor electrode was passed through a separate channel of a high input impedance electrometer, low-pass filtered to remove 60 Hz noise, and then connected to a high input impedance differential amplifier (model 11-4113-01, Gould Electronics, Cleveland, OH). Because of the opposite polarity of the two excitation electrodes (Figure 2.2), the outputs of the two sensor channels were expected to have a phase difference of 180°; hence, differential recording enhanced the measured signal while suppressing common-mode noise[6]. The driving current signal and differential probe output were monitored on a Gould Brush 2200 chart recorder and digitally sampled and stored by the computer. On-line Fourier analysis determined the amplitude and phase, relative to the applied current signal,

[6]See Section C.1.1 and Figure C.1 for experimental verification of this assumption.

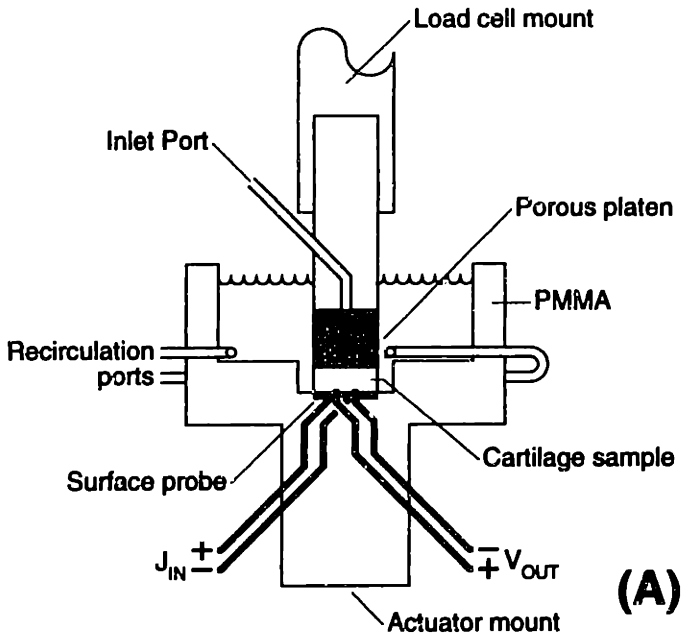

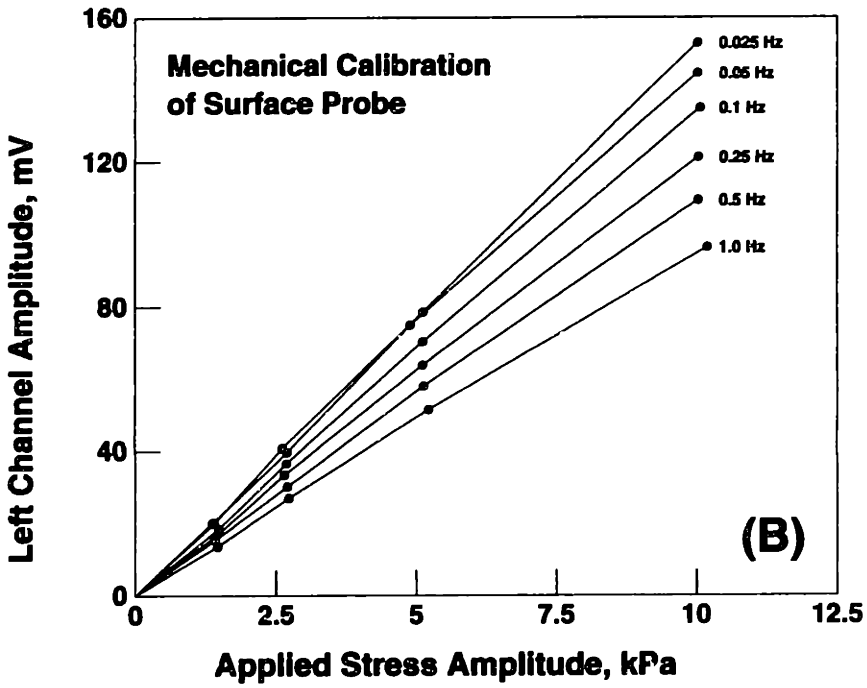

Figure 2.3: **A**: Schematic illustration of test chamber used for electrokinetic surface probe experiments. **B**: Mechanical calibration data for one channel of a typical surface probe. At each frequency, output amplitude was proportional to applied stress amplitude ($r > 0.996$), while phase (not shown) was approximately independent of amplitude.

of the fundamental component and the next four higher harmonics of both signals. The response was taken to be linear if the total harmonic distortion (THD) was less than 5–10% (THD = $\sqrt{\sum x_n^2}$, where x_n is the fractional content of the nth higher harmonic).

2.3.3 Sensor Calibration

Immediately prior to each experiment, mechanical calibration of each channel of the piezoelectric sensor was performed with no cartilage in the chamber (Figure 2.3B). Sinusoidal stresses having amplitudes up to 10 kPa, at frequencies from 0.025 to 1 Hz, were applied to the probe (superimposed on the 50 kPa static offset stress) by the Dynastat and the resulting dynamic output voltage from each sensor channel was recorded. For each calibration that was performed, the probe output from each channel was found to be proportional to the applied dynamic stress amplitude ($r > 0.996$) at each frequency, with THD less than 5%. A calibration coefficient (mV/kPa) was determined for each frequency by computing, for both channels, the slope of the linear least-squares regression line relating output voltage to applied stress at that frequency and then averaging the results for the two channels (which typically differed by less than 10%) to obtain a single voltage/stress ratio for each frequency. This ratio varied from probe to probe and trial to trial (possibly due to slight variations in fabrication and in mounting the chamber in the Dynastat) but typically was in the range 10–20 mV/kPa at all frequencies.

2.3.4 Current-Generated Stress in Cartilage: Surface Probe Measurement

Following sensor calibration, a cartilage disk was mounted between the probe and the porous platen and allowed to equilibrate in the bath for at least 30 min. The bath solution consisted of 0.15 *M* NaCl at pH 7.0, plus the protease inhibitors 2 m*M* [ethylenedinitrilo]tetraacetic acid (EDTA), 5 m*M* benzamidine-HCl, 10 m*M* *N*-ethylmaleimide (NEM), and 1 m*M* phenylmethylsulfonyl fluoride (PMSF) to minimize matrix degradation [192]. Current-generated stress (amplitude and phase) was measured in response to current densities of 5 and 10 A/m^2, at frequencies ranging from 0.025 to 1 Hz; total time for the complete

frequency sweep measurement on a given specimen was approximately 5 min. These applied current densities produced sinusoidal stress amplitudes that were less than 2% of the static offset stress (see Section 2.4). The corresponding maximum matrix displacements were estimated to be less than 1 μm ($\sim$0.1% strain) [211]; hence, the resulting tissue motions correspond to *small-amplitude sinusoidal perturbations* about the static offset. The advantage of using small-amplitude sinusoidal excitations is that even if there is a slow drift in the "static offset," Fourier decomposition may be used to isolate the sinusoidal component of the response (which is at the same frequency as the sinusoidal input) from the baseline drift.

2.3.5 Chemical Modification: pH Titration

In one series of experiments, current-generated stress was determined as a function of bath pH in 5 disks. The bath pH, continuously monitored with an Orion Ross combination electrode, was decreased in increments down to 2.0 by sequentially adding aliquots of 1 N HCl, following 30 min of pre-equilibration in the chamber at neutral pH. After each addition of HCl, the tissue was allowed to equilibrate for 45–60 min before the stress was measured. The minimum pH value was well below the predicted isoelectric point of the tissue but caused only a 7% increase in bath ionic strength, thus minimizing the effect of varying ionic strength on electrokinetic transduction [64]. Disks were immediately removed at the end of each experiment, blotted dry to remove surface water, and stored in vials at -20°C for subsequent measurement of hydration and GAG content.

2.3.6 Chemical Modification: Trypsin Digestion

To assess the ability of the surface probe to detect changes in tissue properties due to selective loss of the highly charged PG molecules from the matrix, current-generated stress was measured over time in a series of cartilage disks digested with trypsin. The bath solution for these experiments consisted of 0.1 M NaCl and 0.05 M Na_2HPO_4, adjusted to pH 7.2, as used previously in enzymatic extraction studies [44]. Following pre-equilibration

of the cartilage disk, an initial ("t = 0") stress measurement was made. Trypsin (type III from bovine pancreas, Sigma, St. Louis, MO) was then added to the bath to achieve a concentration of 1 mg/ml, and measurements of current-generated stress were taken after 1, 2, 3, 4, 10, and 20 hours. Between measurements, the 50 kPa static load was removed in order to facilitate diffusion of the enzyme into the tissue; the static load was reapplied 15 min before each measurement to allow re-equilibration to occur. Four cartilage samples were digested with trypsin; in addition, 3 control disks were subjected to the same protocol, but without trypsin. Protease inhibitors (2 mM EDTA, 5 mM benzamidine, 10 mM NEM, 1 mM PMSF, and 1 μM pepstatin) were added to the controls to inhibit endogeneous enzymatic activity. All disks and bath solutions were stored at −20°C for subsequent biochemical analysis.

2.3.7 Biochemical and Histological Analysis

Wet and dry weights of each disk and corresponding annular ring were determined and used to compute the hydration, defined as the ratio of water to solid weight, of each sample. The cartilage specimens were then digested with 1 ml/disk papain (125 μg/ml in 0.1 M sodium phosphate, 10 mM EDTA, and 10 mM cysteine at pH 6.5) at 60°C for 12–16 h. The sulfated GAG content of each sample was determined by a quantitative dimethylmethylene blue (DMB) dye-binding assay [60], using shark chondroitin sulfate (Sigma) standards. In addition to the disks that had been tested with the probe, several "uncompressed control" disks were harvested from joint surfaces and immediately weighed and assayed for GAG content.

In order to examine the kinetics of trypsin-induced GAG loss, a series of cartilage disks were assayed for GAG content as described above after being mounted in the chamber and digested with trypsin for varying lengths of time (1, 4, 10, and 20 h). Each disk was weighed wet and then cut with a razor blade to yield two approximately semicircular pieces; one piece was weighed and assayed for GAG content, while the other half was fixed using ruthenium hexaammine trichloride [110], sectioned, and stained with toluidine blue in a

pH 4 buffer as a qualitative histochemical indicator of tissue GAG content and distribution.

2.4 Results

2.4.1 Current-Generated Stress in Bovine Articular Cartilage

Small periodic current densities (5–10 A/m^2) at frequencies of 0.025 to 1 Hz applied to the surface of an adult bovine cartilage disk induced periodic mechanical stresses at the same frequency (Figure 2.4). The recording shown illustrates (1) the linearity of the response and (2) the 90° phase difference between current and stress, as predicted by the theoretical model [211]. (The slight drift in the output signal was confirmed to be due to amplifier drift and not tissue behavior). The dependence of the response on the amplitude and frequency of the current stimulus is shown in Figure 2.5. The data are mean ± SD for 5 disks to illustrate the range of sample-to-sample variation. In addition, the response of *each* individual disk was proportional to the applied current density amplitude at each frequency ($r > 0.96$), and the variation with frequency of each disk was similar to that seen in Figure 2.5B for the mean. The magnitude of the response was inversely proportional to the frequency of the current excitation, consistent with uniaxial measurements of current-generated stress [64] as well as the theoretical model for a 2-dimensional surface excitation [211]. These results are also consistent with previous probe experiments using 1 mm thick calf cartilage [68,213], except that the stress amplitude measured with adult bovine cartilage was only one-third that of calf AC. This difference may reflect differences in cartilage electromechanical parameters resulting from age-related changes in tissue composition and structure [93].

2.4.2 Effect of Bath pH on Current-Generated Stress

The dependence of current-generated stress on bath pH is shown in Figure 2.6. For each frequency, the amplitude has been normalized to the response at pH 7. For clarity, data from a single disk is shown; the normalized responses for all 5 disks tested were qualitatively similar. As the bath pH was lowered from its initial value of pH 7, the stress

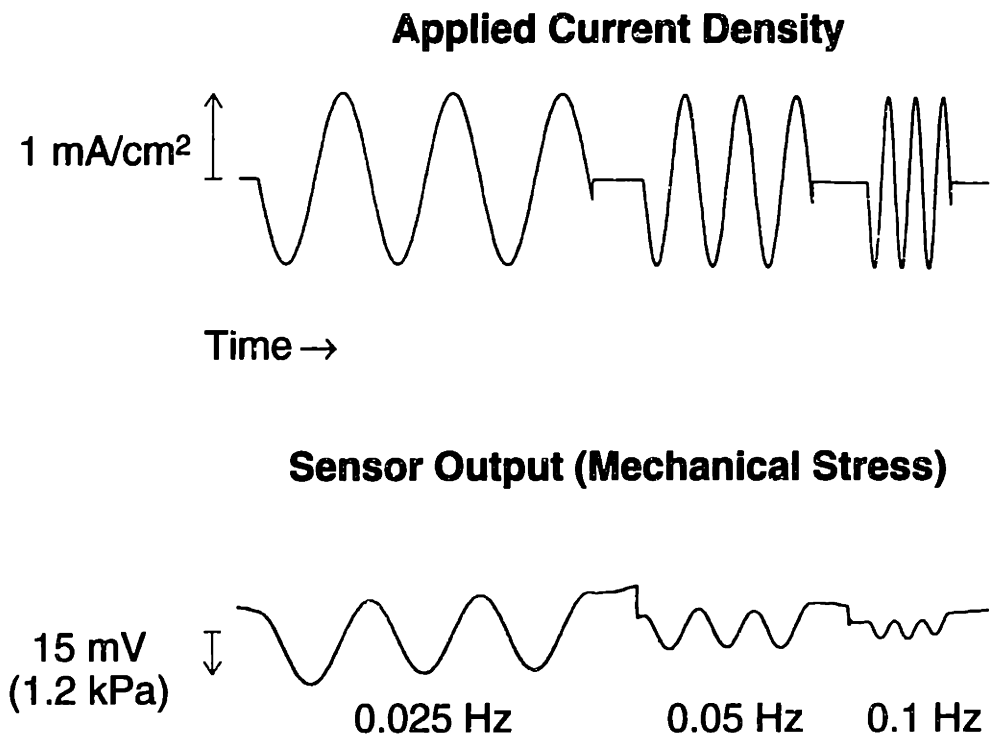

Figure 2.4: Chart recorder tracing of applied current density (top) and differential piezo sensor output (bottom), for frequencies of 0.025, 0.05, and 0.1 Hz, with a current density amplitude of 10 A/m^2. Mechanical stress amplitude was computed from calibration curves as in Figure 2.3.

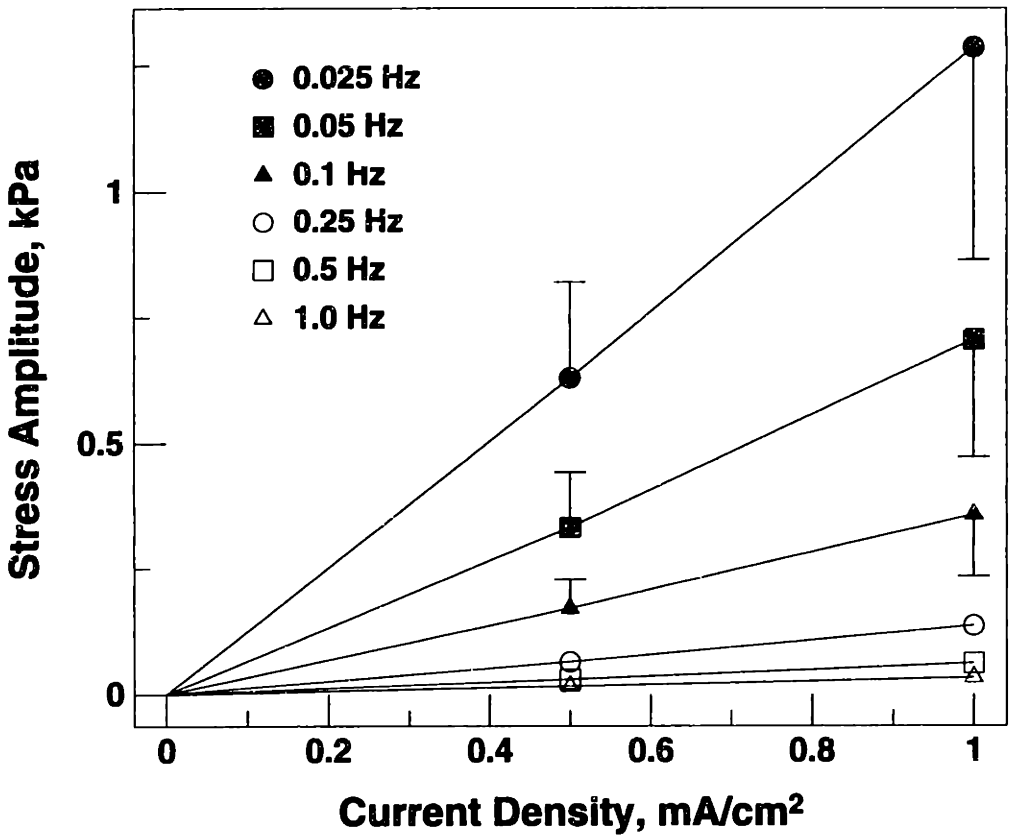

Figure 2.5: Amplitude of the fundamental component of current-generated stress versus applied current density amplitude. Bath solution was 0.15 M NaCl at neutral pH with protease inhibitors. Data are mean $\pm$ SD for 5 disks; error bars are omitted from the higher-frequency curves for clarity but ranged from 10–54% of the corresponding mean. In addition, the response amplitude of each individual disk at each frequency was proportional to the applied current density ($r > 0.96$), particularly for $f \leq 0.25$ Hz ($r > 0.996$).

amplitude decreased markedly, reaching a minimum at a value that varied monotonically with frequency but was always in the range pH 2.4–2.8 (Figure 2.6A). As the pH was lowered beyond this point, the stress amplitude increased, while the phase angle underwent an abrupt 180° transition (Figure 2.6B), indicating that the direction of the current-generated stress had reversed. These results suggest that the isoelectric pH (IEP), the pH value at which the tissue is electrically neutral, was in the range pH 2.4–2.8 for each disk. Independent determination of the fixed charge density of strips of adult bovine femoropatellar cartilage by means of chemical titration as a function of bath pH [67], shown in Figure 2.6C, confirmed that the IEP lies within this pH range.

The hydration (water to solid weight ratio) and GAG content of disks titrated to pH 2, controls maintained at pH 7 in the chamber, and uncompressed controls are shown in Figure 2.7, along with that of the corresponding annular rings. The hydration of the pH 2 disks was only 50% of the corresponding rings (2.19 ± 0.23 vs. 4.55 ± 0.99, $p < 0.02$ by paired t-test). This value was also found by one-way analysis of variance (ANOVA) to be significantly lower than the hydration of the pH 7 control disks (3.21 ± 0.26, $p < 0.005$) and the uncompressed controls (3.67 ± 0.23, $p < 0.0005$), indicating that these titrated disks were less resistant to compression produced by the 50 kPa static load. However, no significant differences in GAG content, expressed as a percentage of tissue dry weight, were found (by ANOVA) between any of the populations of disks and rings. Thus, there was no significant loss of GAG from the titrated disks.

2.4.3 Effect of Enzymatic Degradation on Current-Generated Stress

The normalized stress amplitude versus time after addition of trypsin is shown in Figure 2.8 (filled circles), along with trypsin-free controls (open circles), at a single frequency (0.025 Hz). At all frequencies, digestion with trypsin resulted in a mean decrease in stress amplitude of approximately 40% after 4 hours and a 70% decrease by 20 hours, while the phase (not shown) remained constant. In the control disks (with protease inhibitors), the stress amplitude decreased by 20% during the first 3 hours, then remained essentially

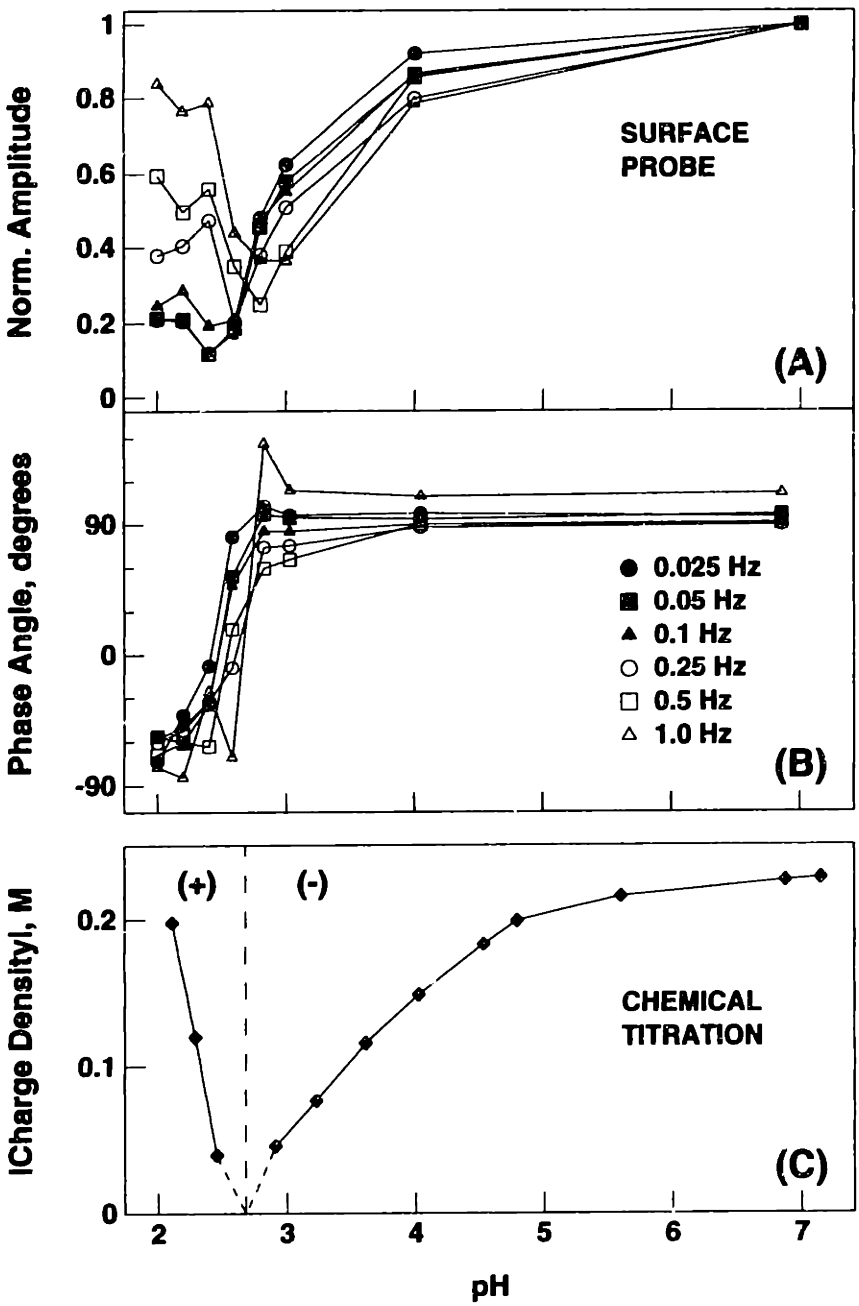

Figure 2.6: Current-generated stress amplitude (**A**), normalized to response at pH 7, and phase (**B**) versus equilibrium bath pH for a single adult bovine cartilage disk, tested in the range 0.025 to 1 Hz with an applied current density amplitude of 10 A/m^2. Following pre-equilibration at pH 7 in a bath of 0.15 *M* NaCl·(with protease inhibitors), the bath pH was lowered by sequential addition of HCl. A minimum in stress amplitude, as well as an abrupt 180° phase shift, occurred in the range pH 2.4–2.8. **C:** Magnitude of fixed charge density measured in adult bovine femoropatellar groove cartilage by chemical titration (adapted from [67]). The net charge changes sign as it passes through the isoelectric point (IEP), located in the range pH 2.4–2.8.

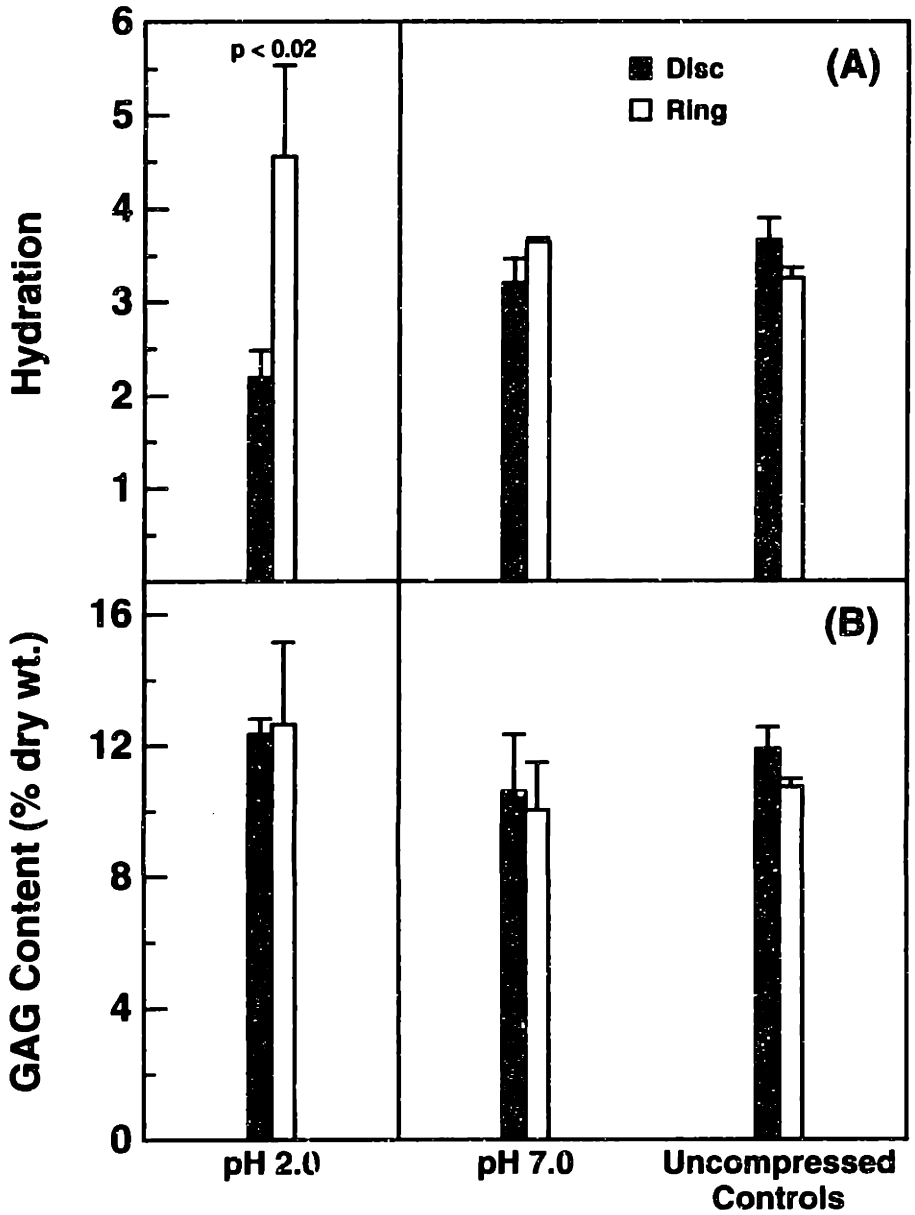

Figure 2.7: Hydration (**A**) and GAG content (**B**) of disks titrated to pH 2 ($N = 5$), controls maintained at pH 7 in the test chamber ($N = 2$), and uncompressed controls ($N = 3$), as well as corresponding annular rings. Hydration of the pH 2 disks was only 50% of the corresponding rings ($p < 0.02$ by paired t-test). In addition, hydration of the pH 2 disks was lower than the pH 7 disks ($p < 0.005$) and the uncompressed controls ($p < 0.0005$) by ANOVA. No significant differences in GAG content were found. All bars are mean + SD.

unchanged. This result may be due to the differences in stress history between earlier and later time points; with longer intervals between measurement, the tissue would have an increased chance to recover from the 50 kPa load.

The percentage of GAG remaining in a cartilage disk versus duration of exposure to trypsin is shown in Figure 2.8 (bars). With the assumption that all GAG initially present in each sample either remained in the disk or was released into the bath solution, the percentage of GAG remaining was computed as the ratio of the GAG in the disk to the total GAG in the disk and bath. The data at 20 h (mean ± SD) include the 4 tested samples and 3 controls (Figure 2.8, circles), plus one additional trypsin-digested disk and control, while the bars at 1, 4, and 10 h each represent a single disk. The amount of GAG remaining in the disks decreased monotonically with increasing time of trypsin digestion, reaching 7.44 ± 2.50% by 20 hours. In contrast, control disks that were maintained in the chamber for 20 hours with protease inhibitors retained 85.57 ± 11.56% of their initial GAG content. A disk that was allowed to swell freely in a trypsin bath (not shown) lost all but 2.04% of its GAG by 24 hours, while a free-swelling control disk retained 95.70%. Histological specimens stained with toluidine blue (not shown) revealed progressive loss of staining with increasing time of trypsin exposure; the loss of staining proceeded inward from the surfaces of the cartilage sample and was essentially complete by 10 h. The degree of staining with toluidine blue provides only a *qualitative* indication of PG content, since the stain exhibits a threshold effect; cartilage depleted of only ~58% of its normal GAG content completely loses its staining ability [196].

2.5 Discussion

We have measured current-generated stress in bovine articular cartilage using a new surface probe and have characterized the dependence of the measured stress on the amplitude and frequency of the applied current as well as changes in the stress in response to specific chemical modifications of the extracellular matrix.

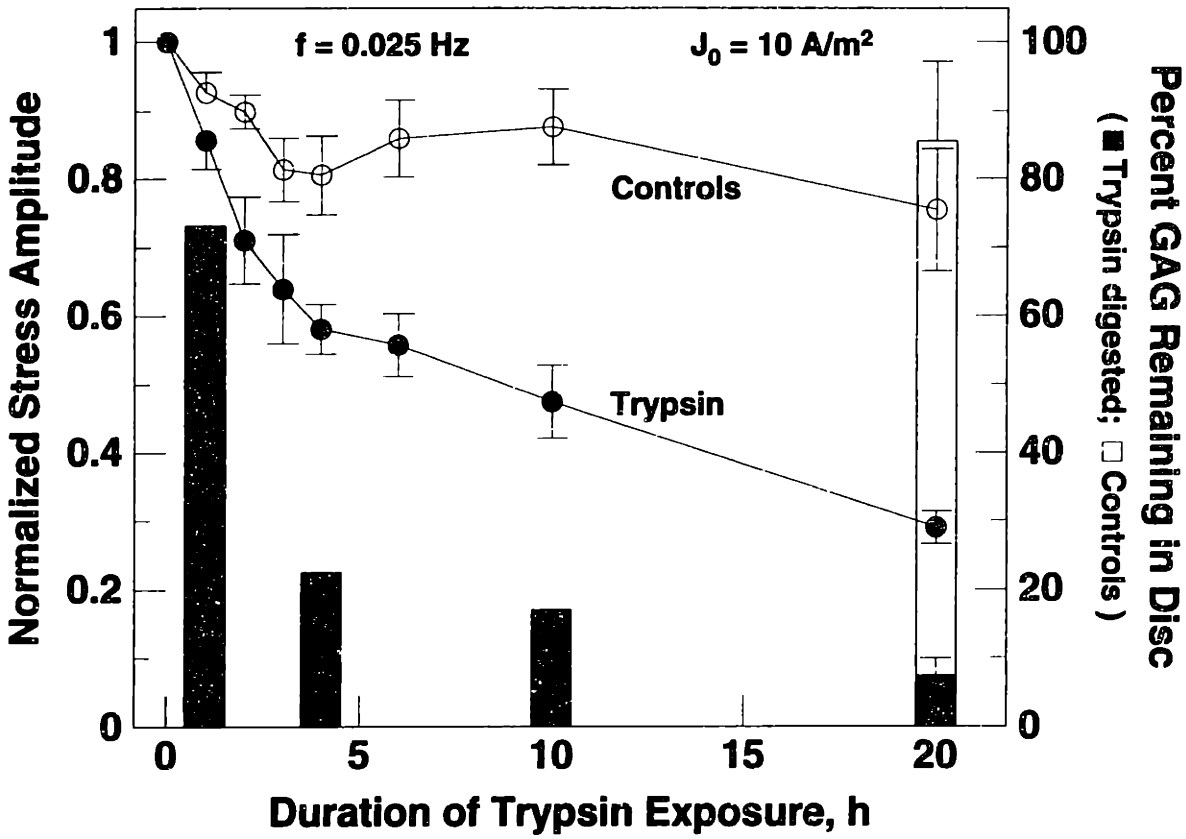

Figure 2.8: Current-generated stress amplitude (mean ± SEM) versus time after addition of 1 mg/ml trypsin (filled circles, N = 4) for a single frequency (0.025 Hz), normalized to the response prior to addition of trypsin (t = 0). Trypsin digestion resulted in a significant loss of signal as compared to controls (open circles, N = 3), which had protease inhibitors added instead of the enzyme. Bars indicate percentage of GAG (chondroitin sulfate) remaining in samples after digestion with trypsin for varying lengths of time, relative to GAG content prior to addition of trypsin (t = 0). Data at 20 h are mean ± SD for 5 trypsin-digested disks and 4 controls; the other bars each correspond to a single disk. (This figure was adapted from [11] and [15]).

2.5.1 Effect of pH

The mechanism of current-generated stress depends on the fixed charge density (FCD) of the extracellular matrix, which is a function of intratissue pH. At physiologic pH, the aggrecan GAG chains have a high negative FCD, while the ionized carboxyl and amino groups of the type II collagen fibrils are present in equal amounts and thereby contribute no further *net* charge to cartilage [161]. As the bath pH is lowered, however, hydrogen ions diffuse into the tissue and neutralize, initially, the GAG and collagen carboxyl groups in such proportion as to decrease the tissue's net charge density [67,161]. This resulted in a concomitant decrease in the current-generated stress amplitude measured by the probe. At the isoelectric pH (IEP), there is no net charge on the matrix, so the stress response should theoretically be zero. At pH values below the IEP, the matrix has a net *positive* charge, mainly due to ionized amino groups on lysine and arginine side chains on the collagen fibrils [67,161], with a corresponding excess of *negative* ions in the electrical double layer. At pH values below the IEP, therefore, applying current to the cartilage surface produces a stress, but in a direction opposite to that generated at pH values above the IEP because the signs of the fixed and mobile charges have been reversed.

The observed dependence of the amplitude and phase of the stress on pH (Figure 2.6) is consistent with the electrokinetic model described above; the minimum in amplitude and 180° phase shift indicate the presence of an IEP in the range pH 2.4–2.8. The measured stress amplitude never reached zero, possibly because the exact IEP fell between the discrete pH values at which measurements were taken. The finding of no significant GAG loss from disks that were titrated to pH 2 (Figure 2.7B) supports the hypothesis that the decrease in stress produced by decreasing pH was due to neutralization of the matrix fixed charge groups rather than loss of the charged GAG residues from the tissue. The decreased hydration of such disks (Figure 2.7A) corresponds to an increased creep deformation in response to the 50 kPa static stress, indicating that the neutralized GAG charge groups were less able to contribute to the electrostatic repulsive forces necessary for the compressive stiffness of normal cartilage.

The observed IEP value is also consistent with the results of previous experiments. For example, the streaming potential amplitude of adult bovine AC, measured in uniaxial compression, reached a minimum at pH ~2.75, with a 180° in phase at the same pH [66]. Measurements of FCD in adult bovine AC (Figure 2.6C), using a titration method [67], and in human femoral head cartilage, using a radioactive tracer technique [161], showed that the charge density decreased with decreasing pH, passing through zero at pH ~2.75 in both cases. Recently, using nuclear magnetic resonance (NMR) techniques, Lesperance *et al.* [139] found that the FCD of adult bovine AC changed sign as the pH was lowered from 3.0 to 2.0. Thus, surface measurement of current-generated stress appears to be a reliable, non-destructive means of assessing changes in FCD associated with the PG content of cartilage.

2.5.2 Effect of Trypsin Digestion

Digestion of cartilage with trypsin has been used as a model for the degradative changes seen in the early stages of osteoarthritis, although the degeneration in that disease is believed to be mediated by metalloproteinases and/or other endogenous proteases [197,216]. Trypsin, a serine protease, can cleave the core protein of aggrecan at multiple cleavage sites (the enzyme cleaves on the carboxyl side of lysine and arginine residues [231], 94 of which are present in aggrecan [51]). Trypsin has previously been shown to extract 88–96% of galactosamine residues (found in chondroitin sulfate) and 75–91% of glucosamine residues (found in keratan sulfate) of adult bovine femoropatellar groove cartilage within 24 hours [66] but resulted in minimal loss of collagen after 24 hours of digestion [217][7]. The small PG fragments resulting from trypsin digestion readily diffuse out of the tissue, decreasing the fixed charge density of the matrix.

Trypsin digestion resulted in a significant decrease in stress amplitude measured via the surface probe (Figure 2.8). Biochemical analysis (Figure 2.8, bars), along with

[7]Furthermore, *in vitro* biochemical studies have shown that exposure of intact collagen to trypsin at 20°C results in only minimal cleavage of intramolecular bonds within the non-helical telopeptide region of the tropocollagen molecules, with essentially no damage to the triple-helical body of the molecule [53,106,133].

histological examination, confirmed that treatment with trypsin resulted in progressive loss of GAG from the tissue, with a time course similar to that of the decrease in measured stress. Although the trypsin-digested disks lost 93% of their GAG content by 20 h, the stress amplitude decreased by only 70%. This difference may be due to the fact that the 50 kPa offset stress during testing caused increasing creep compression of the tissue as enzymatic digestion proceeded, which may have partially offset the decrease in fixed charge density produced by GAG extraction. The results of Figure 2.8 were comparable to previous studies in which a prototype surface probe was used to measure stress in trypsin-digested calf cartilage; Salant [213] and Frank *et al.* [67] observed a 20–40% decrease in amplitude by 4 hours and a 55–80% decrease by 20 hours. (Streaming potential, measured in a uniaxial geometry, has also been shown to decrease markedly in response to trypsin digestion: Frank *et al.* [66] found an 80% decrease in adult bovine AC after 12 hours, while Paguio [188] observed a decrease of 74–90% in calf AC by 16 hours, with a similar time course). Taken together, these results suggest that measurement of current-generated stress using the surface electrokinetic probe is a sensitive means of detecting molecular-level degradation of cartilage extracellular matrix.

2.5.3 Dependence of Current-Generated Stress on Frequency and Wavelength

The dependence of the current-generated stress amplitude on the amplitude and frequency of the applied current (Figure 2.5B) is qualitatively consistent with the predictions of the theoretical poroelastic-electrokinetic model of Sachs and Grodzinsky [211]. The amplitude and frequency dependence of the stress measured with the probe were also consistent with measurements made in uniaxial confined compression [64], the latter corresponding to the "infinite wavelength" limit of the model. According to this theory, higher temporal frequencies result in lower developed stress because the current-induced electroosmotic flow of interstitial fluid and concomitant electrophoretic migration of matrix (which together determine the mechanical stress) have less time to develop during each cycle. The theory also predicts that the current-generated stress amplitude is proportional to the amplitude

of the applied current density. By incorporating previously measured values for the equilibrium moduli, hydraulic permeability, and electrokinetic coupling coefficients of adult bovine cartilage in 0.15 M NaCl [64] into the surface spectroscopic model, Sachs and Grodzinsky [211] calculated values of the surface stress amplitude. Based on these values, the predicted stress generated by an applied current density of 10 A/m^2 at a frequency of 0.025 Hz, with an imposed spatial wavelength of 5 mm, has an amplitude of approximately 1 kPa, consistent with measurements obtained using the present surface probe configuration (Figure 2.5).

This reasonable agreement between the theory and experimental data for normal cartilage was observed despite the idealized assumptions inherent in the model and the differences between theoretical and actual boundary conditions. For example, the model predictions [211] assume an electrically insulating cartilage-bone interface (z = 1 in Figure 2.1), while in the actual experiments the cartilage disk was in contact with an electrically conducting (buffer-saturated) porous platen in order to allow transport of protons, protease inhibitors, and/or trypsin into the tissue. Thus, for electric current penetration depths less than or on the order of the sample thickness, δ, the measured stress response appears to be relatively insensitive to the conductivity of material located greater than distance δ away from the electrodes (e.g., the porous platen). The model also assumes that the tissue is homogeneous and that the current excitation is a purely sinusoidal standing wave. For future application to degraded cartilage, the poroeleastic theory will be extended to the case of an inhomogeneous tissue sample excited by a discrete electrode structure in order to more accurately reflect the geometry of the probe and the actual cartilage structure. Comparison of surface probe measurements with the predictions of the model will then enable tissue material parameters, including equilibrium modulus, electrokinetic coupling coefficient, hydraulic permeability, and electrical conductivity, to be determined via parameter estimation techniques [254].

2.5.4 Fabrication Issues

The prototype probe utilized a piezoelectric PVDF stress transducer because PVDF is commercially available, relatively inexpensive, and easy to work with. However, the material exhibits a large temperature-dependent (pyroelectric) effect as well as significant baseline drift, as high as 1 mV/s, resulting from charge accumulation across the capacitance of the sensor. To compensate for this drift, a ramp voltage waveform with adjustable slew rate was added to the output stage of each electrometer channel. In the future, a microfabricated silicon device having either a piezoresistive stress sensor or an integrated silicon-PVDF transducer [232], along with on-board integrated circuitry for signal amplification and filtering, could eliminate some of these problems. In addition, such a device would be better suited for incorporation into a self-contained instrument for use, for example, in intact joints at the time of arthroscopy.

The present version of the surface probe has two electrodes and thus a single imposed spatial wavelength (~5 mm) equal to twice the electrode separation. This wavelength is long enough to allow full-thickness penetration of the 800 μm cartilage disks (Figure 2.1A). Since the penetration depth is proportional to the wavelength, varying the imposed wavelength could enable sequential depths of the tissue to be "probed." One strategy for obtaining multiple-wavelength capability with a single device is to use an array of independently addressable electrodes; the wavelength can then be varied by changing the external connections of each electrode, as illustrated in Figures 2.1B,C for a 12-electrode array. Variable-wavelength surface spectroscopy would enable *spatial localization* of focal tissue degradation (e.g., at surface versus deeper regions). Future versions of the probe will incorporate this capability.

2.6 Conclusion

We have measured current-generated stress in bovine articular cartilage using a surface electrokinetic probe. The dependence of the measured stress on the amplitude and frequency

of the current excitation were consistent with previous electrokinetic measurements as well as a previously derived theoretical model. The changes in the stress amplitude and phase in response to chemical modification and enzymatic digestion of the tissue suggest that surface measurement of current-generated stress (1) is a reliable means of assessing electrokinetic transduction in cartilage and (2) is a sensitive means of detecting cartilage degradation. Future work will investigate the ability of a multiple-electrode (variable-wavelength) probe to spatially localize focal inhomogeneities in the tissue. Although the present series of experiments were performed on excised cartilage disks, the technique requires access only to a single surface of the tissue and can be used to make *in vitro* or *in vivo* measurements in intact joints. Electromechanical surface spectroscopy thereby provides a means of *nondestructively* assessing electrokinetic transduction in articular cartilage and, when combined with appropriate models and parameter estimation techniques, of determining material properties. Ultimately, this technology could be incorporated into an arthroscopic instrument for use in detecting very early degradative changes in cartilage associated with diseases such as osteoarthritis.

Chapter III

Multiple-Wavelength Spectroscopy of Normal and Enzymatically Degraded Cartilage

3.1 Summary

[1] This study focuses on a new approach for nondestructive measurement of electrical and mechanical properties of articular cartilage via an *electrokinetic surface probe* placed on the articular surface. The long-term goal of this work is to enable detection of early stages of tissue degradation based on the sensitivity of cartilage electromechanical properties to changes in biochemical composition. Previously, we described the design and construction of the surface probe and the sensitivity of probe measurements to induced changes in tissue fixed charge density. We have now developed a new multiple-wavelength version of the probe and used this device to test the hypothesis that variable-wavelength measurements of current-generated stress can be used to detect and localize focal degradation of surface vs. deep regions of tissue. We measured current-generated stress in both normal cartilage and in tissue that was subjected to controlled enzymatic extraction of aggrecan from the cartilage surface (as a model for certain degradative changes seen in diseases such as osteoarthritis). Surface probe measurements using variable wavelength and frequency were capable of distinguishing normal cartilage from nonuniformly degraded tissue, as indicated by a decrease in the ratio of short-wavelength to long-wavelength response after enzymatic digestion. These results support the feasibility of surface electromechanical spectroscopy with variable wavelength and frequency as a means of spatially imaging regions of focal cartilage degradation at various depths into the tissue.

[1] A version of this chapter appears as Reference [13]; preliminary results also appear in References [10–12]. Supplemental data pertaining to the experiments described in this chapter are found in Appendix D.

3.2 Introduction

The functional mechanical properties of the articular cartilage necessary for normal joint function are determined by the composition and structure of the complex extracellular matrix of the tissue. The high negative fixed charge density of the matrix, due to highly ionized glycosaminoglycan (GAG) constituents of matrix aggrecan molecules [34], is balanced by an excess of mobile counterions in the fluid phase. This arrangement of fixed anions and mobile cations gives rise to electromechanical transduction behavior in cartilage, via *electrokinetic* mechanisms. For example, mechanical compression of cartilage produces flow of interstitial fluid and entrained counterions relative to the fixed charge groups; the resulting separation of charge generates a voltage gradient (*streaming potential*) in the direction of fluid flow [66,90,136]. Conversely, electrical-to-mechanical transduction has also been observed in cartilage [64]. Application of a sinusoidal electric current density across a cartilage disk in uniaxial compression exerts an electrophoretic force on the negatively charged matrix and an opposite force on the mobile counterions, resulting in electroosmotic flow of tissue fluid; these coupled fluid and solid motions produce a deformation within the matrix and a mechanical *current-generated stress* which is measurable at the tissue surface. The amplitude and phase of this stress have been successfully modeled in a uniaxial geometry [65] by combining linear electrokinetic coupling laws [49] with a theory [180] that relates stress, strain, and fluid flow in poroelastic media such as cartilage.

Cartilage degradation is characterized by distinct pathological changes in the tissue, ultimately leading to full-thickness loss from the joint surface [153]. The earliest biochemical features, which precede gross pathological changes, include nonuniform loss of aggrecan, an increase in tissue water content, and damage to the tissue's collagen network [153,161]. Loss of aggrecan decreases the ability of the cartilage to withstand compressive loading [126]; hence, early aggrecan loss should be detectable by measurement of tissue material properties. To test this hypothesis, Dashefsky [48] used a mechanical indenter attached to a miniature stress transducer to assess cartilage compliance during arthroscopy; of 90 knees whose cartilage was evaluated as being "soft," more than

half showed no visual abnormalities in the articular surface. More recently, Kiviranta *et al* [130], using an arthroscopic indenter instrumented with strain gauges, detected only 30–40% decreases in cartilage stiffness in the most severely affected regions of the patellar cartilage of patients with known chondromalacia as well as much smaller decreases in stiffness elsewhere in the knee joint, even in regions of the joint surface that appeared visually to be normal.

Since electrokinetic effects in cartilage are directly dependent on aggrecan charge density, early degradative changes should be detectable by *electromechanical* measurements as well. This hypothesis was tested by Hoch *et al* [105], who compared early biochemical, mechanical, and electromechanical changes in the knee joint cartilage of ambulating rabbits as a function of time after meniscectomy, a well established surgical model for osteoarthritic-like degradation [177,223]. Early focal loss of aggrecan was consistently found in medial tibial plateau cartilage, with an associated decrease in streaming potential measured in cartilage plugs removed from the same joint surface. In an *in vivo* model for cartilage degradation, Bonassar *et al* [24] found that one-hour intraarticular injection of stromelysin (MMP-3) into rabbit joints resulted in loss of aggrecan constituents from the superficial region (top 10–15%) of the tissue, producing a significant decrease in electrokinetic coefficient but little or no change in mechanical properties (equilibrium modulus, dynamic stiffness, and hydraulic permeability). Thus, measurement of electrokinetic phenomena such as current-generated stress has been shown to provide a more sensitive indicator of molecular-level degradative changes than purely mechanical tests [24,66].

Although previous measurements of current-generated stress and streaming potential in cartilage utilized a uniaxial configuration, theoretical analysis [211] suggested that a spatially periodic standing wave of sinusoidal current applied to the cartilage surface via an array of electrodes could also produce a current-generated stress by the same electrokinetic mechanisms, measurable at the surface (Figure 3.1). In contrast to uniaxial compression, which requires an excised cartilage specimen to be placed between two electrodes [64], the surface spectroscopic approach requires access only to the articular surface and thus

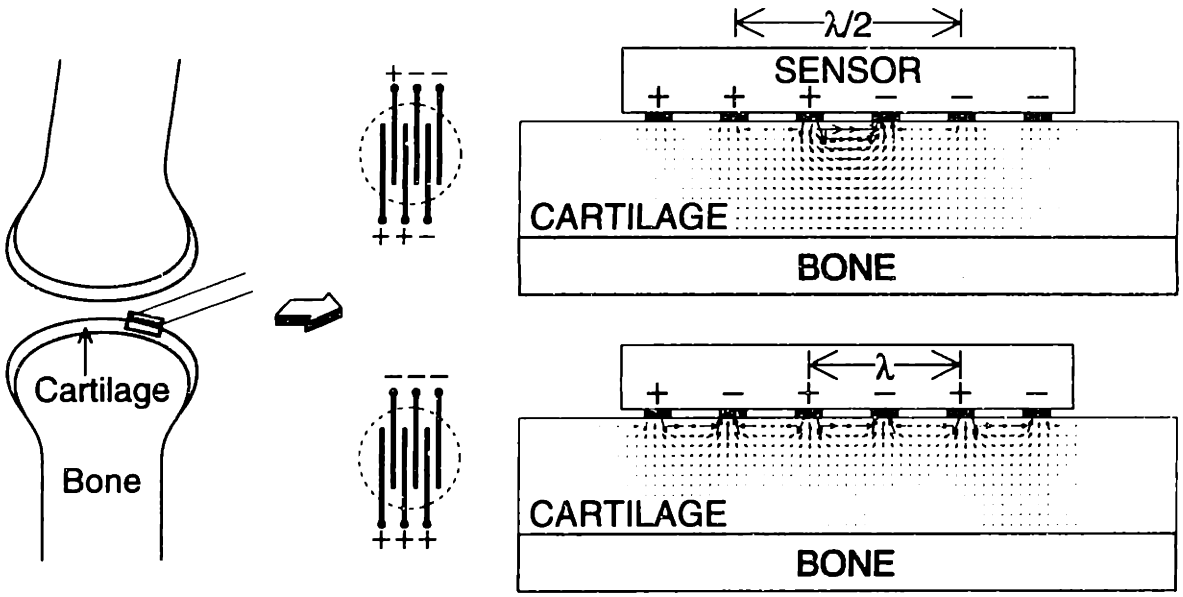

Figure 3.1: Theoretical distribution of current density within the bulk of a cartilage specimen resulting from an array of six electrodes applied to the tissue surface [211], configured for either long-wavelength (top) or short-wavelength (bottom) excitation. Arrows indicate the direction and relative magnitude of current density. The current penetration depth is proportional to the effective spatial wavelength, λ, which is equal to twice the electrode spacing. Dashed lines outline area of electrodes in contact with cartilage surface.

enables measurements to be made nondestructively. Ultimately, this approach could be incorporated into a diagnostic instrument for making *in vivo* measurements at the time of arthroscopy.

Previously, we have described the design and construction of an *electrokinetic surface probe* for measuring current-generated stress in cartilage via surface electrodes [14]. Probe measurements were found to be a sensitive indicator of matrix charge density, as indicated by the changes in measured stress resulting from controlled chemical modification of the tissue (pH titration to neutralize matrix charge groups and global enzymatic extraction of aggrecan using trypsin). Those experiments used a version of the probe having two electrodes and thus a single, fixed wavelength. We now report (1) the dependence of the measured stress on the imposed spatial wavelength, and (2) the ability of multiple-

wavelength and frequency surface spectroscopy to detect localized regions of aggrecan loss from the articular surface produced by controlled one-dimensional enzymatic digestion.

3.3 Methods

3.3.1 Probe Construction

Electrokinetic surface probes (250 μm thick) were constructed as previously described [14]. A sinusoidal current imposed at the cartilage surface by etched silver-silver chloride excitation electrodes (Figure 3.2) produces a spatial standing wave of current density (Figure 3.1), which induces a similar standing wave of mechanical stress within the cartilage at the same frequency. The normal stress at the surface has the same spatial periodicity as the current but is temporally out of phase; this normal component of stress can be measured by an overlying piezoelectric stress sensor (Figure 3.2), producing a sinusoidal output voltage at the sensor electrodes. The depth to which current penetrates into the tissue is proportional to the imposed *spatial wavelength,* λ, which is defined as twice the electrode spacing; the penetration depth is approximately $\lambda/3$. The piezoelectric stress sensor was constructed from 52 μm thick polyvinylidene fluoride (PVDF) film (AMP Inc. Piezo Film Sensors, Valley Forge, PA), electrically shielded from the current-injecting electrodes in order to minimize stray capacitive coupling [14]. For the present studies, we developed a new version of the probe [12] having six *independently addressable* electrodes; by varying the external connections to each electrode, multiple wavelengths could be obtained with a single device. For the present studies, this multiple-wavelength probe was configured with either a "long" wavelength of 5 mm (Figure 3.1, top) or a "short" wavelength of 1.68 mm (Figure 3.1, bottom).

3.3.2 Experimental Setup and Specimen Preparation

For testing, the probe was mounted in a cylindrical poly[methyl methacrylate] (PMMA) chamber; 35 ml of bath solution was added to the chamber and continuously recirculated.

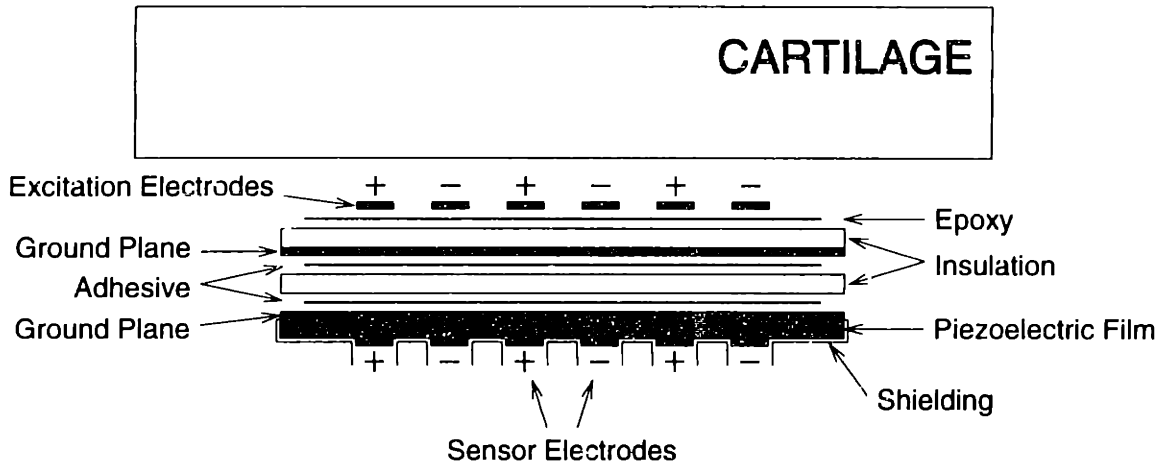

Figure 3.2: Schematic cross-section of surface probe, showing six Ag/AgCl excitation electrodes (top) which apply current to cartilage surface, and piezoelectric stress sensor (bottom). Sensor electrodes develop electrical charge proportional to the normal component of stress at the overlying cartilage surface. Intermediate layers and shielding serve to electrically isolate the sensor output from the excitation electrodes. The actual device is 250 μm thick; width of the electrode array is 4.5 mm.

The bath solution consisted of 0.15 M NaCl at pH 7.0, plus the proteinase inhibitors 2 mM [ethylenedinitrilo]tetraacetic acid (EDTA), 5m M benzamidine-HCl, 10 mM N-ethylmaleimide (NEM), and 1 mM phenylmethylsulfonyl fluoride (PMSF) to minimize matrix degradation by endogenous proteinases [192].

Saddle sections (femur and tibia with intact knee joint) of newborn calves were obtained from a local abbatoir (A. Arena, Hopkinton, MA) within 24 hours of slaughter. Cylindrical plugs of cartilage (9.5 mm diameter), with underlying subchondral bone, were drilled from the medial and lateral facets of the femoropatellar groove using a hollow coring bit. For testing, full-thickness cartilage-bone plugs (with intact articular surface) were placed in the PMMA chamber and held in unconfined compression at a constant static offset stress of 50 kPa using a Dynastat mechanical spectrometer (IMASS, Hingham, MA) in order to ensure good contact between the tissue surface and the probe electrodes.

Small-amplitude sinusoidal currents were generated by a bipolar operational am-

plifier (Kepco, Flushing, NY), configured as a current source and driven by a computer-controlled programmable frequency synthesizer (Rockland Systems, West Nyack, NY). The output of each piezoelectric sensor electrode was passed through a separate channel of a high input impedance electrometer, low-pass filtered to remove 60 Hz noise, and then connected to a high input impedance differential amplifier (model 11-4113-01, Gould Electronics, Cleveland, OH). Because the two sensor outputs ("+" and "−") were expected to have a phase difference of 180° [14], recording the *difference* between the two channels enhanced the measured signal while suppressing common-mode noise. The driving current signal and differential probe output were monitored on a Gould Brush 2200 chart recorder and digitally sampled and stored on a computer. On-line Fourier analysis determined the amplitude and phase, relative to the applied current signal, of the fundamental component and the next four higher harmonics of both signals. The response was taken to be essentially linear if the total harmonic distortion (THD) was less than 5–10% (THD = $\sqrt{\sum x_n^2}$, where x_n is the fractional content of the nth higher harmonic). Immediately prior to each experiment, mechanical calibration of the piezoelectric sensor was performed as described previously [14], so that the mechanical stress could be determined from the voltage output of the piezoelectric sensor.

3.3.3 Measurement of Current-Generated Stress

Following sensor calibration, a cartilage-bone plug was mounted in the chamber, allowed to equilibrate in the bath for at least 30 min, and tested using the multiple-wavelength probe, sequentially configured for both long- and short-wavelength excitation. Ten plugs (1–4 from each of six calves) were tested using this protocol. Four plugs (each from a different calf) were tested both before and after 2 h of surface trypsin digestion as described below. Current-generated stress (amplitude and phase) was measured at frequencies ranging from 0.025 to 1.0 Hz; total time for a complete frequency sweep on a given specimen was approximately 5 min. The small current densities used (up to 10 A/m^2) produced estimated matrix displacements of less than 1 μm (<0.1% strain) [211]; hence, the resulting

tissue motions correspond to small-amplitude cyclic perturbations about a static offset [14]. Fourier analysis enabled the sinusoidal component of the response (which is at the same frequency as the applied current) to be isolated from baseline drift.

3.3.4 Trypsin Digestion

A system was developed for producing one-dimensional (nonuniform with respect to depth) loss of aggrecan from cartilage, as a model for certain biochemical changes seen in cartilage degradation [21,103,118]. Cartilage-bone plugs with intact articular surface were mounted in a cylindrically confining chamber (Figure 3.3, inset) and exposed to a bath of 0.1 *M* NaCl and 0.05 *M* Na_2HPO_4, adjusted to pH 7.2, as used previously in enzymatic extraction studies [44]. Trypsin (type III from bovine pancreas, Sigma, St. Louis, MO) was then added to the bath to achieve a concentration of 1 mg/ml. Digestion of cartilage with trypsin, which cleaves the core protein of aggrecan at multiple sites [51] but has produces only minimal loss of collagen from the tissue [217], has been used as a model for certain aggrecan-related degradative changes seen in osteoarthritis, although the matrix damage in that disease is believed to be mediated by other proteinases (e.g., metalloproteinases, aggrecanase, etc. [197,216]). Because of the geometry of the chamber, the enzyme could only diffuse into the tissue and aggrecan could only leave the tissue, via the articular surface. During digestion, the chamber was sealed using paraffin film and the bath was continuously stirred using a magnetic stirrer.

The spatial distribution of aggrecan loss produced by this protocol was assessed by histological staining, using dimethylmethylene blue (DMB) dye during fixation [111], of plugs that had been digested for 1, 4, 8, and 24 hours as well as an unexposed control plug. Immediately following trypsin digestion, slices (~1 mm thick) were cut perpendicular to the articular surface and extending approximately 4 mm into the tissue. Each slice was fixed at room temperature for 96 h in 2% (v/v) glutaraldehyde, 0.2% (w/v) DMB, and 0.05 *M* sodium cacodylate. Slices were then washed in 65 m*M* NaCl and 0.1 *M* sodium cacodylate (pH 7.4), stored in 70% ethanol at 4°C, and sectioned for light microscopy

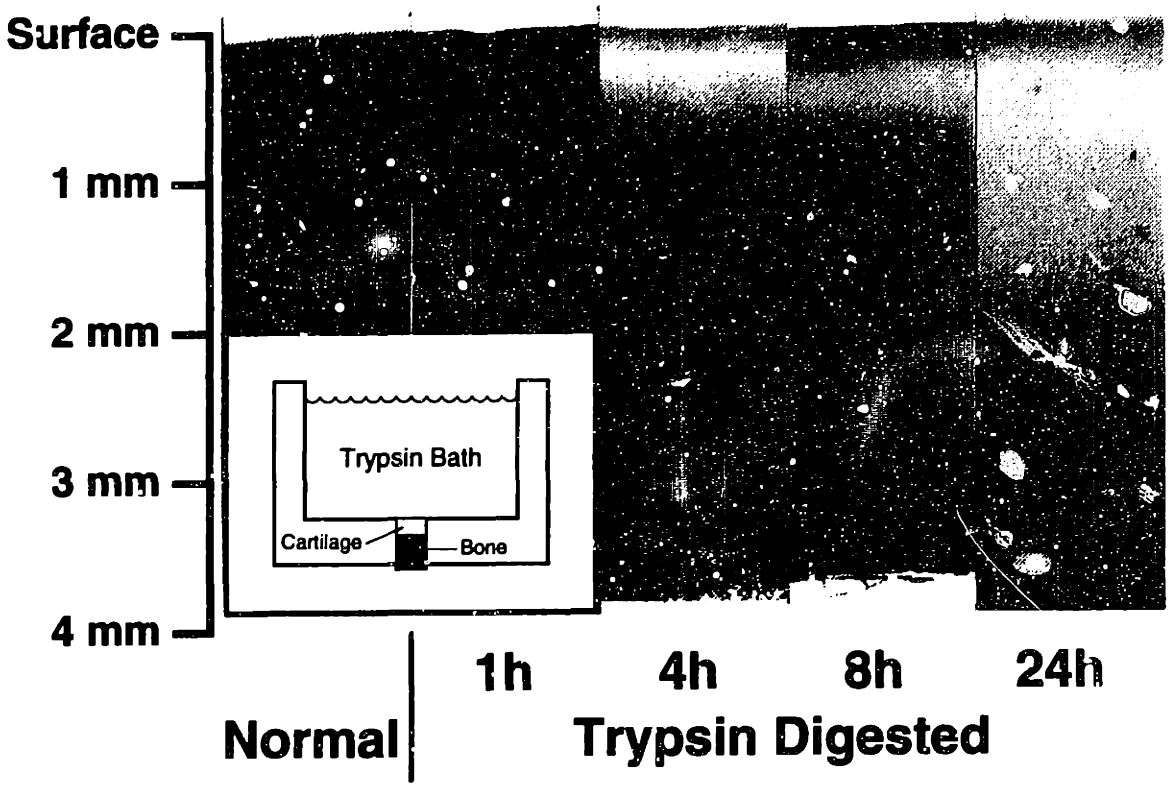

Figure 3.3: Dimethylmethylene blue (DMB) staining of calf cartilage following surface digestion with trypsin. Full-thickness cartilage-bone plugs were mounted in a chamber (inset) such that only the intact articular surface was exposed to the enzyme. Slices (~4 mm deep) were cut perpendicular to the surface of a normal cartilage-bone plug as well as plugs that had been digested with trypsin for 1, 4, 8, and 24 h. Each slice was stained with 0.2% (w/v) DMB during histological fixation for 96 h with 2% glutaraldehyde and 0.05 *M* sodium cacodylate [111]. Subchondral bone is visible at the deep edge of the 4 h and 8 h specimens.

(Pathology Services, Cambridge, MA). Surface digestion of calf cartilage-bone plugs with trypsin resulted in progressive loss of aggrecan from the tissue (as indicated by loss of DMB staining), proceeding inward from the articular surface (Figure 3.3).

To quantify the spatial profile of aggrecan loss, the GAG content of sequential 200 μm slices from trypsin-digested plugs was determined. For each duration (1, 4, 8, 24 hours), 3 plugs were simultaneously digested; in addition, 3 control plugs were also analyzed. Wet and dry weights of each 200 μm slice were determined, before and after 12–16 h of lyophilization, respectively. Each specimen was then digested with 0.5 ml of papain (2.77 units/ml in 0.1 M Na_2HPO_4, 10 mM EDTA, and 10 mM cysteine at pH 6.5) at 60° for 12–16 h. The sulfated GAG content of each digested sample was determined by a quantitative dimethylmethylene blue (DMB) dye-binding assay [60], using shark chondroitin sulfate (Sigma) standards. For the assay, 20 μl aliquots of each digested sample (diluted 1 : 10) were added to 200 μl of DMB in 96-well plates and the optical absorbance at 580 nm was determined using a microplate reader (Vmax, Molecular Devices, Menlo Park, CA).

3.3.5 Statistical Analysis

Statistical comparisons were made using multivariate analysis of variance (ANOVA). All statistical computations were performed using the SAS data analysis software package. Results were considered significant at the $p < 0.05$ level.

3.4 Results

3.4.1 Dependence of current-generated stress on wavelength and frequency (normal cartilage)

The multiple-wavelength probe with six independently addressable electrodes was tested with 10 full-thickness plugs of calf cartilage, using both the long-wavelength and short-wavelength configurations (Figure 3.4). Based on the theoretical model [211], the normal-

ized stress was postulated to be proportional to a negative power of the excitation frequency. For each wavelength, the frequency dependence of the data was fit using the Levenberg-Marquardt nonlinear least-squares technique [199]; the best-fit exponents were found to be 0.74 ± 0.13 for long-wavelength excitation and 0.59 ± 0.12 for short-wavelength excitation. At each frequency, the short-wavelength response was significantly less than the long-wavelength response (Figure 3.4A) ($p < 0.01$ by ANOVA). The *ratio* of short- to long-wavelength stress response also varied with frequency, ranging from 0.43 ± 0.12 at 0.025 Hz to 0.68 ± 0.29 at 1 Hz (Figure 3.4B). The dependence of current-generated stress on wavelength and frequency in these cartilage-bone plugs comprises the *electromechanical spectroscopic behavior* of normal cartilage.

3.4.2 Trypsin digestion model

Biochemical assessment of tissue GAG content quantitatively confirmed the histological observations after surface trypsin digestion for various lengths of time (Figure 3.5). After one hour of digestion, GAG content was decreased by 30% at the surface but reached normal levels by the second 200 μm slice of tissue. In contrast, 24 h of trypsin digestion resulted in a region of decreased GAG extending more than 3 mm into the tissue. The GAG distribution of normal tissue was nonuniform as well; GAG content increased from $2.45 \pm 0.29\%$ of wet weight in the most superficial 200 μm to $4.90 \pm 1.06\%$ in the 20th slice. A similar distribution has been previously reported for human femoral head cartilage [161]. Although the specimens stained with DMB dye exhibited an abrupt transition between stained and unstained regions (Figure 3.3), the assay results indicated that the spatial profile of GAG content within the tissue underwent a gradual transition, with no abrupt changes. We note that when GAG content was less than 50–70% of normal at any given depth, DMB staining was lost. This threshold behavior is similar to that previously reported by Poole [196] for staining of cartilage with toluidine blue.

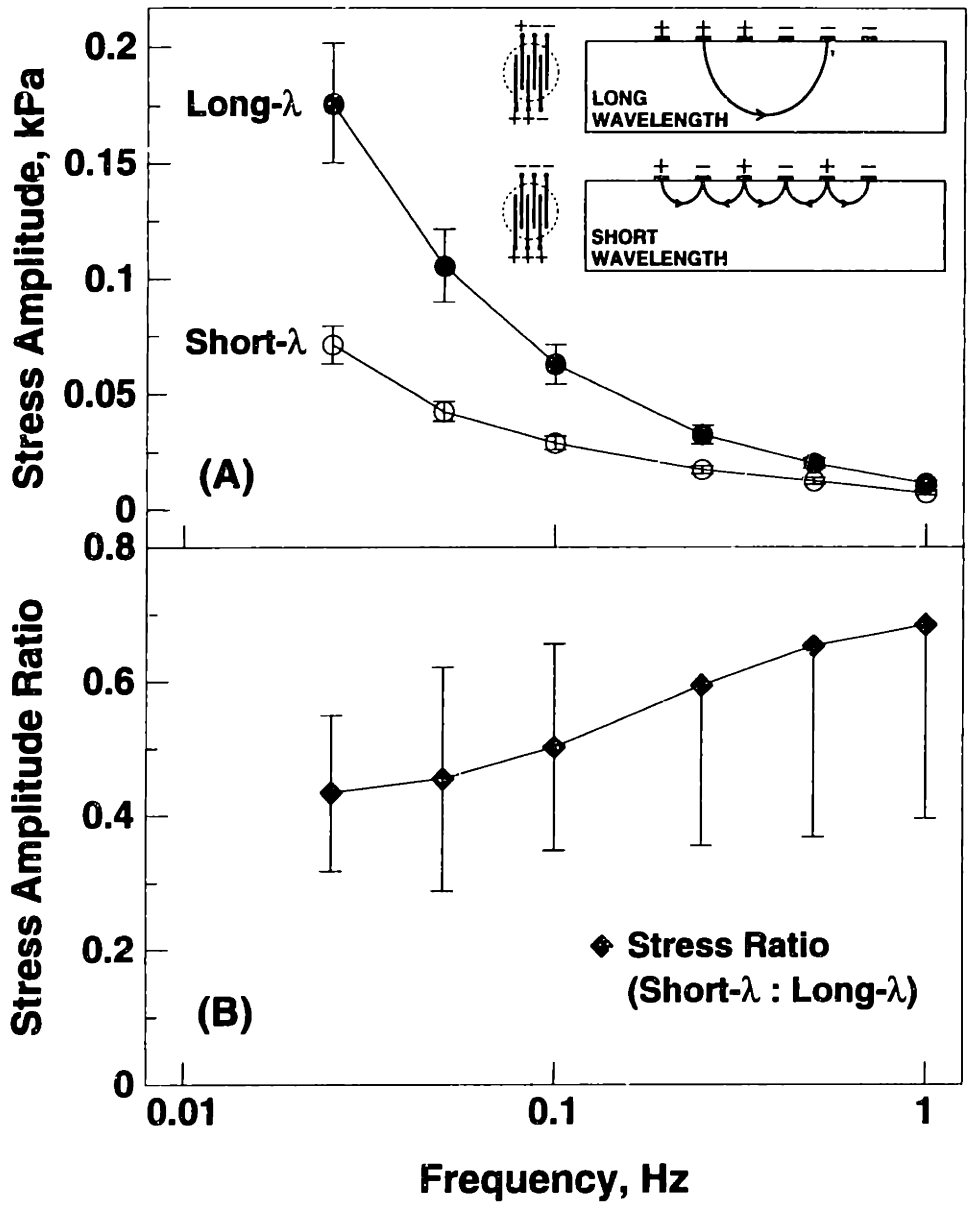

Figure 3.4: (**A**) Current-generated stress amplitude measured in 9.5 mm diameter full-thickness calf cartilage-bone plugs (with intact articular surface) using the multiple-wavelength probe in both the long-wavelength (filled circles) and short-wavelength (open circles) configurations (N = 10, mean ± SEM). Differences between long- and short-wavelength response are significant at all frequencies ($p < 0.01$ by ANOVA). (**B**) Ratio of current-generated stress amplitude in response to short-wavelength excitation (using multiple-wavelength probe) to long-wavelength response in full-thickness calf cartilage-bone plugs (N = 10, mean ± SD).

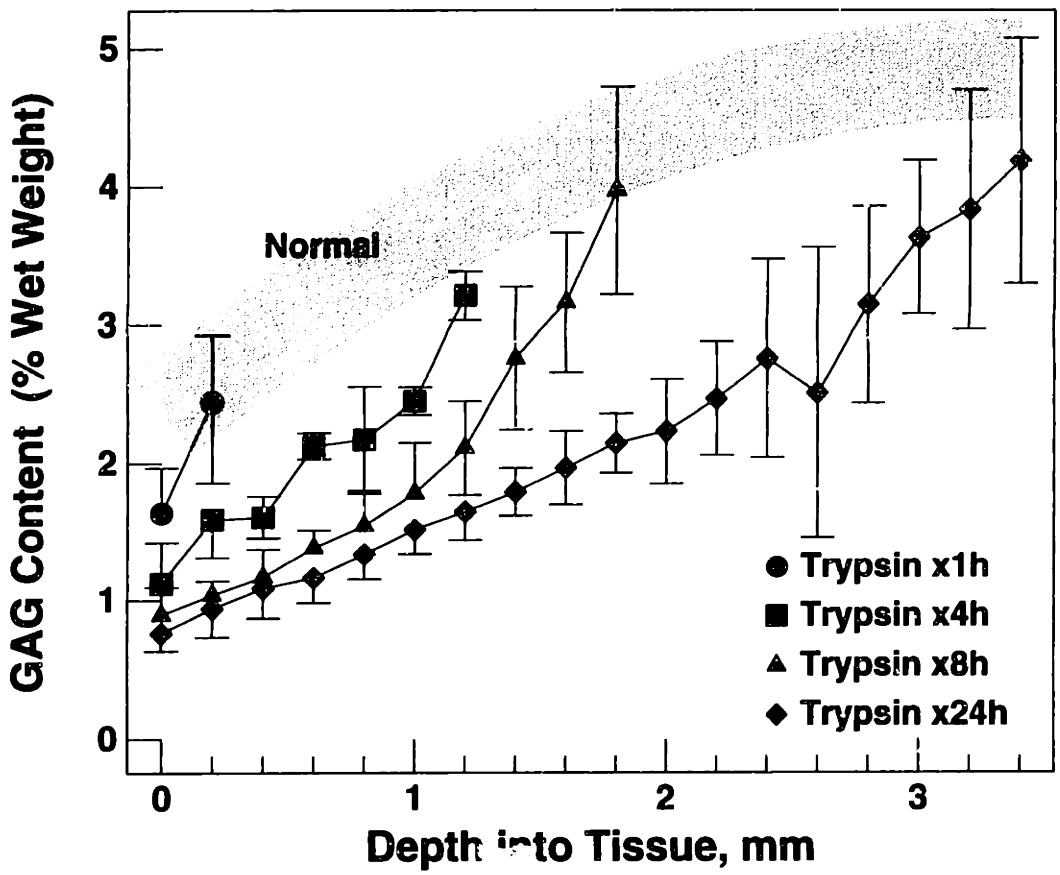

Figure 3.5: Sulfated GAG content (as percentage of tissue wet weight) of sequential 200 μm thick slices from calf cartilage-bone plugs digested with trypsin for 1, 4, 8, and 24 h (N = 3 for each duration, mean ± SD), determined using a DMB dye-binding assay [60]. Gray band represents range of GAG content measured in normal controls (N = 3, mean ± SD). For clarity, GAG content of trypsin-digested specimens is plotted only until the depth at which GAG content reached normal levels.

3.4.3 Multiple-wavelength spectroscopy of nonuniformly digested cartilage

Four full-thickness cartilage-bone plugs were tested with the multiple-wavelength probe (using both the long- and short-wavelength configurations), both before and after 2 h of surface trypsin digestion (Figure 3.6). Based on the assay results (Figure 3.5), this duration of enzyme exposure was estimated to produce a region of GAG loss extending ~ 0.6 mm into the tissue, with an overall GAG loss of 25% from this region. Prior to trypsin digestion, the ratio of short- to long-wavelength stress response exhibited the frequency dependence characteristic of normal cartilage (Figure 3.6, solid squares). Trypsin digestion resulted in a significant decrease in this ratio, particularly at low frequencies; at 0.025 Hz, the short : long wavelength stress ratio (mean $\pm$ SEM) after trypsin treatment was 0.18 ± 0.05, as compared to 0.35 ± 0.05 before digestion ($p < 0.01$ by ANOVA). With increasing excitation frequency, the difference in short : long ratio between pre-digestion and post-digestion measurements became less pronounced and was not statistically significant for frequencies above 0.25 Hz.

3.5 Discussion

We have measured current-generated stress in bovine articular cartilage using electromechanical surface spectroscopy with multiple wavelengths and frequencies. These results extend our previous studies [14], in which the sensitivity of surface probe measurements to global chemical modification of tissue charge density was demonstrated. We have now extended the capability of the probe so that both the frequency and imposed spatial wavelength of the applied electric current can be varied and tested the device with full-thickness cartilage plugs having an intact articular surface. Using a trypsin digestion model, we have produced controlled profiles of nonuniform aggrecan loss as a model for cartilage degradative changes. We have demonstrated the ability of wavelength- and frequency-scanning spectroscopy to detect focal regions of cartilage degradation produced by this model. Ultimately we hope to assess the clinical utility of surface probe measurements, using multiple

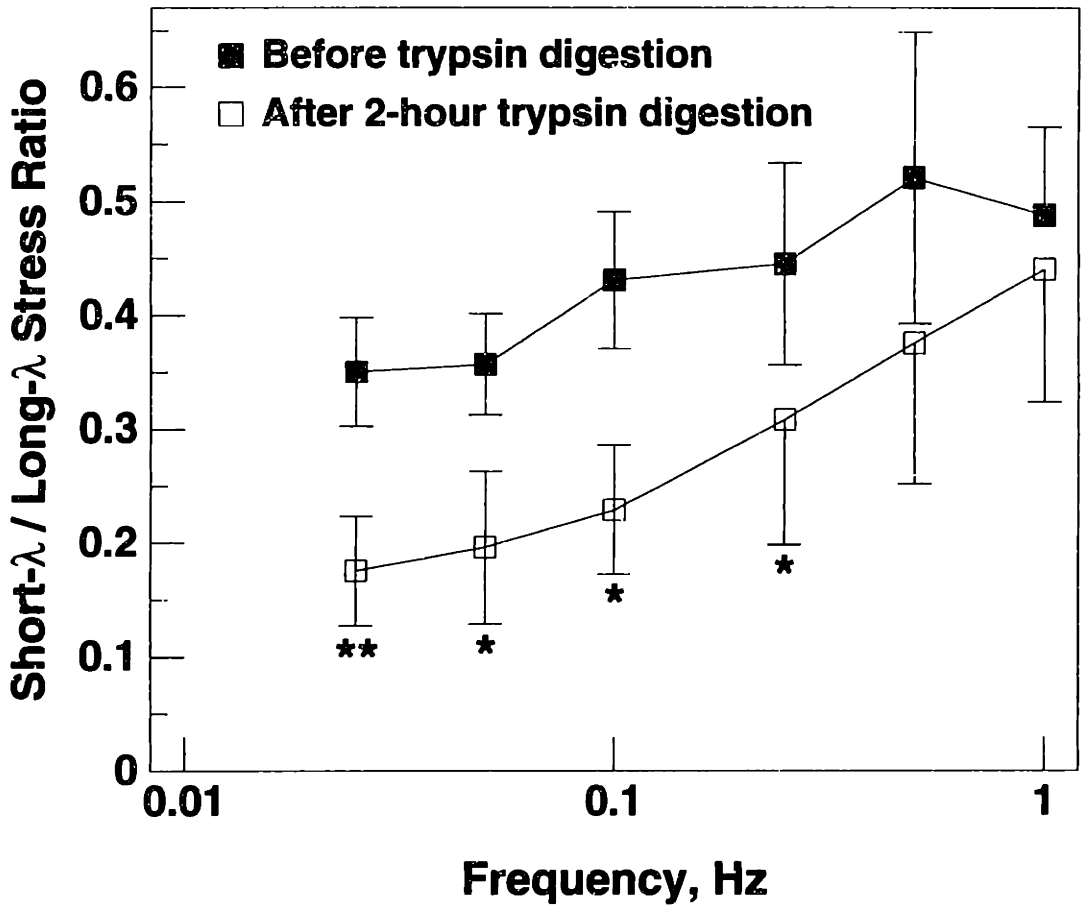

Figure 3.6: Ratio of short-wavelength to long-wavelength stress response measured in full-thickness calf cartilage-bone plugs, both before (filled squares) and after (open squares) 2 h of surface trypsin digestion (N = 4, mean ± SEM). Stress was measured using the multiple-wavelength probe. At frequencies up to 0.25 Hz, post-digestion values were significantly different from pre-digestion values ($* p < 0.05$, $** p < 0.01$ by ANOVA).

wavelengths and frequencies, in order to quantitatively compare the electromechanical spectroscopic behavior of normal and degraded cartilage *in vivo*.

3.5.1 Multiple-wavelength probe

For *in vivo* clinical applications of the probe technology, it is desirable to be able to make measurements over a range of wavelengths and frequencies using a single device (Figure 3.4, inset). Motivated by this need, we developed a six-electrode probe with independently addressable electrodes. By varying the external connections to each electrode, long- and short-wavelength measurements can be made sequentially; in contrast, with the fixed-wavelength probes, the cartilage specimen must be removed from the testing chamber between measurements and then repositioned and re-equilibrated once the other probe has been mounted in the chamber. The distribution of current produced by the long-wavelength configuration of the multiple-wavelength probe approximates the distribution produced by the two-electrode probe used in previous studies.

The multiple-wavelength probe was tested with full-thickness cartilage-bone plugs having an intact articular surface, in order to provide a more appropriate model for *in vivo* applications. Instead of an insulating platen, as used previously, the cartilage surface distal to the probe electrodes in these studies was delineated by the insulating cartilage-bone interface, which was not necessarily parallel to the articular surface. However, since the cartilage thickness was always on the order of or larger than the imposed wavelength for this study and hence greater than the current penetration depth (which is approximately $\lambda/3$), the stress response was not expected to be sensitive to the precise shape or conductivity of this interface.

As reported in our previous studies [14], a small-amplitude sinusoidal current applied to the surface of bovine articular cartilage induced a sinusoidal stress at the same frequency, with a phase difference of approximately 90° (not shown). At low frequencies, the stress measured with the short-wavelength configuration was less than half the response measured with the long-wavelength configuration (Figure 3.4B). However, with

increasing frequency, the ratio of short-wavelength to long-wavelength current-generated stress increased monotonically, reaching 0.68 by 1 Hz. The convergence of the long- and short-wavelength responses with increasing frequency may result from the frequency dependence of the *mechanical diffusion depth,* the distance into the tissue over which the poroelastic response can develop [211]. With increasing frequency, this distance decreases, even though the distribution of current (which depends only on the spatial wavelength) remains unchanged. Thus, at low frequencies, the depth to which cartilage properties are "sensed" by the probe is limited by the current penetration depth, while at higher frequencies, the mechanical diffusion depth increasingly limits the depth to which tissue properties can influence the response.

At both wavelengths used, the measured stress amplitude was inversely proportional to a fractional power of the frequency of the applied current, consistent with the theoretical poroelastic-electrokinetic model of Sachs and Grodzinsky [211]. This frequency dependence is also consistent with previous surface probe measurements [14] as well as measurements of current-generated stress made in uniaxial confined compression [64], which corresponds to the "infinite wavelength" limit of the model. According to the theory, higher temporal frequencies result in lower developed stress because the current-generated solid and fluid motions which together determine the mechanical stress have less time to develop during each cycle.

3.5.2 Detection of focal cartilage degradation

In the present studies, only the (intact) articular surface of cartilage-bone plugs was placed in contact with the enzyme; thus, trypsin could only penetrate in, and aggrecan breakdown products could only diffuse out, through this surface. This protocol produced a relatively mild loss of GAG; even after 24 h of digestion, the GAG content (as a percentage of tissue wet weight) never decreased below 50% of normal levels (Figure 3.5). Progressive loss of aggrecan from the articular surface is an appropriate model for the histological changes seen in early osteoarthritis [103,118]. Based on the observed kinetics of surface aggrecan loss

induced by trypsin digestion for 1, 4, 8, and 24 h, two-hour trypsin digestion was estimated to produce a region of approximately 25% GAG loss extending $\sim$ 0.6 mm into the tissue. This distance is approximately equal to the current penetration depth resulting from the short-wavelength excitation used with the multiple-wavelength probe (Figure 3.4). Thus, with short-wavelength excitation, the current would be expected to remain confined within this degraded region with its decreased aggrecan content, while with long-wavelength excitation, current would penetrate beyond the degraded region to sense the underlying normal tissue as well. The observed attenuation of the short- to long-wavelength stress ratio resulting from two-hour trypsin digestion (Figure 3.6) is consistent with this hypothesis. The reduction in this ratio was less pronounced at higher frequencies, however, because the shorter mechanical diffusion depth at these frequencies preferentially weights the response of the superficial (degraded) region while limiting the response due to deeper (normal) tissue. Although the 2 h trypsin digestion resulted in only 25% GAG loss from the degraded region, the stress ratio decreased by up to 50%; thus, multiple-wavelength spectroscopy is a sensitive indicator of partial-thickness degradative changes. Ongoing studies are aimed at incorporating the surface probe into a device for arthroscopically making measurements on intact joints, in order to assess the ability of electromechanical spectroscopy to detect and localize cartilage degradation *in vivo*.

Chapter IV

Comparison of Probe Measurements with a Theoretical Model of Surface Spectroscopy

4.1 Summary

[1]The mathematical model [210,211] describing the mechanical response of a charged, poroelastic medium such as cartilage to a sinusoidal current density imposed at the surface has now been solved with boundary conditions that correspond to the geometry of the electrode arrays used in probe experiments. Using this model, electrical and mechanical fields, forces, and flows resulting from surface excitation were simulated. While the penetration depth of current into the tissue was predicted to be proportional to the imposed spatial wavelength (independent of frequency), the simulated mechanical response was also governed by a frequency-dependent mechanical diffusion depth, which decreased with increasing frequency. The theory predicted both a nonuniform normal stress (with peak values at the electrode edges) and a much larger shear stress component at the surface of the tissue; these two stress components exhibited different phase behavior and frequency dependence. Simulations of normal surface stress (averaged over the electrode area) were compared with (1) measurements made using two-electrode and six-electrode fixed-wavelength probes, tested with 7 mm diameter disks of calf cartilage (0.1–1.8 mm thick), and (2) data from the multiple-wavelength probe, tested with full-thickness cartilage plugs as described in Chapter III. The measurements made with both the fixed-wavelength and multiple-wavelength probes showed the same inverse dependence on frequency as the simulated stress over the frequency range tested, consistent with a poroelastic mechanism. However, the model predicted a strong dependence of the surface stress on cartilage thickness, varying as the inverse third power of the thickness (for specimens thinner than the current penetration

[1]Supplemental simulations and data pertaining to the results described in this chapter are presented in Appendix F. The mathematical model is summarized in Appendix E.

depth), which was *not* seen in the measurements made with the fixed-wavelength probe. The stress amplitudes and short : long-wavelength stress ratio obtained with the multiple-wavelength probe were well fit by the model if thicknesses of 0.7–0.9 mm were used, even though the actual cartilage-bone plugs tested had a cartilage layer 4–6 mm thick. Several possible reasons for the discrepancy between theory and measurement are discussed.

4.2 Introduction

The arrangement of fixed matrix charge groups and mobile counterions in articular cartilage gives rise to electrokinetic transduction phenomena in the tissue. For example, mechanical compression of a cartilage specimen gives rise to an electrical *streaming potential* [66,90,136]. Conversely (as described in Chapter I), application of an electric current density across a cartilage disk produces a mechanical *current-generated stress* which is measurable at the tissue surface [64]. Since these electrokinetic effects in cartilage are directly dependent on the presence of highly charged matrix aggrecan molecules, loss of these macromolecules, such as occurs in osteoarthritic degradation [153], should be detectable by measurement of electromechanical properties of the tissue. Several studies [24,66,105] have demonstrated that electromechanical measurements provide a more sensitive indicator of molecular-level degradative changes in the tissue than purely mechanical tests, such as indentation testing.

Although previous measurements of streaming potential and current-generated stress used a uniaxial configuration (Figure 1.4), theoretical analysis [210,211] suggested that a spatially periodic standing wave of sinusoidal current applied to the cartilage surface via an interdigitated electrode array could also produce a current-generated stress, measurable at the surface by an overlying stress sensor (Figure 1.6). Based on this principle of *electromechanical surface spectroscopy,* the electrokinetic surface probe described in Chapters II and III was developed and tested under a variety of experimental conditions [10–15]. Theoretically, the converse (mechanical-to-electrical) phenomenon can also be demonstrated in cartilage; i.e., an imposed sinusoidal mechanical displacement at the cartilage surface

would give rise to an electrical streaming potential, measurable by surface electrodes [212].

Determining the fields, forces, and flows resulting from surface excitation of a poroelastic medium such as cartilage requires solving a system of linear equations (derived in Appendix E), subject to the appropriate electrical and mechanical boundary conditions. Sachs [210,211] analyzed the case of a purely sinusoidal current density applied to the surface of a homogeneous, isotropic material. Since the governing equations are linear, however, the (theoretical) response to more spatially complex excitations can be represented as a superposition of modal solutions, each scaled by a corresponding Fourier coefficient (determined by the imposed boundary conditions). Calculating the appropriate coefficients for an array of discrete electrodes requires solving a mixed boundary value problem, since the electrical *potential* is constrained to be constant over the surface of each electrode but the *normal current density* is constrained to be zero between the electrodes. A method of solution has been developed by Eliot Frank (as described in Appendix E) and implemented in software. Thus, using the poroelastic theory, the response to an arbitrary number of surface electrodes, of specified width and spacing, can now be modeled.

This chapter describes the results of a series of numerical simulations of electrical and mechanical quantities using the theoretical model of Sachs [210,211], modified to include discrete surface electrodes. The mathematical model is briefly derived, and the method of solution described, in Appendix E. Selected results of these simulations are presented in order to illustrate some basic principles underlying the probe measurements. The normal surface stress predicted by the model is compared with the surface probe measurements of current-generated stress at a variety of frequencies, wavelengths, and cartilage thicknesses. Appendix F contains additional simulations and data pertaining to the results presented in this chapter.

4.3 Methods

4.3.1 Mathematical Simulations

Theoretical profiles of electrical (current density, potential) and mechanical (fluid pressure, solid displacement, relative fluid velocity, and normal and shear surface stresses) quantities were determined using the poroelastic theory as summarized in Appendix E. For a specified electrode configuration and a specified number of spatial modes (typically 200), the modal solution was determined for each wavenumber. Next, the mixed boundary value problem was solved in order to determine the Fourier coefficient corresponding to each mode; the total solution was then determined as the weighted sum of the modal solutions. The computations were performed using software, in the C Programming Language, written by Eliot Frank.

Unless otherwise indicated, the material parameter values shown in Table 4.1 were used in all simulations; these values were taken from the literature [58,65,137,179]. The lower boundary of the tissue was assumed to be impermeable to fluid flow and electrically insulating, as a model for the cartilage-bone interface or the interface between the distal edge of the cartilage disk and the PMMA platen used in some experiments. An array of either two or six evenly-spaced electrodes, with the corresponding geometric parameters (width and spacing) shown in Table 4.2, was specified for each simulation[2]. A "reflecting" lateral boundary was imposed at a distance of 10 mm from the center of the electrode array. For comparison with probe measurements, a current density amplitude of 10 A/m^2 was used in all simulations.

[2]Although the center-to-center spacing of the actual six-electrode probes was 0.84 mm, a spacing of 0.85 mm was used in the simulations so that a grid spacing of 0.05 mm could be used for the computations, in order to ensure that the points at which the solution would be computed would include the edges of each electrode.

Symbol	Parameter	Value
k_{11}	Hydraulic Permeability	$1 \frac{\mu m/s}{MPa/mm}$
k_{22}	Electrical Conductivity	1.0 S/m
$k_e = k_{21}/k_{22}$	Electrokinetic coefficient	10 mV/MPa
ν	Poisson's ratio	0.4
ϕ_0	Porosity	0.8
$H_A = 2G + \lambda_L$	Equilibrium modulus	0.5 MPa

Table 4.1: Default material parameter values used in mathematical simulations; values are taken from the literature [58,65,137,179].

Number of electrodes	Electrode width, mm	Electrode spacing (center-to-center), mm
2	1.5	2.5
6	0.3	0.85

Table 4.2: Geometric parameters (electrode width and spacing) used for simulations

4.3.2 Measurement of Current-Generated Stress vs. Thickness

To assess the dependence of current-generated stress on cartilage thickness, disks of calf cartilage of various thicknesses were tested with probes having either two (Figure 4.1A) or six (Figure 4.1B) electrodes and thus a fixed spatial wavelength of either λ = 5 mm or λ = 1.68 mm, respectively. Four cartilage-bone plugs (9.5 mm diameter) were obtained from calf knee joints as described in Section B.3. Disks of thickness 1.0, 0.1, 0.18, and 1.8 mm were sequentially cut from each plug using a sledge microtome; one 1.8 mm thick disk, however, contained significant subchondral bone and was not used. A concentric 7 mm diameter disk was then cored from each 9.5 mm disk using a metal punch and held in the PMMA chamber with a 9.5 mm diameter PMMA platen at a 50 kPa static load. The bath solution consisted of 0.15 M NaCl at pH 7.0, plus the proteinase inhibitors 2 mM [ethylenedinitrilo]tetraacetic acid (EDTA), 5m M benzamidine-HCl, 10 mM N-ethylmaleimide (NEM), and 1 mM phenylmethylsulfonyl fluoride (PMSF). Current-generated stress (amplitude and phase) was measured with both fixed-wavelength probes at frequencies ranging from 0.025 to 1.0 Hz, using a current density of 10 A/m^2.

4.3.3 Comparison of Theoretical and Measured Current-Generated Stress

Current-generated stress measured using the surface probe was compared with the simulated stress predicted by the poroelastic model. The simulated stress was averaged over the positive electrode area; the amplitude was then multiplied by two in order to account for the differential recording technique used in probe measurements. For one series of comparisons, stress measured in cartilage disks of thickness 0.1–1.8 mm using the two- and six-electrode fixed-wavelength probes (as described above) was compared with simulations using the same thicknesses and electrode configurations. In another series, the multiple-wavelength probe data from Chapter III (tested with full-thickness cartilage-bone plugs) was compared with simulations using a six-electrode array configured for both long- and short-wavelength excitation (Figure 3.1).

Statistical comparisons were performed using multivariate analysis of variance

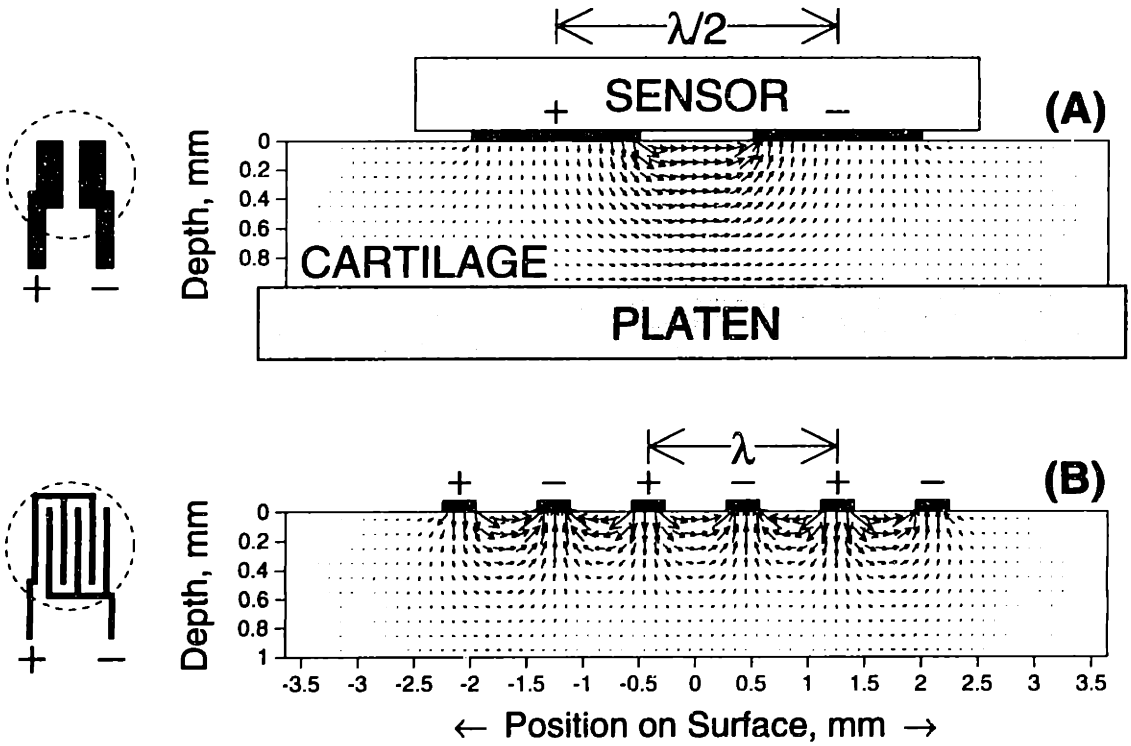

Figure 4.1: Theoretical distribution of current density within the bulk of a cartilage specimen resulting from an array of either (**A**) two or (**B**) six electrodes applied to the tissue surface [211]. Arrows indicate the direction and relative magnitude of current density. Electrode patterns of two- and six-electrode fixed-wavelength probes are shown at left; dashed circles outline area in contact with surface of cartilage disk.

(ANOVA). All computations were performed using the SAS data analysis software package. Results were considered significant at the $p < 0.05$ level.

4.4 Results

4.4.1 Mathematical Simulation of Electrical and Mechanical Variables

Simulation: Current Density

The theoretical distribution of current density, $\vec{J}$, within the tissue is governed by Laplace's equation, as derived in Appendix E (Equations E.9–E.12), subject to the boundary conditions imposed by the electrode geometry. Because the current density is Laplacian, the fields are assumed to be quasistatic, and the electrode array is spatially periodic, the current density amplitude will decay with increasing depth into the tissue, over a length scale proportional to the electrode periodicity (i.e., the spatial wavelength). Thus, the *penetration depth* of current into the tissue is proportional to the spatial wavelength. For example, with two widely spaced electrodes (Figure 4.1A), current penetrates the full thickness of the specimen, while with more closely spaced electrodes (Figure 4.1B), the current remains confined to a more superficial region[3]. This dependence of penetration depth on imposed wavelength predicted by the poroelastic model forms the basis of the multiple-wavelength experiments described in Chapter III.

Although the electrical potential is constrained to be constant over the surface of each electrode, the predicted current density was nonuniform with position on the electrode surface (Figure 4.2). For example, with a nominal current density amplitude $J_0 = 10\ \mathrm{A/m^2}$ applied to a two-electrode array, the resulting normal component of current density reached $80\ \mathrm{A/m^2}$ at the inner edge of the electrodes and rapidly decreased with increasing distance outward. This phenomenon is consistent with the larger arrows seen at the inner edges of the electrodes in Figure 4.1A.

[3]See also Figures 1.8, 1.9, 2.1, and 3.1.

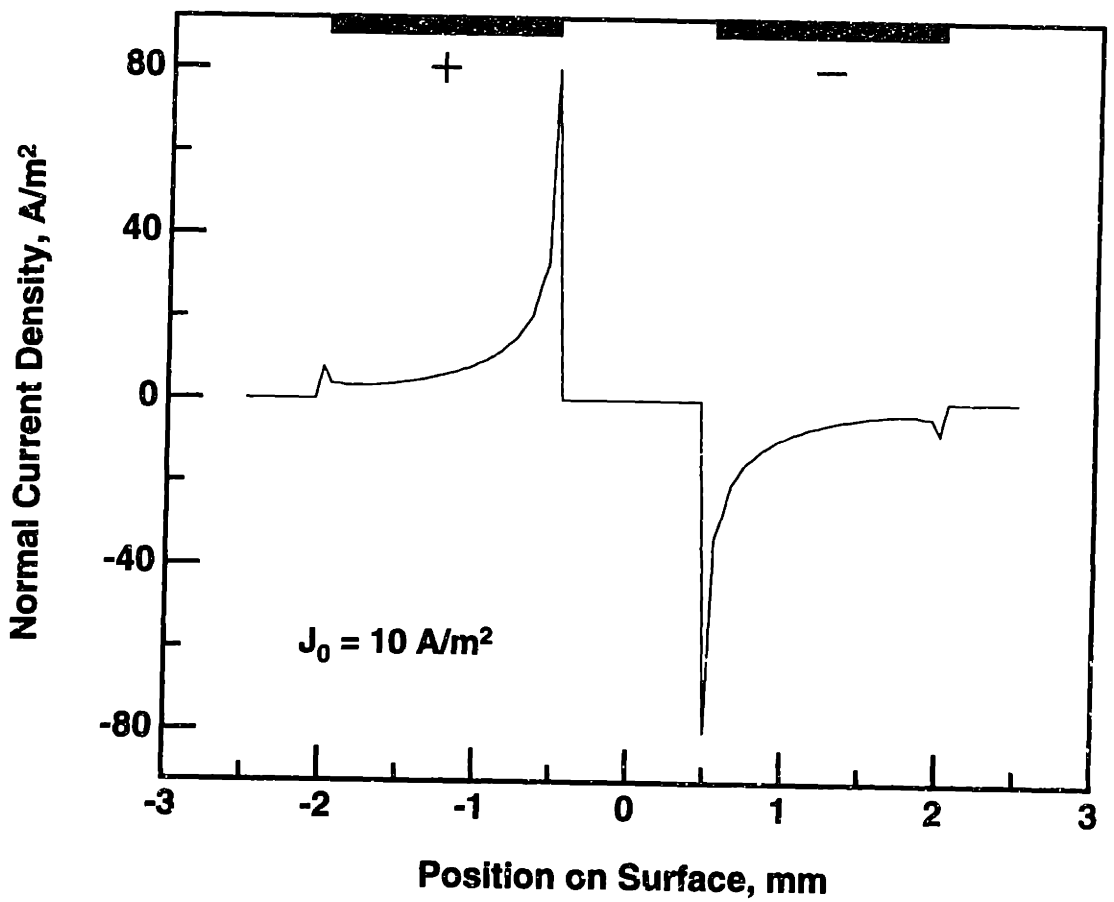

Figure 4.2: Normal component of current density vs. position on cartilage surface for a simulated two-electrode array with a nominal current density amplitude of $J_0 = 10\ A/m^2$. Heavy lines at top indicate electrode positions and polarity.

Simulation: Fluid Velocity

The vector field of relative fluid velocity, $\vec{U}$, was computed for a two-electrode array at two different frequencies (Figure 4.3). Comparing the two profiles shows that while at 0.001 Hz there was a relatively uniform-appearing distribution of velocity across the depth of the tissue (Figure 4.3, top), at 1.0 Hz the fluid velocity was markedly higher toward the surface than at deeper levels, especially at the inner edges of the electrodes (Figure 4.3, bottom). As the frequency was increased, the vertical component of the relative fluid velocity, U_z, exhibited a progressively larger maximum value (Figure 4.4, top), with a relatively narrower peak located closer to the surface of the tissue (Figure 4.4, bottom). Similarly, the total relative fluid velocity amplitude, $|\vec{U}|$ (which is dominated by the horizontal component), was relatively higher toward the surface at higher frequencies (Figure 4.5) and decreased more rapidly with increasing depth into the tissue.

The frequency-dependent shift in the location of the peak fluid velocity is due to the existence of a *mechanical diffusion depth,* Δ, the depth into the tissue over which the poroelastic response can develop. This depth decreases with increasing frequency; the modal theory [210,211] predicts that for a single spatial mode (spatially sinusoidal surface excitation), the diffusion depth is given by

$$\Delta = \sqrt{\frac{H_A k_{11} \phi_0}{\omega}}, \tag{4.1}$$

where H_A, k_{11}, and ϕ_0 are the equilibrium modulus, Darcy hydraulic permeability, and porosity, respectively, of the tissue. For typical values of these parameters (Table 4.1), this depth decreases from 0.25 mm at 0.001 Hz to 8 μm at a frequency of 1.0 Hz. Thus, although the distribution of current density does not depend on the temporal frequency, the mechanical response becomes increasingly limited by the diffusion depth at higher frequencies.

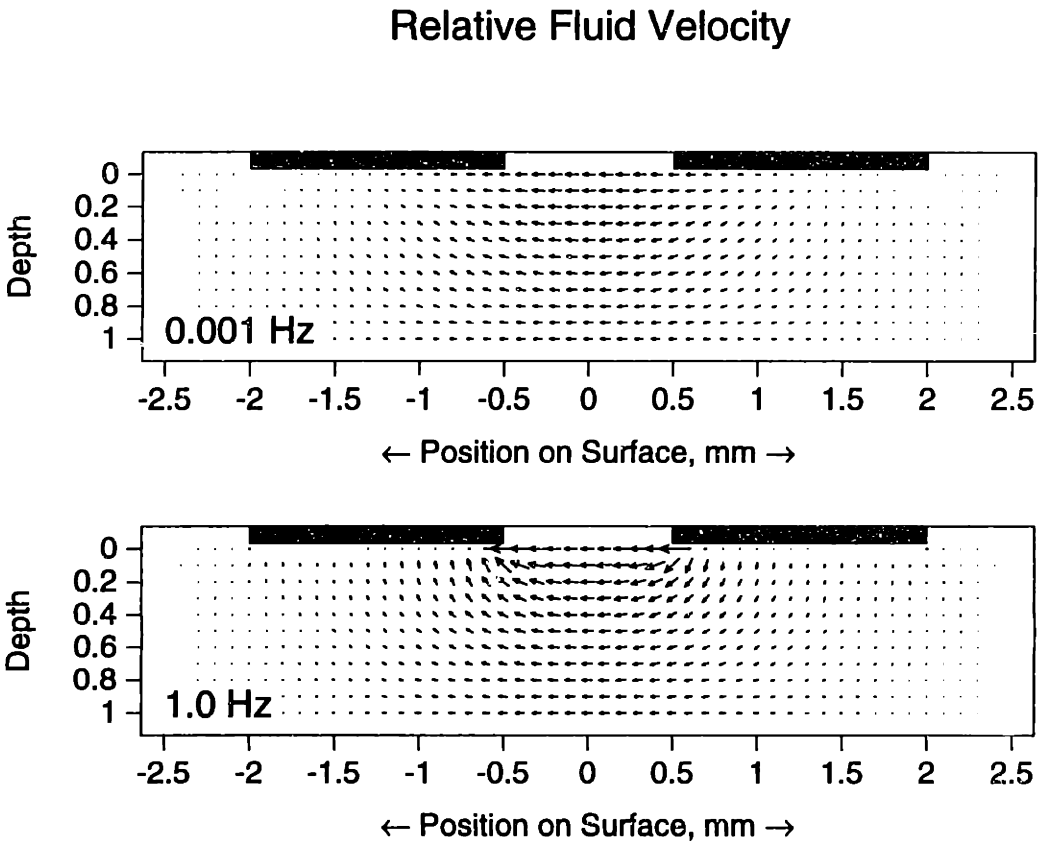

Figure 4.3: Theoretical profile of relative fluid velocity, $\vec{U}$, computed using the poroelastic model, for a two-electrode array with excitation frequencies of 0.001 Hz (top) and 1.0 Hz (bottom) applied to the surface of a 1 mm thick specimen. At the higher frequency, the fluid velocity is relatively greater toward the surface, particularly in the region between the two electrodes.

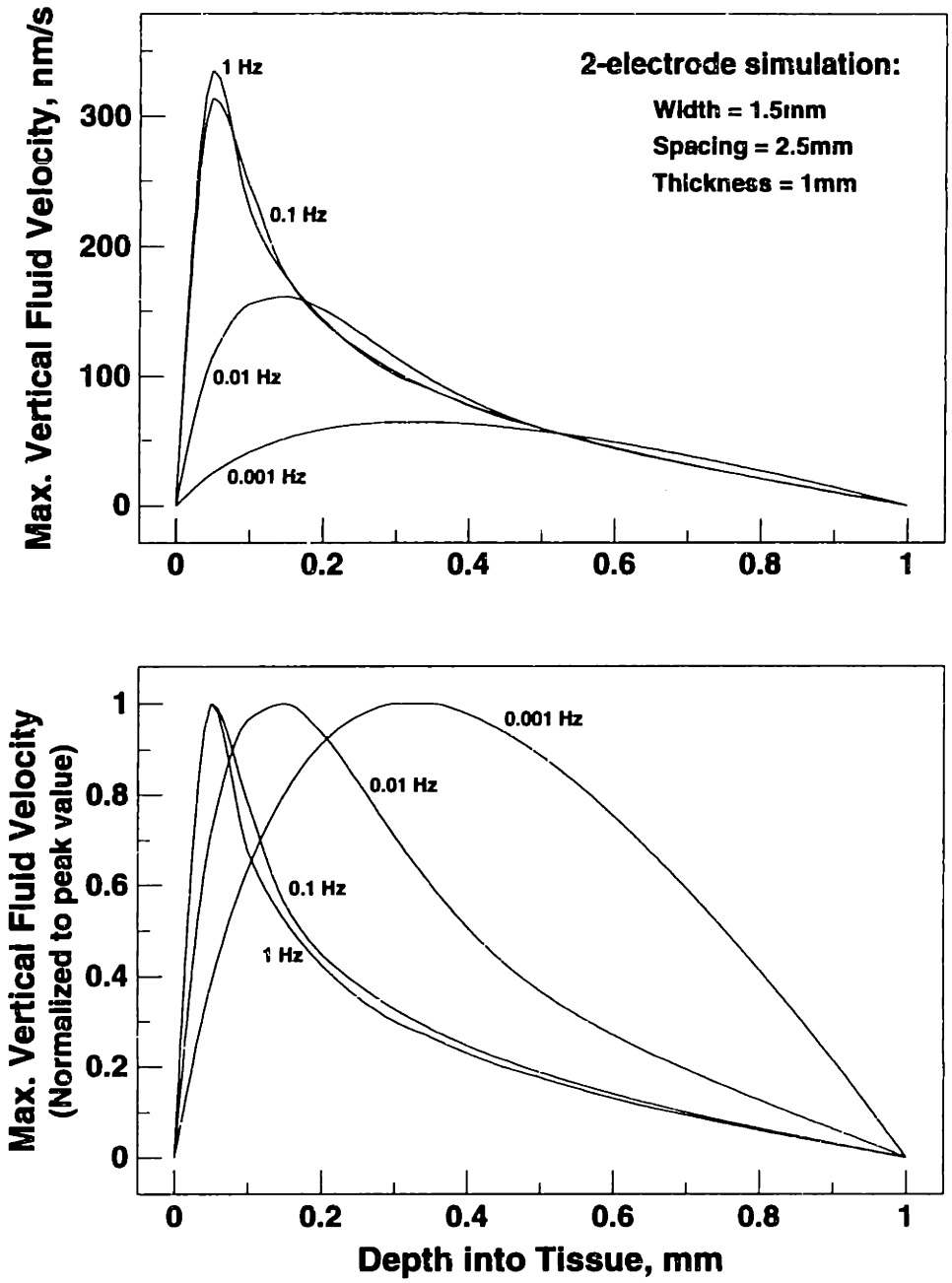

Figure 4.4: Theoretical maximum vertical relative fluid velocity amplitude, U_z, vs. depth into tissue (1 mm thick) for a two-electrode array, with a current density of 10 A/m^2, computed using the poroelastic model. At each depth, the maximum value over the plane at that depth has been plotted. Bottom: Same data normalized to peak value at each frequency.

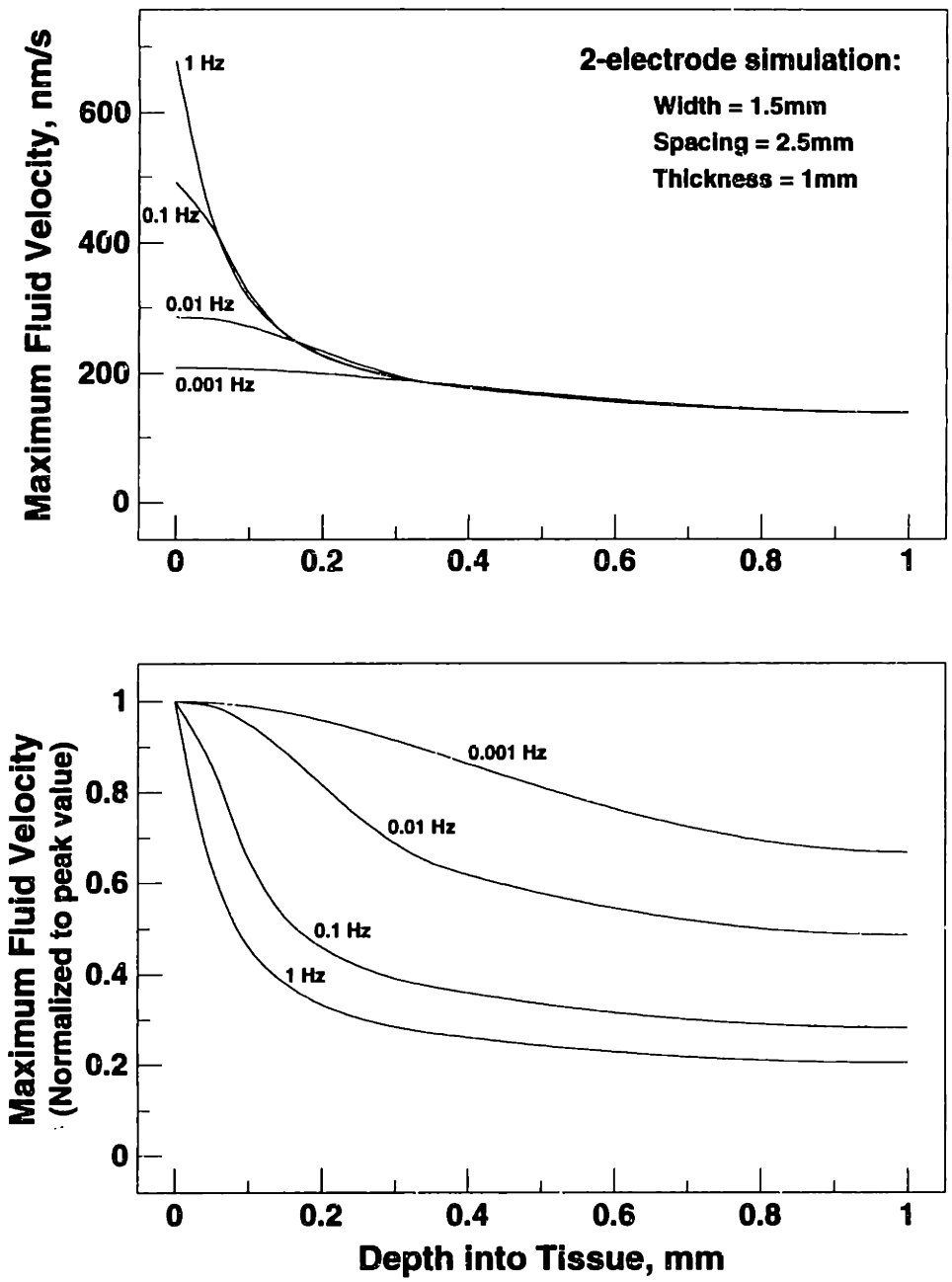

Figure 4.5: Theoretical maximum relative fluid velocity amplitude, $|\vec{U}|$, vs. depth into tissue (1 mm thick) for a two-electrode array, with a current density of 10 A/m^2, computed using the poroelastic model. At each depth, the maximum value over the plane at that depth has been plotted. Bottom: Same data normalized to peak value at each frequency.

Simulation: Normal and Shear Stress at Surface

Normal and shear stresses acting at the surface of a 1 mm thick specimen were simulated, with a current density of 10 A/m^2 at a frequency of 0.025 Hz (Figures 4.6, 4.7); the real and imaginary parts of the complex stress predicted by the model are plotted. With both the two- and six-electrode structures, the normal stress at the surface was nonuniform over the area of each electrode, with a peak at the edge of the electrode (Figure 4.6) that was similar to the peak in normal current density at this position (Figure 4.2). A piezoelectric stress sensor positioned directly over one of the excitation electrodes (as implemented in the probe sensor) would develop an output voltage proportional to the *average* stress over the electrode surface. Over most of the electrode area, the response was dominated by the imaginary component; thus, the phase angle (relative to the imposed current) is expected to be approximately 90° over the positive electrodes and −90° over the negative electrodes. Because the normal stress is antisymmetric about the midpoint ($y = 0$) of the electrode array (Figure 4.6), recording the *difference* between the stresses on the positive and negative electrodes (as is done by the probe) would yield a signal with *twice* the average stress amplitude on the positive electrodes and with a phase angle of +90°.

For both electrode arrays, the theoretical shear stress at the surface had a peak amplitude 50–100 times greater than the peak normal stress (Figure 4.7). The shear stress was dominated by its real part, which was negative over both electrodes in the two-electrode array (Figure 4.7, top). With the six-electrode array (Figure 4.7, bottom), the influence of adjacent electrodes resulted in a shear stress that was alternatively positive and negative between adjacent pairs of electrodes and which changes sign over the area of each electrode; however, the *average* stress over each electrode was real and negative. Thus, with both electrode arrays, the phase angle of the average shear stress is expected to be ±180°. Unlike the normal stress, the surface shear stress is *symmetric* about the midpoint; thus, even if the large shear stress component were to produce a response in the piezoelectric sensor, differential recording would be expected to eliminate this component of the signal.

The shear and normal components of the (theoretical) surface stress exhibited dif-

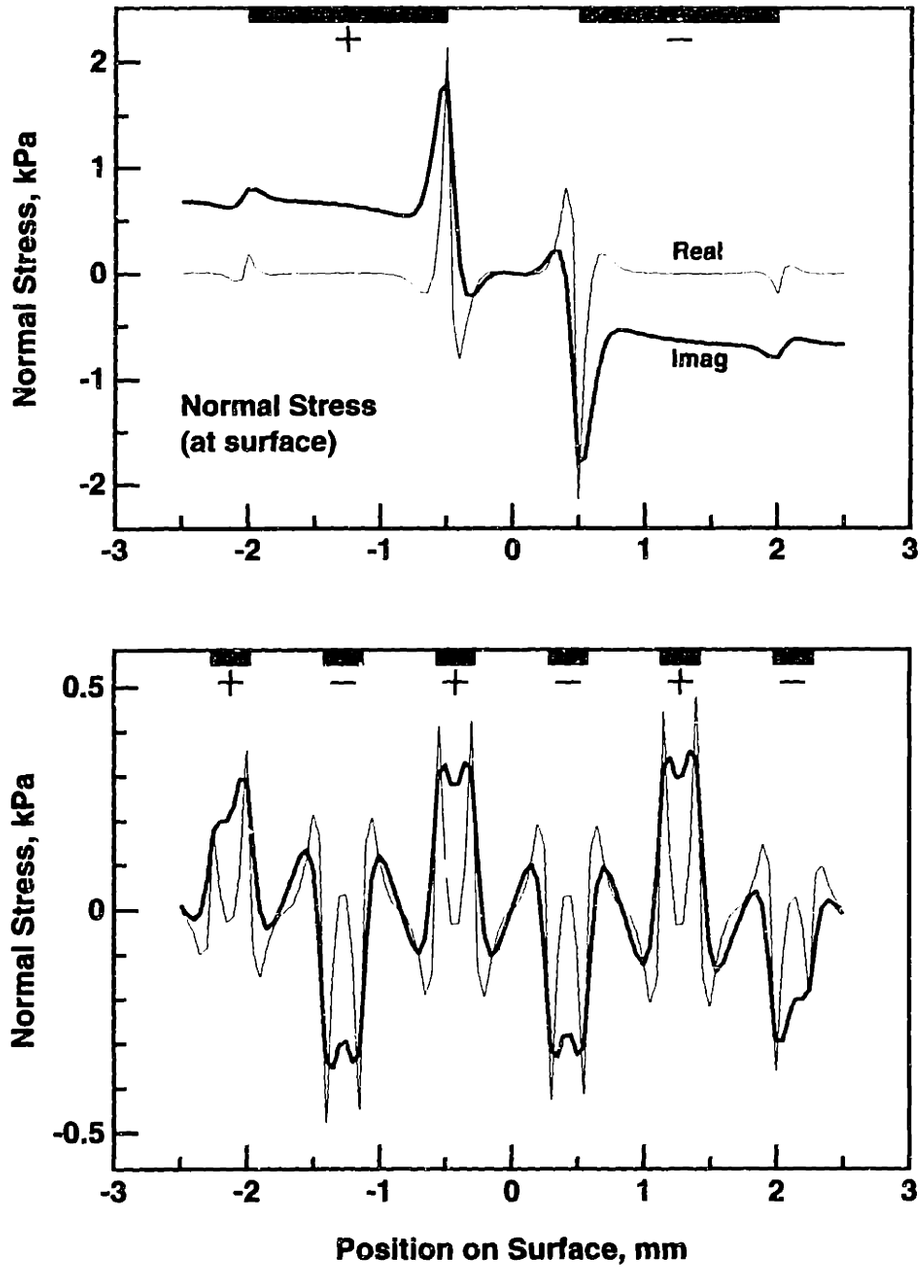

Figure 4.6: Simulated surface normal stress (real and imaginary parts) vs. position on the surface of a 1 mm thick specimen in response to a current density of 10 A/m^2 at 0.025 Hz imposed by either a two-electrode (top) or six-electrode (bottom) array. Heavy lines at the top of each plot indicate electrode positions and polarity. Positive stress is defined as a compressive stress on the sensor electrodes.

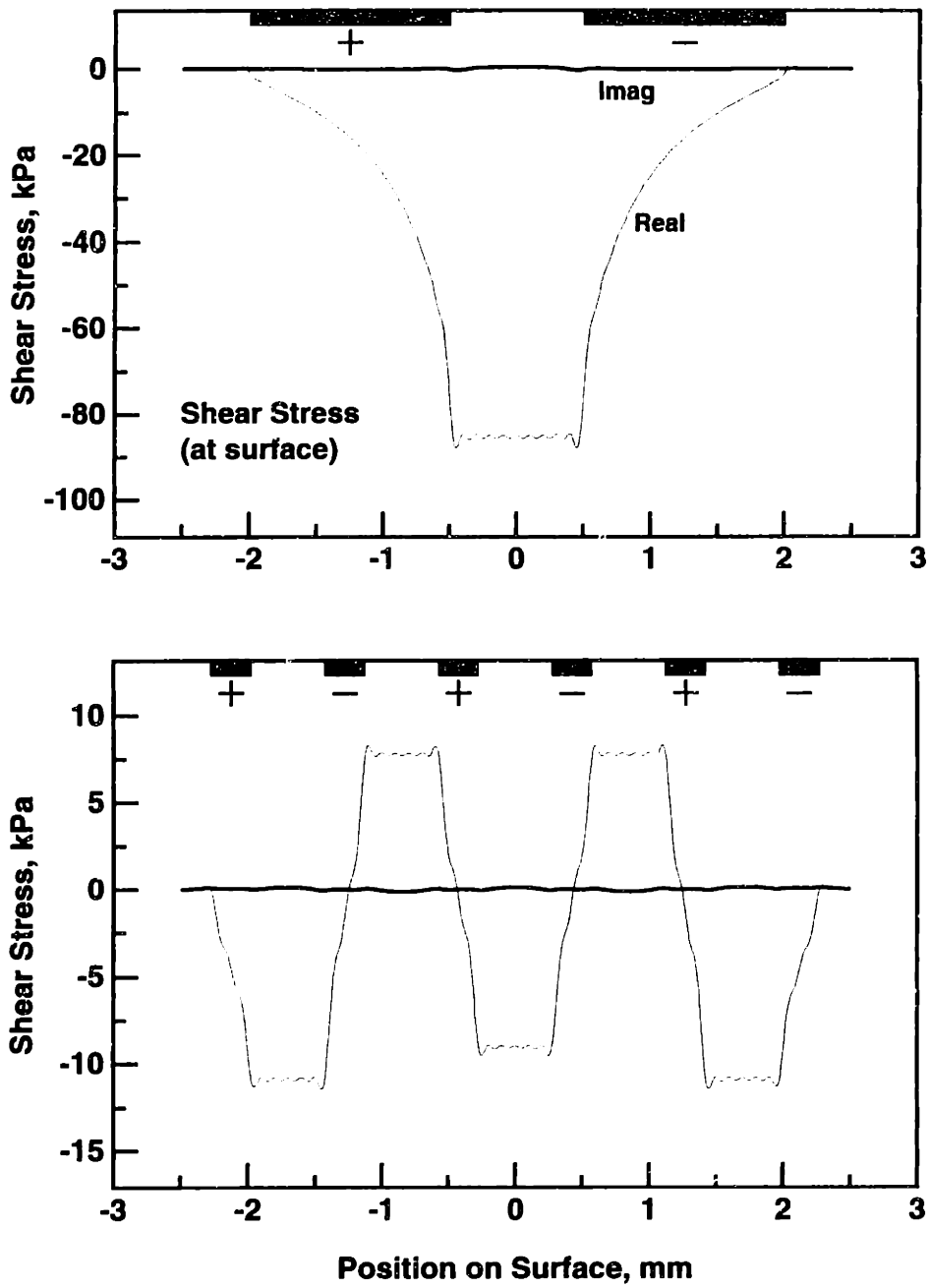

Figure 4.7: Simulated surface shear stress (real and imaginary parts) vs. position on the surface of a 1 mm thick specimen in response to a current density of 10 A/m^2 at 0.025 Hz imposed by either a two-electrode (top) or six-electrode (bottom) array. Heavy lines at the top of each plot indicate electrode positions and polarity. Positive stress is defined in the $+y$ (right) direction.

ferent behavior with respect to frequency (Figure 4.8). At higher frequencies, the normal stress amplitude (averaged over the positive electrode area) was inversely proportional to frequency, with a phase angle of approximately 90°, while in the low-frequency (quasistatic) range, the amplitude reached a plateau and the phase angle approached zero. The transition between the two regions occurred at approximately 1.4×10^{-4} Hz for the two-electrode probe. This behavior is consistent with a poroelastic response. With the six-electrode probe, the transition in amplitude and phase behavior was less abrupt, with a lower plateau value for the amplitude. In contrast, the simulated shear stress for both wavelengths reached a plateau at both low and high frequencies, while the phase angle remained approximately $\pm 180°$ (Figure 4.8, bottom). Since a purely shearing motion would not involve relative fluid flow, it is reasonable that the shear component did not exhibit the inverse frequency dependence characteristic of a poroelastic phenomenon.

4.4.2 Current-Generated Stress: Comparison of Theory and Measurements

Fixed-Wavelength Probes

Calf cartilage disks (7 mm diameter) having thicknesses of 0.1, 0.18, 1.0, and 1.8 mm were tested using both the two-electrode (λ = 5 mm) and six-electrode (λ = 1.68 mm) fixed-wavelength probes (Figure 4.9). At each wavelength and frequency, the measured stress did not vary significantly with cartilage thickness, as determined by analysis of variance (ANOVA). In contrast to the probe data, the poroelastic model predicted a strong dependence of stress amplitude on the cartilage thickness (Figure 4.10). With thin specimens, the simulated stress was inversely proportional to the third power of the thickness, while with larger thicknesses, the stress asymptotically approached a constant value. Although the measured stress was within a factor of 2–4 of the predicted stress (for both wavelengths) with 1 mm and 1.8 mm thick tissue, the response measured in 0.1 mm thick cartilage using the six-electrode probe was smaller than the predicted value by a factor of 300 and the response measured with the two-electrode probe was three orders of magnitude smaller than predicted. In addition, the predicted stress for the six-electrode case reached a lower

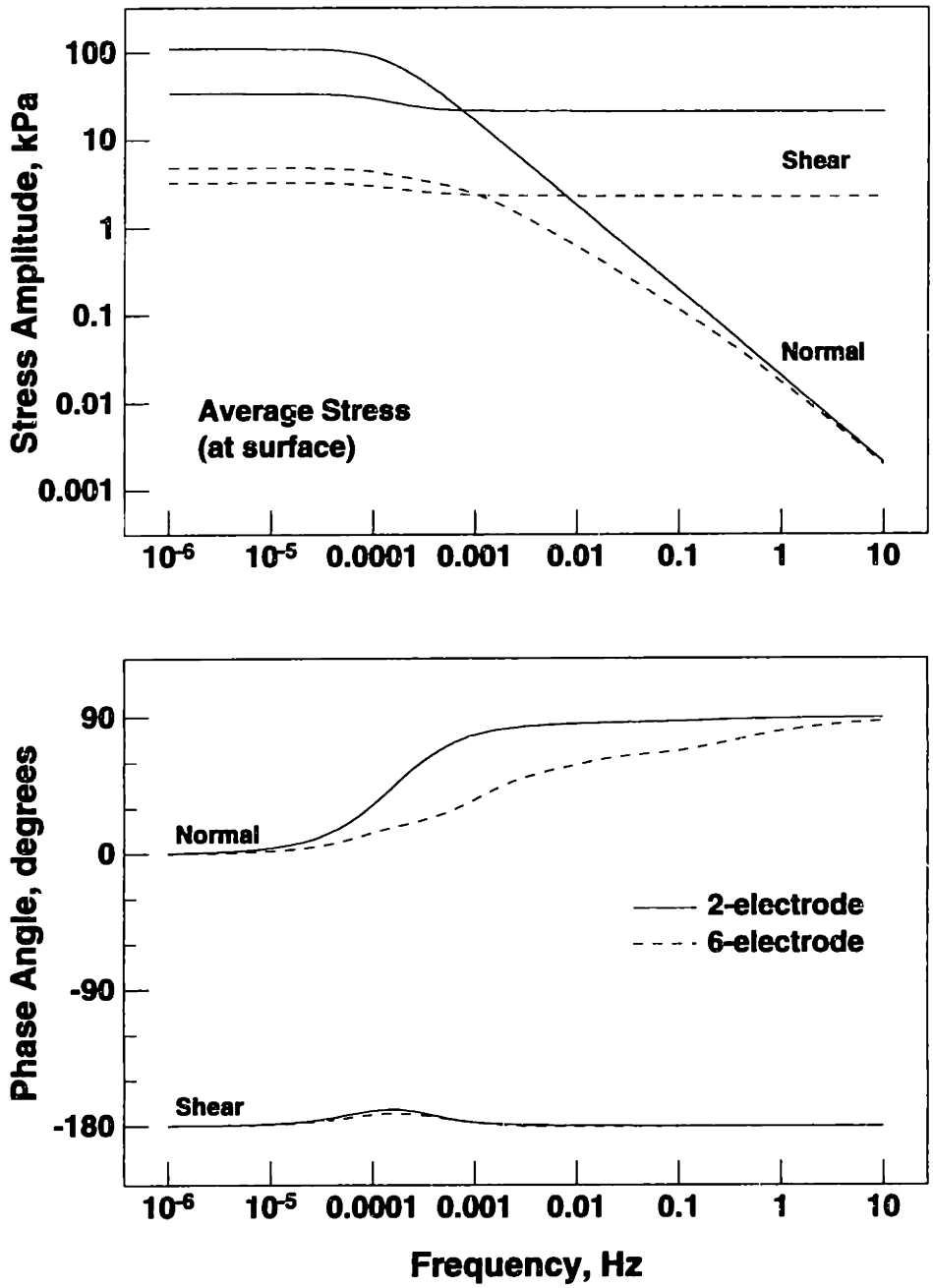

Figure 4.8: Simulated normal and shear stresses (amplitude and phase), averaged over the positive electrode area, produced at the surface of a 1 mm thick specimen in response to a current density of 10 A/m^2 imposed by two-electrode (λ = 5 mm, solid lines) and six-electrode (λ = 1.68 mm, dashed lines) arrays, vs. frequency.

plateau value than than the two-electrode response, with the curves crossing at a thickness of approximately 1.5 mm. However, the measured stress, even for 1.8 mm thick disks, was always lower when measured with the six-electrode probe. While the predicted phase angle remained between 60 and 90° at all thicknesses for both wavelengths, the measured phase angle ranged from 87–105° with the two-electrode probe and 68–131° with the six-electrode probe (Figure 4.10).

The stress amplitude measured with the two-electrode (λ = 5 mm) probe was inversely proportional to the frequency of the applied current for all four thicknesses (best-fit exponents, determined by the Levenberg-Marquardt nonlinear least-squares algorithm [199], ranged from -0.91 ± 0.09 to -1.02 ± 0.19). With the six-electrode (λ = 1.68 mm) probe, the best-fit exponents ranged from -0.73 ± 0.04 for 0.1 mm thick cartilage to -1.03 ± 0.05 for the 1.8 mm thick specimens. This frequency dependence of the measured stress is consistent with previous measurements of current-generated stress in uniaxial compression [64]. The best-fit exponents for the dependence of the *predicted* stress amplitude on frequency (-0.94 to -1.00 for the two-electrode configuration and -0.78 to -0.97 for the six-electrode configuration) were comparable to those of the measured stress.

Multiple-Wavelength Probe

Current-generated stress amplitude and phase were simulated for the case of a six-electrode array, configured for both long-wavelength (Figure 3.1A) and short-wavelength (Figure 3.1B) excitation, for thicknesses of 0.1–10 mm and frequencies of 0.025–1.0 Hz (Figure 4.11). At each frequency, the predicted stress amplitude was inversely proportional to the third power of the thickness for small thicknesses and reached a plateau at larger values; both curves reached approximately the same plateau value (0.05 kPa, for a frequency of 0.025 Hz). The predicted phase angle varied from 60–90° over the range of thicknesses simulated. The *ratio* of the predicted short-wavelength to long-wavelength stress amplitude was found to vary with both thickness and frequency (Figure 4.12, top). For thicknesses less than 0.25 mm, this ratio remained in the range 0.19–0.23 over the range of frequencies

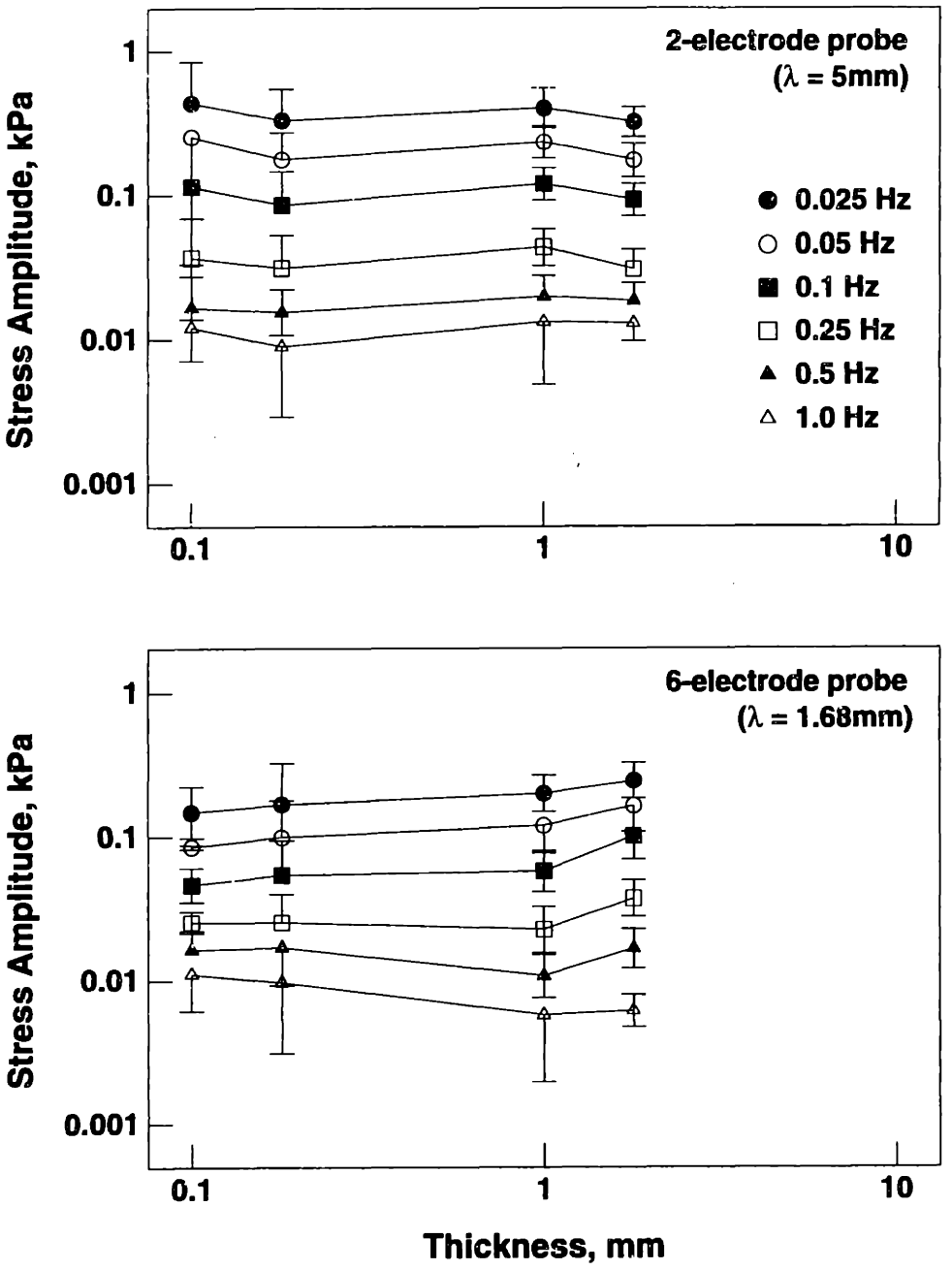

Figure 4.9: Current-generated stress amplitude vs. cartilage thickness by frequency, measured in calf cartilage disks (0.1–1.8 mm thick) using both the two-electrode (λ = 5 mm) and six-electrode (λ = 1.68 mm) fixed-wavelength probes with an applied current density amplitude of 10 A/m^2. All data points are mean ± SD; N = 4 disks for thicknesses of 0.1, 0.18, and 1.0 mm, while N = 3 for 1.8 mm thick disks. At each frequency and wavelength, stress amplitude did not vary significantly with cartilage thickness (by ANOVA).

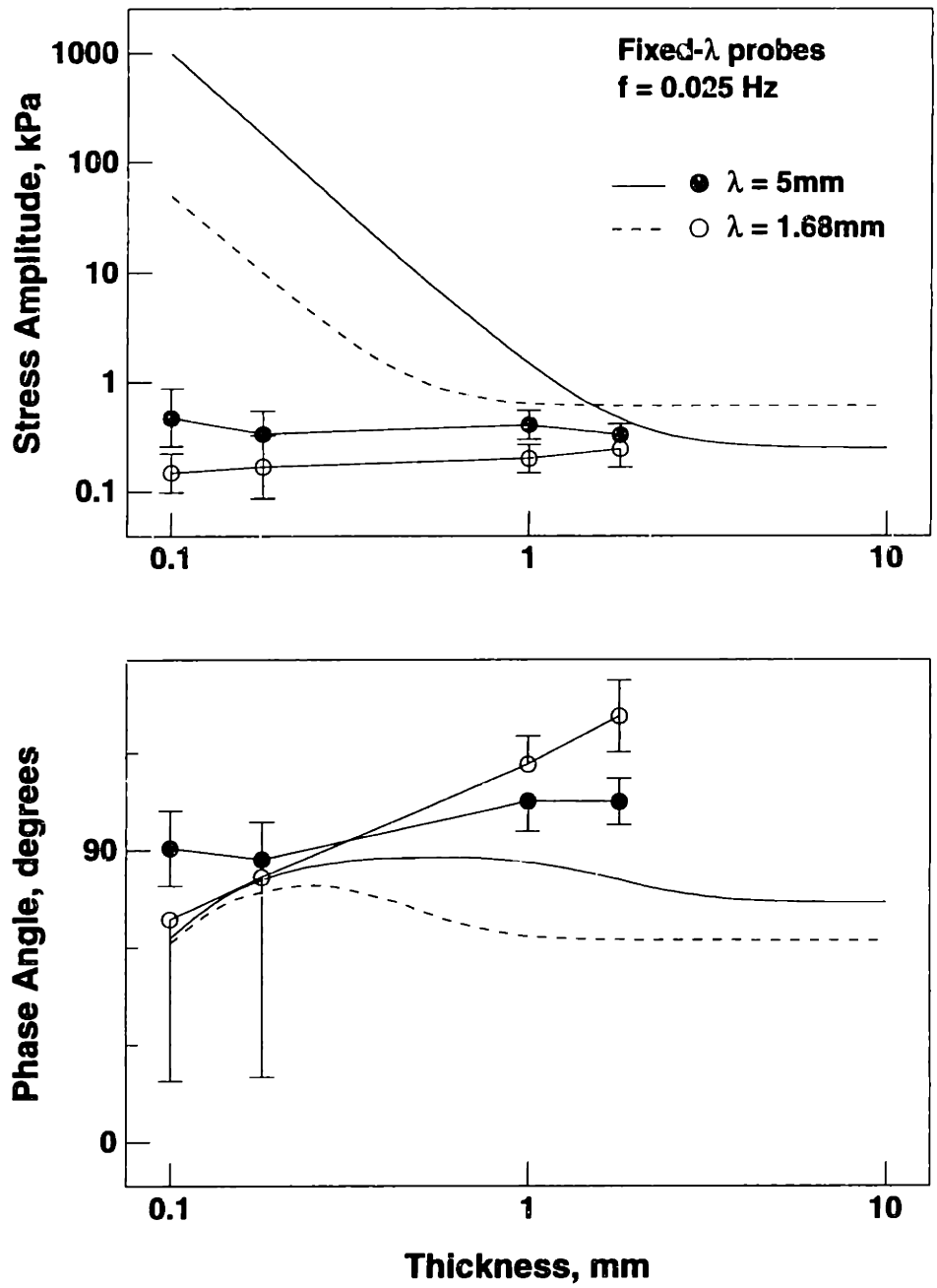

Figure 4.10: Current-generated stress (amplitude and phase), measured using two- and six-electrode fixed-wavelength probes (circles), and simulated stress predicted by poroelastic model (solid and dashed lines), vs. cartilage thickness, with a current density of 10 A/m^2 at a frequency of 0.025 Hz.

tested. When the thickness increased above 2.5 mm, however, the ratio was approximately 1.0 (because the curves for both wavelengths had converged to the same plateau value).

Using thicknesses in the range 0.7–0.9 mm in the simulation, the predicted ratio of short- to long-wavelength stress amplitudes agreed reasonably well with the stress measured in cartilage-bone plugs using the multiple-wavelength probe (Figure 4.12, bottom), even though the full-thickness plugs used for these measurements typically had a cartilage layer that was 4–6 mm thick (which is well within the plateau region of both curves in Figure 4.11 and thus would have a predicted stress ratio of 1.0). The actual stress amplitudes predicted by the model (not shown) were 6–10 times greater than the measured stress at 0.025 Hz and 4–6 times greater at 1.0 Hz.

4.5 Discussion

As with any mathematical model of a complex physical system, the poroelastic theory for an electromechanically coupled medium driven by surface electrodes [210,211] is an attempt to capture the essential physical behavior of the system in a series of equations which, in this case, can be solved analytically (see Appendix E). Typically, it is necessary to make some general assumptions which, while simplifying the analysis and making the problem computationally feasible, can potentially decrease the accuracy with which the model describes the behavior of the actual system. Simulating the response of a cartilage specimen to an imposed current density can provide insight into the mechanisms underlying the stress measured with the probe. Several aspects of the simulated response are discussed with respect to their impact on probe performance and interpretation of data obtained using the device.

4.5.1 Wavelength and Penetration Depth

In principle, because of the Laplacian nature of the electrical current density (Equation E.12), the current density amplitude within the bulk of the cartilage should decay over a length scale proportional to the spatial period of the surface excitation. For a spatially sinusoidal surface

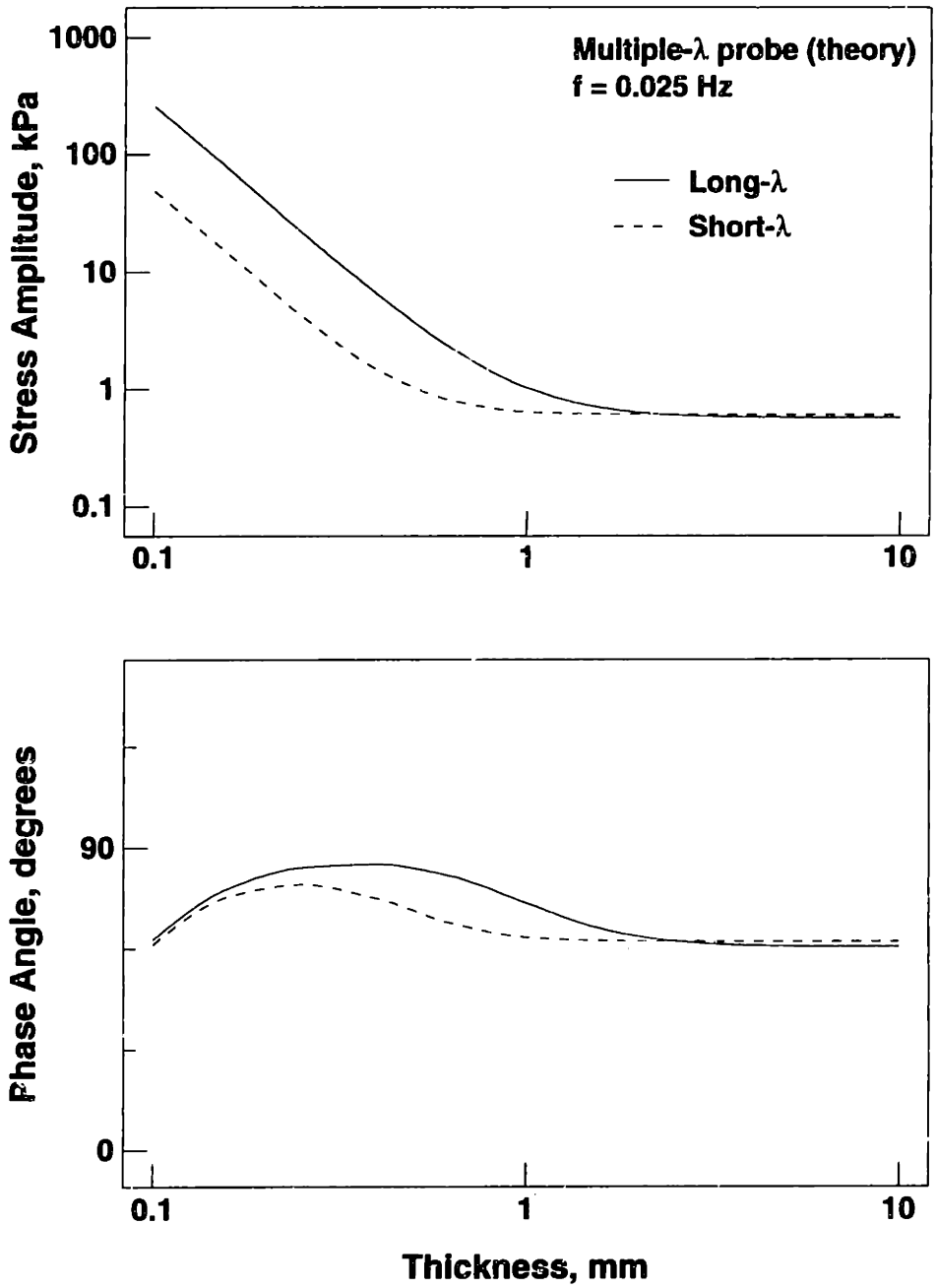

Figure 4.11: Theoretical stress (amplitude and phase) vs. specimen thickness produced by the multiple-wavelength probe configured for both long-wavelength (solid lines) and short-wavelength (dashed lines) excitation at a single frequency (0.025 Hz), with a current density of 10 A/m^2.

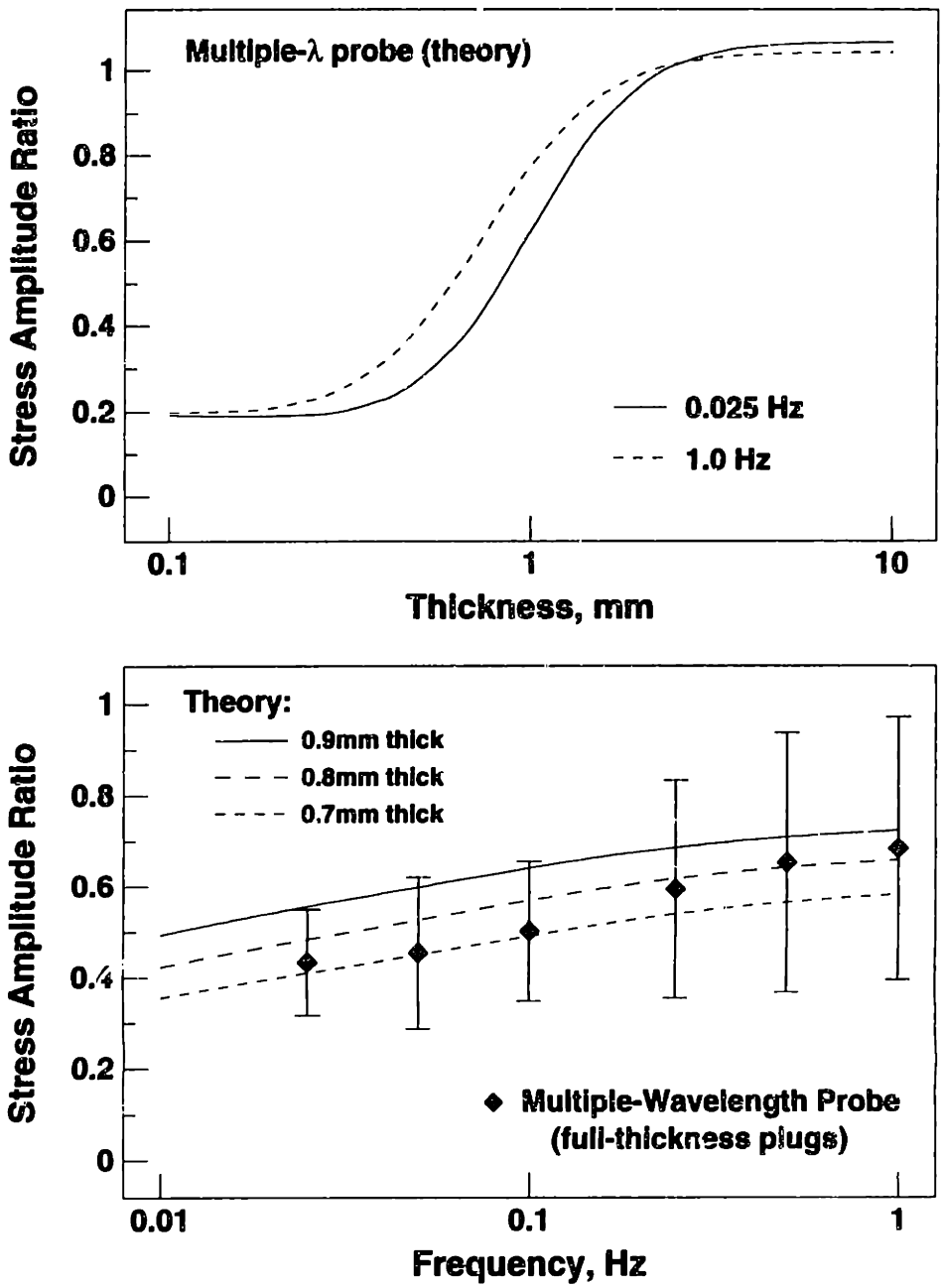

Figure 4.12: Top: Ratio of theoretical short-wavelength to long-wavelength stress amplitude vs. specimen thickness produced by the multiple-wavelength probe, with a current density of 10 A/m^2 at frequencies of 0.025 Hz and 1.0 Hz. Bottom: Stress amplitude ratio vs. frequency, measured in full-thickness calf cartilage-bone plugs using the multiple-wavelength probe, and theoretical stress amplitude ratio computed for a specimen thickness of 0.7, 0.8, and 0.9 mm.

excitation with wavelength λ, i.e., a current density at the surface which is proportional to $\sin\left(\frac{2\pi y}{\lambda}\right)$, the current density would decay exponentially with depth, z, into the tissue in proportion to $e^{-2\pi z/\lambda}$. If $z = \lambda/3$ is defined as the penetration depth, then this is the depth at which the current density has decayed to approximately 12% of its amplitude at the surface (and 88% of the total current is contained superficial to this depth). With an infinite array of evenly spaced electrodes (of alternating polarity), the current density at the surface can be expressed as a superposition (Fourier series) of modal excitations, each with an associated spatial wavelength and corresponding penetration depth. The furthest depth to which current will penetrate depends on the longest (fundamental) wavelength, which is equal to the dominant spatial period, or twice the center-to-center electrode spacing. Thus, in theory, the penetration depth should depend only on the electrode spacing.

The simulation results suggest that the dependence of the penetration depth on geometric parameters of the electrode array may be more complicated. For example, with a two-electrode array, although the electrical potential is constrained to be constant over each electrode, both the normal current density (Figure 4.2) and the resulting normal stress (Figure 4.6, top) are nonuniform with respect to position, with a large peak at the inner edge of each electrode. Thus, at least with a two-electrode array, the behavior would appear to depend on the *gap* between the electrodes rather than the center-to-center spacing. The penetration depth can be estimated from the dependence of the theoretical stress on specimen thickness. Plotting the simulated normal stress as a function of cartilage thickness (Figures 4.10, 4.11) indicates that for thin specimens, the simulated stress amplitude is inversely proportional to the thickness cubed, while for larger thicknesses, the curves plateau. The transition point between these two regions may be defined as the intersection of the asymptotes to the two portions of the curve. The transition thickness measured in this manner was approximately 1.7 mm for the two-electrode (λ = 5 mm) probe and 0.5 mm for the six-electrode (λ = 1.68 mm) probe. These results are consistent with a penetration depth of approximately $\lambda/3$; as the thickness is further increased, current does not penetrate significantly beyond the penetration depth and thus the additional tissue would

not be expected to affect the response.

With a six-electrode array configured for long-wavelength excitation (Figure 3.1A), however, the asymptotes intersect at a thickness of 0.9 mm (Figure 4.11, solid line), even though the nominal spatial wavelength is 5 mm, the same as that of the two-electrode array. Thus, the effective penetration depth in this case is less than 20% of the spatial wavelength. Comparing Figures 4.1A and 3.1A, it is qualitatively apparent that with the six-electrode long-wavelength array, the current density is concentrated in the narrow region between the inner pair of electrodes, which have a narrower gap than the two-electrode probe, and does not penetrate as deeply as the current imposed by the two-electrode array. Thus, the effective penetration depth may be a function of more parameters than simply the spatial wavelength. For ultimate *in vivo* applications, in which a multiple-wavelength device would likely be used, it may be necessary to more thoroughly characterize the dependence of current penetration on the various geometric parameters in order to optimize the electrode size and spacing.

4.5.2 Normal and Shear Components of Surface Stress

The current-generated stress at the tissue surface predicted by the poroelastic model has both normal and shear components. The predicted normal stress is nonuniform with respect to position on the surface, with the peak stress occurring at the edges of the electrodes (Figure 4.6). The surface probe contains piezoelectric PVDF sensor electrodes, which develop an output voltage proportional to the *average* stress over the metallized area (see Section A.1). Thus, it is important that the sensor electrodes are positioned directly over the excitation electrodes so that the large peak in the normal surface stress actually compresses a metallized area of the piezoelectric film; a slight shift in the alignment could result in a marked decrease in the average stress detected by the sensor. Care was taken during the photofabrication process to ensure that the excitation and sensor electrode patterns were visually aligned. However, in future versions of the probe, it may be desirable to incorporate sensor electrodes that are slightly wider than the excitation electrodes, rather than having

the same dimensions as in the present version.

The theory predicts that the shear component of the surface stress is considerably larger than the normal stress over the range of frequencies used in probe experiments. However, the inverse dependence of the measured stress on frequency, along with the phase angle of approximately 90° typically seen in probe measurements, is consistent with the hypothesis that only the normal stress component is actually detected by the sensor. There are several reasons why the probe would not be expected to measure surface shear stress. First, the PVDF film used as the stress sensing element in the probe does not (at least to first order) develop a voltage across the film in response to an applied shear stress, as such stresses produce only minimal rotation of dipoles away from the transverse axis of the film [32]. Second, because the probe's sensor output is recorded differentially, any shear component that is transduced would be expected to be canceled, as the shear stress (unlike the normal stress) has the same phase along the positive and negative electrodes (Figure 4.7). An experiment in which the separate output channels ("+" and "−") of the two-electrode probe were recorded (Figure C.1) confirmed that the responses of the two sensor channels are 180° out of phase with respect to each other; however, the convergence of the phase angles at 1.0 Hz may represent transduction of a fraction of the shear stress component as well. Since the measured stress amplitudes (0.014–0.033 kPa) are only 0.07–0.16% of the predicted shear stress (Figure 4.8, top), the fraction of the shear component, if any, present in the sensor output is small. Thus, although a significant shear stress is produced by the surface electrodes, the response measured by the surface probe predominantly represents the normal stress component.

4.5.3 Frequency Response of Normal Stress

Over the range of frequencies used in probe experiments, the current-generated stress measured using the surface probe exhibited the same inverse dependence on frequency as predicted by the model (because at higher frequencies, the fluid and solid motions in the matrix which produce the current-generated stress have less time to fully develop during

each cycle). At lower frequencies however. the system is quasistatic, with fluid flow occurring slowly enough that the response is dominated by the purely elastic behavior of the solid matrix (Figure 4.8). The transition between these regimes is determined by the ratio of the spatial wavelength to the frequency-dependent mechanical diffusion depth, Δ; for a single spatial mode, the low-frequency limit is reached when

$$k\Delta = \frac{2\pi}{\lambda}\sqrt{\frac{H_A k_{11}\phi_0}{\omega}} \gg 1; \tag{4.2}$$

i.e., for frequencies such that

$$f \gg \frac{2\pi H_A k_{11}\phi_0}{\lambda^2}. \tag{4.3}$$

Using the parameter values of Table 4.1, this transition frequency is approximately 10^{-4} Hz for the two-electrode (λ = 5 mm) probe and 10^{-3} Hz for the six-electrode probe, which agrees well with the behavior seen in Figure 4.8. Since the low-frequency stress is proportional to the equilibrium modulus, H_A, while the transition frequency is proportional to the product of the modulus and permeability, $H_A k_{11}$, both of these parameters can, in principle, be determined from stress measurements using parameter estimation techniques (as has been done in uniaxial compression experiments [65]). This could be accomplished by making measurements at or near the transition frequency, which would require using frequencies too low to be practical for *in vivo* applications; at 10^{-4} Hz, for example, a single cycle would require nearly three hours. Using shorter wavelengths would shift the transition to a higher frequency, but with a corresponding decrease in the depth to which material properties would be sensed. Alternatively, the $H_A k_{11}$ product could be estimated from purely mechanical measurements (e.g., measuring stress relaxation in response to an applied step load). Then, using these estimates, the electrokinetic coefficient, k_e, could be determined from the higher-frequency region of the current-generated stress frequency response.

4.5.4 Dependence of Normal Stress on Thickness

Although the probe measurements exhibited the same frequency dependence as the model, the agreement between theory and data with respect to cartilage thickness was less satisfactory. For each wavelength, the normal stress predicted by the model was inversely proportional to the third power of the thickness (for thicknesses shorter than the penetration depth), reaching values as high as 1 MPa for 0.1 mm thick cartilage at 0.025 Hz. This dependence on thickness cubed is also consistent with an analytical expression for the asymptotic "long-wave limit" (i.e., spatial wavelength much greater than cartilage thickness) derived by Sachs [211] for a purely sinusoidal surface excitation. This strong dependence on thickness arises in part because (1) tissue impedance varies inversely with thickness; thus, for a given applied current density, the electrical potential will be greater in thinner tissue, and (2) in thinner cartilage, a given displacement of the solid matrix will correspond to a proportionally larger strain, and thus a higher resulting stress. In contrast, current-generated stress measured with the probe did not vary significantly as a function of tissue thickness with 0.1–1.8 mm thick cartilage disks.

Boundary Conditions

There are several possible explanations for the lack of a strong dependence of measured stress on cartilage thickness. One major source may be the difference between the idealized boundary conditions assumed in the model and the actual configuration of the cartilage specimens used in experiments. For example, the theory assumes that a periodic array of infinitely long electrodes is applied to the surface of a cartilage slab of infinite extent in the horizontal direction, with a surface between the electrodes that is electrically insulating and impermeable to fluid flow into or out of the tissue (see Appendix E). The actual specimens, however, are cartilage disks or plugs with a cut lateral (radial) border that is permeable and in contact with the bath solution, while the actual electrodes are finite in length and number. Thus, fluid may be freely exchanged between the tissue and bath across the lateral edge and, since the tissue is unconfined, it can potentially undergo radial deformation (bulging). With

a very thin cartilage specimen, particularly for a long spatial wavelength, fluid would be preferentially extruded and imbibed at the edges of the tissue, rather than flowing through the very thin region between the electrodes, with its high hydraulic resistance.

At a free surface in contact with bath solution, the fluid pressure in the tissue must go to zero. In all the simulations described in this chapter, however, a "reflecting" lateral boundary was imposed at distance of 10 mm from the center of the electrode array, with no constraint on the pressure at the "tissue edge" (i.e., 3.5 mm from the center for a 7 mm diameter disk). Using this lateral boundary condition with a two-electrode array (Figure 4.10), the predicted stress amplitude in 0.1 mm thick cartilage is nearly 4000 times higher than the plateau value. This simulation was repeated with a "periodic" lateral boundary imposed at a distance of 3.5 mm from the center, in order to force the pressure to be zero at that point; this boundary condition, however, also changes the current distribution. In this case, the stress amplitude at a thickness of 0.1 mm decreased by nearly half but was still 2000 times the plateau value and more than 500 times higher than the stress in 1 mm thick tissue. In addition, an approximate finite element solution to the problem was developed (by Marc Levenston); preliminary simulations predicted a stress amplitude in thin (0.1 mm) tissue that was 140 times higher than in 1 mm thick cartilage. Thus, allowing the pressure to reach zero at a specified lateral boundary does decrease the predicted stress amplitude, but not by a large enough factor to completely account for the discrepancy between theory and data. However, in all of these simulations, it is assumed that the electrodes are infinitely long; thus, possible fringing effects at the ends of the actual finite-length electrodes are not included in the model.

The theory also assumes that all current applied to the cartilage surface actually penetrates the tissue. However, in the actual disks tested, there may be current flow through the lateral edges of the disk, shunting of current between the regions of the excitation electrodes that are not in contact with the tissue (outside the dashed circles in Figure 4.1), as well as a flow of surface current between the electrodes. The issue of shunting of current is addressed in Chapter V, which describes a series of experiments in which the impedance

of cartilage disks was measured with the probe and compared with the theory.

Other Sources

There are several other possible sources for the discrepancy between the theoretical and measured stress amplitudes. Because the peak normal stress occurs so close to the edge of the sensor electrodes (Figure 4.6), for example, a large enough horizontal displacement component (which would occur in very thin cartilage, especially at low frequencies) could shift this peak far enough laterally that it is no longer detected by the overlying sensor electrode. However, this effect would be expected to reduce the measured differential stress by at most a factor of two, as the other (negative) peak would be shifted further *into* the region sensed by the other sensor electrode and thus would still contribute to the differential piezoelectric sensor output. Another possibility is that the output of the piezoelectric sensor may become nonlinear when the dynamic stress amplitudes approach or exceed the 50 kPa static load and thus not reflect the true stress amplitude. However, the total harmonic distortion was not significantly increased in thinner tissue, indicating that the current-generated stress response was still linear.

Implications

Although the theoretical model does not fully capture the behavior of the probe measurements, the lack of a dependence of measured stress on cartilage thickness is not necessarily a shortcoming of the surface spectroscopy technique and may, in fact, be an advantage. Loss of cartilage thickness, which occurs in later stages of osteoarthritic degeneration [176], can already be measured using currently available imaging techniques such as magnetic resonance imaging (MRI) [42,191,209]. The potential benefit of the surface probe is in detecting biochemical abnormalities (loss of GAG) characteristic of *early* disease, before gross loss of tissue has occurred. It is not yet known whether the insensitivity of measured stress to changes in tissue thickness observed in the excised cartilage disks used in the present studies will persist when testing cartilage on an intact joint surface, which imposes

different geometric boundary conditions. However, if such *in vivo* measurements are also independent of thickness, then the tissue thickness would *not* need to be known in order to interpret the stress measurements.

4.5.5 Nonuniform Material Properties

The poroelastic model assumes that the material properties of the tissue specimen are homogeneous throughout the bulk of the tissue. However, the GAG content of even normal tissue is known to vary with depth [70,143,161,202,228], while enzymatic degradation with trypsin produces a marked variation in GAG content, and thus charge density, with depth into the tissue (Figure 3.5). Thus, in order to accurately simulate the response of nonuniformly degraded tissue to an imposed current, it will be necessary to extend the model to include nonuniform material parameters. A *layered* model, in which an inhomogeneous medium is approximated as a series of thin layers, each with associated (homogeneous) parameter values, has been developed for electrokinetic transduction in cartilage in a uniaxial geometry [63], based on the "transfer relation" approach of Melcher [171]. Implementing such an approach for the more complicated two-dimensional fields produced by surface excitation would be computationally more difficult, but ultimately could provide insight into the expected current-generated stress response of partially degraded tissue. Alternatively, a finite elements approach could be used to numerically solve the problem, rather than deriving a complicated analytical solution.

Chapter V

Electrical Impedance of Articular Cartilage Measured Using the Surface Probe

5.1 Summary

[1]The electrical impedance of calf cartilage plugs and disks (0.1–1.0 mm thick) was measured using two- and six-electrode fixed-wavelength surface probes as well as the multiple-wavelength probe configured for three different wavelengths. A 1 kHz sinusoidal current was applied across the excitation electrodes, and the impedance was calculated as the ratio of the voltage drop to the load current. The measured impedance was modeled by an equivalent circuit containing a series term, due to the electrode-electrolyte interface, and a parallel term, representing shunting of current. The impedance of full-thickness cartilage plugs did not change significantly after removal of the articular surface. For each wavelength, shunt and series impedances were estimated from measurements made with an insulating rubber disk or only bath solution in the chamber, respectively. Using these values in the equivalent-circuit model, the equivalent impedance predicted by the model agreed well with the measurements. Comparison of the shunt impedances with the theoretical cartilage impedance suggested that with the fixed-wavelength probes tested in the *in vitro* configuration described in Chapter III, up to 75% of the applied current may be shunted and thus does not contribute to producing a current-generated stress.

5.2 Introduction

The principle of using electromechanical surface spectroscopy to measure current-generated stress in articular cartilage is based on a theoretical model for surface excitation of an electromechanically coupled poroelastic medium [210,211]. An array of silver/silver chlo-

[1]Supplemental data pertaining to the results described in this chapter are presented in Appendix G.

ride electrodes imposes a standing wave of current density at the tissue surface, which produces a mechanical stress within the tissue that is measured by an overlying piezoelectric stress sensor at the surface. One of the assumptions inherent in this model is that all current flow occurs within the bulk of the tissue; i.e., there is no shunting or surface current. Because the mechanical stress is directly proportional to the imposed current density, any decrease in the amount of current which penetrates the tissue would result in a proportionate decrease in the developed stress. As discussed in Chapter IV, it was hypothesized that the existence of a shunt pathway or pathways in the actual surface probe system may account, at least in part, for the discrepancy between the theoretical stress amplitude and the measured current-generated stress in thin (< 1 mm) cartilage specimens as tested in the *in vitro* configuration of Figure 2.3A. Because both the current delivered to the excitation electrodes and the voltage drop between the electrodes can be monitored, it is possible to determine the electrical impedance of the cartilage specimen as the ratio of load voltage to current. Thus, a series of experiments was performed in which cartilage impedance was measured with the surface probe and compared to the theoretical impedance predicted by the model, in order to estimate how much of the current actually penetrates the tissue.

Conceptually, the impedance, Z_{eq}, measured across the excitation electrodes of the probe may be represented by an equivalent-circuit model (Figure 5.1). The impedance of all shunt paths can be lumped into a single equivalent shunt impedance, Z_{sh}, in parallel with the impedance of the cartilage specimen, Z_c. In addition, although the measurements described in this chapter were made at 1 kHz (in order to minimize capacitive effects), a significant series impedance, Z_{ser}, may be be present at the electrode-electrolyte interface. For example, Geddes [79] has reported a measured electrode impedance of 200–225 Ω in silver/silver chloride electrodes having an area (0.03–0.25 cm^2) and chloride deposit (1000 mA-sec/cm^2) comparable to the surface probe electrodes, when tested in 0.15 *M* saline at 10 kHz. This series component of the equivalent impedance is assumed to be evenly distributed between the positive and negative electrodes (Figure 5.1). Because a current source was used to supply current to the excitation electrodes, this series impedance

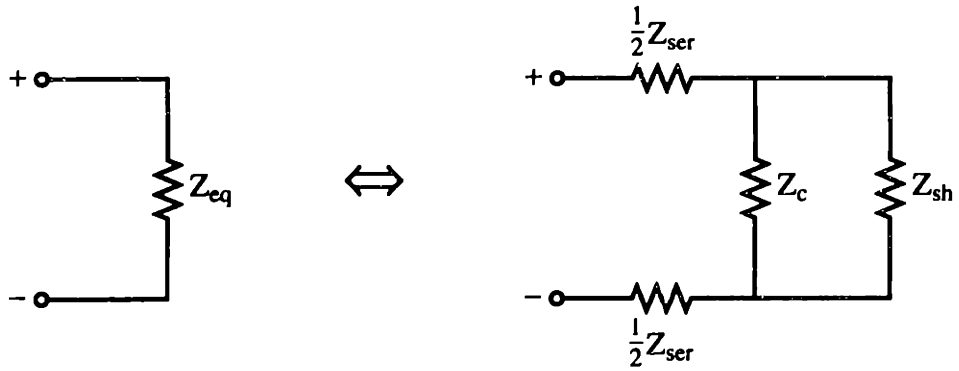

Figure 5.1: Equivalent-circuit model for equivalent impedance, Z_{eq}, measured with the surface probe. An equivalent shunt impedance, Z_{sh} is modeled in parallel with the cartilage impedance impedance, Z_c; in addition, a series component, Z_{ser}, is assumed to be present at the electrode-electrolyte interface, evenly divided between the positive and negative electrodes.

would not affect the total amount of current penetrating the tissue; however, it must be taken into consideration when interpreting any measurements of impedance using the probe (and could theoretically alter the spatial distribution of current density at the electrode surface).

5.3 Methods

5.3.1 Measurement of Electrical Impedance

The complex electrical impedance, Z_{eq}, across the probe inputs was determined by applying a sinusoidal current at a frequency of 1 kHz via a bipolar operational amplifier/power supply (Kepco, Flushing, NY), configured as a current source (Figure 5.2) and driven by a frequency synthesizer (Rockland Systems, West Nyack, NY), and measuring the output voltage developed by the current source in order to maintain this current level. Empirically, it was determined that $I_c = V_m/(3.37\,k\Omega)$, where I_c is the load current through the cartilage; the output level of the frequency synthesizer was adjusted to achieve a current amplitude of approximately 100 μA. Because measurements were performed at 1 kHz, all impedances were assumed to be predominantly resistive (real-valued). The measured impedance across the probe inputs, Z_{meas}, was computed as the ratio of the voltage drop across the load to the

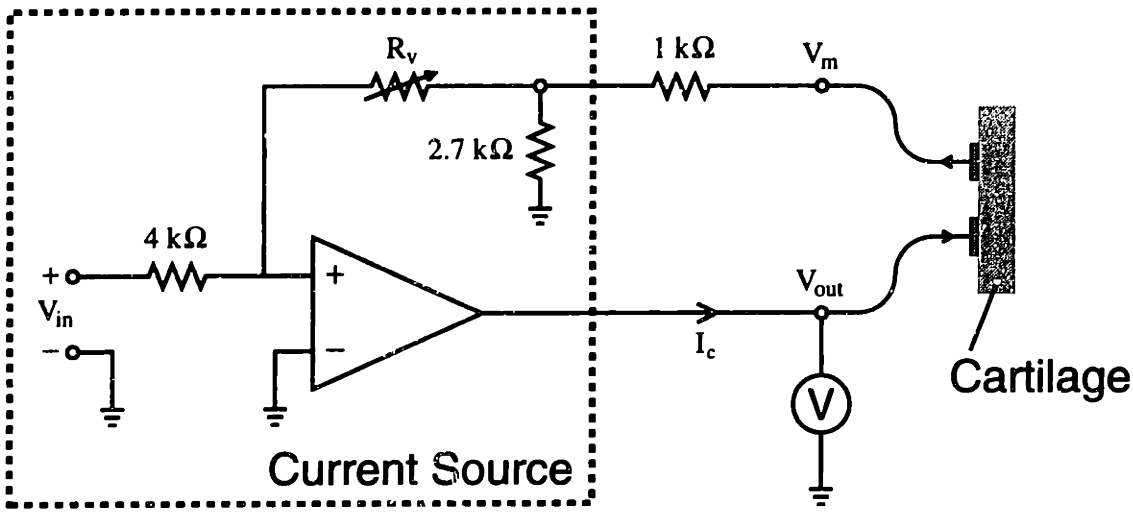

Figure 5.2: Schematic diagram of the current source used for impedance measurements. A sinusoidal input voltage (V_{in}) at a frequency of 1 kHz resulted in a proportional load current, I_c, through the cartilage. Impedance across the probe inputs was computed from V_{out}, measured with a digital multimeter, and the calculated current, I_c.

calculated load current:

$$Z_{meas} = \frac{V_{out} - V_m}{I_c} = \frac{\sqrt{2} \cdot V_{RMS}}{I_c} - 3.37\,k\Omega, \tag{5.1}$$

where V_{RMS} is the root-mean-square value of the sinusoidal output voltage as measured by a Keithley digital multimeter operating in AC voltmeter mode. The measurement system was validated by measuring the impedance of several resistors (with nominal resistances in the 100 Ω–1 kΩ range) placed across the current source outputs; the values determined in this manner agreed within 1% of the resistance values independently measured with a Fluke digital ohmmeter.

Fixed-Wavelength Probes

A two-electrode and a six-electrode fixed-wavelength probe (Figure 4.1) were each mounted in the PMMA chamber (Figure 2.3A) and tested with four calf cartilage plugs using the fol-

lowing protocol: First, the impedance was measured with only bath solution (0.15 *M* NaCl plus 2 m*M* EDTA, a protease inhibitor) in the PMMA chamber. Next, a frozen cartilage-bone plug (9.5 mm diameter) was thawed in bath solution at room temperature, placed in the chamber, and held in unconfined compression at a static load of 50 kPa using a Dynastat mechanical spectrometer (IMASS, Hingham, MA); after measuring the impedance, the top 40–100 μm of the articular surface was removed using a sledge microtome and the measurement was repeated. Disks of thickness 0.1, 0.2, 0.5, and 1.0 mm were then cut from the plug using the microtome and sequentially tested. The impedance of each 9.5 mm disk was measured with the disk held against a 9.5 mm diameter PMMA platen; the measurement was repeated with a concentric 7 mm disk cored from the full disk using a metal punch. Finally, each 7 mm diameter disk was tested using a 7 mm platen, both with and without an insulating machined polytetrafluoroethylene (PTFE, Teflon) collar (7 mm inner diameter, 9.5 mm outer diameter, 10.7 mm tall) in place around the disk and platen. After each disk had been tested, the procedure was repeated with insulating rubber disks (1 mm thick) of the same diameters in place of cartilage. Each measurement was made in triplicate; the mean of the three readings was taken to be the impedance.

Following these measurements, a piece of cellophane tape was placed over the excitation electrodes of the six-electrode probe, with a 7 mm diameter hole over the active area of the electrodes, in order to minimize current flow between regions of the electrodes not in contact with the cartilage. An additional four plugs were tested, using the above protocol, with this modified six-electrode probe. A two-electrode probe was similarly modified (with a 6 mm diameter hole in the tape) and tested with 7 mm diameter disks and the 7 mm platen only, both with and without the Teflon collar.

Multiple-Wavelength Probe

The same protocol was used with a single multiple-wavelength probe, tested with four calf cartilage plugs; however, for each condition (bath, plug, disks), the impedance was sequentially measured using *three* different electrode configurations (Figure 5.3): "short-

wavelength" (Figure 5.3A) and "long-wavelength" (Figure 5.3B) configurations, as used in the multiple-wavelength experiments presented in Chapter III, as well as a "very long-wavelength" configuration (Figure 5.3C) in which the outer two pairs of electrodes were connected (with opposite polarity) while the two middle electrodes were unconnected and thus electrically "floating." The dominant spatial wavelength with the very long-wavelength configuration was 6.7 mm, as opposed to 5 mm and 1.7 mm with the long- and short-wavelength configurations, respectively.

5.3.2 Simulation of Electrical Impedance

The theoretical impedance was computed using the poroelastic model [210,211], extended (by Eliot Frank) to solve the mixed boundary-value problem imposed by finite-width surface electrodes[2]. For all simulations, the material parameters in Table 4.1 and electrode dimensions in Table 4.2 were used, with an excitation frequency of 1 kHz, current density of $J_0 = 1\ \mathrm{A/m^2}$, and cartilage thicknesses in the range 0.1–10 mm. For each electrode configuration, the potential at the positive electrode, Φ, was simulated using the model; the cartilage impedance, Z_c, was then calculated as the ratio of the voltage drop, ΔV, between the positive and negative electrodes to the total current, I:

$$Z_c = \frac{\Delta V}{I} = \frac{2\Phi}{J_0 A}, \tag{5.2}$$

where A is the positive electrode area ($A = 6.0\ \mathrm{mm^2}$ for the two-electrode probe, $4.05\ \mathrm{mm^2}$ for the six-electrode fixed-wavelength probe and the long- and short-wavelength configurations of the multiple-wavelength probe, and $2.7\ \mathrm{mm^2}$ for the very long-wavelength configuration).

[2]Details of the mathematical model can be found in Appendix E.

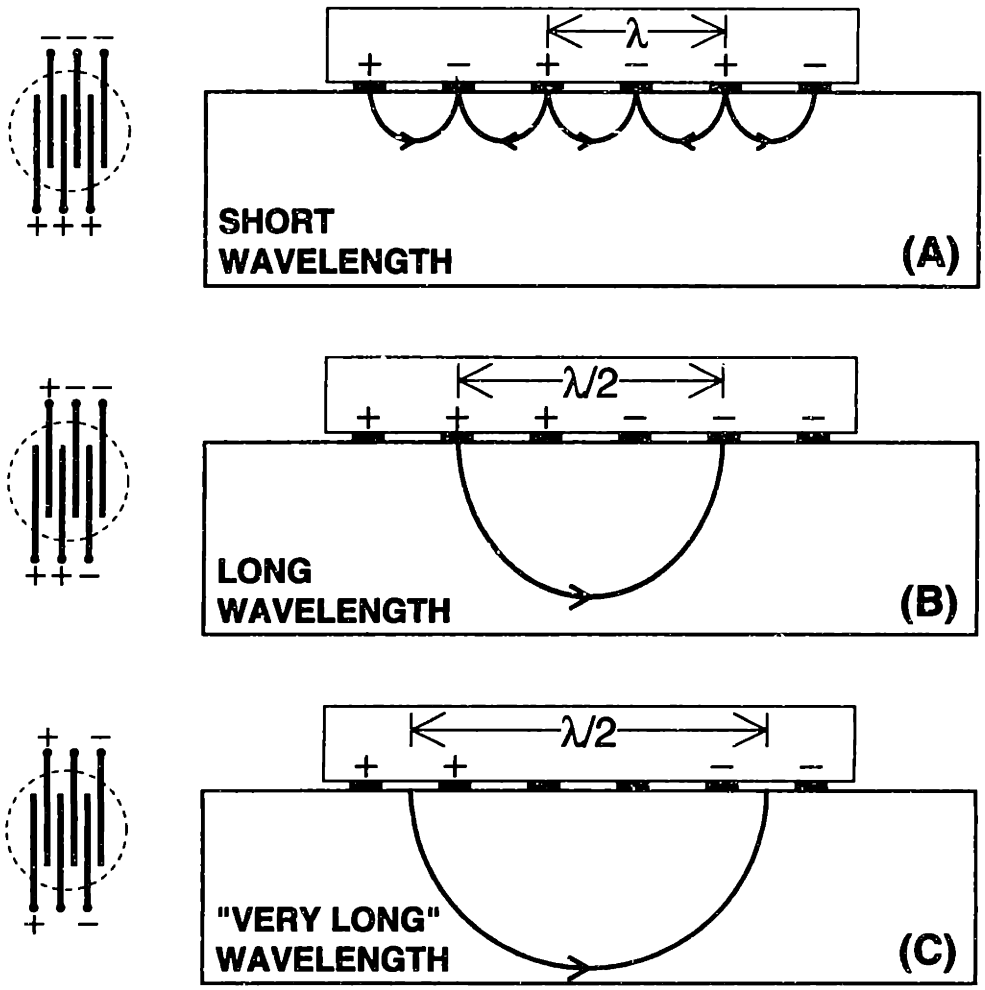

Figure 5.3: Electrode configurations of the multiple-wavelength probe used for impedance measurements and simulations: (**A**) short-wavelength (λ = 1.7 mm), (**B**) long-wavelength (λ = 5 mm), and (**C**) "very long"-wavelength (λ = 6.7 mm) excitation, determined by varying the polarity of each electrode. The arrows schematically indicate relative penetration of current into the tissue. Dashed circles at left indicate area of electrodes in contact with 7 mm diameter cartilage disk.

5.3.3 Estimation of Series and Shunt Impedances

Based on the equivalent-circuit model (Figure 5.1), the measured impedance, Z_{eq}, was assumed to depend on the actual cartilage impedance, Z_c, as well as series and shunt terms:

$$Z_{eq} = Z_{ser} + \left\{ \frac{1}{Z_c} + \frac{1}{Z_{sh}} \right\}^{-1}, \tag{5.3}$$

where Z_{ser} and Z_{sh} are the series and shunt components, respectively, which were estimated as described below.

Series Impedance

For each plug, the series component, Z_{ser}, of the equivalent impedance (Figure 5.1) was taken to be the difference between the measured and theoretical impedance values with only bath solution in the chamber. For each wavelength, the theoretical bath impedance was determined by computing the theoretical electrical potential using the poroelastic model as described above. For these simulations, an electrokinetic coefficient of $k_e = 0$ was used (since no electromechanical coupling would occur in free solution). The electrical conductivity, k_{22}, of the bath solution used in the simulations was estimated using the relation for a mono-monovalent binary electrolyte:

$$k_{22} = \Lambda_{eq} c_b, \tag{5.4}$$

where Λ_{eq} is the *equivalent conductance* of a binary electrolyte and c_b is the bath concentration. With $c_b = 0.15\ M$ and $\Lambda_{eq} = 106.69 \times 10^{-4}$ m^2·S/mol (the equivalent conductance reported for 0.1 M aqueous NaCl [247]), Equation 5.4 yields a conductivity of $k_{22} = 1.6$ S/m. Bath impedances were computed in this way for each electrode configuration (Table 5.1). For each wavelength, the mean and standard deviation of the series impedance for the four plugs tested were determined.

Electrode Configuration		Bath Impedance, Ω
Fixed-wavelength	2-electrode	200.10
	6-electrode	66.00
Multiple-wavelength	Short-λ	66.00
	Long-λ	141.55
	Very long-λ	358.99

Table 5.1: Theoretical bath impedances (of 0.15 *M* NaCl) measured using fixed-wavelength and multiple-wavelength probes, calculated using poroelastic model with an estimated conductivity of 1.6 S/m and no electromechanical coupling.

Shunt Impedance

The shunt component, Z_{sh}, of the equivalent impedance (Figure 5.1) was estimated, for each electrode configuration and each combination of disk and platen diameters, as

$$Z_{sh} = Z_{rubber} - Z_{ser}, \tag{5.5}$$

where Z_{rubber} is the impedance measured with the rubber disk (of corresponding diameter) in the chamber and Z_{ser} is the series impedance, determined from the bath impedance as described above. Because the rubber disks were electrically insulating, it was assumed that all current flow with a rubber disk in the chamber would occur only via the shunt paths (i.e., surface conduction and flow between electrode regions not covered by the disk). For each wavelength, the mean and standard deviation of the shunt impedance for the four plugs tested were determined.

According to the equivalent-circuit model (Figure 5.1), the current delivered by the current source is divided between the cartilage specimen and the shunt paths. Thus, the fraction of the current which penetrates the tissue can be calculated using the current divider relation,

$$\% \text{ penetrating} = 100 \times \frac{Z_{sh}}{Z_{sh} + Z_c}, \tag{5.6}$$

where Z_{sh} is the equivalent shunt impedance, calculated as described above, and Z_c is the

theoretical cartilage impedance.

Shunt Through Lateral Edges of Disk

In using the impedance measured with a rubber disk in the chamber to estimate the equivalent shunt impedance, it was assumed that shunting of current occurred predominantly via two pathways: (1) flow between areas of the excitation electrodes not covered by the cartilage specimen ("non-active" areas), and (2) surface current flow (through the thin fluid film coating the surface of the disk). However, another possible source of current shunting is flow through the lateral edges of the cartilage disk, as the disks were held in *unconfined* compression except when tested with the Teflon collar in place. In order to assess the possible contribution of this pathway to the total shunt, the impedance measured in 7 mm diameter cartilage disks using the two- and six-electrode probes with tape over the non-active region of the electrodes was compared with and without the presence of the Teflon collar around the disk. The probes with tape were used in order to minimize the effect of shunting between regions of the electrode not in contact with the cartilage (which would also be decreased by the presence of the Teflon collar) and thus isolate the effect of flow through the lateral edges.

The decrease in impedance when the collar was removed was assumed to be due to an additional shunt path (through the disk edges) in parallel with the other contributions. Thus, the equivalent impedance, Z_+, with the collar in place can be written

$$Z_+ = Z_{ser} + \left\{ \frac{1}{Z_c} + \frac{1}{Z'_{sh}} \right\}^{-1}, \tag{5.7}$$

and the equivalent impedance, Z_-, without the collar is given by

$$Z_- = Z_{ser} + \left\{ \frac{1}{Z_c} + \frac{1}{Z'_{sh}} + \frac{1}{Z_{edge}} \right\}^{-1}, \tag{5.8}$$

where Z_{edge} is the equivalent impedance due to shunting through the edges of the disk and Z'_{sh} is the equivalent impedance due to all *other* shunt sources. Solving these two equations

for Z_{edge} yields the expression

$$Z_{edge} = \left\{ \frac{1}{Z_- - Z_{ser}} - \frac{1}{Z_+ - Z_{ser}} \right\}^{-1}. \tag{5.9}$$

5.3.4 Statistical Analysis

Statistical comparisons were performed using multivariate analysis of variance (ANOVA). All computations were performed using the SAS data analysis software package. Results were considered significant at the $p < 0.05$ level.

5.4 Results

5.4.1 Measured Impedance of Cartilage Plugs

The impedance of full-thickness cartilage plugs with the articular surface intact, as measured using the surface probe (Figure 5.4, solid bars), varied with the electrode configuration used, ranging from $261.6 \pm 14.9\,\Omega$ with the six-electrode fixed-wavelength probe to $449.0 \pm 79.3\,\Omega$ with the very long-wavelength configuration of the multiple-wavelength probe. Removing the articular surface resulted in a slight decrease in the mean impedance at each wavelength (Figure 5.4, open bars); however, these differences were not statistically significant (as determined by ANOVA).

5.4.2 Theoretical Impedance of Articular Cartilage

For each electrode configuration, the theoretical impedance of a cartilage specimen (at a frequency of 1 kHz) was inversely proportional to the cartilage thickness for small thicknesses but reached a plateau value for larger thicknesses (Figure 5.5). With the fixed-wavelength electrode configurations, the predicted plateau value for the two-electrode probe ($288\,\Omega$) was approximately three times the plateau value for the six-electrode probe ($95\,\Omega$); however, with a thickness of 0.1 mm, the theoretical impedance measured with the two-electrode probe was 13 times greater than the impedance with the six-electrode probe (Figure 5.5, top).

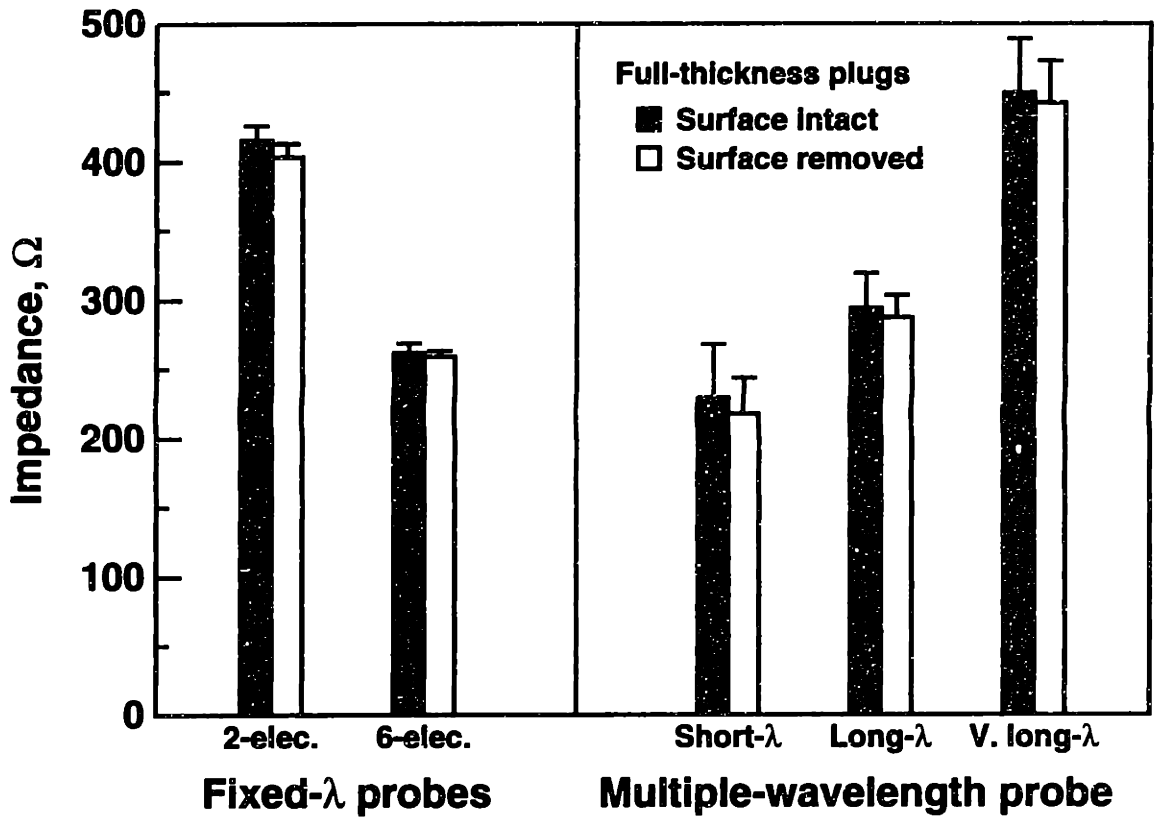

Figure 5.4: Electrical impedance of full-thickness cartilage-bone plugs, with intact articular surface (solid bars) and after removal of most superficial 40–100 μm using a microtome (open bars), as measured using the two- and six-electrode fixed-wavelength probes as well as the multiple-wavelength probe configured for short-, long-, and very long-wavelength excitation. Each bar is mean + SEM for $N = 4$ plugs.

With the multiple-wavelength probe, the plateau impedance with the very long-wavelength configuration (517 Ω) was approximately 2.5 times the impedance with the long-wavelength configuration (204 Ω) and more than five times greater than the short-wavelength configuration (95 Ω); these differences increased at smaller values of the cartilage thickness (Figure 5.5, bottom).

5.4.3 Comparison of Measured Impedance with Equivalent-Circuit Model

For each electrode configuration, the estimated series and shunt impedances were combined with the theoretical cartilage impedance values according to the equivalent-circuit model (Figure 5.1). Using Equation 5.3, the equivalent impedance was calculated and compared with the impedance measured by the probe (Figures 5.6, 5.7). For each wavelength, the equivalent impedance was calculated using the mean value of the series and shunt components, the mean plus one standard deviation of both components, and the mean minus one standard deviation. For comparison with the probe measurements described in Chapter IV, the results shown are for 7 mm diameter disks with the 9.5 mm platen. There was good agreement between the predicted and measured impedance, particularly with the six-electrode fixed-wavelength probe (Figure 5.6, bottom); in this case, the measured impedance at each thickness was within 2% of the predicted value (using the mean series and shunt values). The largest discrepancy between theory and measurement occurred with the two-electrode probe tested with 0.1 mm thick cartilage (Figure 5.6, top); in this case, the measured value was 25% lower than the predicted equivalent impedance.

For each electrode configuration, the fraction of current penetrating into the tissue was calculated according to Equation 5.6, using the mean estimated shunt impedance for 7 mm diameter disks tested with the 9.5 mm platen (Figure 5.8). With both fixed-wavelength probes (Figure 5.8, top), 84–85% of the current penetrated the tissue for cartilage thicknesses greater than approximately 3 mm; with 0.1 mm thick tissue, however, the estimated penetration fractions were 65% for the six-electrode probe and only 31% for the two-electrode probe. With the multiple-wavelength probe (Figure 5.8, bottom), the penetration fraction

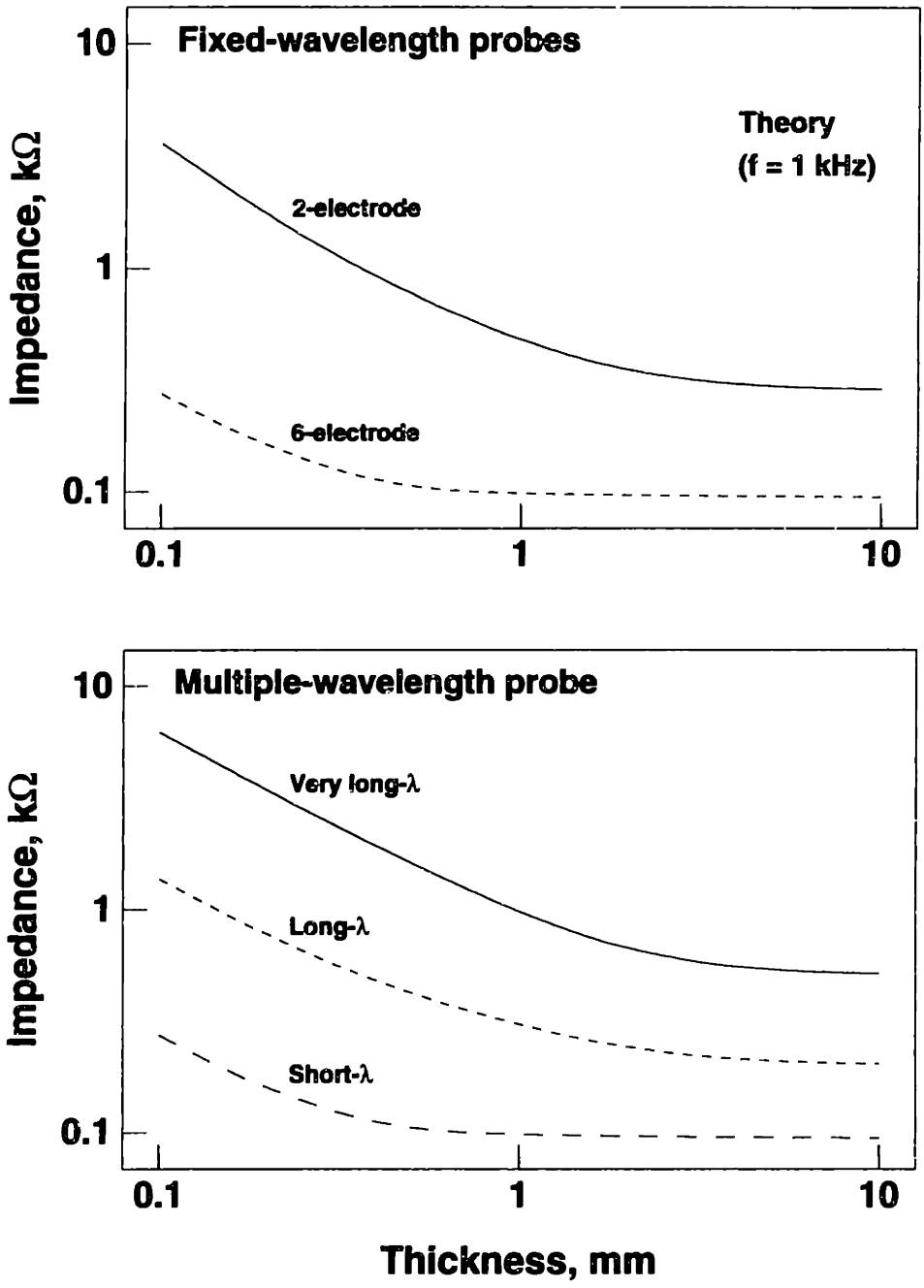

Figure 5.5: Theoretical impedance of calf articular cartilage at 1 kHz, measured with electrode configurations corresponding to the fixed-wavelength (top) and multiple-wavelength (bottom) probes. Impedance was calculated, using Equation 5.2, from the electrical potential computed using the poroelastic model.

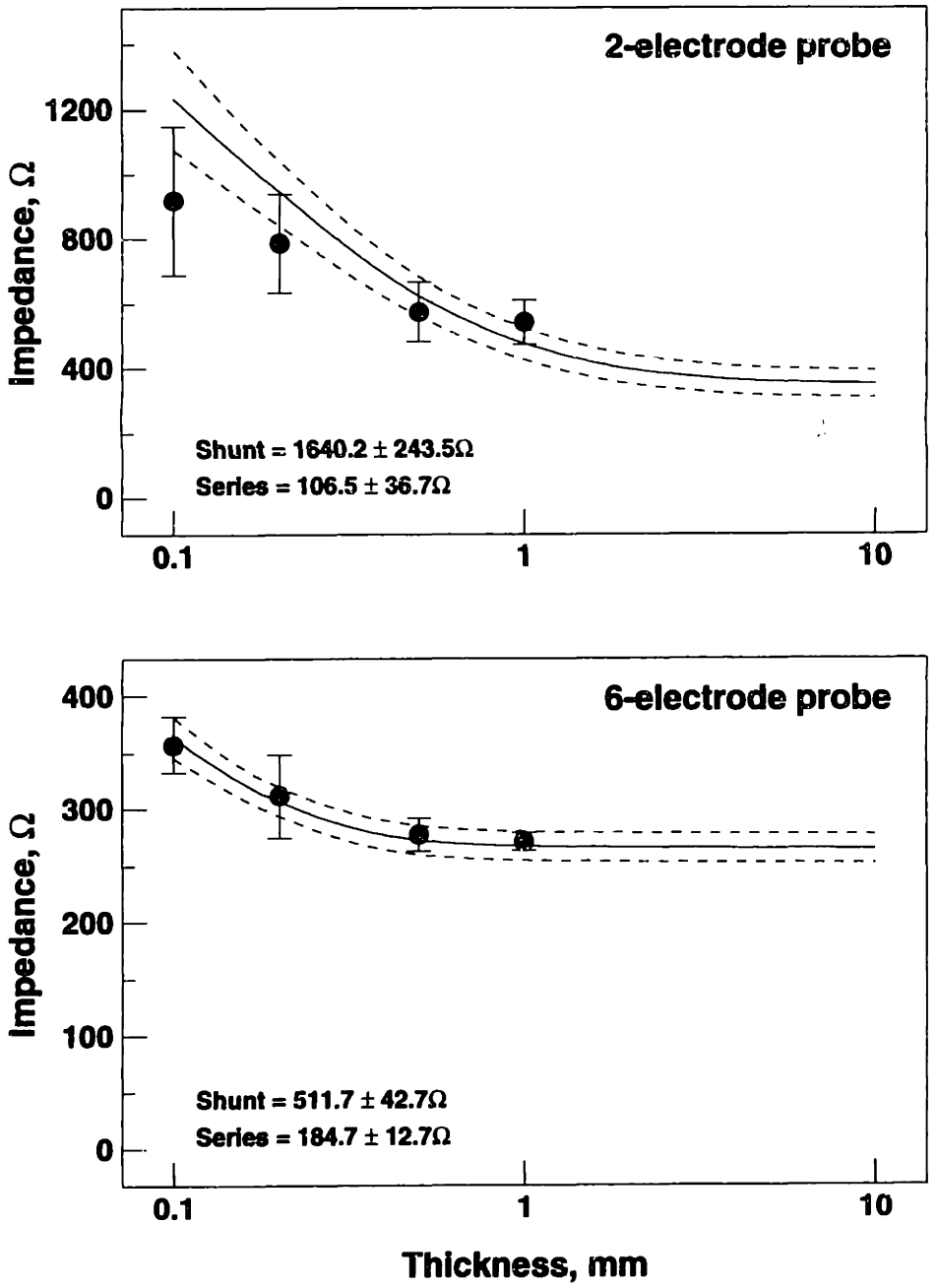

Figure 5.6: Impedance of calf cartilage disks (0.1–1.0 mm thick) measured using two-electrode (top) and six-electrode (bottom) fixed-wavelength probes, and impedance predicted by equivalent-circuit model. Data (circles) are for 7 mm diameter disks tested with 9.5 mm platen (N = 4, mean ± SD). Equivalent impedance was calculated from equivalent-circuit model (Equation 5.3), using estimated series and shunt impedances. Solid lines indicate equivalent impedance using mean series and shunt values; dashed lines indicate equivalent impedance computed using mean ± 1 SD for both series and shunt impedances.

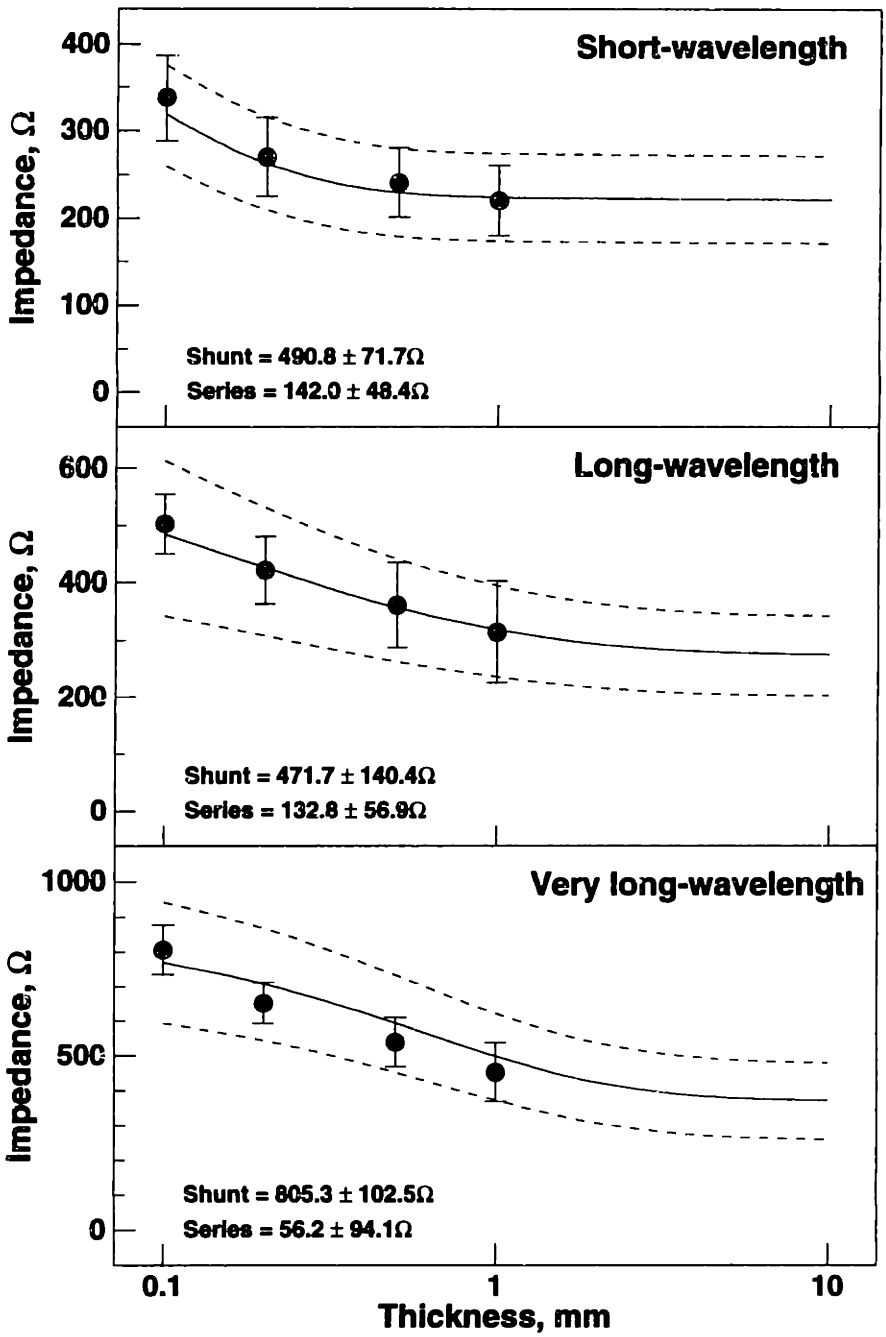

Figure 5.7: Impedance of calf cartilage disks (0.1–1.0 mm thick) measured using multiple-wavelength probe with short- (top), long- (middle), and very long-wavelength (bottom) configurations, and impedance predicted by equivalent-circuit model. Data (circles) are for 7 mm diameter disks tested with 9.5 mm platen (N = 4, mean ± SD). Equivalent impedance was calculated from equivalent-circuit model (Equation 5.3), using estimated series and shunt impedances. Solid lines indicate equivalent impedance using mean series and shunt values; dashed lines indicate equivalent impedance computed using mean ± 1 SD for both series and shunt impedances.

at each thickness for the short-wavelength configuration was similar to that of the six-electrode fixed-wavelength probe, while the penetration achieved with the long-wavelength probe was slightly lower than the two-electrode probe, ranging from 25–70%. The fraction of current penetrating was lowest with the very long-wavelength configuration; when tested with 0.1 mm thick cartilage, less than 12% of the current actually penetrated the tissue.

5.4.4 Contribution of Current Flow Through Lateral Edges of Disk

Using Equation 5.9, the impedance due to current flow through the lateral edges of the tissue, Z_{edge}, was calculated for the two- and six-electrode probes with tape over the non-active area of the electrodes; the mean value was 3.63 kΩ for the two-electrode probe and 919 Ω for the six-electrode probe[3]. Incorporating this additional shunt impedance into the equivalent-circuit model (Figure 5.1) for the two-electrode probe resulted in a 31% decrease in the equivalent shunt impedance and a better agreement between the predicted equivalent impedance and the probe measurements (Figure 5.9, top). In addition, there was a 4–22% decrease in the overall equivalent impedance and the percentage of current penetrating the tissue decreased (Figure 5.9, bottom), ranging from 24% in 0.1 mm thick tissue to 80% for larger thicknesses. With the six-electrode probe, the additional shunt decreased the equivalent shunt impedance by 36% and the overall equivalent impedance by 2–8% (Figure 5.9, top); the percentage of current penetrating the tissue ranged from 54–78% (Figure 5.9, bottom).

5.5 Discussion

The electrical impedance of articular cartilage, determined as the ratio of the voltage drop between the positive and negative excitation electrodes to the total current through the load, was measured using surface probes with various electrode configurations. The piezoelectric

[3]The higher impedance with the two-electrode probe is likely due to the smaller overall dimensions of the electrode array (4 × 4 mm, as opposed to 4.5 × 4.5 mm with the six-electrode array); the electrode edges are thus further from the edge of the disk.

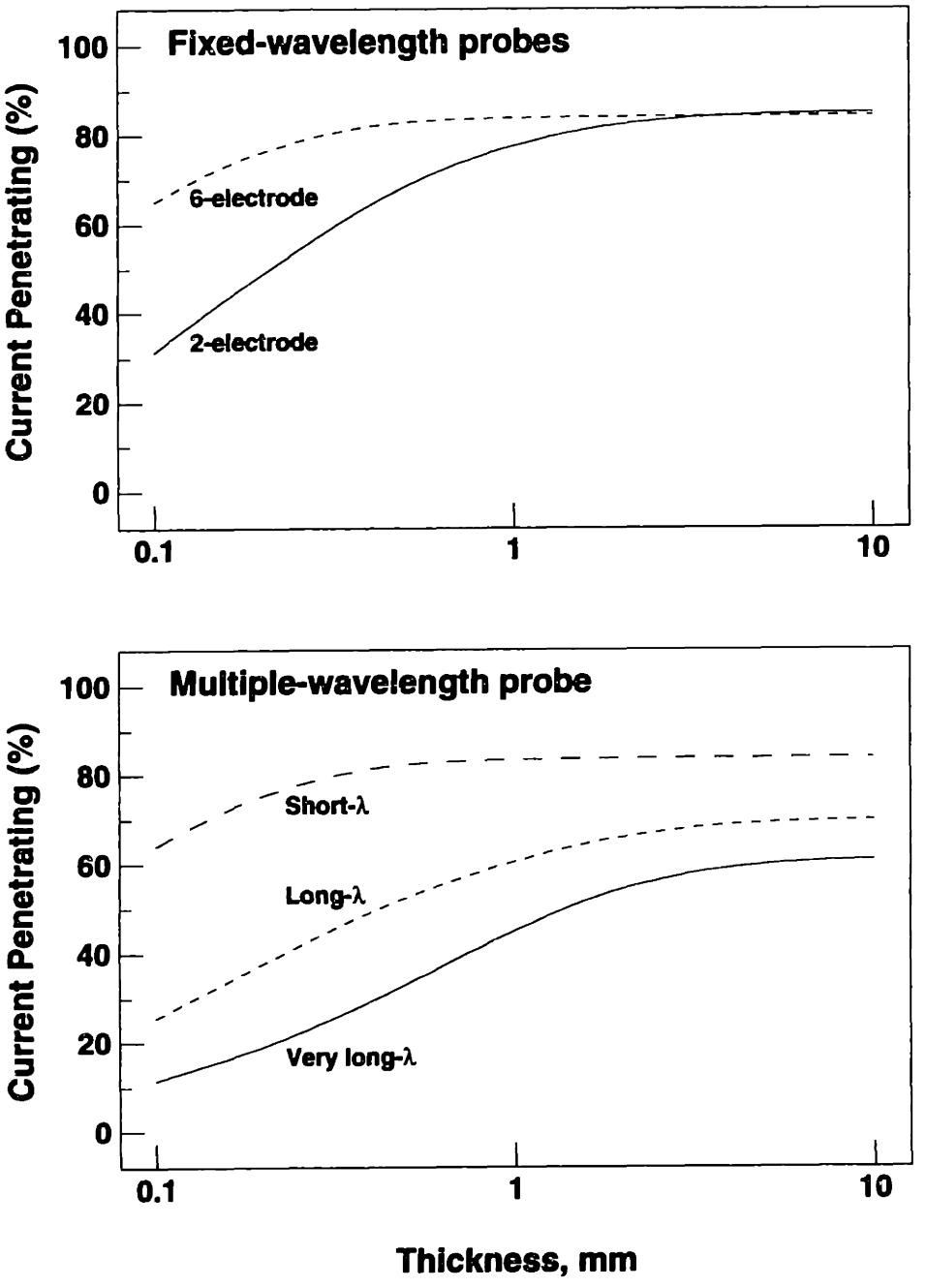

Figure 5.8: Percentage of current penetrating cartilage specimen, for fixed-wavelength (top) and multiple-wavelength (bottom) probes, calculated from current divider relation (Equation 5.6) using mean estimated shunt impedance (for 7 mm disks with the 9.5 mm platen) for each electrode configuration.

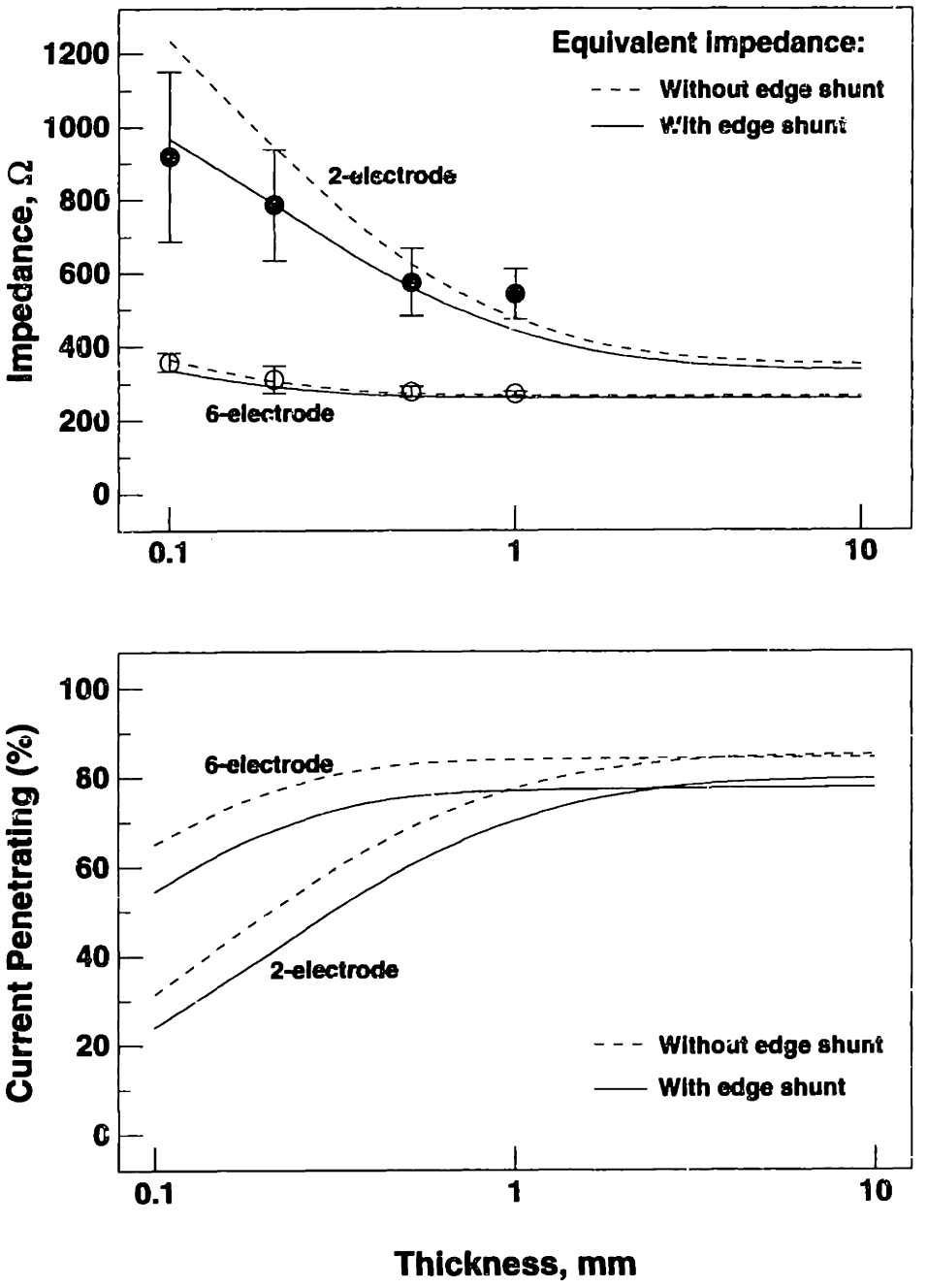

Figure 5.9: Equivalent impedance (top) and percentage of current penetrating cartilage specimen (bottom), computed for two- and six-electrode fixed-wavelength probes tested with 7 mm diameter disks, both with (solid lines) and without (dashed lines) shunting through lateral edges of the disk. For comparison, measured impedance (circles, mean ± SD for N = 4 plugs) is also plotted.

stress sensor of the probe was not used in these measurements. Measurements were made at a frequency of 1 kHz in full-thickness cartilage plugs as well as disks (0.1–1.0 mm thick). The overall impedance across the probe electrodes was modeled by an equivalent-circuit representation (Figure 5.1); by comparison of the measured impedance with the theoretical impedance predicted by the poroelastic model, both series and shunt components predicted by the model could be estimated.

5.5.1 Simulation of Cartilage and Bath Impedance

Although the poroelastic model [210,211] was used to compute the electrode potential, and hence the electrical impedance, of cartilage, it is expected that at frequencies as high as 1 kHz, the electrokinetic effects would be negligible. Thus, the impedance would be determined entirely by the spatial distribution of current, which is governed by Laplace's equation (Equation E.12), and the electrical conductivity, k_{22}, of the tissue. For computing the bath impedance, the poroelastic model was also used, with the electrokinetic coefficient, k_e, explicitly set to zero. Thus, the difference between the theoretical impedance of cartilage and normal saline for a given electrode configuration depends only on the difference in k_{22}, which results from the difference in ionic mobilities of sodium and chloride between free solution and tissue as well as perturbation of intra-tissue ion concentrations due to Donnan partitioning in the presence of matrix fixed charge groups (Equation D.5).

5.5.2 Effect of Articular Surface

Measurement of impedance in full-thickness plugs before and after removal of the articular surface revealed *no* statistically significant change in impedance, indicating that the presence or absence of the articular surface does not influence the series or shunt components of the equivalent-circuit model. Thus, there was apparently good electrical contact between the excitation electrodes and the tissue surface, despite the fact that the surface of the intact plugs was often not perfectly flat. The 50 kPa static stress imposed by the Dynastat may have been sufficient to flatten out any slight curvature of the tissue. These observations are

consistent with a preliminary study in which current-generated stress was measured in full-thickness plugs both before and after removal of the articular surface, with no significant difference in amplitude or phase (Figure D.12). However, for making current-generated stress measurements on intact joints (the ultimate goal of this work), it is not clear how much of an influence the curvature of the intact articular surface would have, or whether a 50 kPa static load would be sufficient to ensure good electrical contact with the tissue surface in this case. As newer versions of the device for use in intact joints are developed, this issue will need to be further studied.

5.5.3 Theoretical Impedance of Cartilage

For each electrode configuration, the impedance of cartilage (as measured by the surface probe) was inversely proportional to the cartilage thickness for thin specimens and reached a plateau at larger thicknesses, with the transition between these two behaviors occurring over a range of thicknesses corresponding approximately to the penetration depth of current for that wavelength. Thus, as the thickness is decreased, the decreased cross-sectional area through which current can flow results in a proportionate increase in impedance, while adding additional thickness beyond the penetration depth does not further change the impedance since there is very little penetration of current into the deeper regions. For a given thickness, the theoretical impedance is higher with longer wavelengths, as the positive and negative electrodes are further apart.

5.5.4 Series and Shunt Impedances in the Probe-Cartilage System

Both a series impedance (due to the electrode-electrolyte interface) and a shunt impedance (due to shunting of current around the cartilage) were postulated in the equivalent-circuit model (Figure 5.1). By comparing the measured bath impedance with theoretical values (Table 5.1), the series impedance was estimated for each electrode configuration. The impedances calculated in this manner ranged from 56–185 Ω, in approximately the same range as previously reported measurements of silver/silver chloride electrodes in contact

with 0.15 *M* NaCl, measured at frequencies in the kHz range [79].

The shunt impedances for 7.0 mm disks tested with the 9.5 mm platen (estimated from the impedance with the rubber disk in the chamber) varied with the electrode configuration used, ranging from 471–1640 Ω. Using the theoretical cartilage impedance values and the mean estimated series and shunt impedances, the equivalent-circuit model generally agreed well with the measured impedances, although the agreement was not as good for the two-electrode probe tested with 0.1 mm thick disks. However, including the additional shunt component due to current flow through the lateral edges of the disk (Figure 5.9, top) resulted in a substantial improvement. With the six-electrode probe, since the estimated shunt impedance without the edge shunt contribution was lower than that of the two-electrode probe, the additional shunt source had a relatively smaller effect on the equivalent impedance.

The shunt impedance values were low enough, relative to the cartilage impedance, that a significant fraction of the total current did *not* penetrate the cartilage specimen (and thus did not contribute to producing the current-generated stress) in the configuration of Figure 2.3A, as calculated by Equation 5.6. In the experiments described in Chapter IV, current-generated stress was measured in 7 mm diameter cartilage disks (0.1–1.8 mm thick), with a 9.5 mm platen, using both the two- and six-electrode fixed-wavelength probes. With thicker disks, the fraction of current shunted is estimated to be less than 25% for both probes (Figure 5.8), while for 0.1 mm thick tissue, nearly half of the current is shunted when the six-electrode probe is used (including shunting through the lateral edges) and more than 75% with the two-electrode probe. Although this shunting of current would result in a proportionate decrease in the developed current-generated stress, this effect would change the predicted stress in 0.1 mm tissue by at most a factor of four, far less than the discrepancy that was found between the predicted and measured stress (Figure 4.10). Thus, other factors, such as the different mechanical boundary conditions between the model and the actual probe-cartilage system, would have to be invoked to fully explain this discrepancy.

5.5.5 Impedance Spectroscopy of Cartilage

Making impedance measurements using the surface probe is technically easier than using the device to measure current-generated stress, because much higher frequencies can be used (so that the measurement is made almost instantaneously), there is no mechanical calibration step required, and the measurement does not depend on the sensitive behavior of the piezoelectric sensor (so that no signal processing is required to recover the measurement). Thus, it is tempting to extend these studies as an additional method of characterizing normal and degraded cartilage. Indeed, electrical impedance spectroscopy (tomography) has been used as a means of nondestructive materials characterization [149] and biomedical imaging of a variety of tissue types [80,206].

Detecting cartilage degradation in this manner would rely on detecting changes in tissue conductivity resulting from loss of aggrecan charge groups. As derived in Appendix D, even complete loss of GAG from the tissue would decrease the electrical conductivity by only 28%, while the electrokinetic coupling, and thus the current-generated stress amplitude, would decrease to zero. Thus, as is the case with purely mechanical measurements of cartilage material properties [24,66,105,136,175], measurement of purely electrical parameters, such as tissue impedance, would be expected to be a less sensitive indicator of degradative changes than measurement of electromechanical quantities such as current-generated stress. However, impedance measurements can be made simultaneously with measurement of current-generated stress (at least at the low frequencies used for these measurements), simply by monitoring the voltage across the probe inputs. Alternatively, measuring impedance using frequencies in the kHz range would require only a few additional seconds after making the stress measurement. Measurement of cartilage impedance over a range of frequencies (impedance spectroscopy) could potentially provide additional information about the tissue, such as an estimate of cartilage thickness.

Chapter VI

Summary, Conclusions, and Future Work

6.1 Summary of Results Presented in this Thesis

This thesis has documented the development of an electrokinetic surface probe for non-destructively detecting degradation of articular cartilage by exploiting the known electro-mechanical transduction behavior of the cartilage extracellular matrix. The principal results and conclusions of this work are summarized below.

6.1.1 Two-Electrode Probe

The first phase of this work used a probe having two electrodes (the simplest possible geometry), with a fixed spatial wavelength of $\lambda = 5\,\text{mm}$, as used in earlier, preliminary studies [68,69,213]. Etched silver/silver chloride electrodes applied current to the cartilage surface, and the resulting current-generated stress at the tissue surface was measured by an overlying stress sensor fabricated from piezoelectric PVDF film. Initial efforts were focused on improving the fabrication protocol and testing the device with excised disks of adult bovine cartilage. Applying a sinusoidal current density to the surface of a cartilage disk produced a sinusoidal mechanical surface stress at the same frequency, transduced to a sinusoidal output voltage by the piezoelectric stress sensor. By using a purely sinusoidal input, the fundamental component of the response could be isolated (using Fourier analysis) from noise and electrode drift; in addition, the total harmonic distortion of the output could be quantitatively determined. The *differential* output of the sensor electrodes was recorded in order to enhance the signal and suppress common-mode noise. The measured stress was found to be proportional to the imposed current density and varied inversely with frequency, consistent with a poroelastic mechanical response; at higher frequencies, the fluid and solid motions in the extracellular matrix which together produce the current-generated stress have less time to develop during each cycle of the stimulus.

6.1.2 Chemical Modification Experiments: pH and Trypsin

In one series of experiments, the stress was measured as a function of bath pH, which was gradually titrated from 7.0 down to 2.0 by sequential addition of 1 *N* HCl. The stress amplitude reached a minimum at approximately the isoelectric pH of the tissue, the pH value at which there is zero net charge on the tissue. As the pH was further lowered, however, the amplitude increased, while the phase angle underwent an abrupt 180° transition, indicating that the direction of the measured stress had reversed. These changes in the mechanical stress closely paralleled known changes in tissue fixed charge density with pH, as determined by independent titration studies [67]. This phenomenon was found to be reversible, and biochemical assay of the disks subjected to this protocol revealed no significant loss of GAG from the tissue. Thus, these results provided strong evidence that the stress measured by the probe reflected the underlying charge density of the matrix, as reversibly neutralizing these charge groups produced similar changes in the measured stress. In another series of chemical modification experiments, cartilage disks were digested with trypsin for up to 20 h, producing a significant and steady decline in the measured stress. In this case, loss of charged GAG residues from the tissue (due to enzymatic cleavage of the core protein of matrix aggrecan molecules) resulted in parallel changes in the stress measured by the probe.

6.1.3 Multiple-Wavelength Spectroscopy of Cartilage

One of the key features of the theory underlying electromechanical surface spectroscopy is that the penetration depth of current into the tissue is directly proportional to the imposed spatial wavelength, which is equal to twice the electrode spacing. Thus, by making measurements at different spatial wavelengths, different depths of the tissue could, in theory, be tested. Since the earliest biochemical changes in degradative conditions such as osteoarthritis include nonuniform loss of GAG from the tissue, it was hypothesized that measuring current-generated stress over a range of wavelengths and frequencies could enable partial-thickness degradative changes to be detected. To test this hypothesis, a new version of

the probe having six independently addressable electrodes was developed, and the PMMA testing chamber was extensively modified to accommodate the additional electrical connections required. By externally changing the polarity of each electrode, multiple wavelengths could thus be achieved with a single device. The device was tested with full-thickness calf cartilage plugs having an intact articular surface, as a more appropriate model than excised disks for ultimate *in vivo* use. Two different electrode configurations were used: a "long-wavelength" (λ = 5 mm) configuration and a "short-wavelength" (λ = 1.68 mm) configuration. The *ratio* of short : long-wavelength stress amplitude showed a characteristic frequency dependence in normal cartilage.

6.1.4 Surface Trypsin Digestion as a Model for Cartilage Degradation

A model system was developed for producing nonuniform loss of GAG from cartilage plugs, as a model for certain biochemical changes seen in the early stages of cartilage degradation. The plugs were mounted in a chamber and exposed to trypsin in such a way that the enzyme could only diffuse in from the articular surface. Histological staining with DMB revealed progressive loss of GAG with increasing duration of enzyme exposure, proceeding inward from the surface. Biochemical assay of GAG content of sequential 200 μm thick slices from normal and trypsin-digested plugs quantitatively confirmed these findings and allowed the overall loss of GAG from the degraded region to be estimated. Four plugs were tested with the multiple-wavelength probe, before and after digestion with trypsin for 2 h using this protocol. This duration of trypsin exposure produced an estimated 25% loss of GAG from a region extending 0.6 mm into the tissue, approximately the penetration depth of the short-wavelength current excitation. Prior to trypsin digestion, the short : long-wavelength stress amplitude ratio exhibited the frequency dependence characteristic of normal cartilage. After enzyme exposure, however, this ratio decreased, with the most marked change (50%) at lower frequencies, indicating that the short-wavelength response, in which current was essentially confined to the degraded region, was more attenuated than the long-wavelength response, in which current could penetrate into the underlying normal

tissue. Thus, multiple-wavelength spectroscopy was capable of distinguishing a relatively mild degree of focal cartilage degradation from normal tissue.

6.1.5 Predictions of Poroelastic Model

The poroelastic model for surface excitation of cartilage [210,211] which motivates the technique of electromechanical surface spectroscopy was used to simulate the response of cartilage to surface electrodes. Mathematically, the problem was solved analytically as a superposition of modal solutions, each weighted by an appropriate Fourier coefficient (determined by the electrode geometry). Several conclusions were drawn from the simulation results. First, although the theoretical distribution of current within the bulk of the tissue is entirely governed by Laplace's equation and does not vary with frequency, the mechanical response (as assessed by looking at pressure, velocity, and displacement profiles with respect to depth into the tissue) is governed by a frequency-dependent mechanical diffusion depth, which decreases with increasing frequency. The model predicts a nonuniform normal surface stress over the excitation electrodes, with a phase angle and frequency dependence characteristic of a poroelastic response. The peak stress occurs at the edge of the electrodes; thus, alignment of the sensor electrodes (which develop an output voltage proportional to the *average* stress over the electrode area) the with the excitation electrodes is important in order that the piezoelectric sensor output truly reflects the actual stress. The model also predicts a shear stress component at the surface, with a much larger amplitude that does not vary with frequency (and hence is not a poroelastic effect). However, this component of the stress would *not* be expected to contribute to the sensor output because the piezoelectric film does not (to first order) transduce shear stresses and the shear component is a common-mode signal, which would be eliminated by differential recording.

6.1.6 Comparison of Theory and Measurement

A series of stress measurements (using two-electrode and six-electrode fixed-wavelength probes) were made on calf cartilage disks of thickness 0.1–1.8 mm and compared with

the predictions of the poroelastic theory. Although the theory and data showed the same inverse dependence on frequency, the theory predicted a strong inverse dependence of the stress amplitude on cartilage thickness; in contrast, the stress measured with the probes did *not* vary significantly with thickness. To explain this discrepancy, several of the assumptions inherent in the model were examined. For example, while the model assumes that the cartilage specimen is an infinite slab (in the horizontal direction) with an insulating, impermeable, surface, in the actual system, the cartilage plugs and disks had a lateral edge which was permeable and in contact with the bath solution. In addition, it was postulated that shunting of current in the actual system might account for at least part of the difference; if a greater fraction of the current is shunted when the specimen thickness is small, then a correspondingly smaller fraction would penetrate the tissue and produce a stress response. To test this hypothesis, a series of impedance measurements were made on cartilage plugs and disks.

6.1.7 Impedance Measurements

Cartilage impedance was measured by applying a 1 kHz sinusoidal current to a specimen mounted in the PMMA chamber and simultaneously measuring the voltage drop across the probe inputs. The impedance of full-thickness cartilage plugs measured using this technique did not change when the articular surface was removed. With cartilage disks, the measured impedance was modeled by an equivalent circuit containing a series element (representing the electrode-electrolyte interface) and a shunt element (representing shunting of current via all possible paths). For each specimen, the shunt and series components were estimated from measurements made with an insulating rubber disk or only bath solution in the chamber, respectively. When these values were combined with theoretical cartilage impedance values (predicted by the poroelastic model) in the equivalent-circuit model, the predicted equivalent impedance agreed well with the measured impedance values. Based on this model, it was estimated that for the range of thicknesses tested, up to 75% of the current imposed by the excitation electrodes does *not* penetrate the tissue. The convenience

with which impedance measurements can be made suggests that impedance spectroscopy of cartilage could be performed in conjunction with measurement of current-generated stress.

6.2 Ongoing and Future Work

Based on the work described in this thesis, a variety of further studies are suggested to extend these results and to work toward the goal of being able to make *in vivo* measurements of current-generated stress in intact joints using the surface probe technology.

6.2.1 Chamber-Mounted Probe

Using the chamber-mounted version of the surface probe (which was used for all the studies presented in this thesis), several different areas of further *in vitro* investigation can be considered, including:

- **Enzymatic digestion of aggrecan:** Using the model system for surface digestion described in Chapter III, further studies could be carried out using trypsin, chondroitinase, or metalloproteinases such as stromelysin (believed to be involved in the pathogenesis of osteoarthritic degradation) in order to further quantify the ability of multiple-wavelength spectroscopy to detect and localize focal regions of enzymatically induced aggrecan loss extending to various depths of the tissue.

- **Collagen degradation:** Although all studies to date have focused on aggrecan loss as a model for cartilage degradation, denaturation to the collagen network has also been reported in osteoarthritic tissue [108]. Collagen does not contribute directly to the electromechanical coupling in cartilage; however, collagen damage would be expected to decrease the equilibrium modulus of the tissue, with resulting changes in the poroelastic response. Testing cartilage plugs with the probe after digestion with specific enzymes such as collagenase would address the relative contribution of collagen damage (vs. GAG loss) to changes in current-generated stress.

- **Impedance spectroscopy:** To date, cartilage impedance has only been measured at a frequency of 1 kHz using the probe, as a means of trying to estimate the degree of current shunting in the probe-cartilage system. As discussed in Chapter V, however, impedance measurements of cartilage over a range of frequencies could potentially provide additional information about the state of the tissue. Preliminary studies could be conveniently performed using the chamber-mounted probe.

- **Other issues,** such as the effect of surface fibrillation on measured stress, could also be assessed using the controlled *in vitro* environment of the chamber-mounted probe system prior to *in vivo* testing.

6.2.2 Prototype Hand-Held Probe

As a prototype for making *in situ* measurements on intact joint surfaces, a "hand-held" version of the probe, with the excitation electrodes mounted at the end of a metal tube, has recently been developed [23] and tested with canine knee joints. Converting the probe from the chamber-mounted version to a stand-alone instrument required solving a number of design problems, including making adequate electrical connections to the piezoelectric sensor and providing effective electrical shielding of the sensor outputs [23]. Although the present version has two electrodes, a newer version of the hand-held device having four independently addressable electrodes, and thus multiple-wavelength capability, is currently being developed (by Steven Treppo). For *in situ* and *in vivo* testing using the hand-held probe, several new issues arise which were not present with the chamber-mounted probe, including:

- **Positioning of device:** The new device is held by hand against an intact joint surface. An approximately constant static load is maintained using a constant-force spring-loaded mount; this is needed since the dynamic response of the piezoelectric film is dependent on the static load. There is no direct capability for monitoring the actual imposed static load; it is not yet clear how parallel to the cartilage surface the end

of the device needs to be in order to obtain good electrical contact and an accurate measurement.

- **Curvature and condition of articular surface:** Although the presence or absence of the articular surface did not have any effect on impedance or stress measurements using the chamber-mounted probe, it is not yet clear what effect, if any, curvature of an intact joint surface would have on the contact between the electrodes and the cartilage and on the measured response *in vivo*. In addition, fibrillation of the tissue surface, which would be present in more advanced stages of cartilage degradation, could affect the measurements.

- **Repeatability and variability:** For *in vivo* testing, it will be necessary to assess the variability of repeated measurements within the same subject as well as the range of subject-to-subject variability of stress measured in normal cartilage, in order to obtain an accurate baseline "normal" level with which to compare the response measured in degraded tissue.

- **Pyroelectricity of PVDF film:** In addition to being piezoelectric, the PVDF film used for the stress sensor is also *pyroelectric*; i.e., it develops a voltage in proportion to changes in temperature. This phenomenon could potentially affect measurements when the probe is transferred from a room-temperature environment into an intact joint.

- **Biocompatibility:** It is not yet clear whether contact between the silver chloride electrodes and the cartilage surface can produce any short-term or long-term damage to the tissue.

6.2.3 Theoretical Model

The theoretical model for surface excitation of a poroelastic medium [210,211] could be extended in several ways, in order to more completely capture the physical behavior of the probe-cartilage system.

- **Boundary conditions:** It is hypothesized that the difference between theoretical and measured stress is due, in large part, to the difference in boundary conditions between the idealized two-dimensional model and the actual three-dimensional physical system. For example, the model assumes that the specimen is an infinite slab in the horizontal direction, while the actual cartilage plugs and disks tested have a free lateral surface that is permeable to current and fluid flow. It may be possible to modify the boundary conditions used in the present model in order to more accurately reflect the actual behavior at the lateral edges of the specimen.

- **Nonuniform tissue properties:** At present, the model assumes that the tissue is homogeneous. However, for predicting the response in partially degraded cartilage, it will be necessary to incorporate inhomogeneous material properties (corresponding to the inhomogeneous fixed charge density resulting from loss of aggrecan). With the modal theory, this could be implemented via a *layered* model, in which the tissue is approximated as a series of thin, homogeneous layers. However, this approach would greatly increase the mathematical complexity and computing requirements of the model.

- **Finite element model:** As an alternative to the analytical modal solution, a finite element approach could be used to solve the governing equations numerically, subject to the appropriate boundary conditions. Conceptually, this approach could enable more accurate modeling of the actual boundary conditions, as a more general geometry could be simulated. Software has already been developed (by Marc Levenston) for modeling the mechanical and electromechanical behavior of cartilage in an axisymmetric geometry using a finite elements approach; this technique could be modified to model the actual surface probe geometry as well.

6.3 Ultimate Goals

The work presented in this thesis, as well as the further studies suggested above, is intended as progress toward the ultimate goal of incorporating the surface probe technology into an instrument that can be used to measure current-generated stress in intact joints via arthroscopy. Such a device could provide a sensitive means of detecting early stages of cartilage degradation. The ability to quantitatively monitor disease progression, in human subjects as well as animal models, would be a powerful tool in the development of new antiarthritic drugs as well as new techniques for repairing focal cartilage defects. Given the extremely high prevalence of osteoarthritis and the high costs associated with the disease, the potential benefits of the technology are substantial.

Appendix A

Probe Construction

This appendix describes the details of the probe construction technique, including a description of the piezoelectric stress sensor and an explanation of the photofabrication techniques used. The sequence of steps in the fabrication protocol is summarized in Table A.1.

A.1 Piezoelectric Sensor

To measure the developed surface stress exerted on the excitation electrodes, the probe uses a piezoelectric stress sensor, fabricated from a sheet of polyvinylidene fluoride film (AMP Inc. Piezo Film Sensors[1], Valley Forge, PA) with a 300 nm-thick layer of vacuum-deposited (sputtered) nickel-copper alloy metallization on both sides. Polyvinylidene fluoride (PVDF or PVF_2) is a synthetic polymer composed of long chains of the repeat sequence [-CH_2-CF_2-]. Mechanical stretching or rolling of the film during manufacture orients the polymer chains in a parallel arrangement, converting them from a non-polar configuration (α-phase) to one that is highly polar (β-phase) [32]. Piezoelectric behavior is then imparted by the process of "poling": the material is metallized on both sides, exposed to a strong DC electric field ($\sim$1 MV/cm) at high temperatures (80–120°C) to align the dipoles, and then cooled while still in the field, producing a permanent polarization density within the film [157]. Because the poled PVDF maintains its "frozen-in" polarization density even in the absence of an applied electric field, the material is classified as an *electret* [32].

PVDF has several advantages as a transducer as compared to classical piezoelectric ceramic materials, including a wide frequency range of operation (0.005 to 10^9 Hz), wide dynamic range (10^{-2} to 10^{12} Pa), high elastic compliance, flexibility, and mechanical strength, and relative ease and low cost of fabrication in sheets of arbitrary size or

[1] Formerly manufactured by Atochem North America, and prior to that by Pennwalt Corp. as "Kynar Piezo Film"

Probe Fabrication Protocol

In laboratory:

- Cut silver, PVDF, Mylar, metallized Mylar, rubber adhesive using templates
- Clean silver, PVDF with detergent solution (Pex)
- Bond PVDF, Mylar, and metallized Mylar with rubber adhesive
- Abrade surface of silver; acidify with 15% nitric acid
- Bond silver to Mylar with Tycel 7000/7200 epoxy

In darkroom:

- Dehydration bake (80° × 10 min) in convection oven
- Coat both sides with KPR photoresist; let dry × 20 min
- Prebake to harden resist (80° × 10 min)
- Expose both sides to UV light (15 min) through negative mask
- Develop (30 sec × 2) to remove unexposed photoresist

In laboratory:

- Etch silver with 55% ferric nitrate (heated to 45°)
- Strip remaining photoresist from silver
- Etch PVDF metallization with ferric nitrate
- Strip remaining photoresist
- Chloride deposition on silver electrodes

Table A.1: Sequence of steps in surface probe fabrication protocol.

shape [193]. As a result, the material has been used in a great variety of applications (reviewed in [193] and [157]). In at least one application (an ultrasonic transducer), PVDF has been successfully incorporated with silicon using integrated circuit technology [232]. Recent orthopaedic applications of PVDF include a transducer for measurement of dynamic contact stresses in human cadaver knees [156] and a stress gauge in a device for measuring electrical and mechanical properties of cartilage in uniaxial compression [122].

Piezoelectric films such as PVDF can be considered to be materials that develop an electric charge proportional to an applied mechanical stress or strain, primarily because of small changes in film thickness [31]. For the purposes of the surface probe, only stresses that are *normal* to the surface of the film will be considered; shear stresses (in any direction) do *not* produce a piezoelectric response across the film thickness, at least to first order [32]. A compressive stress of magnitude σ (which may be nonuniform), acting over a metallized area, A, generates a charge, Q, that is independent of the film thickness:

$$Q = d_t \int_A \sigma \, dA = d_t \bar{\sigma} A, \tag{A.1}$$

where $\bar{\sigma}$ is the average stress and d_t is an empirically determined *piezoelectric strain constant.* Regions of the film that are metallized on both surfaces act as a parallel-plate capacitor. The capacitance, C, of a film of thickness δ with metallized area A', is given by $C = \epsilon A'/\delta$, where ϵ is the dielectric constant of the material. Thus, if a portion, A, of the total metallized electrode area, A', is subjected to a compressive stress, then the resulting voltage across the film is

$$V = \frac{Q}{C} = \frac{d_t \bar{\sigma} A}{\epsilon A'/\delta} = \frac{d_t \bar{\sigma} \delta}{\epsilon} \left(\frac{A}{A'} \right). \tag{A.2}$$

For a typical electrode configuration, $A < A'$, since leads and "pads" for making external circuit connections contribute to the metallized electrode area but are not stressed. This passive metallized area acts as a parasitic capacitance in parallel with the active area, thus reducing the measured signal, as indicated by Equation A.2. For the two-electrode probe's

piezoelectric sensor electrodes, the active area, A, measuring 4.0×1.5 mm, comprises approximately 20% of the total metallized electrode surface.

Equation A.2 also indicates that the developed voltage is proportional to the thickness of the sensor, although in practice, the associated cables and electronics can contribute significantly to the overall capacitance across which the developed charge is distributed. However, a thicker film would produce a larger output voltage for a given applied stress. A thinner film, however, would be better able to discriminate between closely spaced stresses. Spatial resolution is an important consideration in probe design because the piezoelectric sensor needs to be able to detect stresses generated by excitation electrodes that are separated by less than 1 mm. PVDF film is commercially available in thicknesses ranging from 9 μm to 110 μm; for the probes used in the present studies, a thickness of 52 μm has been found to yield satisfactory results [213]. For multiple-wavelength probes having more electrodes, and thus a smaller inter-electrode spacing, thinner PVDF film may be needed in order to achieve sufficient spatial resolution.

A.2 Device Assembly

The electrokinetic probe is a 250 μm thick multilaminated structure (Figures 2.2 and A.1) consisting of etched silver/silver chloride (Ag/AgCl) excitation electrodes (Figure A.2) for applying current to the cartilage surface and a piezoelectric PVDF sensor, as described above, electrically shielded from the excitation electrodes. Shielding is provided by a 25.4 μm (1 mil) thick piece of Mylar polyester film, metallized on its lower surface, which is insulated from the piezo sensor by a sheet of 25.4 μm thick non-metallized Mylar. The excitation electrodes were etched from 25.4 μm thick silver foil, while the piezoelectric sensor was constructed from a sheet of 52 μm thick Kynar PVDF film, oriented so that the longitudinal mechanical axis of the film was parallel to the long axis of the electrodes. The silver, PVDF, and metallized Mylar sheets used in construction of the two-electrode and six-electrode fixed-wavelength probes were all 34×23 mm rectangular pieces; the Mylar insulator was slightly wider (32×25 mm), allowing overlap at the edges in order to ensure

good electrical insulation. For the multiple-wavelength probe described in Chapter III (Figure A.2C), the silver, PVDF, and metallized Mylar sheets measured 60 × 20 mm, while the non-metallized Mylar insulator measured 56 × 22 mm. All layers were cut from stock sheets using a sharp blade and a metal straightedge, guided by rectangular paper templates.

Prior to assembly, the silver and PVDF sheets were dipped in a mild detergent solution (Pex Laboratory Glassware Cleaner) and rinsed with deionized water to remove superficial dust and grease. To prepare the silver for photofabrication, both sides were gently abraded for 45–60 seconds with a slurry of Linde Fine Abrasive powder and then dipped in a 15% (v/v) nitric acid solution to mildly acidify the surface. Both the abrasion and acidification steps were found to be crucial in order to ensure adequate adhesion of photoresist to the silver during the etching process (i.e., omitting either of these steps resulted in detachment of the photoresist image from the silver surface before the etching was complete, producing damage to the electrode pattern). The silver was bonded to the metallized Mylar using urethane epoxy (Tycel 7000/7200, Liofil Co., Cary, NC[2]). The epoxy and curing agent were mixed, in approximately a 50 : 1 volume ratio, in a glass dish and diluted with an approximately equal volume of methyl ethyl ketone. The mixture was applied to both the silver and metallized Mylar using an acid swab brush, solvent was allowed to evaporate for 10 min, and the two epoxy-coated surfaces were then pressure-bonded. The other layers (Figure A.1) were pressure-bonded using either 30 × 23 mm (for the fixed-wavelength probes) or 55 × 20 mm (for the multiple-wavelength probe) sheets of 38 μm thick phenolic rubber adhesive (Plymaster 212, Norwood Industries, Frazer, PA[3]). The layers were attached such that the ground shield (metallized Mylar) and the common signal plane of the sensor (PVDF metallization) protruded 1–2 mm at opposite ends, in order to allow external ground connections to be made to the structure.

[2]Formerly manufactured by Lord Corp., Erie, PA

[3]8 × 10-inch sample sheets, with non-stick paper on both sides, were obtained from the manufacturer. Ordinarily the product is sold in rolls measuring 58 inches by 540 feet; one such roll would provide enough adhesive for approximately 100,000 probes.

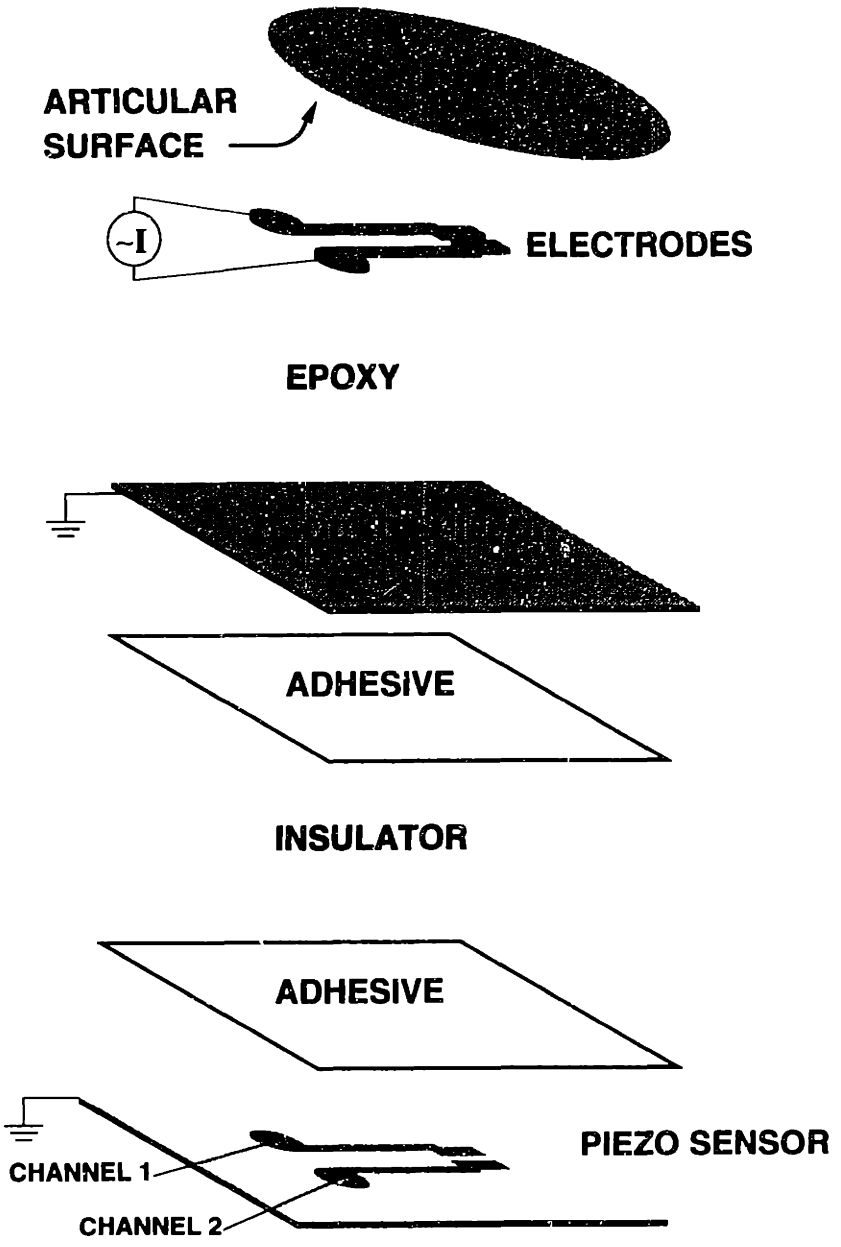

Figure A.1: Exploded view of two-electrode probe, showing details of the multilaminated structure, including Ag/AgCl excitation electrodes (top), piezoelectric PVDF sensor (bottom), and intermediate layers. The ground shield is the metallized surface of 25.4 μm thick metallized Mylar polyester film, while the "insulator" layer is 25.4 μm thick non-metallized Mylar. Excitation electrodes were bonded to the metallized Mylar with urethane epoxy; the other layers were bonded using phenolic rubber adhesive.

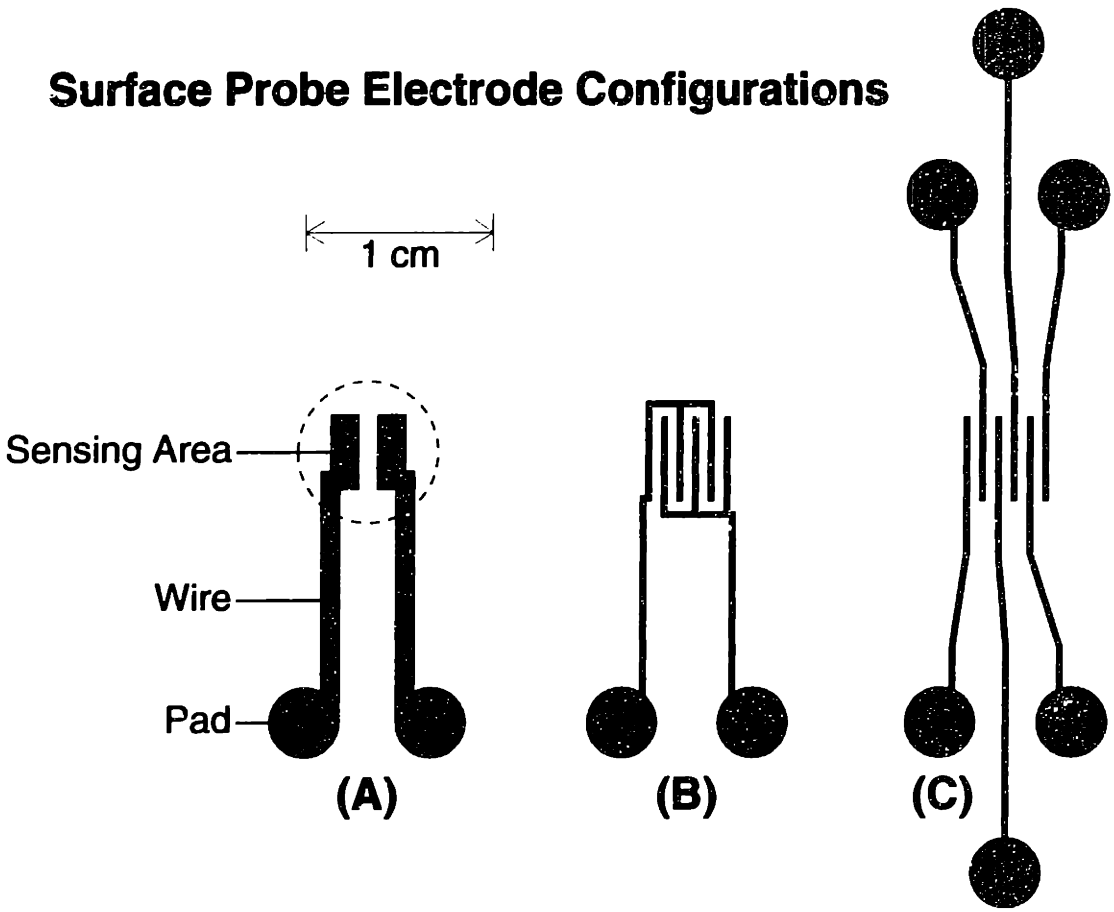

Figure A.2: Electrode configurations of various versions of the electrokinetic surface probe, including **A:** two-electrode (long-wavelength) probe, **B:** six-electrode (short-wavelength) probe, and **C:** independently addressable six-electrode (multiple-wavelength) probe. The "wire" is a thin strip of metallization connecting the active sensing area to the pad, where connection is made to the external circuitry. Dashed line indicates approximate outline of rubber O-ring in the testing chamber.

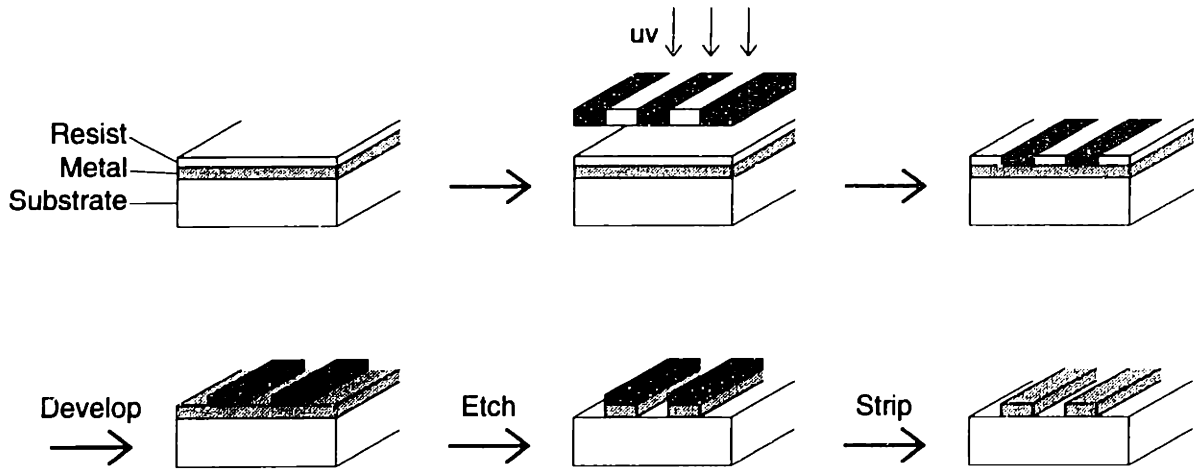

Figure A.3: Schematic illustrating photofabrication technique using a negative-work photoresist (adapted from [54]). The metallized substrate is coated with photoresist and then exposed to ultraviolet light through a negative mask of the electrode pattern, selectively cross-linking the resist. Non-cross-linked (i.e., unexposed) resist is then removed by the developer, leaving a stencil on the surface which protects the electrode pattern from being etched. After etching, the remaining photoresist is removed with a stripping compound.

A.3 Photofabrication

Both the silver excitation electrodes and the piezoelectric sensor electrodes were etched using standard photofabrication techniques (Figure A.3) [46,54]. The general technique is to coat the surface that is to be etched with a light-sensitive organic polymer, the *photoresist,* and then to cross-link the polymer, by selective exposure to ultraviolet light, in order to form a stencil on the surface that will resist the etching agent. The etchant then removes the metal that is *not* covered by the hardened photoresist, leaving the desired electrode pattern on the substrate.

A.3.1 Exposure and Development

The assembled multilaminated probes were baked at 80°C for 10 min in a convection oven to remove residual moisture. Because of the different thermal expansion coefficients of silver and PVDF, the probes (particularly with the longer multiple-wavelength configuration) had a tendency to curl when heated. This problem was minimized by weighting the free end of

each probe before hanging it in the oven. Both surfaces (silver and metallized PVDF) were then coated with a photoresist compound (KPR Photoresist, KTI Chemicals, Sunnyvale, CA), air-dried for 20 min in a darkroom, and then "prebaked" at 80°C for 10 min in the convection oven to harden the resist. Laser printed images of the desired electrode shape were produced using the PostScript language and converted to negative images, or masks, on two 10×12-inch photographic emulsions (Fotobeam-Brookside, Waltham, MA). A resist-coated probe was placed between two masks (aligned so that the positions of the etched excitation electrodes and sensor electrodes would coincide) and exposed to fluorescent ultraviolet light from both sides for 15 min. The masks contained multiple copies of the electrode pattern, so that up to 4 probes could be exposed simultaneously. No "postbake" step was performed [54]. Following exposure, each probe was immersed in a xylene-based developer solution (KPR Developer, KTI Chemicals, Sunnyvale, CA) for 30 sec, transferred to a fresh bath of developer for another 30 sec, and then rinsed under warm running water and blotted dry. The developer removed the unexposed (i.e., non-cross-linked) regions of photoresist, leaving an etchant-resistant image of the electrodes on the surface of the metal. When developing multiple-wavelength probes, it was found necessary to keep the concave surface of the probe face down in the dish of developer; otherwise, abrasion of the resist image against the bottom of dish produced small defects in the resist image which resulted in nicks and gaps in the electrode pattern during etching.

A.3.2 Etching

To etch the electrodes, the probe was mounted in a machined chamber consisting of a Lucite base and a polytetrafluoroethylene (PTFE, Teflon) upper section joined by Nylon screws. The Teflon section contained an oval hole (~3 cm^2 area) which served as a reservoir for the etchant; a rubber O-ring gasket (~22 mm inner diameter) sealed the edge of the reservoir to prevent leakage. For the multiple-wavelength probe described in Chapter III, a larger chamber was constructed, having a reservoir ~7.1 cm^2 in area sealed by a ~39 mm diameter O-ring. To etch the silver excitation electrodes, the probe was mounted in the

etching chamber such that the photoresist image on the silver was centered within the reservoir. Several ml of the etchant, a 55% (w/v) solution of ferric nitrate (Sigma) heated to 45°C, was added to the reservoir and the chamber was gently agitated. The chamber was drained, and fresh etchant added, every 1.5–2 min. When the etching was visibly complete, usually within 10–12 min, the chamber was flushed thoroughly with deionized water. A photoresist stripping compound (PRSK, Kepro Circuit Systems, Fenton, MO) was then added to the chamber to soften the photoresist image; the chamber was gently agitated for 60 sec and then flushed with tap water. The remaining photoresist was easily removed with a cotton-tipped swab, taking care not to detach the metal electrodes from the underlying epoxy. The PVDF sensor electrodes were etched using the same protocol; complete etching required only several seconds, however, since the metallization on the PVDF surface was much thinner. Following each etching procedure, the Lucite portion of the chamber was cleaned using photoresist stripper in order to remove any residual epoxy residue.

A.4 Chloride Deposition

In order to stabilize the electrode potential and decrease the low-frequency electrode-electrolyte impedance of the excitation electrodes [78], a layer of silver chloride was deposited on the surface of each electrode by the following procedure. The probe was mounted in the testing chamber (described in Appendix B) and 1–2 ml of unbuffered 0.1 *M* NaCl, titrated to pH 4.0 with 1 *N* HCl, was added to the bath reservoir. The positive terminal of a variable DC power supply was connected to one of the silver electrodes, in series with an ammeter and a 47 kΩ resistor, while the anode was connected to a platinum strip electrode suspended in the bath. For the two-electrode probe configuration, a DC current maintained at approximately 100 μA was imposed for 10 min to produce a total chloride deposit of 1000 mA·sec/cm^2, which is within the usual range for electrodes used in bioelectrical applications [78,79]. The procedure was then repeated for the other electrode. For chloriding the multiple-wavelength probe configuration, 75 μA was applied to each of the six electrodes for 3 min to obtain the same total chloride deposit.

Appendix B

Experimental Methods

This appendix contains detailed descriptions of the experimental setup (including details of the testing chamber and peripheral electronics), probe calibration technique, cartilage specimen preparation, biochemical assays, and histological methods relevant to the work described in this thesis.

B.1 Experimental Setup

B.1.1 Testing Chamber

For experiments, the probe was mounted in a machined poly[methyl methacrylate] (PMMA, Plexiglas) chamber (Figure B.1), 6.3 cm in diameter by 9 cm high, consisting of two detachable sections joined by four Nylon screws. The upper surface of the lower section was covered with a layer of conductive copper tape, to which both the ground shield of the probe and the common signal plane of the sensor were connected. This section contained copper rods (1/8 inch diameter) that connected the pads of the sensor electrodes with the inner conductors of two miniature coaxial connectors, which served as the output terminals. Each rod was surrounded by a cylindrical copper shield (0.173 inch inner diameter), insulated from the rod by a thin polytetrafluoroethylene (PTFE, Teflon) sleeve. The cylindrical shield connected the outer conductor of the coaxial connector with the copper tape ground plane in order to prevent capacitive coupling ("electrical crosstalk") between the current input signal and the sensor output leads. The chamber was later adapted for use with the multiple-wavelength probe described in Chapter III by adding additional holes and connectors in order to accommodate the four additional electrodes of this probe configuration (Figure A.2C).

The upper section of the chamber contained a 35 ml bath solution reservoir with two fluid recirculation ports, as well as copper input terminals that made contact, via spring-

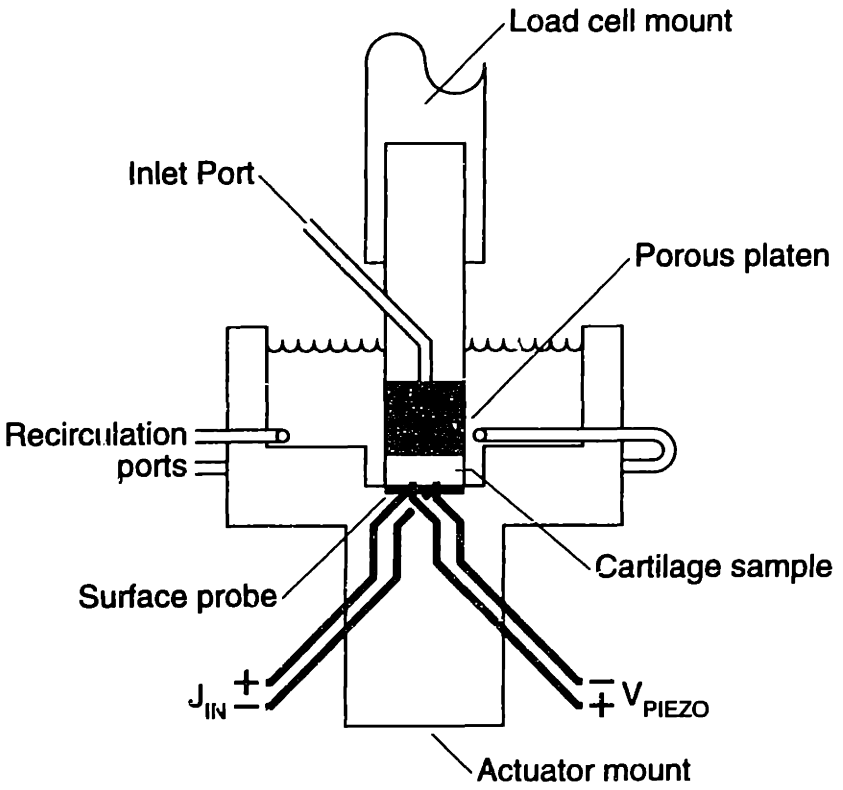

Figure B.1: Schematic illustration of PMMA chamber used for surface probe experiments. The load cell and actuator were used for mechanical calibration of the piezoelectric sensor; during experiments they simply maintained a static offset stress. Current-injecting electrodes, with input J_{IN}, were in contact with a single surface of the cartilage sample. V_{PIEZO} represents the outputs of the piezoelectric sensor, on the underside of the probe.

loaded copper rods (1/8 inch diameter), with the excitation electrode pads. Access to the excitation electrodes was provided by a 9.5 mm (3/8 inch) diameter hole in the center of the reservoir; the hole was later enlarged to 11.1 mm (7/16 inch) to accommodate testing of 3/8 inch diameter cartilage-bone plugs. A rubber O-ring surrounded the active area of the electrodes (dashed line in Figure A.2) to prevent leakage of bath fluid onto the rest of the probe surface, where it could create a low-impedance path between the excitation and sensor electrodes or between the electrodes and the ground plane. For testing, the probe was carefully aligned between the two sections of the chamber, the two halves were tightly bolted together, and the seam between the two sections was wrapped with paraffin film (Parafilm) to prevent capillary seepage of fluid in between the two sections.

Cartilage specimens were placed in the chamber with one surface in contact with the probe electrodes and the other in contact with either a porous platen or an impermeable PMMA platen. The porous platen assembly, used in the experiments described in Chapter II, consisted of a 6.4 mm diameter stainless steel shaft fitted with a polyethylene tip of the same diameter. A 1.6 mm diameter hole in the center of the shaft connected with an inlet port drilled into the side (Figure B.1), allowing fluid to be recirculated directly through the porous platen onto the surface of the specimen. This configuration has been used previously in studies of soft-tissue swelling in uniaxial confined compression [57]. The bathing fluid, which varied according to the experiment, was recirculated through flexible plastic and rubber tubing using a peristaltic roller pump. The tubing typically passed through a constant-temperature bath, maintained at $20 \pm 0.5°C$ by a proportional temperature controller (Cole-Parmer, Skokie, IL), with the temperature sensing element suspended in the chamber. For some experiments, bath pH was continuously monitored by suspending an Orion Ross combination electrode in the bath solution.

B.1.2 Peripheral Electronics

The chamber and the porous platen assembly were mounted in a servo-controlled materials tester (Dynastat Mechanical Spectrometer, IMASS, Hingham, MA), interfaced with a Novas

microcomputer system. The Dynastat was used to apply known sinusoidal stresses to the probe during calibration of the piezoelectric sensor and to maintain a static offset stress of 50 kPa during experiments, in order to ensure good contact between the sample and the probe electrodes.

For each of the electrode configurations shown in Figure A.2, two sensor output channels are defined. For the two-electrode and fixed-wavelength six-electrode probes (Figs. A.2A,B), the two outputs are simply the voltages at the two pads ("left" and "right"), corresponding to the response of the sensor electrodes overlying the positive and negative excitation electrodes, respectively. For the multiple-wavelength probe (Fig. A.2C), however, the polarity of each excitation electrode can be independently determined; for the present experiments, two different configurations were used, as described in Chapter III. In each case, the three sensor electrodes overlying the positive excitation electrodes were connected in parallel, via coaxial T-connectors, to yield the "positive" output channel; similarly, the three sensor electrodes overlying the negative excitation electrodes were connected to yield the "negative" output channel. With three sensor electrodes connected in this manner, the output voltage is determined (by superposition) to be

$$V = \frac{Q_1 + Q_2 + Q_3}{C_1 + C_2 + C_3} = \frac{\sum_{i=1}^{3} V_i C_i}{\sum_{i=1}^{3} C_i}, \tag{B.1}$$

where C_i is the capacitance of the ith channel, Q_i the charge on the ith electrode developed in response to an applied stress, and $V_i = Q_i/C_i$ is the voltage that would develop at the ith electrode alone (i.e., if the other two were not connected in parallel). Thus, each channel represents the *average* of the response of its three contributing sensor electrodes, each weighted by its channel capacitance.

The output of each of the two piezoelectric sensor channels (denoted "left" and "right" for the fixed-wavelength probes, or "positive" and "negative" for the multiple-wavelength probe) was passed through a separate channel of a high input impedance

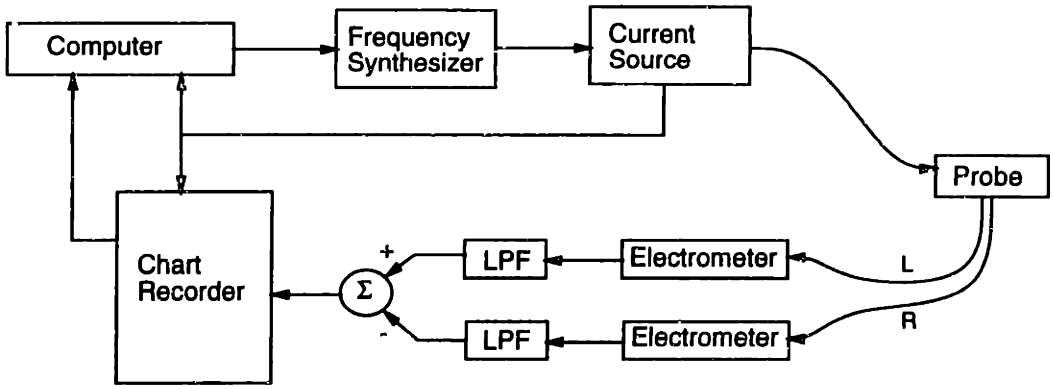

Figure B.2: Block diagram of the experimental setup for probe experiments. Small-amplitude sinusoidal currents were generated by a current source, driven by a computer-controlled frequency synthesizer. The output of each sensor channel (L, R) was passed through a high-impedance electrometer and then low-pass filtered to remove 60 Hz noise. The difference between the two outputs, as well as the current drive, were monitored on a strip chart recorder and processed by the computer.

electrometer, with an adjustable slew-rate ramp voltage offset to compensate for slow electrode drift (resulting from the very small input current drawn by the electrometer). The output of each electrometer channel was low-pass filtered (Model 1022F, Rockland Systems, West Nyack, NY) with a cutoff frequency of 15.7 Hz to eliminate 60 Hz noise and then connected to a high input impedance differential amplifier (model 11-4113-01, Gould Electronics, Cleveland, OH) (Figure B.2). Because of the opposite polarity of the two excitation electrodes (Figure 2.2), the outputs of the two sensor channels were expected to have a phase difference of 180°[1]; hence, differential recording increased the amplitude of the measured signal while suppressing common-mode noise, thus enhancing the signal-to-noise ratio. The differential sensor output was monitored on one channel of a Gould Brush 2200 strip chart recorder and digitally sampled by the computer.

Sinusoidal currents were generated by a bipolar operational power supply/amplifier (Kepco, Flushing, NY), configured as a current source (Figure B.3) and driven by a programmable frequency synthesizer (Rockland Systems, West Nyack, NY) controlled by the microcomputer. The applied current, I_{load}, was monitored by a digital multimeter (Keithley Instru-

[1]See section C.1.1 and Figure C.1 for verification of this assumption.

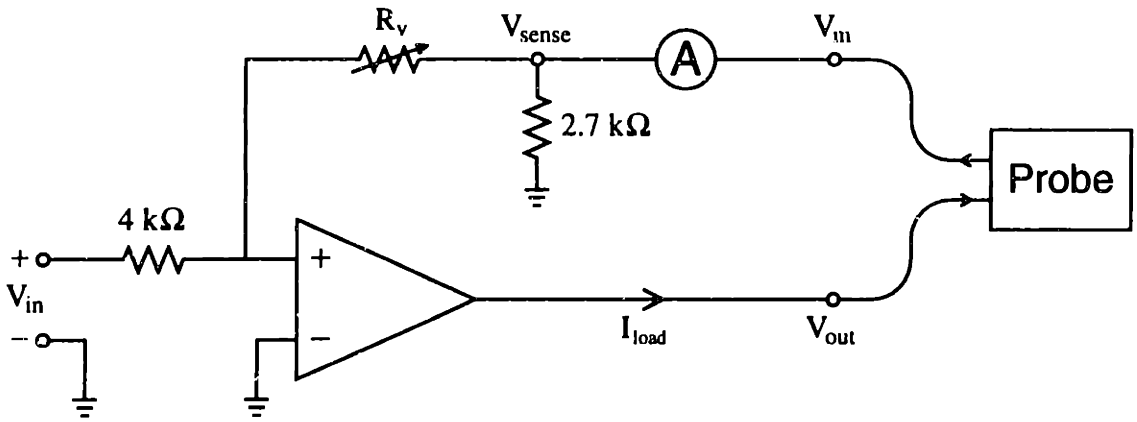

Figure B.3: Schematic diagram of the current source used for probe experiments. A sinusoidal input voltage (V_{in}) results in a proportional current, I_{load}, regardless of changes in load impedance. Applied current was determined by an ammeter and by monitoring either V_{sense} or V_m, both of which are proportional to I_{load}. Load impedance was computed from V_{out} and the calculated current, I_{load}.

ments, Cleveland, OH) in series with the load and by recording either of the voltages V_{sense} or V_m (Figure B.3), both of which are proportional to the load current, on the other channel of the chart recorder. Empirically, it was found that $I_{load} = V_{sense}/(2.41\,k\Omega) = V_m/(3.37\,k\Omega)$. For the impedance experiments described in Chapter V, the complex impedance, Z_{load}, across the probe inputs was computed as the ratio of the voltage drop across the load, $V_{out} - V_m$, to the calculated load current. Since

$$Z_{load} = \frac{V_{out} - V_m}{I_{load}} = \frac{V_{out}}{I_{load}} - 3.37\,k\Omega, \qquad (B.2)$$

the impedance could be determined from measurement of V_{out} and the load current.

The driving current signal and the differential probe output were digitally sampled and stored on the computer. On-line Fourier analysis determined the amplitude and phase, relative to the current signal, of the fundamental component and the next four higher harmonics of both signals. Determination of the higher harmonics allowed characterization of the linearity of the current-generated stress response. The response was taken to be linear if the *total harmonic distortion* (THD) was less than 5–10%. THD was computed as

follows:

$$\text{THD} = \sqrt{\sum_{n=2}^{5} x_n^2}, \tag{B.3}$$

where x_n is the fractional content of the nth harmonic component of the signal.

B.2 Sensor Calibration

Before making measurements using the probe, it was necessary to determine the relationship between the mechanical stress on the PVDF sensor and the resulting output voltage. It was assumed that the response of the sensor is linear and time-invariant (LTI), so that a sinusoidal applied stress, $\sigma = \text{Re}\{\hat{\sigma}e^{j\omega t}\}$, with frequency ω, produces a sinusoidal voltage, $V = \text{Re}\left\{\hat{V}e^{j\omega t}\right\}$, at the same frequency. For an LTI system, the complex amplitudes, $\hat{\sigma}$ and $\hat{V}$, are related by a complex mechanoelectrical transfer function, $H(j\omega) = \hat{V}/\hat{\sigma} = re^{j\theta}$, where $r(\omega)$ and $\theta(\omega)$ are, in general, functions of frequency. Thus, $r(\omega)$ is equal to the ratio of the complex amplitudes of V and σ, while $\theta(\omega)$ is simply the phase difference between V and σ. Determination of $r(\omega)$ and $\theta(\omega)$ completely characterizes the linear response. By applying known stresses over a range of amplitudes and frequencies and measuring the resulting voltage output of the sensor, the transfer function can be determined. Then, using this function, the current-generated stress can be determined from the sensor voltage output recorded during an experiment (by dividing the voltage amplitude by $r(\omega)$ and subtracting $\theta(\omega)$ from the phase).

B.2.1 Calibration Technique

To calibrate the probe, the chamber and platen assembly were placed in the Dynastat and a static stress of approximately 50 kPa was applied. The platen position was adjusted until the amplitudes of the sensor outputs, monitored on separate channels of the chart recorder, were as close as possible. Dynamic stresses having amplitudes of approximately 10, 5, 2.5, and 1.25 kPa, at frequencies of 0.025, 0.05, 0.1, 0.25, 0.5, and 1 Hz, were superimposed on the static stress by the Dynastat, driven by the frequency synthesizer. The amplitude and

phase of the probe response were taken to be the amplitude and phase of the fundamental component of the Fourier decomposition of the output voltage signal. At each frequency, the magnitude of the complex transduction coefficient (transfer function) was estimated as the slope of the linear least-squares regression line, constrained to pass through the origin, relating the amplitude of the output voltage to the applied stress amplitude. The phase of each transduction coefficient was assumed to be independent of stress amplitude and thus was estimated by averaging the phases obtained for each amplitude. Finally, the magnitudes and phases computed for the left and right channels were averaged to obtain a single complex calibration coefficient for each frequency. Typical calibration data (amplitude and phase) is shown in Figures B.4 and B.5.

B.2.2 Dependence of Calibration Coefficient on Static Load

One two-electrode probe was calibrated using the above protocol, with the usual static load of 50 kPa. The calibration procedure was then repeated using static stresses of 12.5, 25, 75, and 100 kPa (Figure B.6). When the static load was increased to 100 kPa, both channels developed a dynamic voltage of only 5.6 mV/kPa. With a static stress of 12.5 kPa, however, the response of the two channels diverged; the coefficients for the left and right channels were 43.9 and 29.9 mV/kPa, respectively. Thus, the magnitude of the dynamic response of the piezoelectric sensor varies with the level of the applied static load.

B.2.3 Comparison with Predicted Response

The magnitude of the electromechanical transduction coefficient of the piezoelectric sensor (typically 10–20 mV/kPa with the two-electrode probe and 5–8 mV/kPa with the multiple-electrode probe) is an order of magnitude greater than that obtained by Salant [213], using a similar probe in a slightly different experimental setup, and by Janselewitz [122], using a 110 μm thick PVDF stress sensor in a uniaxial compression chamber. Manouel [156], however, obtained static calibration coefficients of comparable magnitude (4.79–11.62 mV/kPa) in a device incorporating a 28 μm thick PVDF stress sensor.

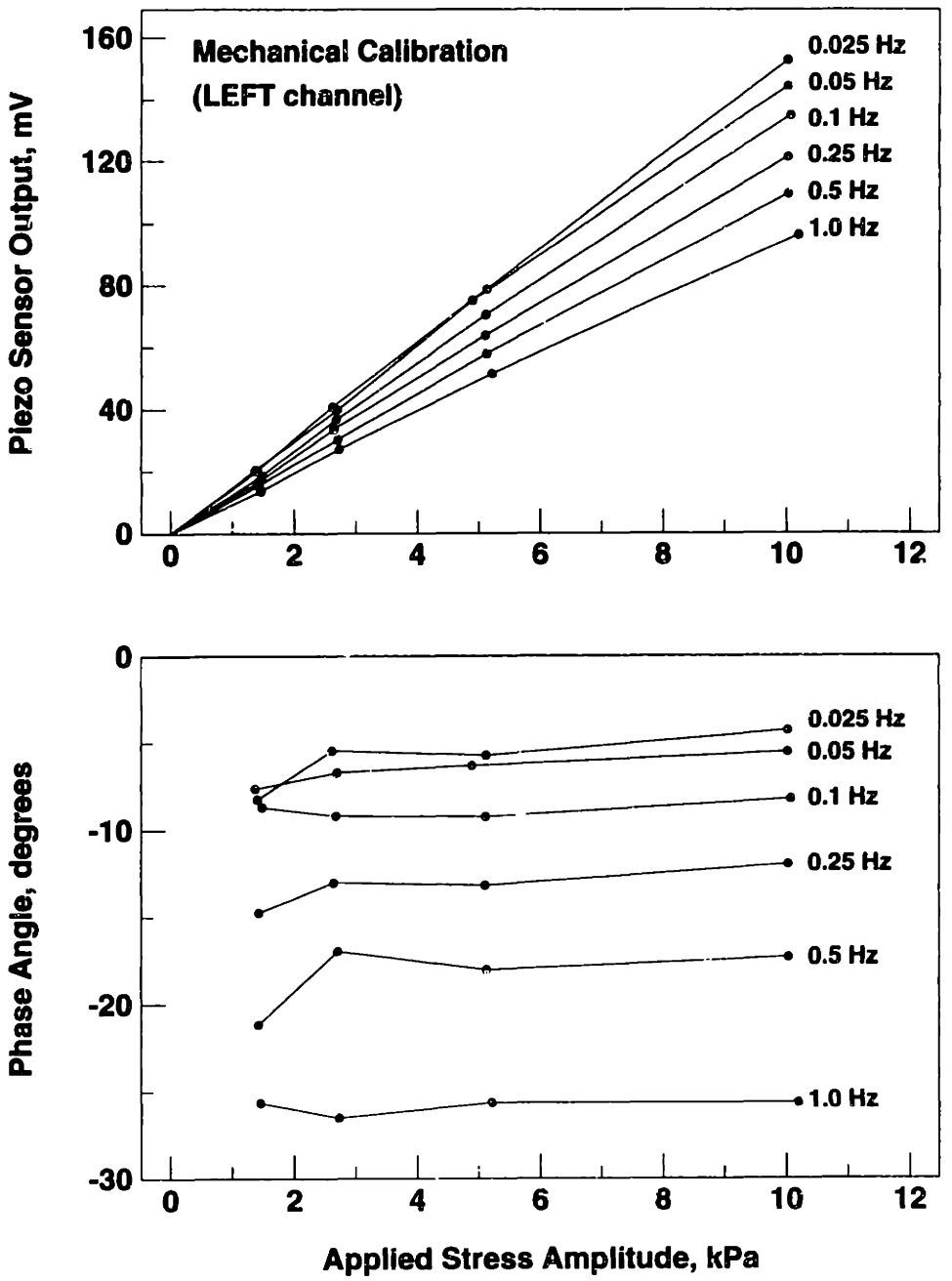

Figure B.4: Typical mechanical calibration curves for *left* channel of two-electrode probe. Sinusoidal stresses were applied and the corresponding output of the piezoelectric sensor (amplitude and phase) was recorded.

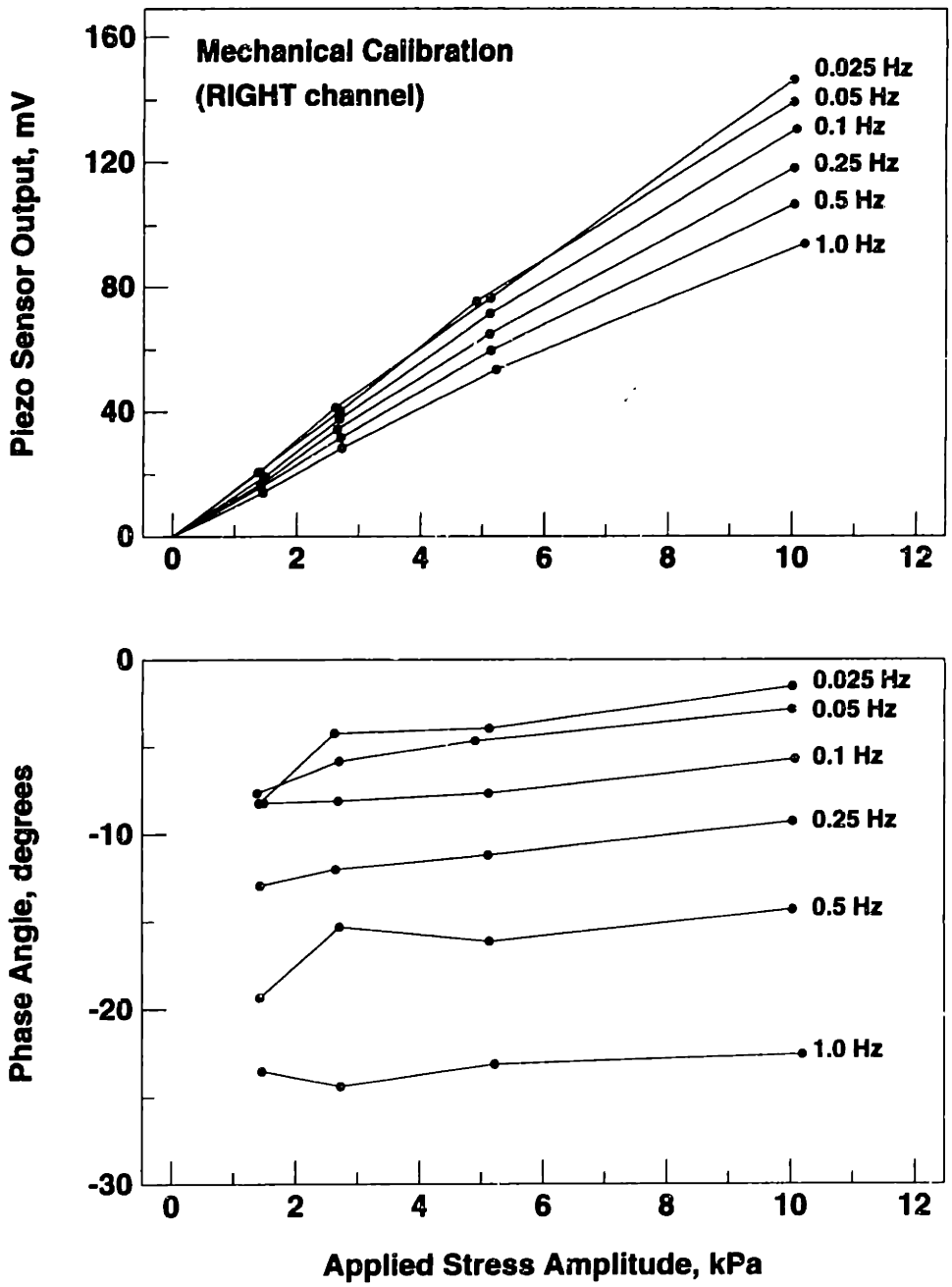

Figure B.5: Typical mechanical calibration curves for *right* channel of two-electrode probe. Sinusoidal stresses were applied and the corresponding output of the piezoelectric sensor (amplitude and phase) was recorded.

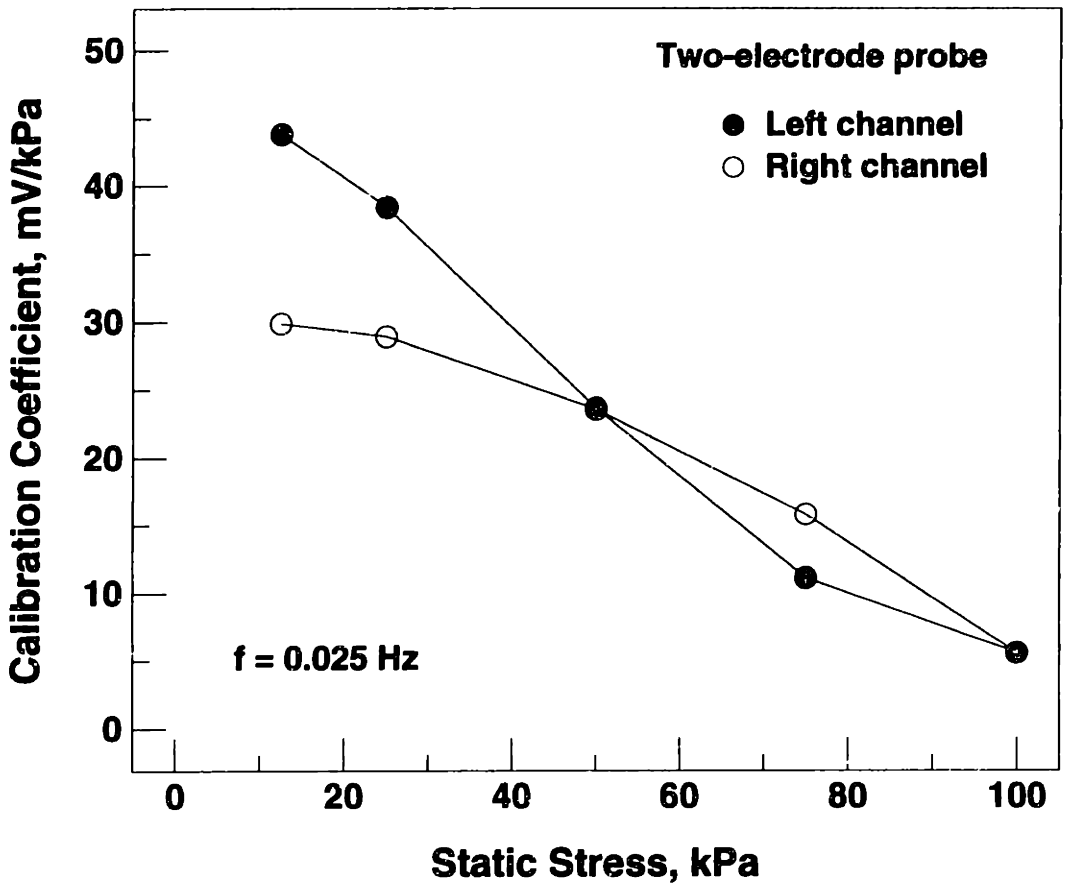

Figure B.6: Calibration coefficient at 0.025 Hz for left and right channels of a two-electrode probe, with applied static loads of 12.5, 25, 50, 75, and 100 kPa.

The calibration coefficients obtained for the probe were also an order of magnitude greater than the predicted value, based on the reported material properties of the PVDF film [193]. For a compressive stress, σ, of 1 kPa, applied over the metallized electrode area of the two-electrode probe, $A = 6.0\,\text{mm}^2$, with a piezoelectric strain coefficient $d_t = 22 \times 10^{-12}$ Coul/m^2-Pa [193], Equation A.1 predicts a developed charge of 1.32×10^{-13} Coul on the film. The total capacitance, C, of a sensor channel, is equal to the electrode capacitance, C_{elec}, plus the parasitic capacitances due to the shielded copper rod, C_{rod}, the coaxial cable connecting the sensor output ports with the electrometer, C_{cable}, and the electrometer input, C_{input}:

$$C = C_{\text{elec}} + C_{\text{rod}} + C_{\text{cable}} + C_{\text{input}}. \tag{B.4}$$

The electrode capacitance is given by

$$C_{\text{elec}} = \frac{\epsilon A'}{\delta}, \tag{B.5}$$

where A' is the total metallized electrode area and δ is the film thickness. With $A' = 30\,\text{mm}^2$ (for the two-electrode probe configuration), $\delta = 52\,\mu\text{m}$, and $\epsilon = 13.5\epsilon_0 = 120\,\text{pF/m}$ for PVDF at frequencies below 1 Hz [193], Equation B.5 yields $C_{\text{elec}} \approx 69\,\text{pF}$. The shielded copper rod acts as a coaxial cylindrical capacitor with Teflon as the dielectric material; thus,

$$C_{\text{rod}} = \frac{2\pi\epsilon_{\text{Teflon}}\ell}{\ln(b/a)}, \tag{B.6}$$

where a is the diameter of the inner conductor, b is the inner diameter of the outer conductor, and ℓ is the length of the rod. With $\ell = 19.7\,\text{mm}$, $b = 0.173\,\text{in}$, $a = 0.125\,\text{in}$, and $\epsilon_{\text{Teflon}} = 2.04\epsilon_0 = 18.1\,\text{pF/m}$ for Teflon [247], Equation B.6 yields $C_{\text{rod}} \approx 7\,\text{pF}$. The five-foot long coaxial cables, with a specified capacitance of 30 pF/ft, contribute a parasitic capacitance of $C_{\text{cable}} = 150\,\text{pF}$, while the specified input capacitance of the electrometer, C_{input}, is only approximately 1 pF. Summing these capacitances yields a total channel capacitance of

Symbol	Source	Capacitance
C_{elec}	Electrode	69 pF
C_{rod}	Rod	7 pF
C_{cable}	Cable	150 pF
C_{input}	Electrometer	1 pF

Table B.1: Sources of capacitance in piezoelectric sensor output (electrode capacitance computed for two-electrode probe)

C = 227 pF (Table B.1). Including the gain of 2 introduced by the electrometer circuit, the predicted output voltage produced by a 1 kPa stress is $V = 2Q/C = 1.16$ mV. Thus, the predicted coefficient, ~1.16 mV/kPa, is 8–16 times smaller than the measured value. This phenomenon is similar to that described by Chwang [45], who consistently found measured transduction coefficients for Kynar PVDF film to be approximately 6 times higher than the predicted value. The discrepancy may be due to incomplete characterization of the material properties of PVDF at very low frequencies.

B.3 Source and Preparation of Cartilage

B.3.1 Adult Bovine Cartilage

Previously frozen intact knee joints of 1.5–2 year-old cattle were obtained from a local meat packer (City Packing, Boston, MA). The medial facet of the femoropatellar groove region of the distal femur, along with overlying cartilage, was removed using a hacksaw, wrapped in aluminum foil, sealed in a plastic bag, and frozen at −20°C. As needed, samples were thawed in 0.15 M NaCl and mounted in a vise with a pivotable base having three rotational degrees of freedom. Cylindrical plugs of AC and attached subchondral bone, 9.5 mm (3/8 inch) in diameter and 1–2 cm long, were cored from the joint surface using a hollow sawtooth drill bit mounted in a drill press. Before drilling, the vise position was adjusted

so that the cartilage surface was approximately perpendicular to the drilling axis. During drilling, the joint surface and drill bit were irrigated with 0.15 *M* NaCl to lubricate the cutting surface and prevent heat buildup. Typically, 5–7 cartilage-bone plugs were obtained from a single joint; the plugs were stored in sealed plastic vials at −20°C until used in an experiment. Just prior to an experiment, a plug was thawed in 0.15 *M* NaCl at room temperature for several minutes, then mounted in a sledge microtome and adjusted so that the surface was as level as possible. Using the microtome, the articular surface was removed and an 800 μm thick plane-parallel disk was cut from the plug. A 7 mm diameter disk was then concentrically cored from the 9.5 mm disk using a punch, leaving an annular ring of cartilage (with approximately the same volume as the 7 mm disk) that was used as a control for biochemical assays.

B.3.2 Calf Cartilage

"Saddle" sections (femur and tibia, with intact knee joint) of newborn calves were obtained from a local slaughterhouse (A. Arena, Hopkinton, MA) within one day of slaughter. The mid-shaft region of the femur was transected using a hacksaw and the distal portion was mounted in a pivotable vise. The tibia, patella, and surrounding soft tissues were removed and the surface of the femoropatellar groove was exposed, taking care not to damage the articular surface. Cartilage-bone plugs were drilled from both the medial and lateral facets of the groove as described above; typically 4–5 specimens were obtained from the medial facet and 3–4 from the lateral facet. The plugs were stored at −20°C until used for an experiment. For some experiments, 7 mm diameter disks of varying thickness (0.1–1.8 mm) were prepared from thawed plugs using the microtome as described above. For other experiments, entire plugs (with intact articular surface) were used without further processing.

Inhibitor	Conc.	Substrate	Preparation
EDTA	2 mM	Metalloproteinases	Aqueous
Benzamidine-HCl	5 mM	Trypsin	100×, in ethanol
NEM	10 mM	Cysteine proteases	100×, in ethanol
PMSF	1 mM	Serine proteases	100×, in isopropanol
Pepstatin	1 μM	Acid proteases	100×, aqueous (frozen)

Table B.2: Protease inhibitors used in probe experiments.

B.4 Protease Inhibitors

To minimize cartilage matrix degradation by endogenous proteases during probe experiments, several protease inhibitors were routinely added to the bath solution (Table B.2) [192], except in enzymatic digestion studies. Originally, the mixture of inhibitors consisted of 2 mM [ethylenedinitrilo]tetraacetic acid (EDTA), 5 mM benzamidine-HCl, 10 mM N-ethylmaleimide (NEM), and 1 mM phenylmethylsulfonyl fluoride (PMSF) to inhibit metalloproteinases, trypsin, cysteine proteases, and serine proteases, respectively; for some experiments, 1 μM pepstatin (an inhibitor of acid proteases such as cathepsin D) was also added. Because some of these inhibitors (particularly PMSF [121]) are known to be unstable in aqueous solution, concentrated solutions at 100 times the desired concentration were prepared in either ethanol or isopropanol (Table B.2) and added to the bath solution at the start of each experiment. Because of concerns that NEM is capable of *activating* endogenous metalloproteinases via a "cysteine switch" mechanism [249], its use was discontinued in later experiments.

B.5 Biochemical Analysis

Wet and dry weights of each AC disk and annular ring were determined, before and after 12–16 hours of lyophilization, respectively. From the wet and dry weights, the

hydration, defined as the ratio of water to solid weight, was computed for each sample. The lyophilized tissue samples were digested with 1 ml of papain solution (125 μg/ml in 0.1 M sodium phosphate, 10 mM EDTA, and 10 mM cysteine at pH 6.5) at 60°C for 12–16 hours. The sulfated GAG content of each sample was then determined by a quantitative dimethylmethylene blue (DMB) dye-binding assay [60]. DMB is a cationic dye that exhibits *metachromasia* in the presence of sulfated GAGs, changing color from an intense blue to a pink or purple hue. For the assay, a 2 ml aliquot of aqueous DMB dye solution (46 μM plus 40.6 mM NaCl, 40.5 mM glycine, and 0.02 g% sodium azide titrated to pH 3.0 with 1 N HCl) was added to a 20 μl aliquot of each papain digest in a polystyrene cuvet and the optical absorbance at 590 nm was measured by a spectrophotometer (Lambda 3B, Perkin-Elmer, Norwalk, CT). The GAG content of the bath solutions was assayed by adding 200 μl aliquots of DMB to 20 μl aliquots of each bath solution in a 96-well plate and reading the absorbance at 580 nm using a microplate reader (Vmax, Molecular Devices, Menlo Park, CA). All assays were performed in duplicate or triplicate. Absorbance readings were converted to GAG concentrations using shark chondroitin sulfate (Sigma) standards, with a second-order polynomial fit relating measured absorbance readings to the known GAG content of the standards. In addition to the disks that had been tested with the probe, several "uncompressed control" disks and corresponding annular rings were prepared as described above (Section B.3) and then immediately weighed and assayed for GAG content.

B.6 Histology

Two techniques were used to prepare cartilage disks for light microscopic examination: (1) fixation using a small cationic dye, ruthenium (III) hexaammine trichloride (RHT), followed by staining with toluidine blue, and (2) simultaneous fixation and staining using dimethylmethylene blue (DMB) dye.

B.6.1 Ruthenium Hexaammine Trichloride (RHT) and Toluidine Blue

Histological fixation of cartilage using a fixative solution supplemented with highly charged dyes of low molecular weight such as RHT was first described by Hunziker *et al.* [110]. The cationic dye molecules readily diffuse into the cartilage matrix, where they bind electrostatically to the negatively charged matrix PGs and precipitate the macromolecules, preventing them from leaking out of the tissue during the fixation process. Prior to fixation, each sample (typically a half-disk) was washed for 15–20 min in phosphate-buffered saline to remove soluble proteins. The prefixative solution consisted of 0.05 M sodium cacodylate (dimethylarsinate) (Polaron, Cambridge, MA) and 0.2 M glutaraldehyde (Polysciences, Warrington, PA), at pH 7.4. Approximately 10 min before fixation, a pre-weighed aliquot of RHT (Polysciences) was added to achieve a concentration of 0.7% w/v (23 mM) in the fixative; the solution gradually changed color from yellow-orange to black. An amount of fixative equal to 25 times the sample volume was added to each specimen and fixation was effected at room temperature for 4.5 hours, followed by 16 hours at 4.5°C. The samples were then washed three times, for 30 min each, in a solution containing 0.1 M sodium cacodylate and 65 mM NaCl, then stored in 70% ethanol at 4°C until processed for light microscopy.

Sectioning of the fixed samples, slide preparation, and staining were performed by a local contractor (Pathology Services, Cambridge, MA). Initially, specimens were stained with toluidine blue in a carbonate buffer at either pH 4.0 or 10.6; for each sample, a slide was prepared using each pH value. A disk which was digested with trypsin for 20 hours (and thus had lost >90% of its GAG, as indicated by Figure 2.8) and then stained using the pH 4.0 buffer exhibited almost no stain uptake, while the corresponding sections prepared using a pH 10.6 buffer showed diffuse pale blue staining. This result suggested that toluidine blue is less selective for proteoglycans at pH 10.6 than at pH 4, possibly because the carboxyl residues of collagen fibrils are negatively charged at high pH [25] and thus capable of binding stain molecules. Therefore, subsequent toluidine blue staining was performed using a pH 4 buffer exclusively.

B.6.2 Dimethylmethylene Blue (DMB)

Recently, cationic dyes other than RHT have been assessed for their ability to precipitate PGs and to simultaneously stain the tissue with an intense, stable color signal [111]; ruthenium red and methylene blue chloride were reported to be the most successful. In assessing the trypsin digestion model described in Section D.1.1 with calf cartilage, some sections were fixed and stained using dimethylmethylene blue (DMB), the same metachromatic dye used in the GAG assay described in Section B.5. The same prefixative was used as for RHT fixation, with 0.2% w/v (5.7 mM) DMB added instead of RHT. Preliminary studies indicated that DMB diffused into the tissue much more slowly than RHT. Thus, it was necessary to use thin ($\sim$1 mm thick) slices, cut perpendicular to the articular surface, and to allow fixation to proceed for 96 hours (at room temperature) in order to ensure adequate dye uptake. Following fixation/staining, the samples were washed 3 times as described above and then stored in 70% ethanol at 4°C. Sectioning and slide preparation were performed by Pathology Services (Cambridge, MA).

Appendix C

Supplemental Data: Two-Electrode Probe Experiments

This appendix contains supplemental data pertaining to the two-electrode probe experiments described in Chapter II (and Reference [14]). The results presented here are divided into (1) general results concerning probe measurements, (2) the effect of bath pH on current-generated stress, and (3) the effect of trypsin digestion on the measured stress.

C.1 Surface Measurement of Current-Generated Stress

C.1.1 Differential Recording of Sensor Output

As discussed in Sections 2.3.2 and B.1.2, the output of the probe's piezoelectric sensor was recorded *differentially* in order to enhance the measured signal and suppress common-mode noise. This benefit of differential recording is predicated on the expectation that the fundamental components of the normal stress exerted on the two sensor electrodes are 180° out of phase with respect to each other because of the opposite direction of current flow induced by each of the corresponding overlying excitation electrodes (Figure 2.1A). To test this hypothesis, several disks of calf cartilage were stimulated using the two-electrode probe configuration with the output of each piezoelectric sensor channel recorded *separately* (and converted to current-generated stress using the appropriate calibration data); typical results are shown in Figure C.1. At all frequencies, the amplitudes of the stresses measured by the two channels were comparable. At lower frequencies ($f \leq 0.25$ Hz), the two channels exhibited a phase difference of approximately 180°, as expected, while at higher frequencies, the phases of the two channels converged, indicating the presence of a significant common-mode component in this frequency range. The total harmonic distortion (not shown) was significantly higher when each channel was recorded separately than when the difference was recorded, confirming the efficacy of differential recording at reducing common-mode noise and thus increasing the signal-to-noise ratio of the measured response.

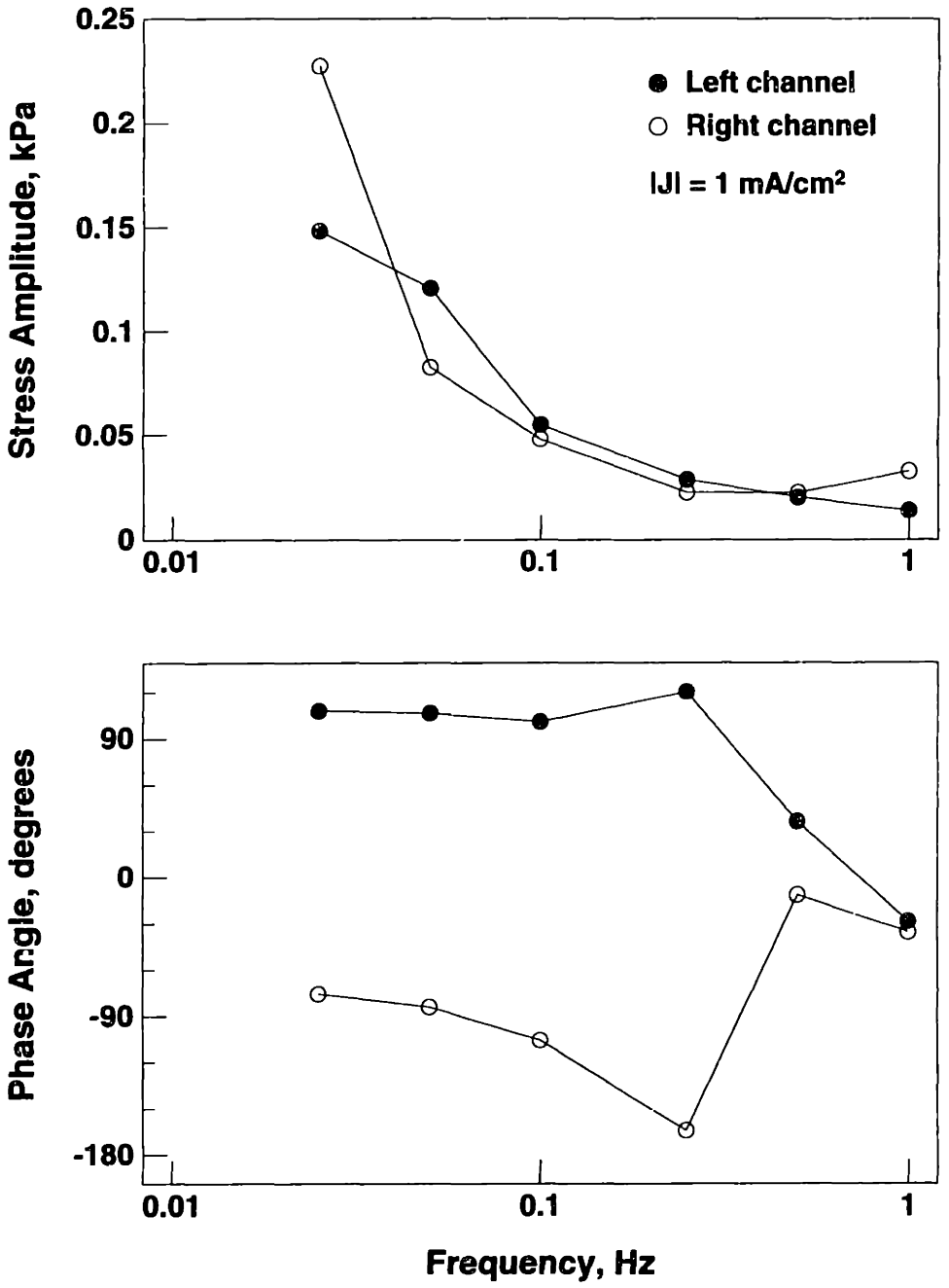

Figure C.1: Current-generated stress (amplitude and phase) measured by each channel of the two-electrode probe tested with 1.8 mm thick calf cartilage. At all frequencies tested, the amplitudes of the two stresses are comparable. There is a 180° phase difference between the two channels at low frequencies, while at higher frequencies the phase angles converge.

C.1.2 Dependence of Stress on Frequency and Current Density

Current-generated stress (amplitude and phase) was measured in nine disks (800 μm thick, 7 mm diameter) of normal adult bovine cartilage, including 5 disks from the pH experiments and 4 disks from the trypsin experiments described in Chapter II, prior to pH titration or addition of enzyme (Figure C.2). Based on the theoretical model [211], the stress amplitude was postulated to be proportional to a negative power of the excitation frequency. For both current densities, the best-fit exponent was determined using the Levenberg-Marquardt nonlinear least-squares technique [199]. In each case, the exponent was not significantly different from 1.0; i.e., the stress amplitude was *inversely proportional* to the frequency. At each frequency, the stress amplitude was directly proportional to the applied current density (for each disk, the Pearson correlation coefficient, r^2, was greater than 0.99 for frequencies from 0.025–0.1 Hz, 0.98 at 0.25 Hz, 0.96 at 0.5 Hz, and 0.93 at 1 Hz). The mean *phase* of the measured stress (Figure C.2, bottom) varied with frequency, ranging from 89–107°. At each frequency, no significant difference in phase between the two current densities was found (by ANOVA).

C.1.3 Comparison of Probe Measurements with Uniaxial Measurements

Data obtained using the two-electrode surface probe were compared with current-generated stress measurements from previous uniaxial confined compression experiments (Figure C.3). The one-dimensional uniaxial geometry (Figure 1.4) corresponds to the "infinite wavelength" limit of the 2-dimensional surface spectroscopic model [211], while the probe imposed a spatial wavelength, λ, approximately six times the cartilage thickness, δ. Both the uniaxial and probe experiments were performed using 800 μm thick disks of adult bovine cartilage, under similar pH and temperature conditions. However, the uniaxial compression experiments were performed using a bath solution of 0.001 M NaCl, while the probe experiments utilized physiologic (0.15 M) saline. At the higher salt concentration, mobile counterions are expected to shield the fixed matrix charge groups, thus reducing electrokinetic coupling [87]. For example, streaming potential magnitude (at 0.1 Hz) was

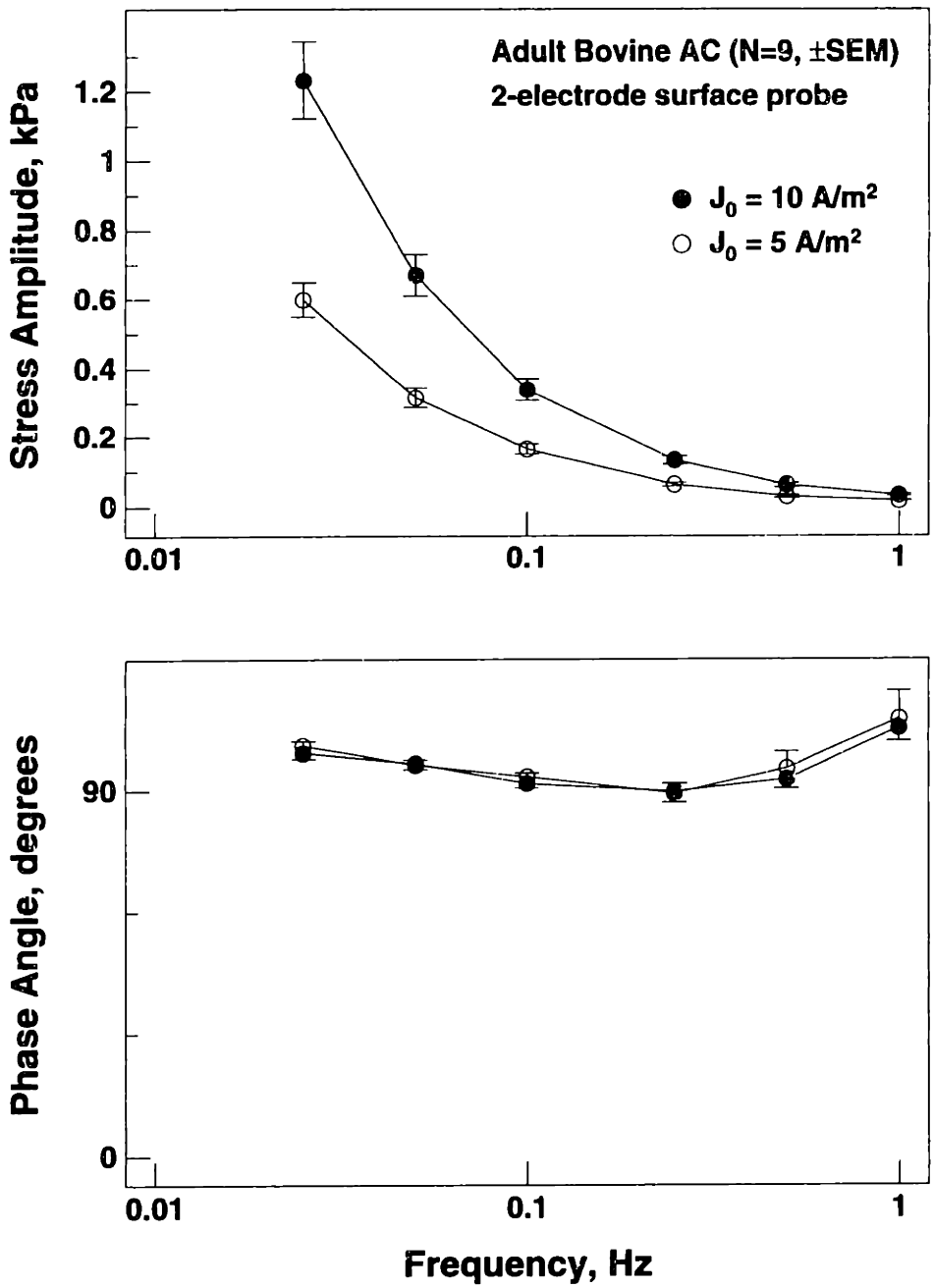

Figure C.2: Current-generated stress (amplitude and phase) vs. frequency measured in adult bovine cartilage disks (800 μm thick, 7 mm diameter) using the two-electrode probe with applied current densities of 10 A/m^2 (filled circles) and 5 A/m^2 (open circles). Data points are mean $\pm$ SEM (N = 9).

shown to decrease by a factor of four when ionic strength was increased from 0.001 M to 0.15 M [64]; the uniaxial data have been scaled to account for this difference in bath ionic strength. The measured stress has also been normalized to the applied current density to account for the different current amplitudes used. The stress amplitude (normalized to current density) measured in uniaxial confined compression (Figure C.3, diamonds) exhibited an inverse frequency dependence that was qualitatively similar to the stress measured in nine disks using the two-electrode surface probe (Figure C.3, circles), with comparable amplitudes and phase angles for the two conditions.

C.1.4 Response of Sensor Without Cartilage Present

As a control, several experiments were performed in which current was applied to the excitation electrodes with 35 ml of bath solution, but *no* cartilage specimen, in the PMMA chamber (Figure C.4). A sinusoidal current density of 10 A/m^2 was applied to the excitation electrodes of the probe and the differential sensor output was recorded in the usual manner. Although there was no cartilage in contact with the probe, the piezoelectric stress sensor produced a sinusoidal output at the same frequency; however, the amplitude was only 10% of that typically measured with cartilage and exhibited distinctly different phase behavior (ranging from 0° at 0.025 Hz to −90° at 1 Hz). This non-zero response in the absence of cartilage may arise from *electrocapillary* effects at the electrode-bath interface [71]: varying the potential of a thin metal strip electrode with one surface in contact with an electrolyte solution produces voltage-dependent changes in the interfacial surface tension (due to changes in the Gibbs surface excess), with a corresponding change in bending moment of the electrode. To test this hypothesis, 5 cm by 1.5 mm silver strips (25.4 μm thick), with one surface epoxied to 25.4 μm (1 mil) thick Mylar, were suspended in a 0.15 M NaCl bath; current was passed between the strip electrode and a platinum anode suspended in the bath. Applying a DC current resulted in slowly progressive curling of the strip electrode, with increasing convexity of the silver surface. Application of a sinusoidal current (at frequencies up to 2 Hz) produced small sinusoidal oscillations of the free end

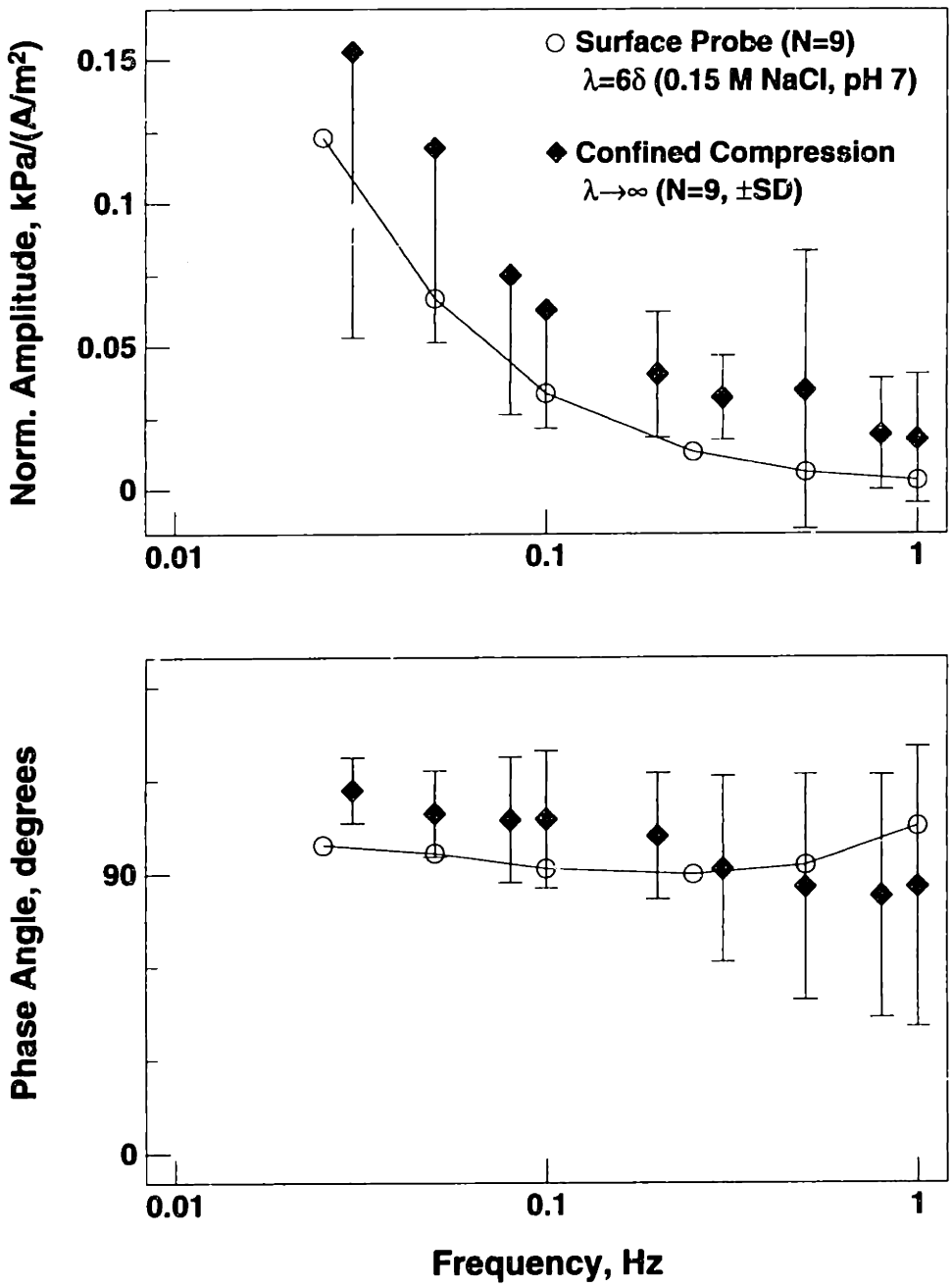

Figure C.3: Current-generated stress (amplitude and phase), normalized to applied current density, measured in uniaxial confined compression (diamonds) and with the surface probe (circles). Both sets of experiments were performed on 800 μm thick disks of adult bovine cartilage at pH 7 and 20°C. Probe data points are mean for $N = 9$ ($J_0 = 10\,\mathrm{A/m^2}$ data from Figure C.2); for clarity, error bars have been omitted. Uniaxial data points ($N = 9$, mean ± SD, from [64]) have been scaled to account for the difference in bath ionic strength between the two experiments.

of the suspended electrode at the same frequency. Thus, in the probe experiments without cartilage, the probe may have been sensing small changes in compressive stress against the piezoelectric sensor resulting from slight bending of the excitation electrodes.

C.2 Effect of Bath pH on Current-Generated Stress

Five disks of 800 μm thick adult bovine AC were tested using the protocol described in Section 2.3.5. In each experiment, current-generated stress was measured over a range of frequencies as the bath pH was titrated from 7 down to 2 by sequential addition of 1 N HCl; the results are shown in Figures C.5–C.9. With each disk, at all frequencies the stress exhibited a minimum in the range pH 2.4–2.8, while the phase angle underwent an abrupt 180° transition in the same range. (The data of Figure C.8 are also shown in Figure 2.6, with the amplitude for each frequency normalized to the response at pH 7).

C.2.1 Frequency Dependence of Low-pH Behavior

As shown in Figure 2.6A for single disk, the apparent isoelectric pH (IEP) of adult bovine cartilage, as determined by the pH value at which the stress amplitude reached a minimum, increased with increasing excitation frequency. Furthermore, the relative increase in stress amplitude above the minimum as bath pH was titrated to values below the IEP was greater at higher frequencies; the response of all five disks tested showed similar trends (Figures C.10 and C.11). As the bath pH was lowered beyond the isoelectric point, the mean stress amplitude at 0.025 Hz (Figure C.10, top) showed little or no further change. In contrast, at 1 Hz (Figure C.11, bottom), the mean stress amplitude returned to 85% of its value at pH 7 as the bath pH was lowered from 2.8 to 2.0. At intermediate frequencies, the degree of stress amplitude recovery at low pH increased monotonically with frequency. At pH 2.0, the stress amplitude was inversely proportional to the square root of the frequency, in contrast to the f^{-1} frequency response seen at neutral pH.

The frequency-dependent behavior at low pH may be explained as follows. The local GAG content of normal cartilage is known to increase with depth from the articular

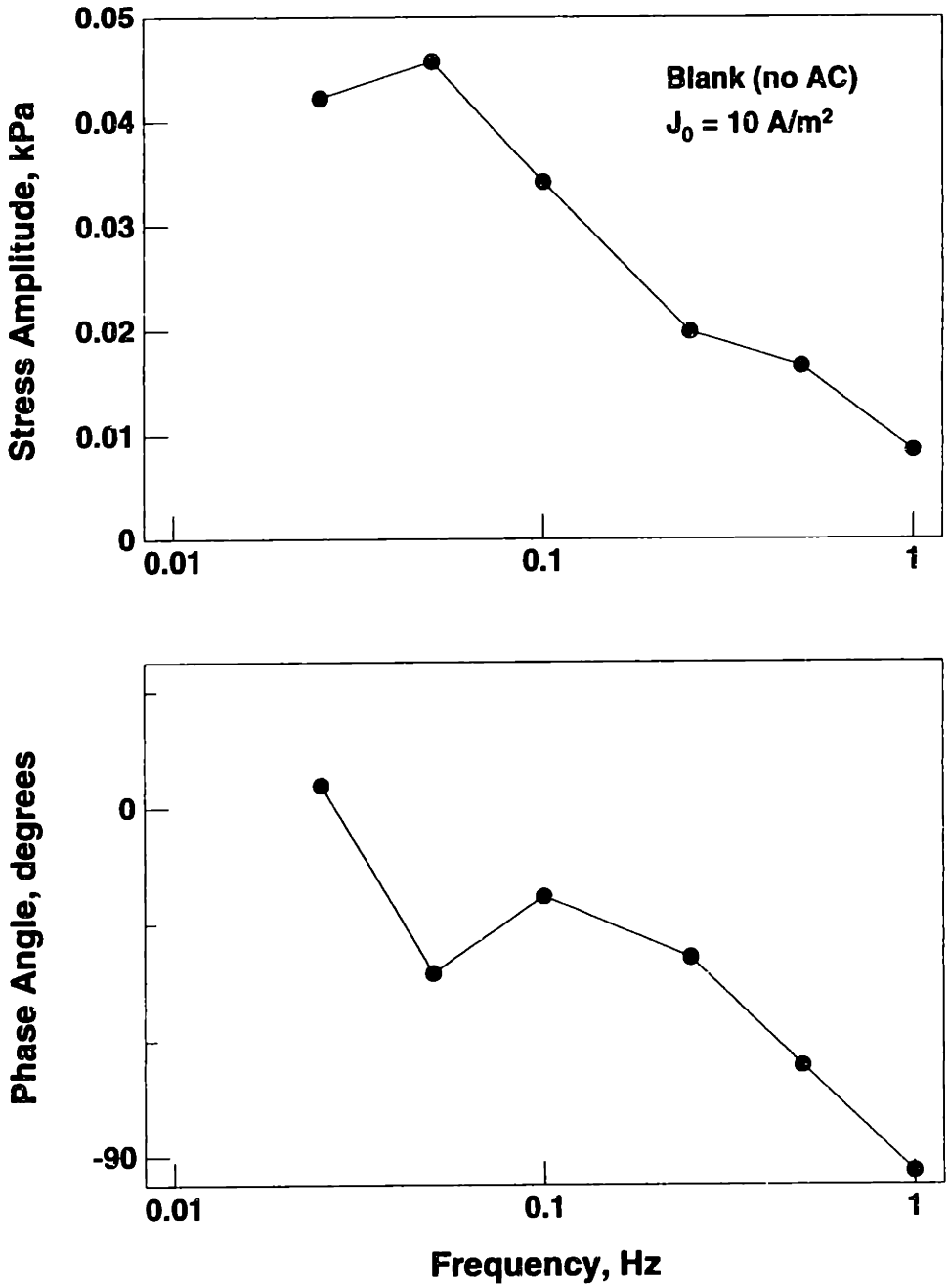

Figure C.4: Response of two-electrode surface probe with bath solution, but *no* cartilage, in chamber. A sinusoidal current density of 10 A/m^2 was applied to the excitation electrodes of the probe and the differential sensor output was recorded in the usual manner. A sinusoidal response was measured; however, the amplitude was only 10% of that typically measured with cartilage and exhibited different phase behavior. This non-zero response with no cartilage present could arise from electrocapillary effects at the electrode-bath interface.

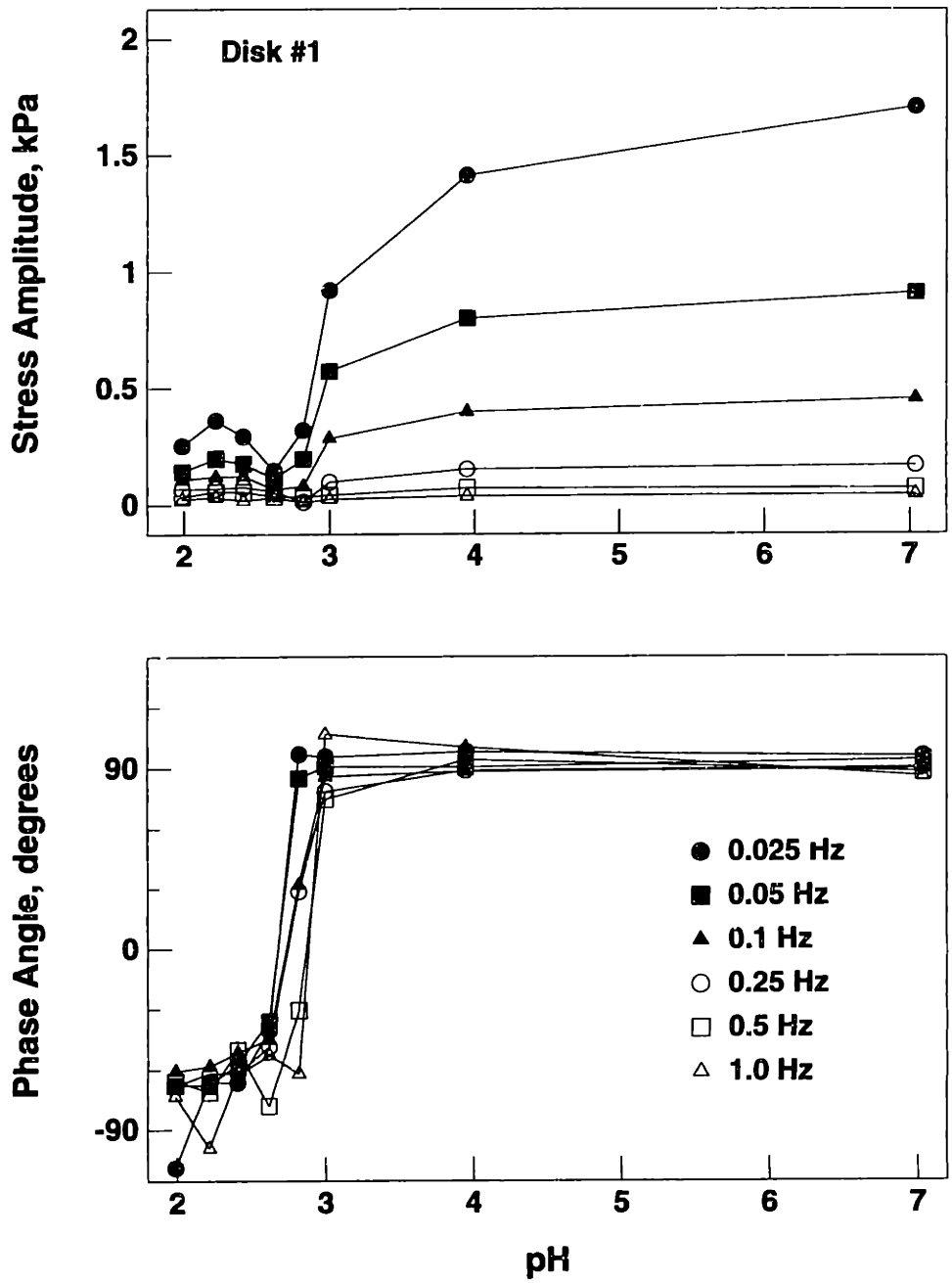

Figure C.5: Current-generated stress amplitude and phase (measured with two-electrode probe) vs. bath pH (adult bovine cartilage disk #1)

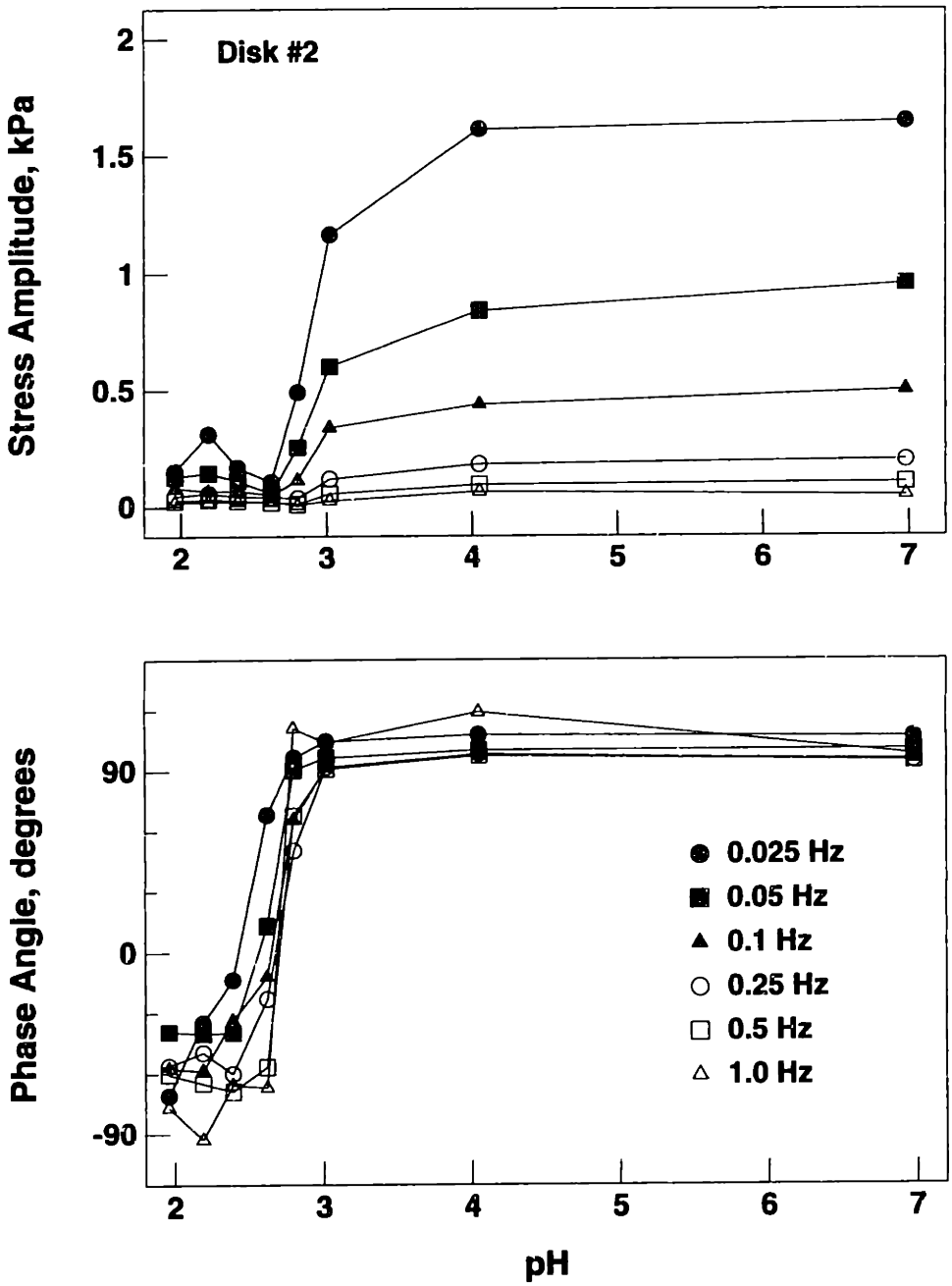

Figure C.6: Current-generated stress amplitude and phase (measured with two-electrode probe) vs. bath pH (adult bovine cartilage disk #2)

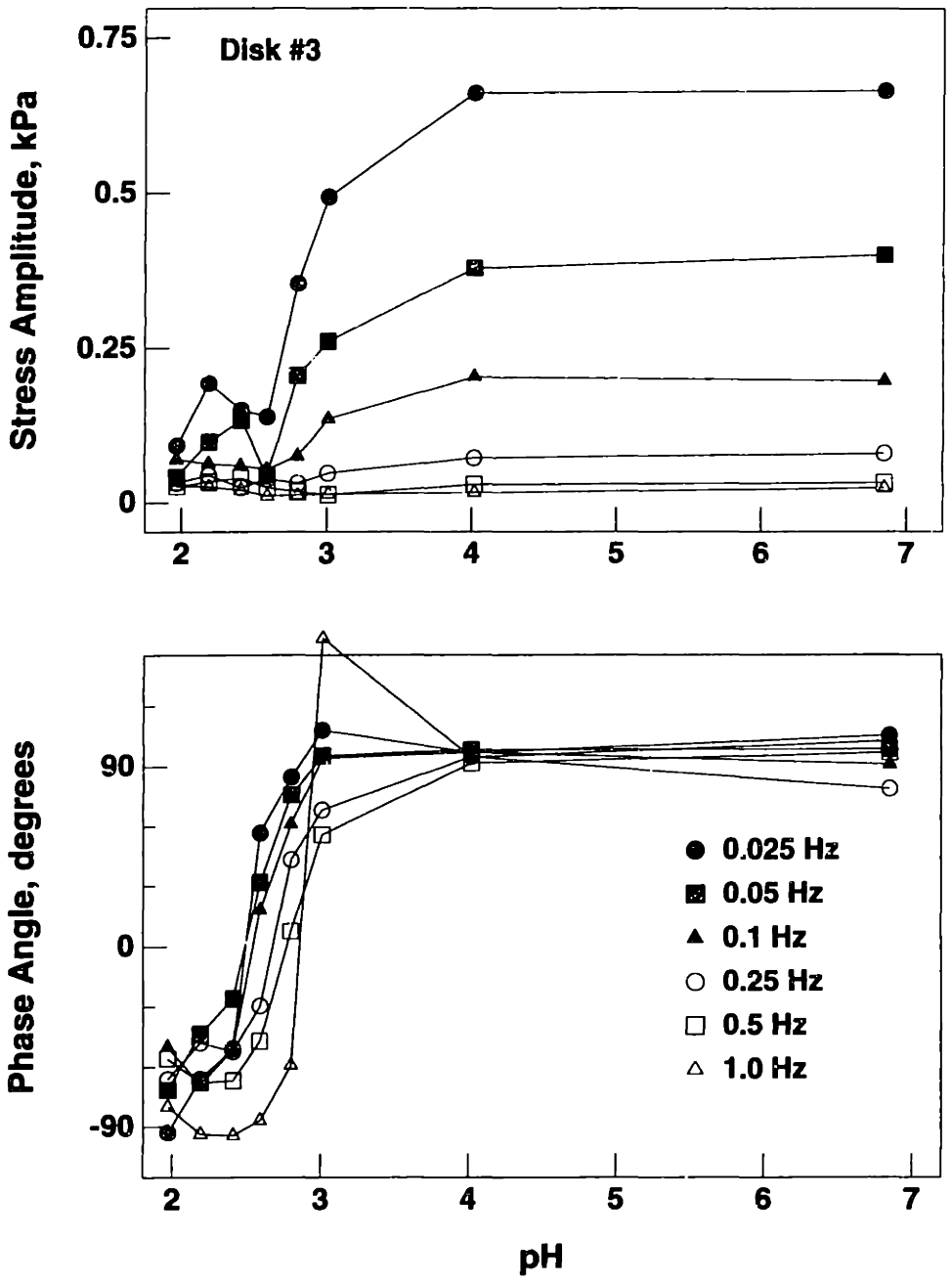

Figure C.7: Current-generated stress amplitude and phase (measured with two-electrode probe) vs. bath pH (adult bovine cartilage disk #3)

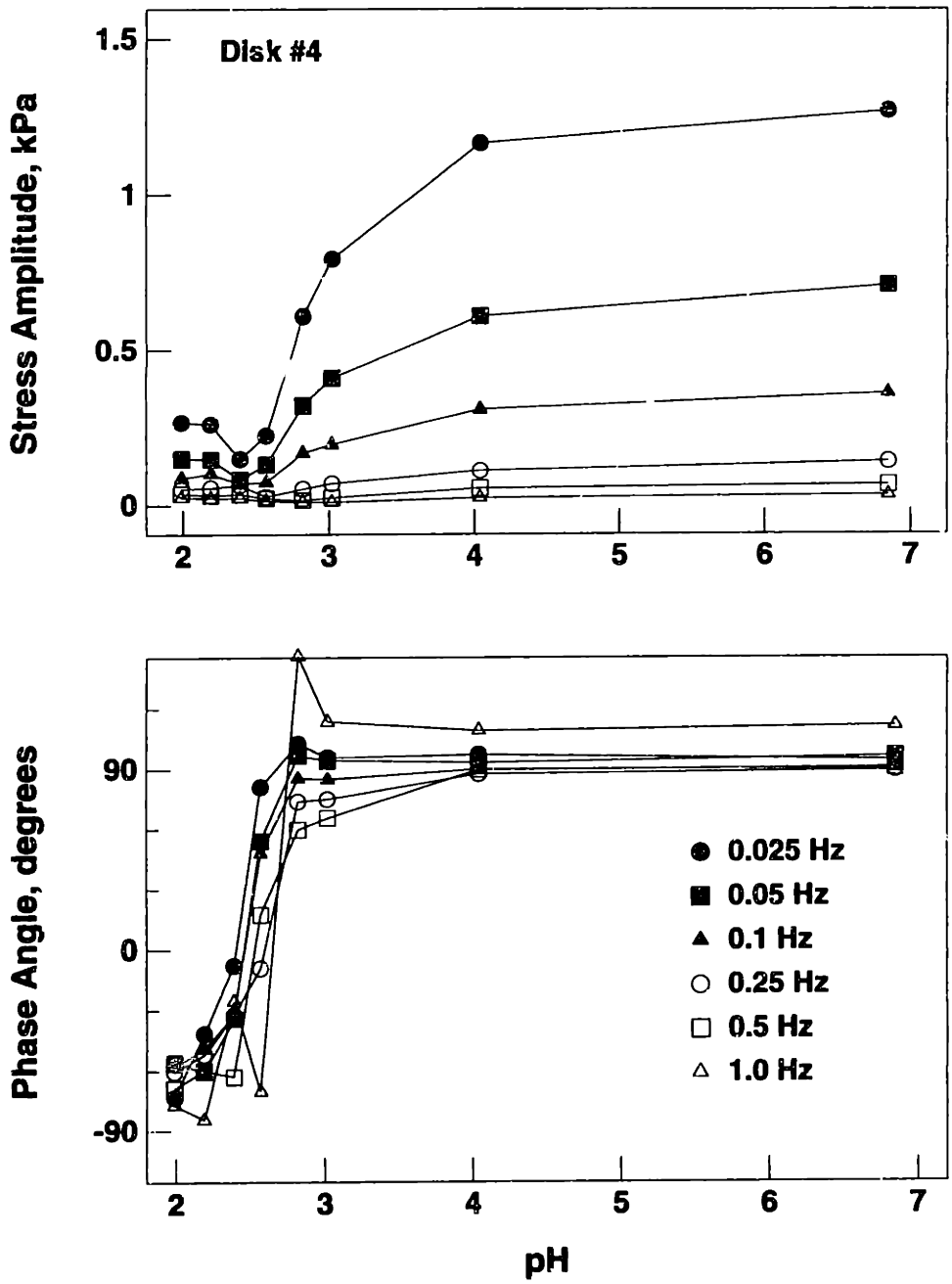

Figure C.8: Current-generated stress amplitude and phase (measured with two-electrode probe) vs. bath pH (adult bovine cartilage disk #4)

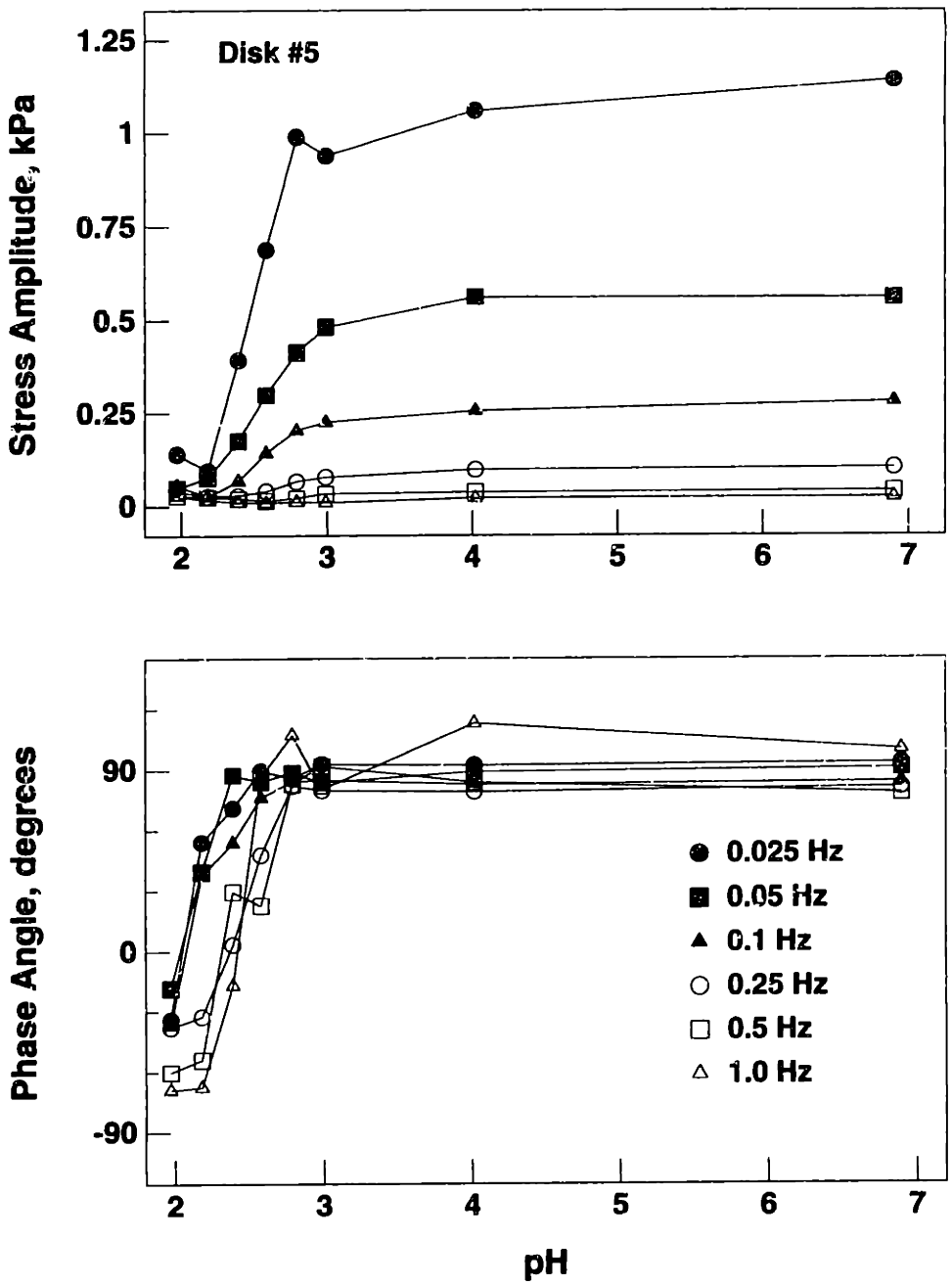

Figure C.9: Current-generated stress amplitude and phase (measured with two-electrode probe) vs. bath pH (adult bovine cartilage disk #5)

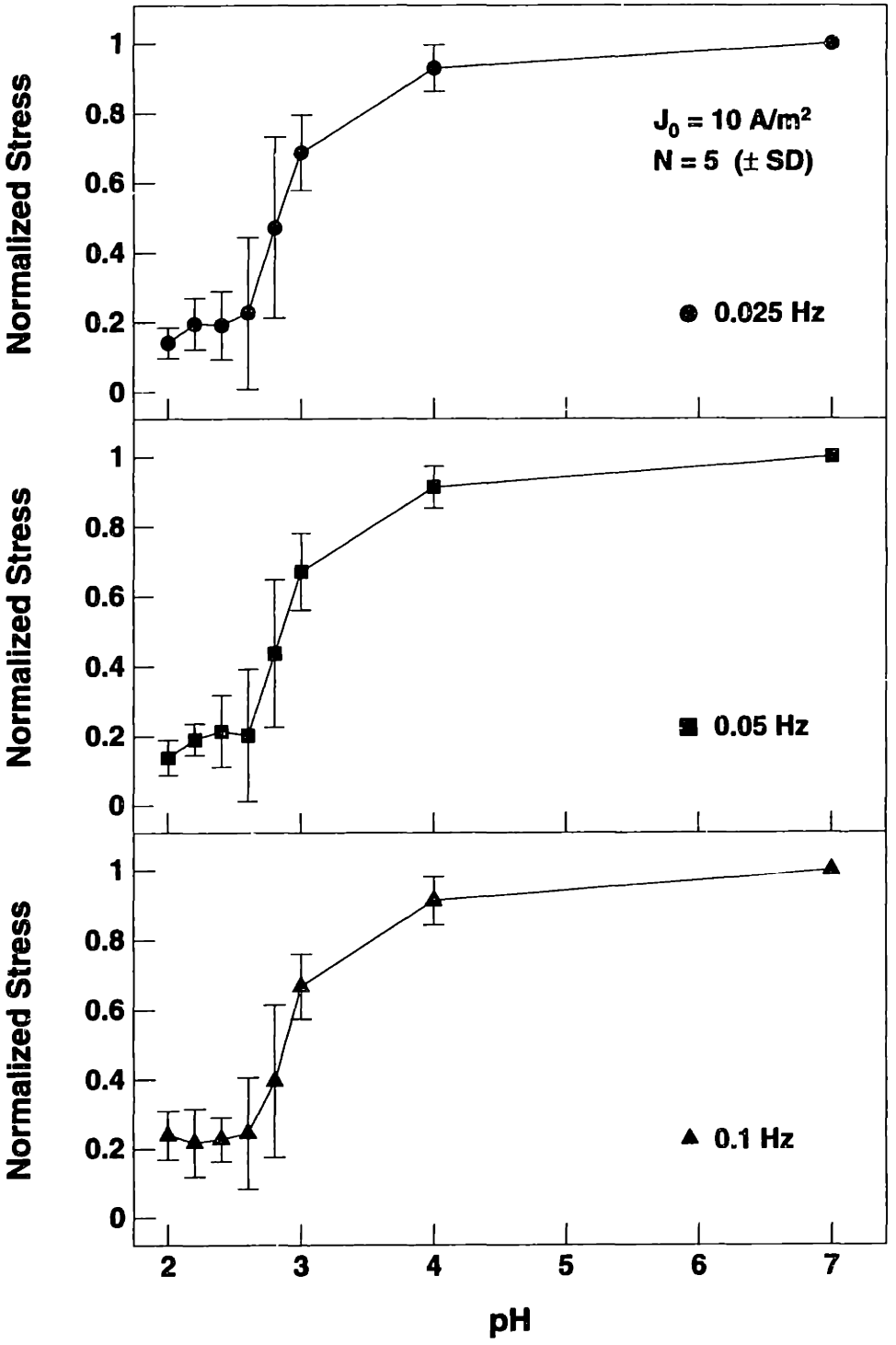

Figure C.10: Current-generated stress amplitude (measured with two-electrode probe) vs. bath pH, normalized to response at pH 7, at frequencies of 0.025 Hz (circles, top), 0.05 Hz (squares, middle), and 0.1 Hz (triangles, bottom). All data points are mean ± SD for 5 disks.

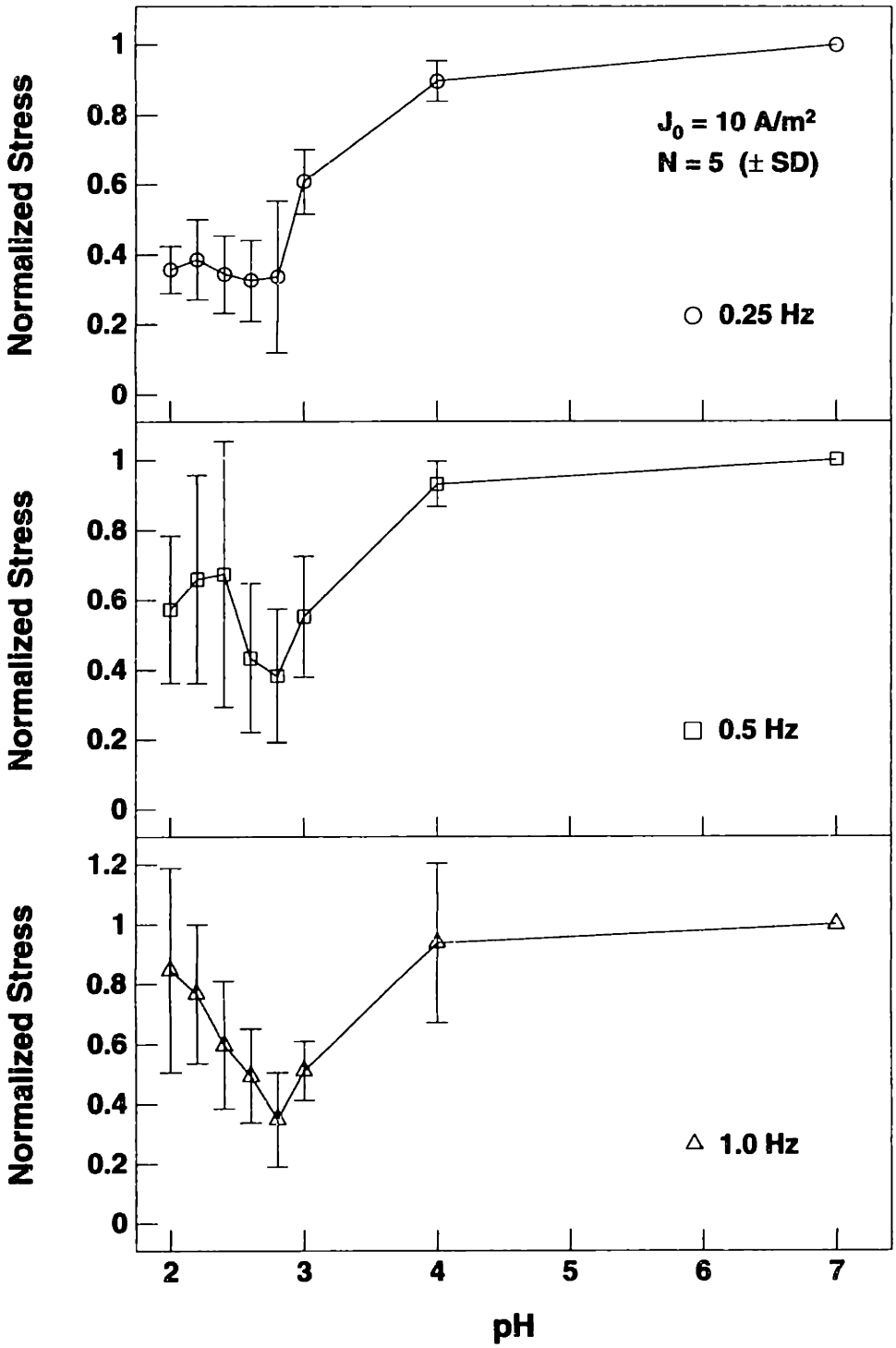

Figure C.11: Current-generated stress amplitude (measured with two-electrode probe) vs. bath pH, normalized to response at pH 7, at frequencies of 0.25 Hz (circles, top), 0.5 Hz (squares, middle), and 1 Hz (triangles, bottom). All data points are mean ± SD for 5 disks.

surface [160]. Thus, the deeper regions of the tissue, having a higher fixed charge density (FCD), require a higher hydrogen ion concentration (i.e., lower pH) to achieve complete neutralization, while the more superficial region in contact with the probe electrodes has a higher IEP since the local FCD is lower. Electrokinetic measurements made with either the surface probe or in uniaxial compression, therefore, reflect aggregate material parameters, averaged over the entire inhomogeneous tissue. Since high-frequency excitations have a shorter mechanical diffusion depth, they will preferentially sense the stress developed near the surface of the tissue and thus exhibit a higher apparent IEP.

An alternative hypothesis is that the change in frequency dependence (from f^{-1} to $f^{-1/2}$) is due to pH-dependent changes in tissue material properties. With the two-electrode probe, both the measured and theoretical stress amplitudes vary inversely with frequency for frequencies above a transition value that is proportional to the product of the equilibrium modulus, H_A, and the permeability, k_{11}, while at lower frequencies, the stress amplitude is independent of frequency (see Appendix F). In normal tissue at pH 7, this transition occurs at approximately 10^{-4} Hz. Changing the frequency response would require increasing this transition frequency, with a corresponding change in the $H_A k_{11}$ product, by two orders of magnitude. This, in turn, would require a significant increase in the permeability (secondary to an increase in the effective pore size of the tissue), as the equilibrium modulus would only be expected to *decrease* as a result of neutralizing tissue fixed charge groups. As the transition frequency is approached, the phase angle would also be expected to approach zero, and the stress amplitude would plateau. However, in all five plugs tested, the phase passed through zero and continued decreasing toward $-90°$, while the stress amplitude at all frequencies *increased* as the pH was lowered beyond the IEP. Thus, the behavior seen with the probe measurements is not consistent with the expected change in frequency response due to changes in tissue permeability and modulus.

C.2.2 Kinetics and Reversibility

To assess the kinetics and reversibility of changes in current-generated stress produced by titration of bath pH, an additional experiment was performed (Figure C.12). Bath pH was lowered, following pre-equilibration, from 7.0 to 2.3 by addition of a single 400 μl aliquot of 1 N HCl. Current-generated stress was then measured every hour for 4 hours, at which time 400 μl of 1 M NaOH was added to increase the pH back beyond the IEP. Since the bath pH had only increased to 3.8 by one hour after adding the NaOH, an additional 100 μl of NaOH was added at that time to yield a bath pH of 5.5, which remained approximately constant until the experiment was terminated four hours later (Figure C.12, bottom). After addition of HCl, the stress amplitude decreased, reaching a minimum approximately one hour after addition of the HCl, then increased, with larger relative increases occurring at higher frequencies (Figure C.12, top). At all frequencies, the phase shifted by 180°; this shift occurred earlier at higher frequencies. These results are consistent with the frequency dependence of the IEP seen in the incremental titration experiments described above. Following addition of the NaOH, the stress amplitude again decreased toward the minimum value and the phase underwent a 180° shift in the opposite direction. However, by the end of the experiment, the stress amplitudes at all frequencies had returned to only 20% of their original values, and the phase shift was not complete for the higher frequencies (Figure C.12, middle). Biochemical analysis of the disk and bath revealed that only 8.9% of the GAG in the tissue was extracted during the 10-hour course of the experiment.

Figure C.12 suggests that the internal pH of the AC disk had reached its aggregate IEP within one hour after addition of HCl; the subsequent increase in amplitude and 180° phase shift indicate that the internal pH had decreased below the IEP. The effect was reversible by addition of NaOH, but with a much slower time course. The asymmetric time course observed in this experiment reflects the kinetics of the combined diffusion-reaction process which governs the distribution of hydrogen ions in the matrix [86,87]. This asymmetry has been described previously in uniaxial streaming potential measurements with cartilage [66] as well as in chemically induced swelling and shrinking of polyelectrolyte

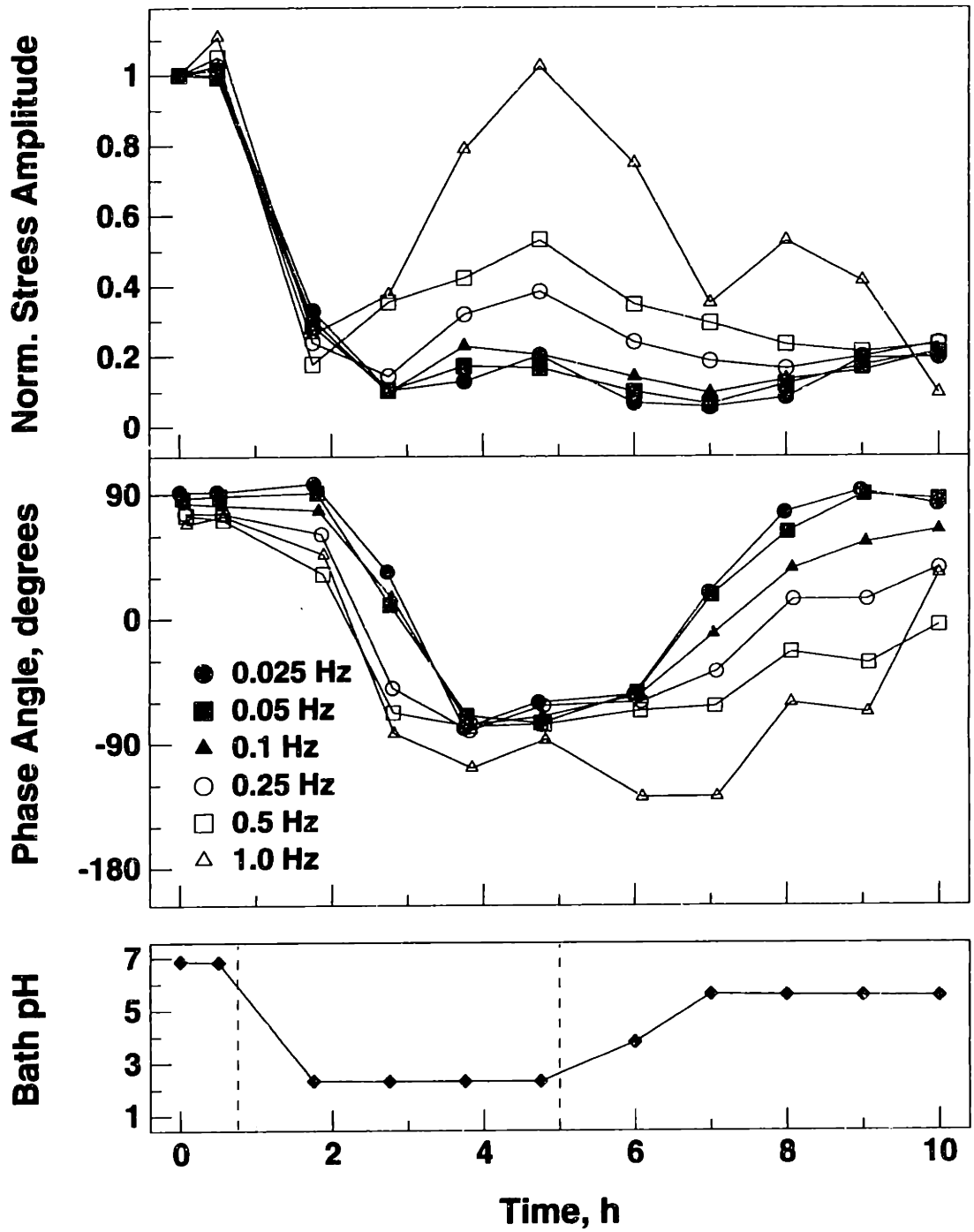

Figure C.12: Current-generated stress amplitude (normalized to initial response) and phase versus time for an adult bovine AC disk, with a current density amplitude of 10 A/m^2. Bath pH was lowered from 7.0 to 2.3 in one step by addition of 1 *N* HCl (left dashed line in bottom plot). At t = 5 h, pH was titrated back toward neutral by addition of 1 *M* NaOH (right dashed line).

gel membranes [86]. The reversibility of the process is consistent with the hypothesis that the decrease in stress produced by decreasing pH results from *neutralization* of matrix charge groups rather than loss of charged GAG residues from the tissue. This conclusion is also supported by the finding of negligible GAG loss from the tissue (Figure 2.7). Although PG aggregates have been shown to dissociate at low pH [94], no evidence of this effect was found in the present study.

C.3 Effect of Trypsin Digestion on Current-Generated Stress

Enzymatic digestion of four adult bovine cartilage disks (800 μm thick), using the protocol described in Section 2.3.6, resulted in a progressive decrease in measured stress amplitude (Figures C.13–C.16). As a control, three additional disks were maintained in the chamber for 20 h with protease inhibitors (as described in Section B.4) added to the bath instead of trypsin (Figure C.17). At all frequencies, trypsin digestion for 20 h resulted in a 65–75% decrease in stress amplitude relative to the stress measured just prior to addition of the enzyme (Figure C.18, solid bars); in contrast, the controls showed only a 7–30% decrease in stress amplitude over the same time course (Figure C.18, open bars)[1]. No significant variation of normalized stress with frequency was found (by ANOVA) in either the trypsin-digested disks or controls. The phase angle of the measured stress remained constant at approximately 90° throughout digestion for low-frequency excitation but diverged from 90° with increasing duration of digestion for higher frequencies (Figures C.13–C.16). Similar behavior of both stress amplitude and phase vs. time were also observed in a single disk (1 mm thick) of calf cartilage subjected to the same trypsin digestion protocol (Figure C.19).

Hydration and GAG content of the trypsin-digested disks, controls (with added protease inhibitors), and uncompressed control disks were determined and compared with the values for the corresponding annular rings (Figure C.20). Preparation of the disks,

[1] The data at $f = 0.025$ Hz in Figure C.18 also appear as the 20 h data points (circles) in Figure 2.8.

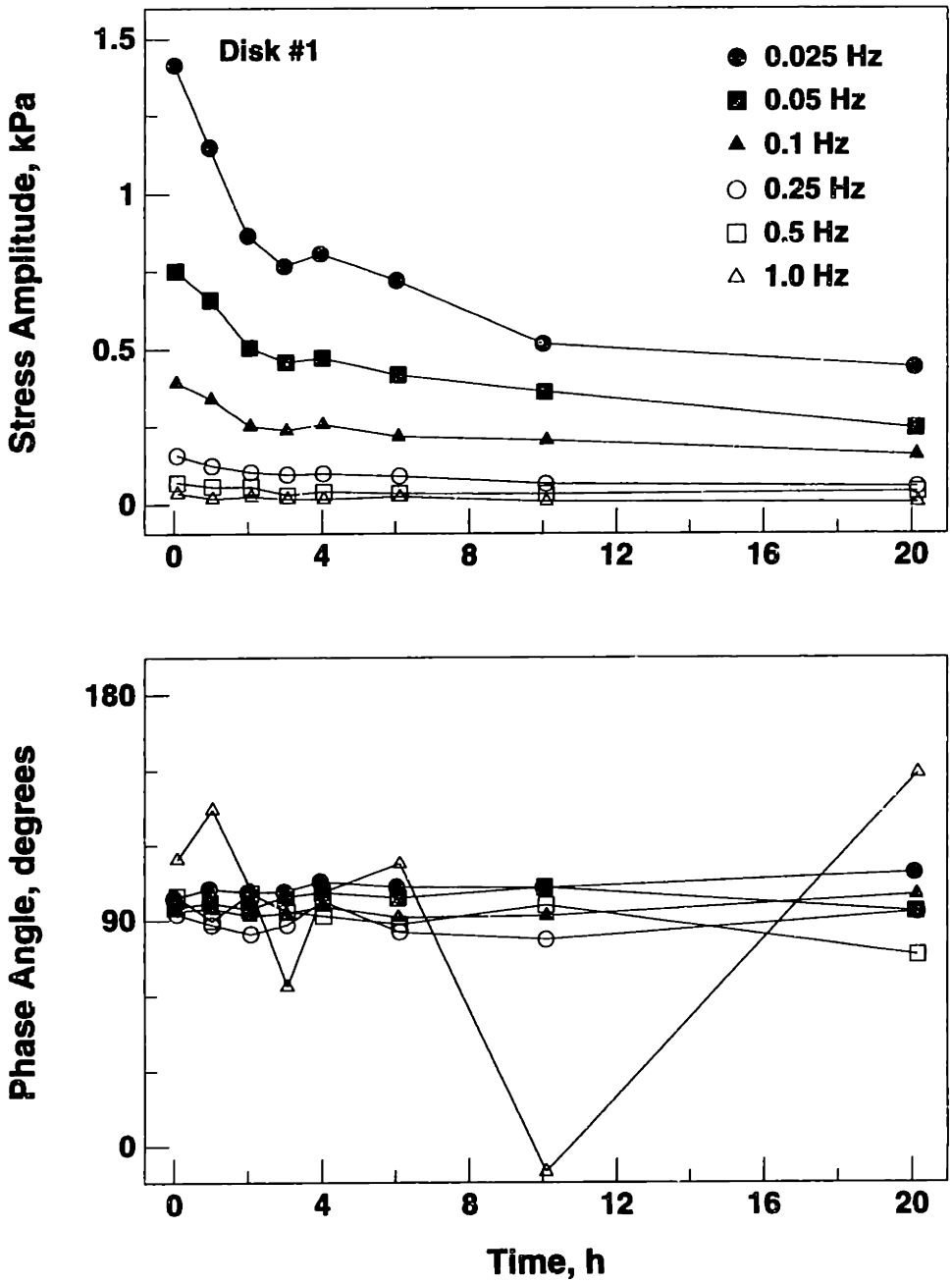

Figure C.13: Current-generated stress amplitude and phase (measured with two-electrode probe) vs. time after addition of trypsin (adult bovine cartilage disk #1)

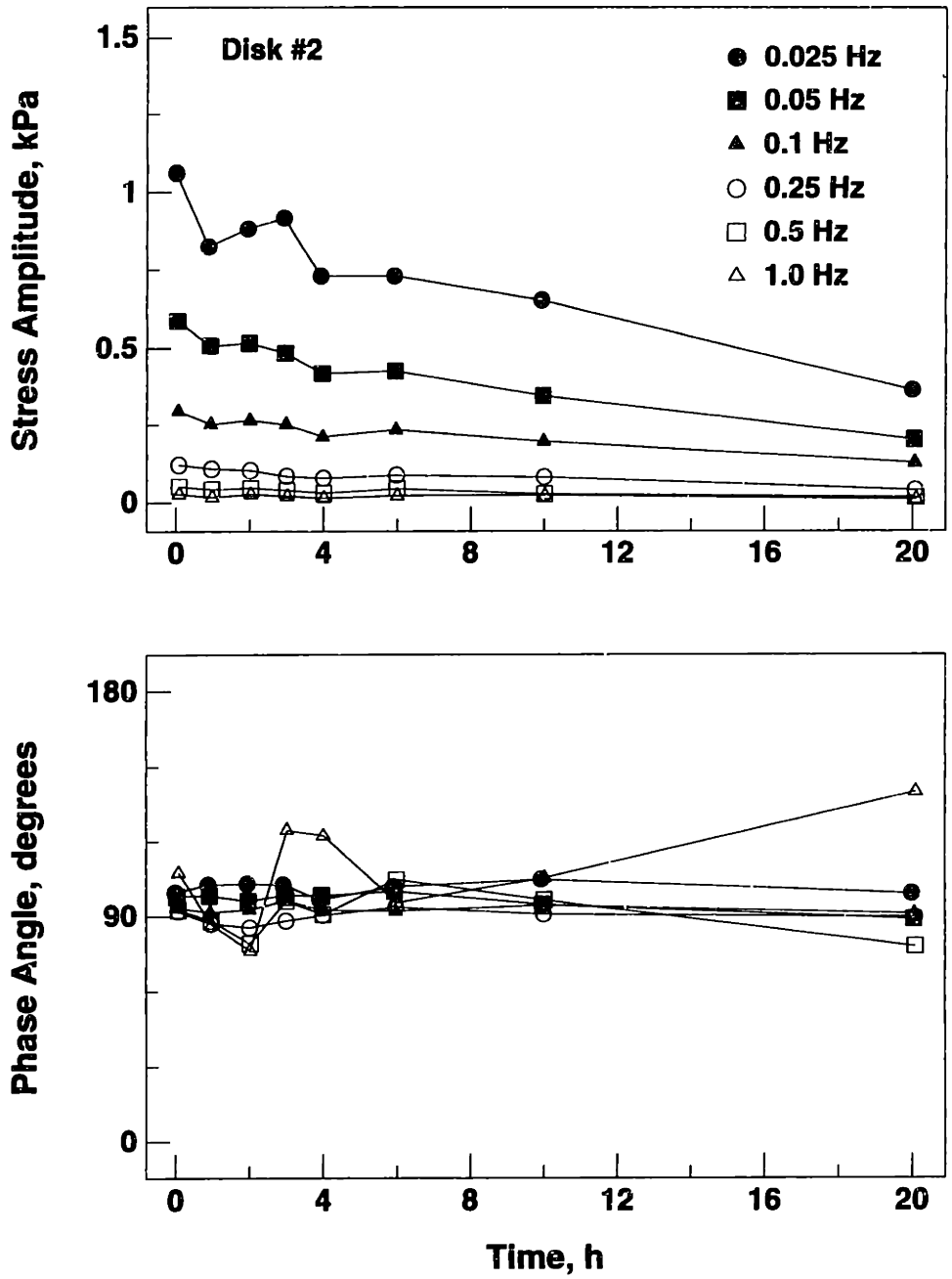

Figure C.14: Current-generated stress amplitude and phase (measured with two-electrode probe) vs. time after addition of trypsin (adult bovine cartilage disk #2)

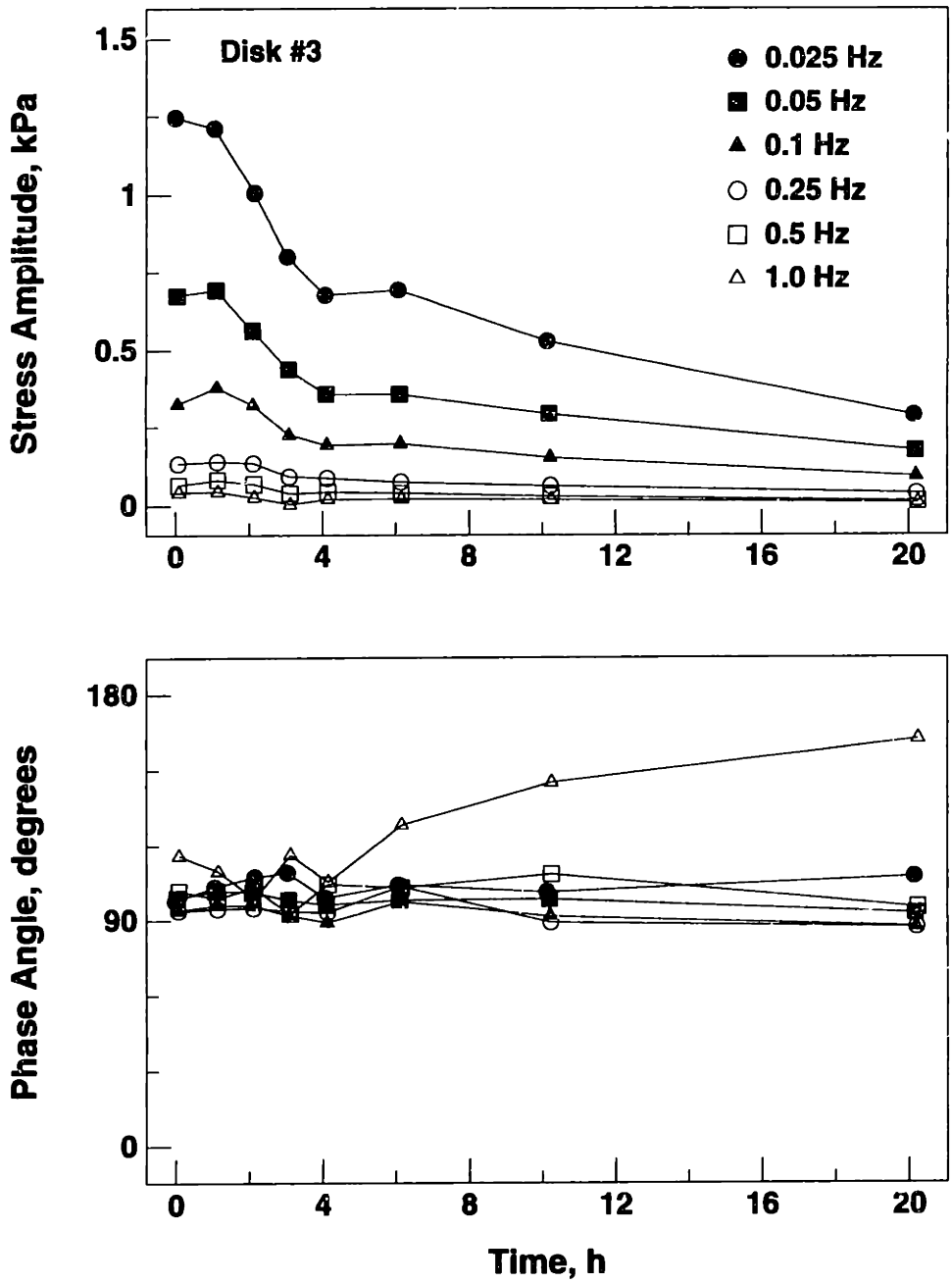

Figure C.15: Current-generated stress amplitude and phase (measured with two-electrode probe) vs. time after addition of trypsin (adult bovine cartilage disk #3)

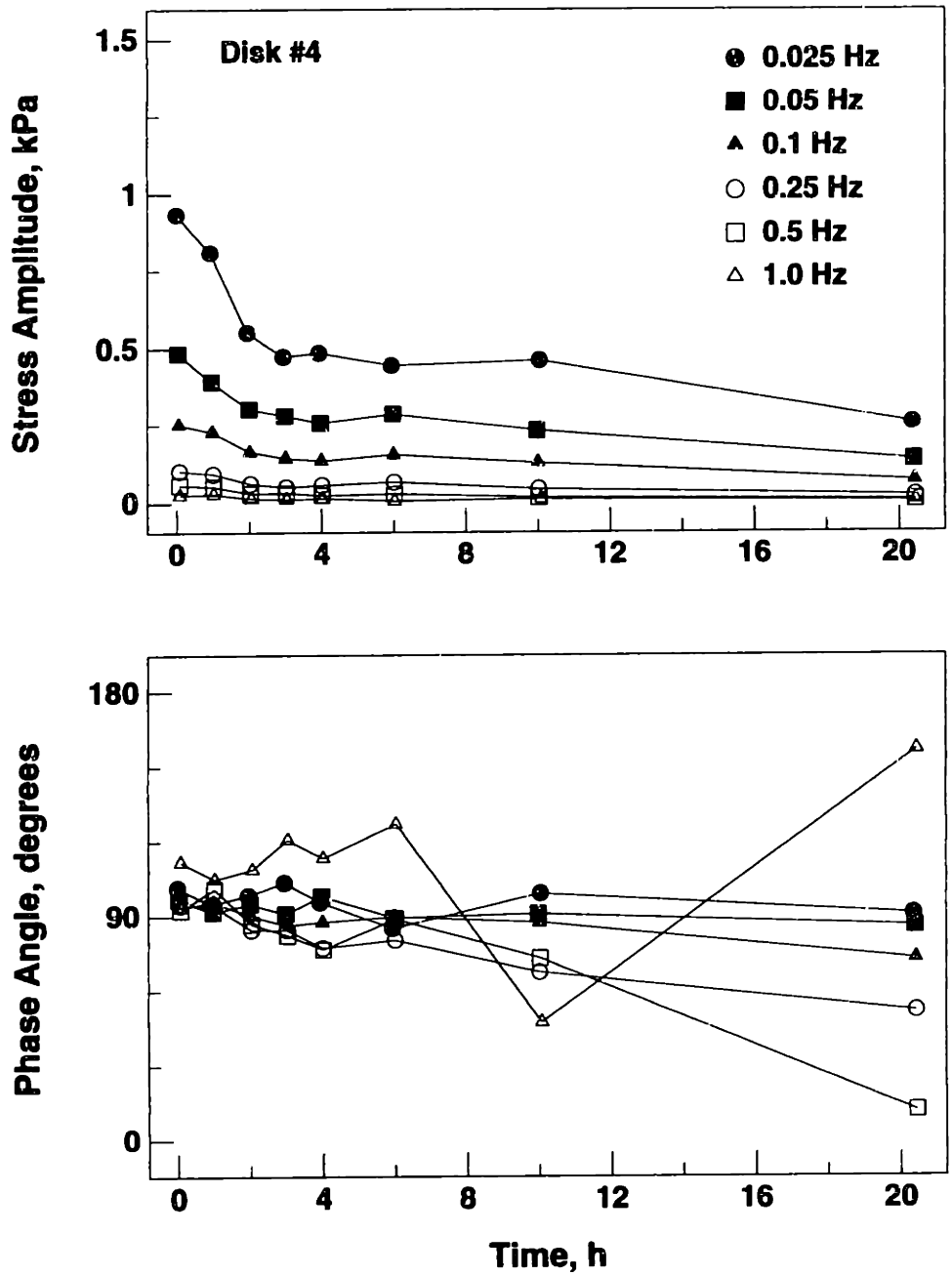

Figure C.16: Current-generated stress amplitude and phase (measured with two-electrode probe) vs. time after addition of trypsin (adult bovine cartilage disk #4)

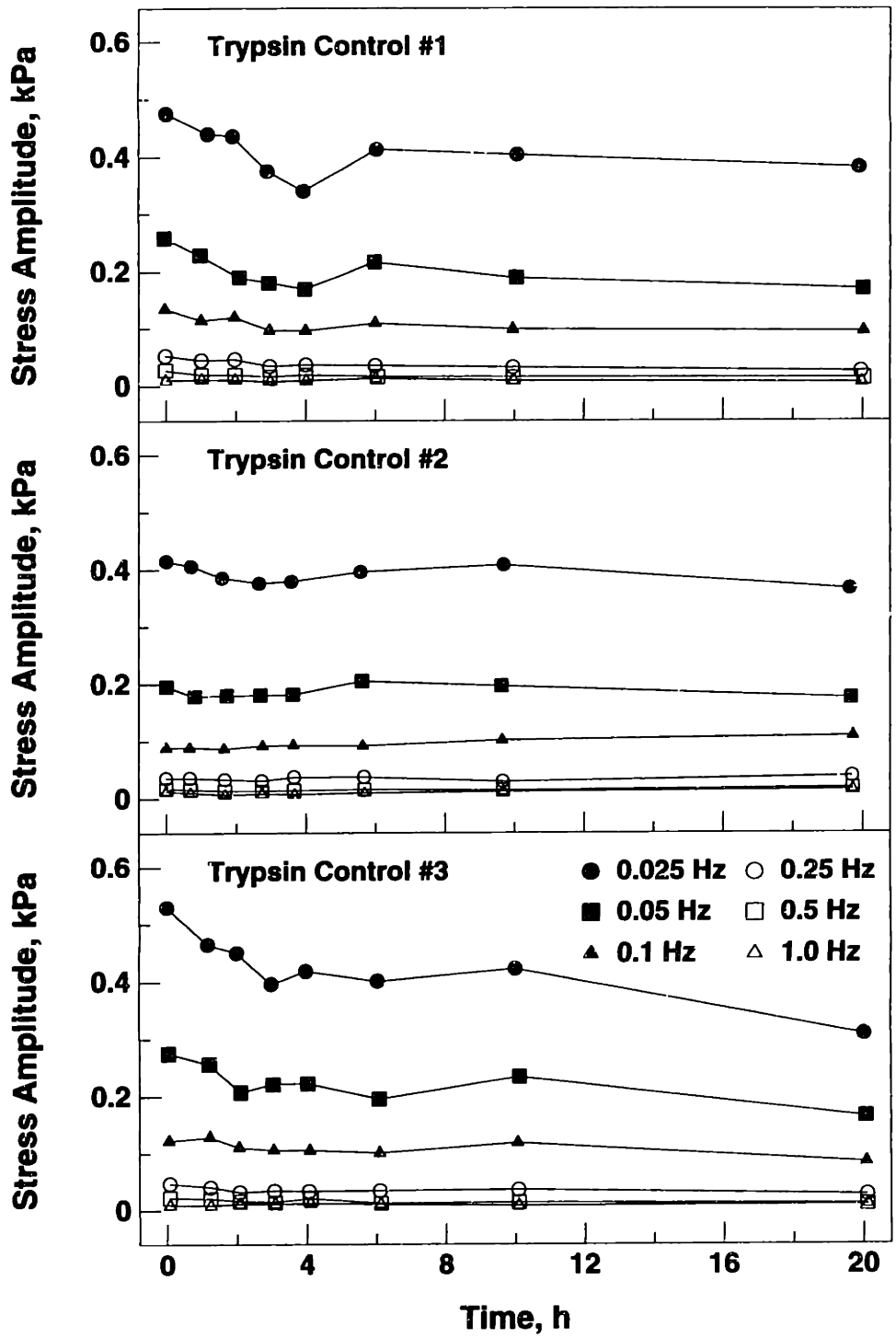

Figure C.17: Current-generated stress amplitude (measured with two-electrode probe) vs. time in chamber measured in 3 adult bovine disks (trypsin controls). Protease inhibitors were added to the bath instead of enzyme.

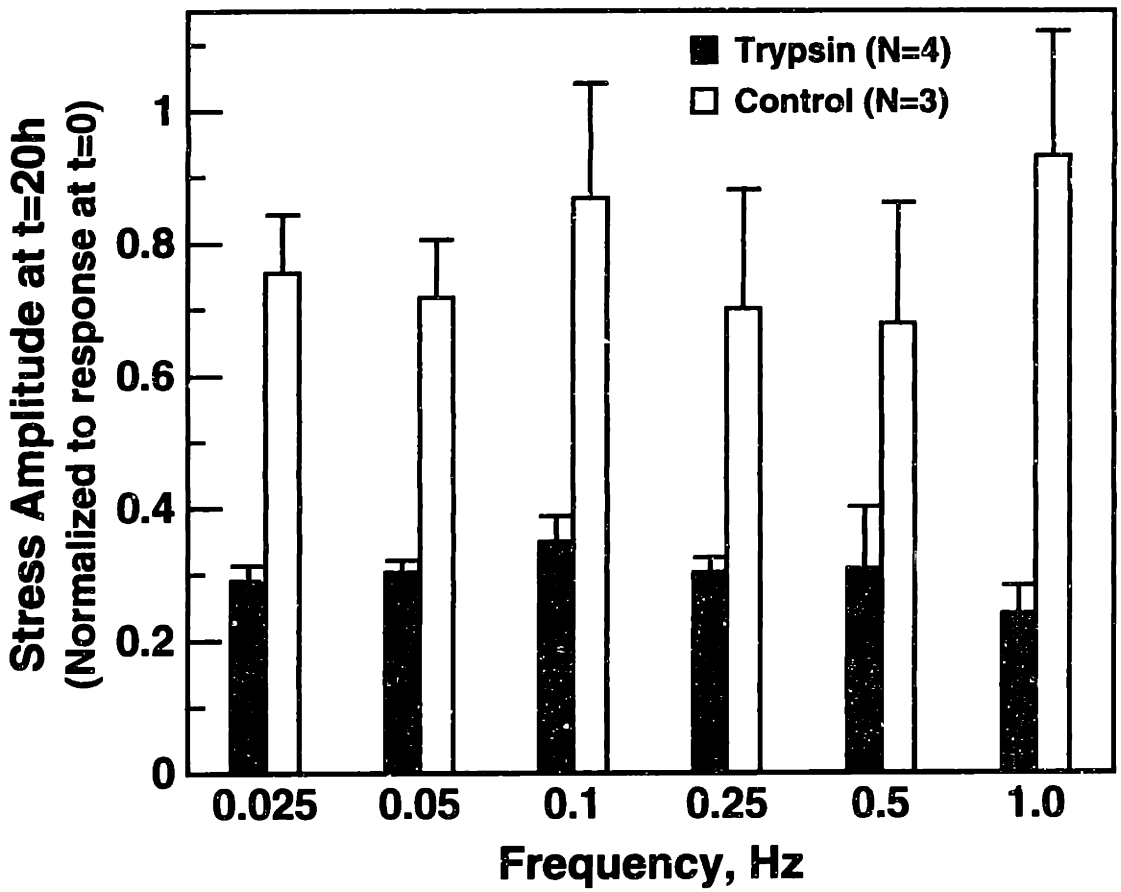

Figure C.18: Stress amplitude (measured with two-electrode probe) after 20 h of trypsin digestion (N = 4, solid bars) or 20 h of exposure to protease inhibitors (N = 3, open bars), normalized to response at t = 0. All data points are mean ± SEM. For both trypsin-digested disks and controls, normalized stress amplitude did not vary significantly with frequency (by ANOVA).

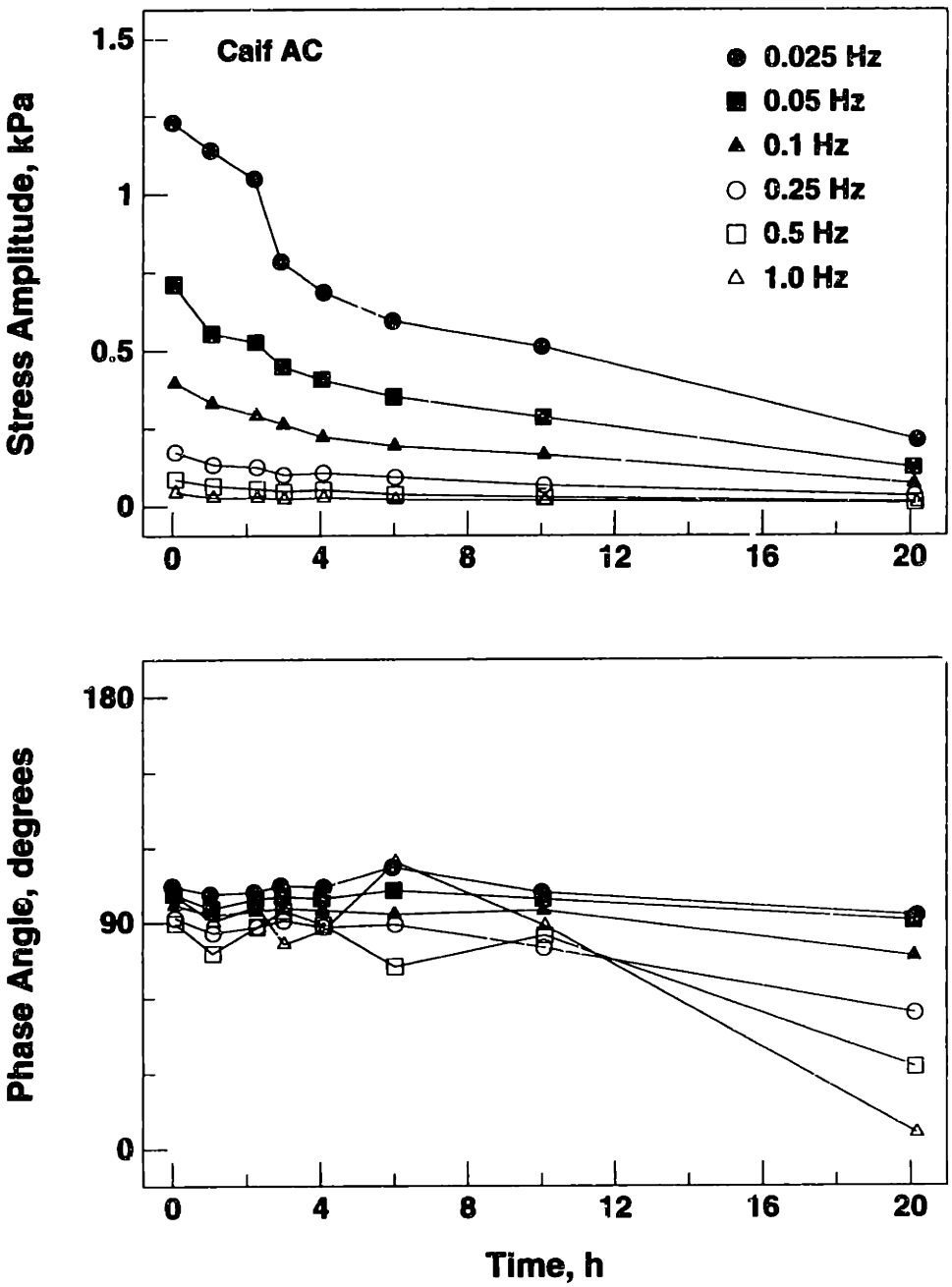

Figure C.19: Current-generated stress amplitude and phase vs. time after addition of trypsin (1 mm thick calf cartilage disk)

rings, and uncompressed controls is described in Sections 2.3.2 and 2.3.7. No significant difference in hydration (defined as water : solid ratio) was found (by ANOVA) between any of the groups of disks and their corresponding rings (Figure C.20A); however, the hydration of the trypsin-digested disks was 37% higher than the uncompressed control disks (3.10 ± 0.18 vs. 2.27 ± 0.05, $p < 0.025$) and the hydration of the trypsin-free control disks was 55% higher than the uncompressed controls (3.51 ± 0.50 vs. 2.27 ± 0.05, $p < 0.05$). Because the disks that were tested in the chamber (both trypsin-digested and trypsin-free controls) were thawed, tested, and then re-frozen, while the uncompressed control disks were thawed immediately before the assays were performed, the increased hydration of the disks in the chamber as compared with the uncompressed controls may represent damage to the collagen component of the extracellular matrix resulting from the additional thawing and re-freezing of these disks. The GAG content (as percentage of tissue dry weight) of the trypsin-digested disks was significantly lower than the corresponding rings ($1.03 \pm 0.19\%$ vs. $11.99 \pm 1.54\%$, $p < 0.005$ by ANOVA) and was also significantly lower than the control disks with added protease inhibitors ($11.57 \pm 1.45\%$, $p < 0.0005$) and uncompressed control disks ($8.54 \pm 0.58\%$, $p < 0.0005$). No significant differences in GAG content between disks and corresponding rings were found for either of the control groups.

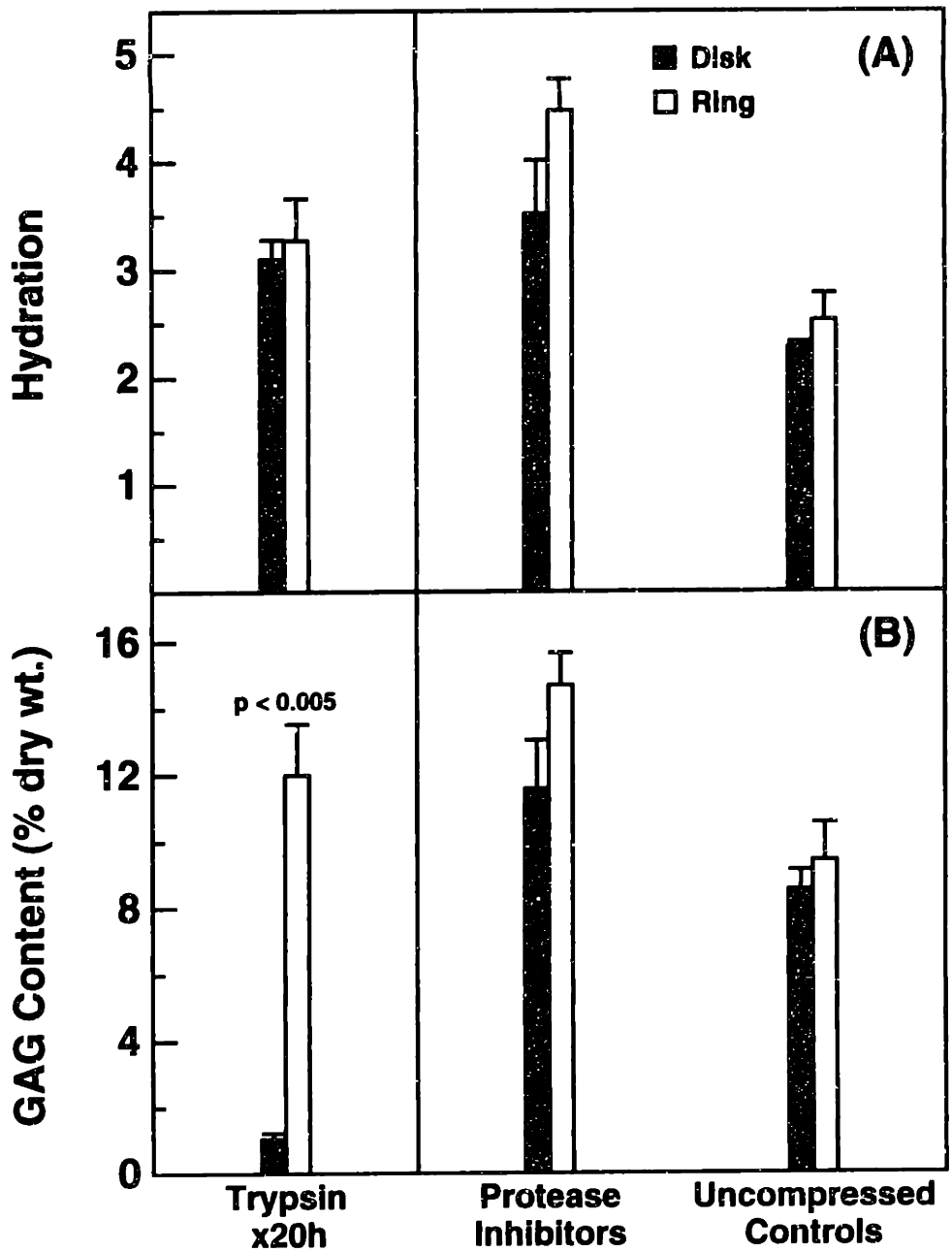

Figure C.20: Hydration (**A**) and GAG content (**B**) of adult bovine cartilage disks digested with trypsin for 20 h (N = 4), controls which were maintained in the chamber for 20 h with protease inhibitors (N = 3), and uncompressed controls (N = 4). GAG content of trypsin-digested disks was significantly lower than corresponding rings, trypsin-free control disks, and uncompressed control disks. Error bars indicate SEM; p value is for disks vs. rings (by ANOVA).

Appendix D

Supplemental Results: Surface Trypsin Digestion and Multiple-Wavelength Spectroscopy of Enzymatically Degraded Tissue

This appendix presents additional results pertaining to the model system for enzymatic extraction of proteoglycan from the surface of cartilage plugs and the multiple-wavelength probe experiments described in Chapter III. These results include further data related to the *spatial profile* of GAG content and hydration produced by surface trypsin digestion, estimation of the overall GAG loss from the digested region and the resulting change in electrical conductivity of the degraded tissue, comparison of the *kinetics* of GAG extraction with a theoretical one-dimensional diffusion model, and preliminary comparison of the collagen content of normal and trypsin-digested tissue (as determined by a colorimetric hydroxyproline assay). In addition, further studies using the multiple-wavelength probe are presented, in which the device was tested with full-thickness plugs with and without an intact articular surface and before and after trypsin digestion for 1 h and 4 h.

D.1 Surface Trypsin Digestion Model

D.1.1 Surface Digestion Protocol

Cylindrical cartilage-bone plugs were mounted in a PMMA chamber (shown schematically in Figure D.1) as used previously in enzymatic digestion studies [175] but modified to accommodate 9.5 mm diameter plugs. Plugs were press-fit into 9.5 mm diameter holes in the top of the chamber such that the articular surface of each plug was approximately flush with the underside of the top of the chamber and was in contact with a 15 ml bath; thus, the enzyme could only penetrate into the cartilage, and degradation products could only leave the tissue, via the articular surface. Up to three plugs could be simultaneously

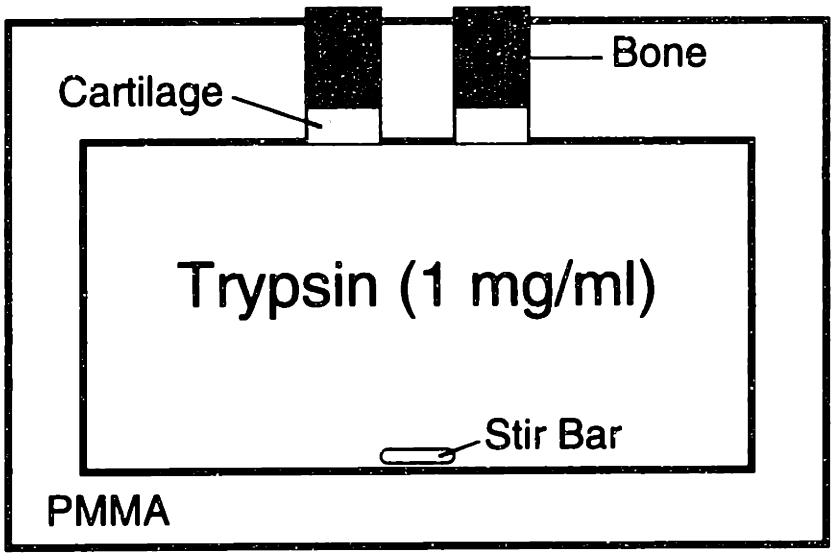

Figure D.1: Schematic illustration of PMMA chamber used to produce surface digestion of cartilage plugs with trypsin. Up to three plugs could be digested simultaneously. The 15 ml bath, containing 1 mg/ml bovine trypsin, was stirred continuously using a magnetic stirrer.

digested in this manner. The bath solution consisted of 0.1 *M* NaCl and 0.05 *M* Na_2HPO_4 at room temperature ($\sim$ 20°), adjusted to pH 7.2, as used previously in enzymatic extraction studies [44,66]; trypsin (type III from bovine pancreas, Sigma, St. Louis, MO) was added to the bath to achieve an enzyme concentration of 1 mg/ml. During digestion, the chamber was sealed using paraffin film (Parafilm) in order to prevent evaporation and the bath was continuously stirred using a magnetic stirrer.

D.1.2 Spatial Profile of GAG Content and Hydration

The spatial profile of PG loss produced by the trypsin digestion protocol was assessed by histological staining, using dimethylmethylene blue (DMB) dye during fixation [111], of cartilage-bone plugs that had been digested for 1, 4, 8, and 24 hours as well as an unexposed control plug. The histological fixation protocol is described in Section B.6 and in Chapter III. Surface digestion resulted in progressive loss of DMB staining, proceeding inward from the articular surface (Figure 3.3).

To quantify the spatial distribution of PG loss, the GAG content of sequential slices from plugs that had been digested for 1, 4, 8, and 24 h, as well as normal (undigested) controls, was determined using the DMB dye-binding assay described in Section B.5. Following trypsin exposure, plugs were mounted in a machined aluminum holder and sequential 200 μm thick slices were cut using a sledge microtome until either (1) 20 slices had been obtained (corresponding to a depth of 4 mm into the tissue) or (2) subchondral bone was reached. Although three plugs were simultaneously digested for each duration, one of the 1 h plugs became detached from the subchondral bone early in the course of microtoming and thus could not be used. The GAG content of each slice was computed as a percentage of both tissue wet weight and dry weight (Figures D.2–D.7). With one hour of trypsin digestion, GAG content was decreased by 30% at the surface but reached normal levels within 200–400 μm into the tissue (Figure D.8). In contrast, 24 h of surface trypsin digested resulted in nearly a 70% loss of GAG at the surface (Figure D.8), with a region of lower than normal GAG levels extending more than 3 mm into the tissue. The spatial profile of GAG content in *normal* tissue was nonuniform as well; GAG content increased from 2.45 $\pm$ 0.29% (15.50 $\pm$ 2.53%) of wet weight (dry weight) in the most superficial 200 μm slice to 4.90 $\pm$ 1.06% (24.24 $\pm$ 0.01%) in the 20th slice (Figure D.7). A similar nonuniform profile of GAG content versus depth, with the lowest concentration at the articular surface, has been reported for normal human femoral head cartilage [161]. Grossly, it was apparent while microtoming the plugs that the slices with decreased GAG content were more compliant than normal and also appeared more highly hydrated. Comparison of wet and dry weights confirmed that surface trypsin digestion resulted in an increase in tissue hydration (water : solid ratio), with the region of increased hydration extending further into the tissue with increasing time of enzyme exposure (Figure D.9).

D.1.3 Estimation of Overall GAG Loss

Based on the GAG assay results, the overall loss of GAG from the degraded regions produced by surface trypsin digestion could be estimated (Table D.1). Because the sequentially cut

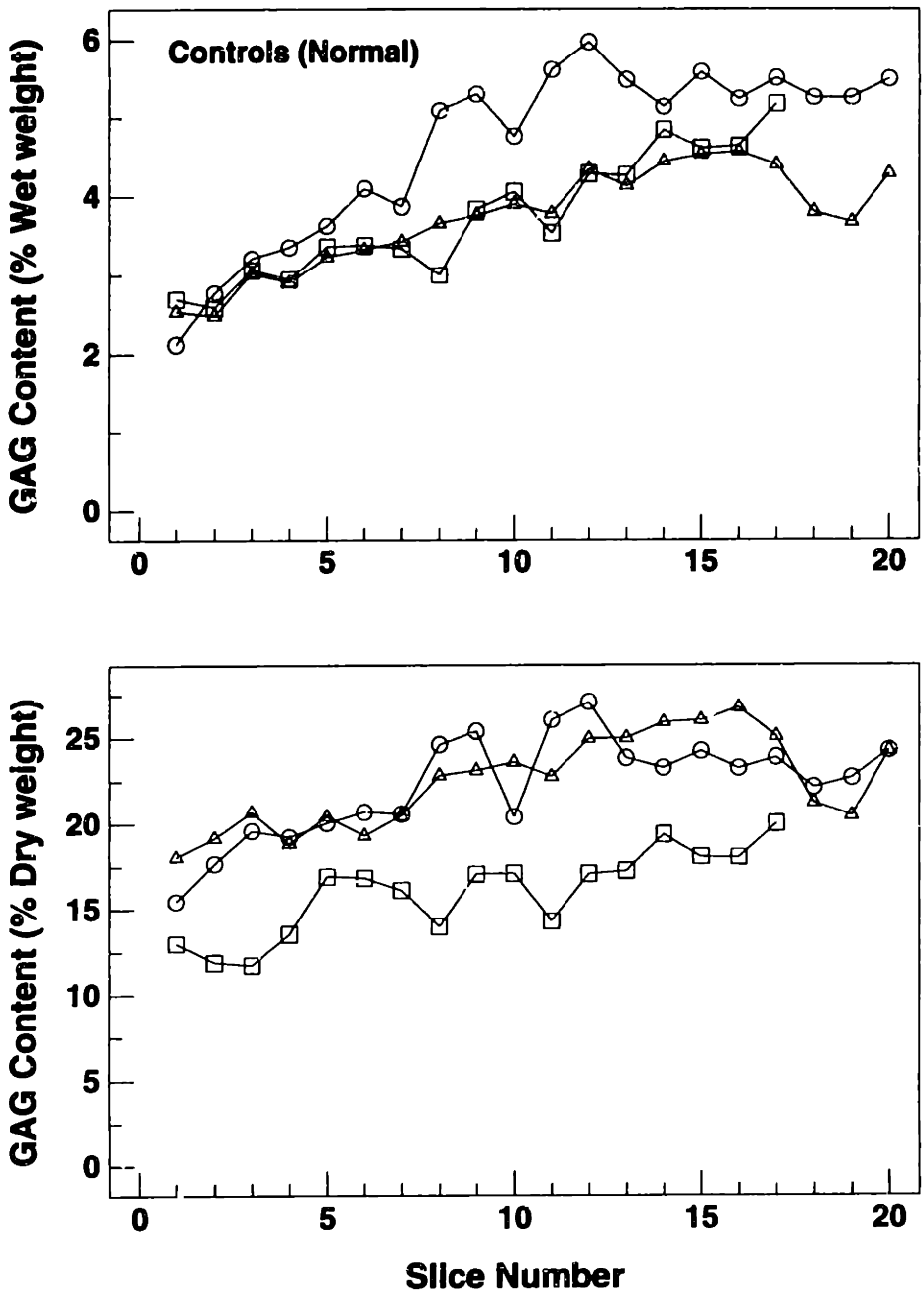

Figure D.2: GAG content of sequential 200 μm slices of normal (i.e., not exposed to trypsin) full-thickness cartilage plugs, as a percentage of tissue wet weight (top) and dry weight (bottom). Slice #1 is the most superficial.

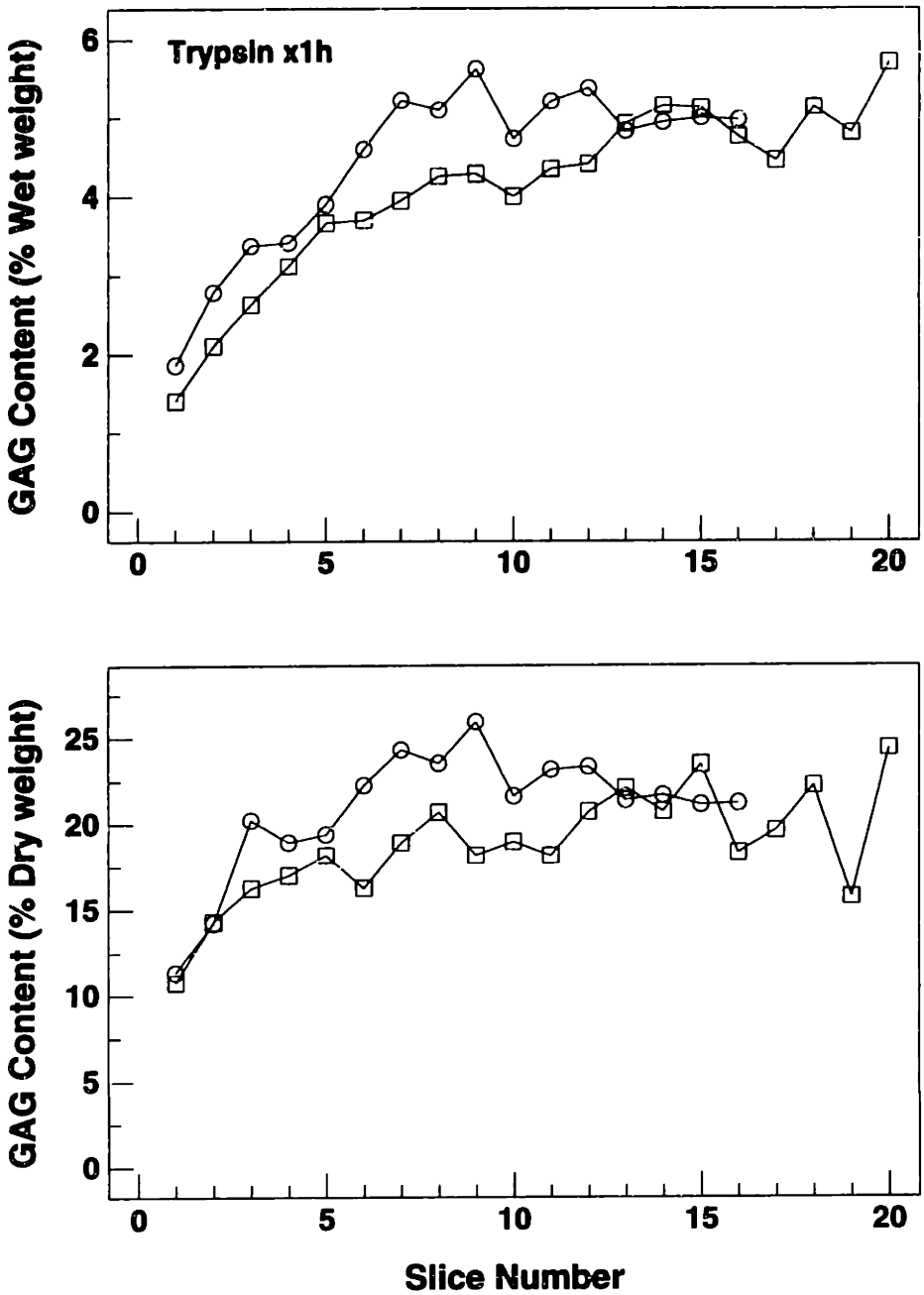

Figure D.3: GAG content of sequential 200 μm slices of full-thickness cartilage plugs digested with trypsin for 1 h, as a percentage of tissue wet weight (top) and dry weight (bottom). Slice #1 is the most superficial.

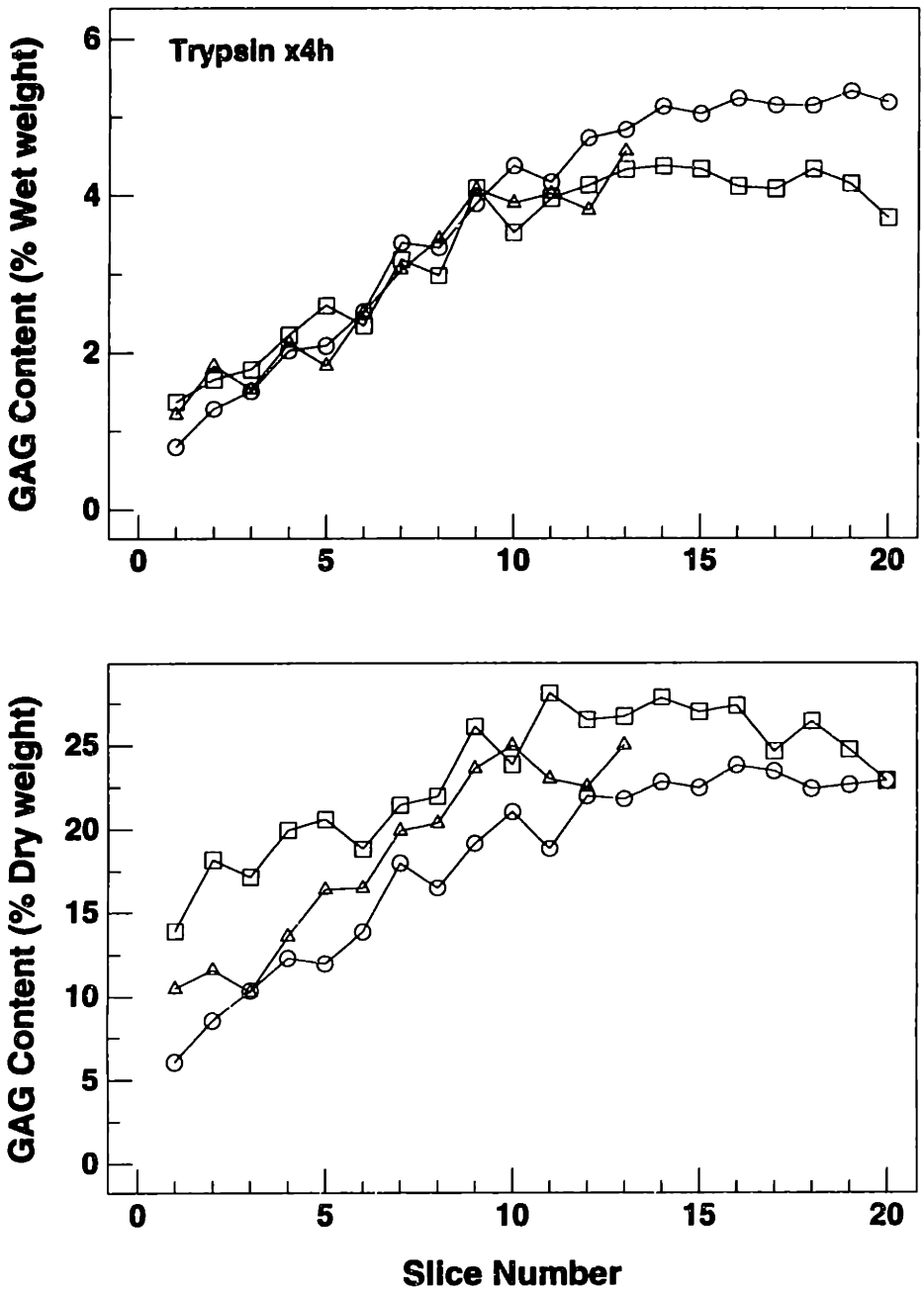

Figure D.4: GAG content of sequential 200 μm slices of full-thickness cartilage plugs digested with trypsin for 4 h, as a percentage of tissue wet weight (top) and dry weight (bottom). Slice #1 is the most superficial.

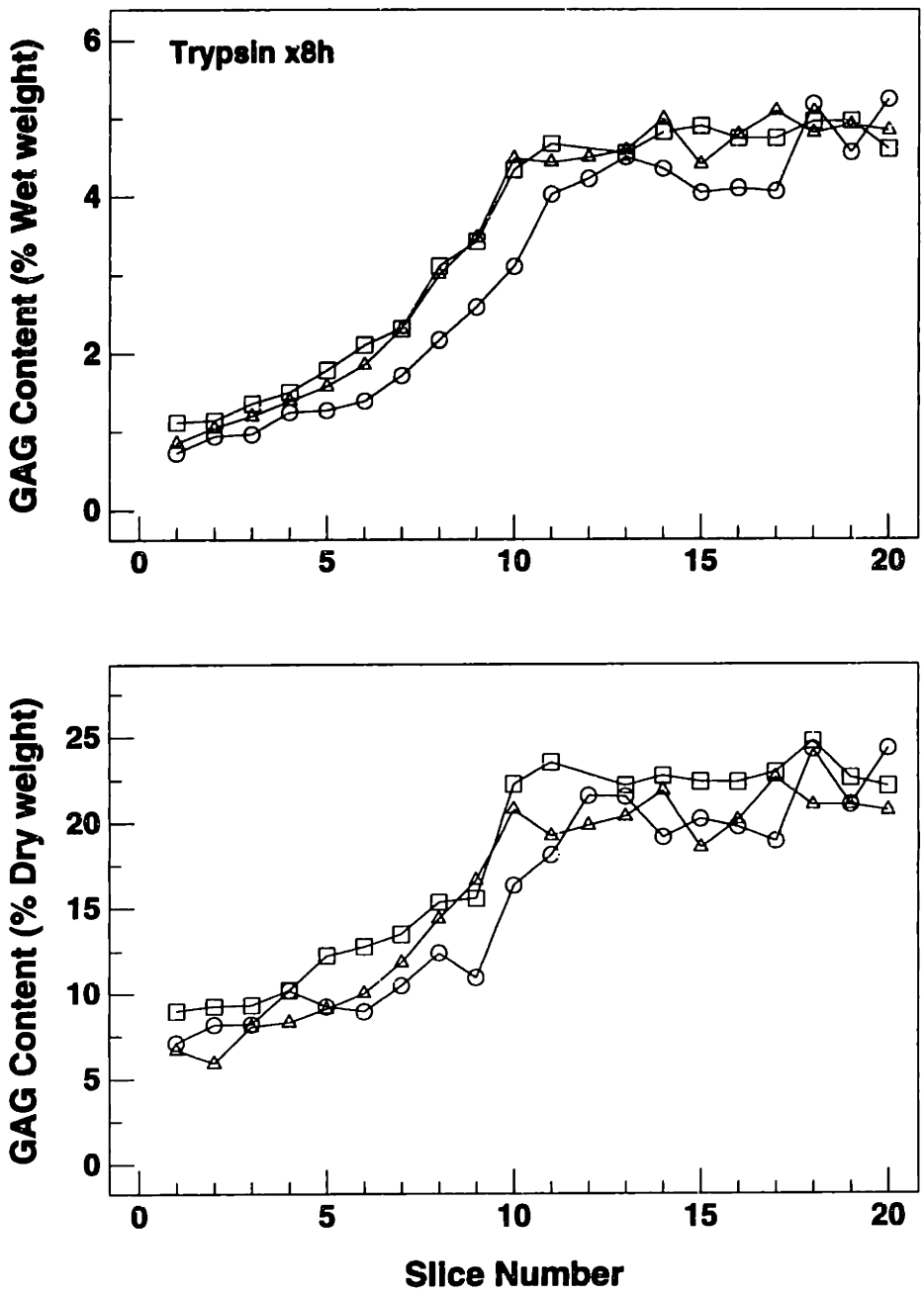

Figure D.5: GAG content of sequential 200 μm slices of full-thickness cartilage plugs digested with trypsin for 8 h, as a percentage of tissue wet weight (top) and dry weight (bottom). Slice #1 is the most superficial.

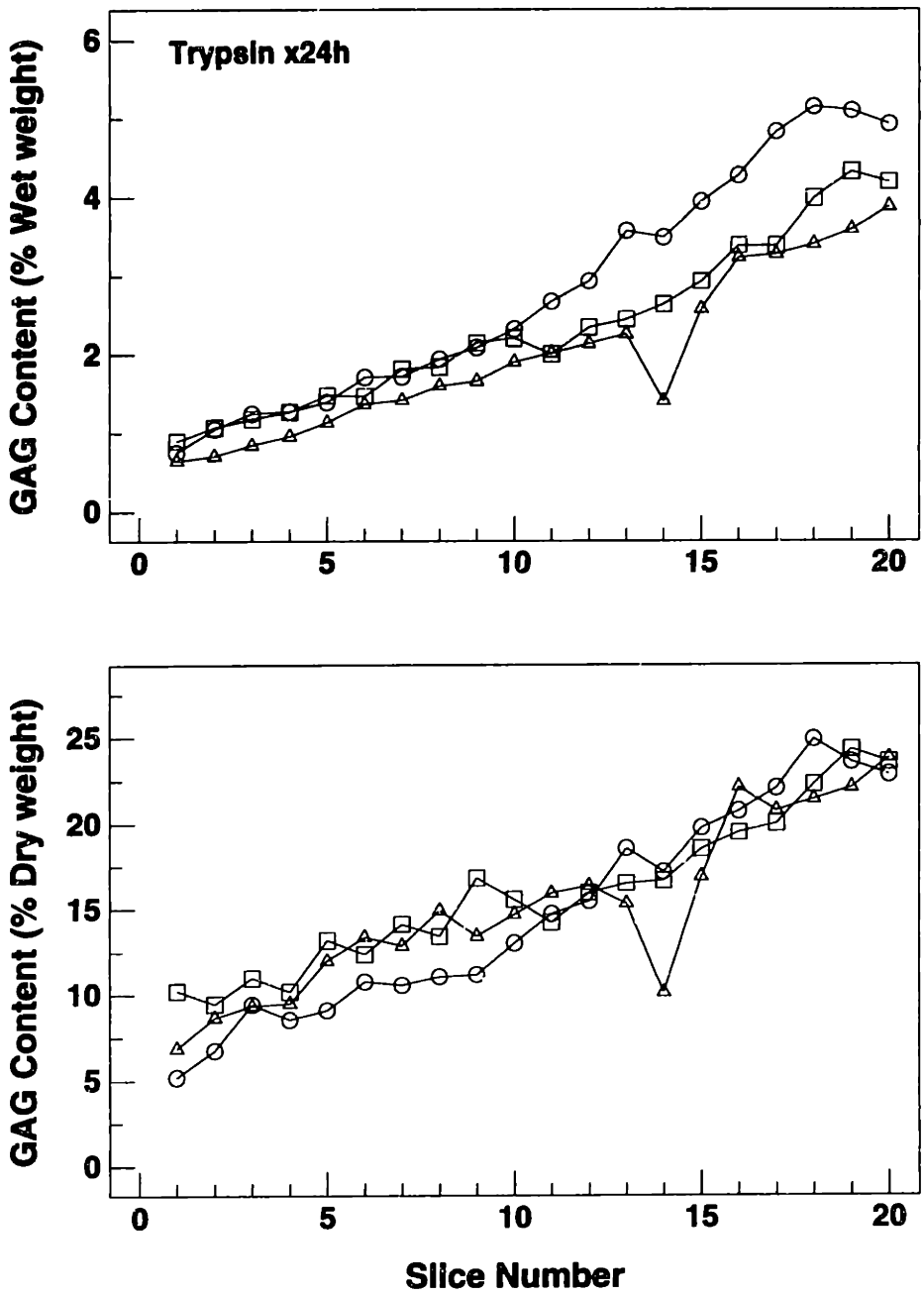

Figure D.6: GAG content of sequential 200 μm slices of full-thickness cartilage plugs digested with trypsin for 24 h, as a percentage of tissue wet weight (top) and dry weight (bottom). Slice #1 is the most superficial.

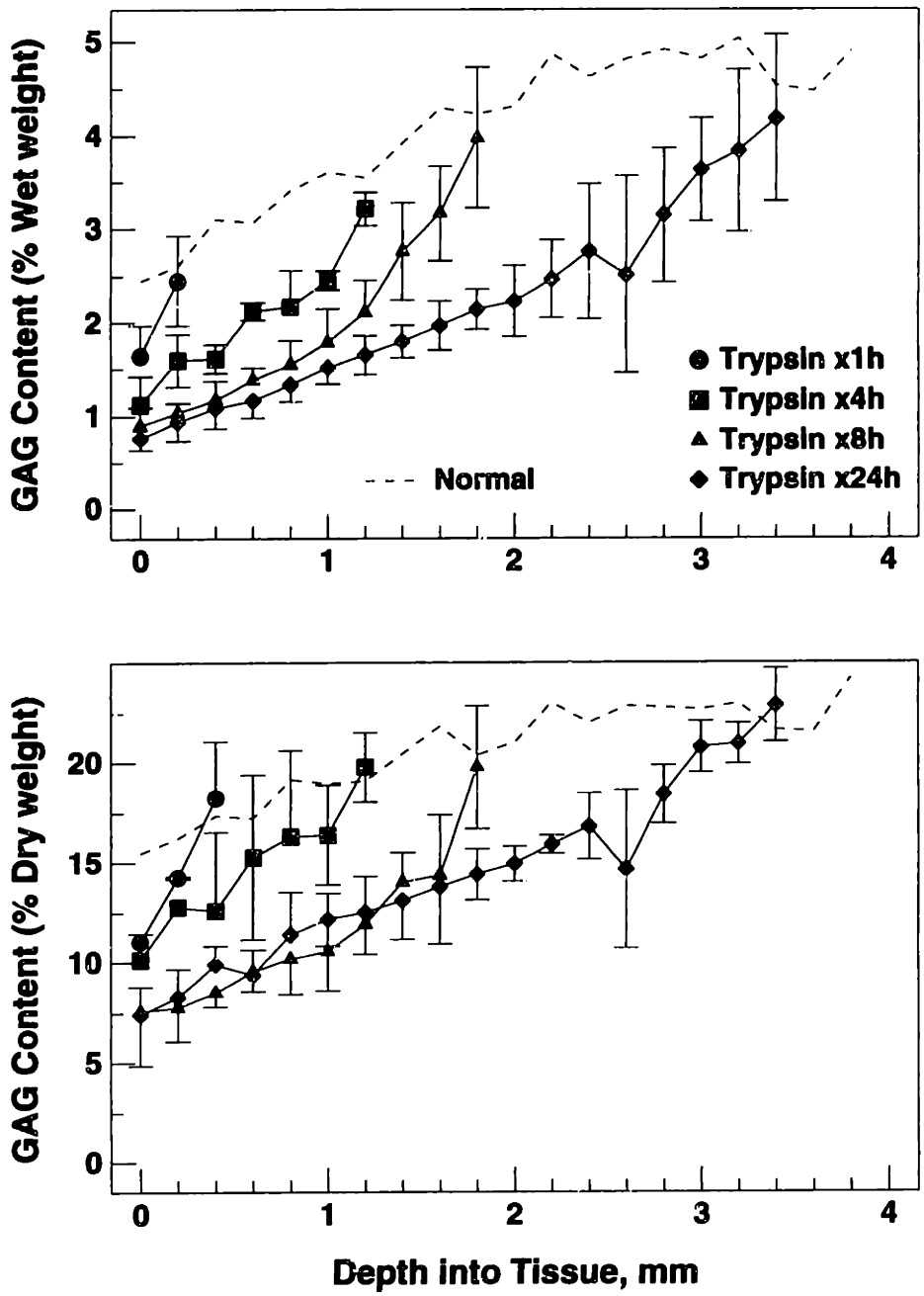

Figure D.7: GAG content, as percentage of wet weight (top) and dry weight (bottom), of sequential 200 μm slices of full-thickness cartilage plugs digested with trypsin for 1, 4, 8, and 24 h (mean $\pm$ SD) as well as normal controls (mean, dashed lines). For clarity, curves are plotted only until the depth at which GAG content approximately equals normal levels. Wet weight data also appear in Figure 3.5.

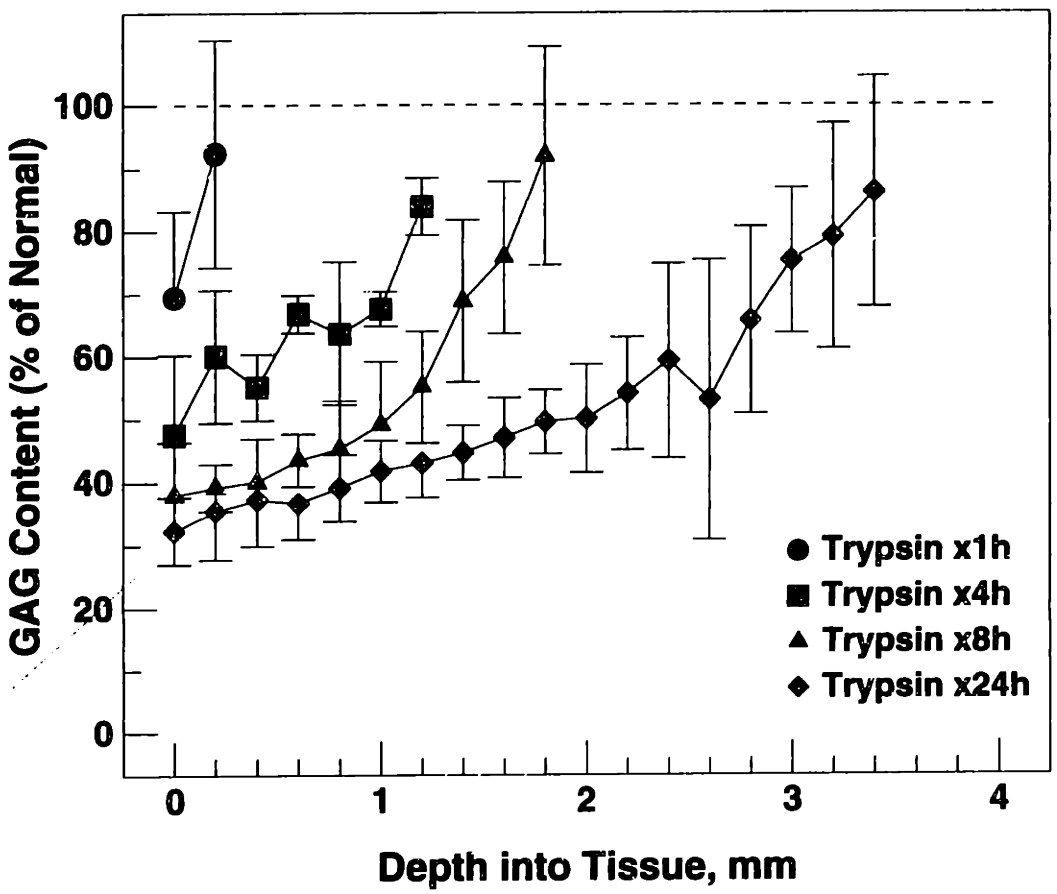

Figure D.8: GAG content (mean ±,SD, as percentage of normal) vs. depth into tissue for cartilage plugs digested with trypsin for 1, 4, 8, and 24 h, computed from data as percentage of wet weight.

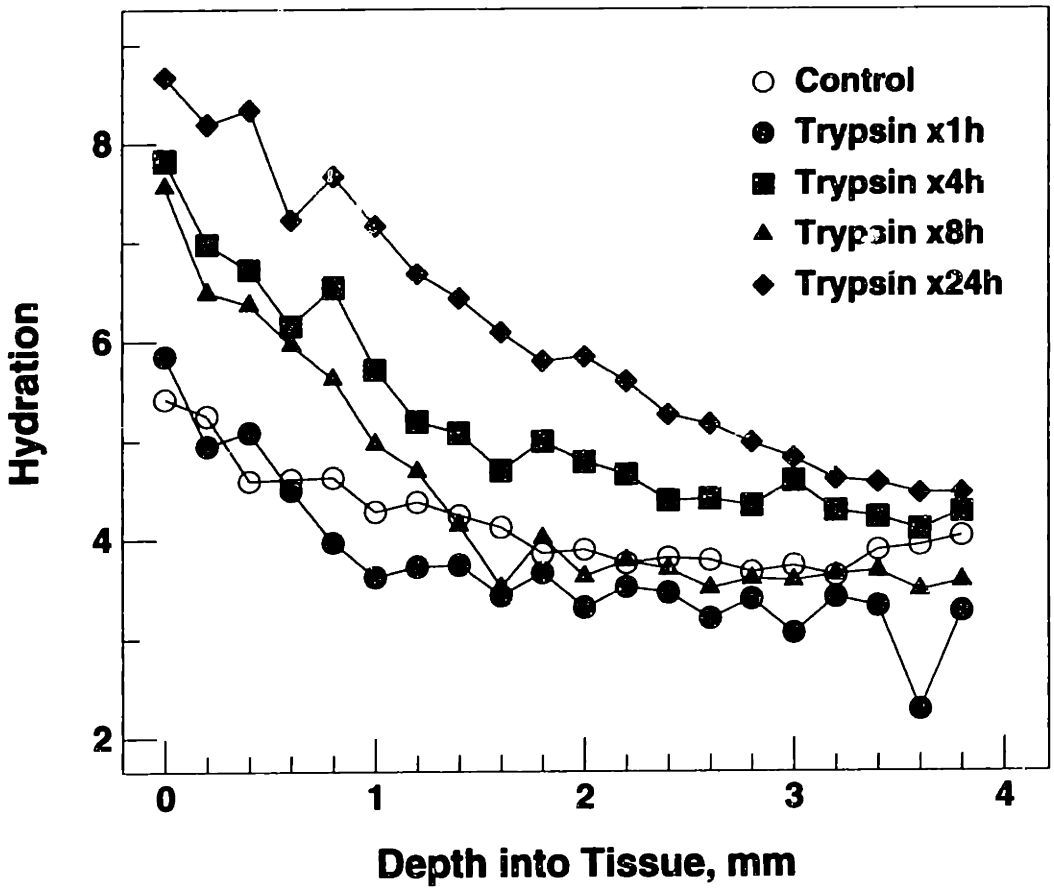

Figure D.9: Hydration (water : solid weight ratio) of 200 μm thick disks from calf cartilage plugs digested with trypsin for 1, 4, 8, and 24 h as well as normal controls. For clarity, error bars have been omitted.

Duration of digestion	Depth of degraded region	GAG lost from region (%)	Electrical conductivity, S/m	Decrease in conductivity (%)
0	0	0	0.90	0
1 h	0.2 mm	18.4	0.84	7.0
4 h	1.2 mm	35.0	0.79	13.0
8 h	1.8 mm	42.5	0.76	15.6
24 h	3.4 mm	45.8	0.75	16.6
2 h	~0.6 mm	~25	0.82	9.7
Complete GAG loss		100	0.65	27.9

Table D.1: Overall GAG loss from trypsin-digested region and electrical conductivity of tissue. GAG loss for trypsin exposure durations of 1, 4, 8, and 24 h was determined from wet-weight data in Figure D.7; result for 2 h digestion was estimated by interpolation. Conductivity was calculated using Equations D.2 and D.5. Decreases in conductivity are relative to initial value of 0.90 S/m.

disks were of uniform thickness (200 μm) and diameter (9.5 mm), the percentage of GAG lost was determined using the formula

$$\text{GAG loss (\%)} = 100 \times \frac{\sum_{n=1}^{N} \left(c_n^0 - c_n^{\text{tr}}\right)}{\sum_{n=1}^{N} c_n^0}, \tag{D.1}$$

where c_n^0 and c_n^{tr} are the GAG concentrations in the nth 200 μm thick slice of normal and trypsin-digested tissue, respectively, and N is the number of the deepest slice in which the GAG content after digestion was lower than normal. Graphically, this procedure is equivalent to estimating the area between the curves for normal and degraded cartilage in Figure D.7, expressed as a percentage of the total area under the "normal" curve (down to the depth of the degraded region). The estimated GAG loss calculated in this manner ranged from 18.4% after 1 h of digestion to 45.8% after 24 h (Table D.1). By interpolation between the data for 1 h and 4 h in Figure D.7, the two-hour trypsin digestion described in Chapter III was estimated to produce an overall GAG loss of 25% extending approximately 0.6 mm into the tissue.

D.1.4 Estimation of Electrical Conductivity of Degraded Cartilage

The electrical conductivity of cartilage is dependent on the intratissue concentrations of sodium and chloride ions, the predominant mobile charged species. The conductivity, σ, of a binary electrolyte solution is given by [87]

$$\sigma = F\left\{|z_+|\,\bar{u}_+\bar{c}_+ + |z_-|\,\bar{u}_-\bar{c}_-\right\}, \tag{D.2}$$

where $F = 9.6487 \times 10^4$ Coul/mol is Faraday's constant and $z_\pm$, $\bar{u}_\pm$, and $\bar{c}_\pm$ are the valences, ionic mobilities, and concentrations, respectively, of the cations and anions within the tissue; for NaCl, $z_+ = z_- = 1$. The ion concentrations within the tissue are assumed to be governed by the Donnan equilibrium relation [87]:

$$\bar{c}_+\bar{c}_- = c_b^2, \tag{D.3}$$

where c_b is the concentration of cations (and anions) in the bath solution and the activity coefficients of both ionic species are assumed to be the same in tissue as in free solution. At equilibrium, the tissue is electrically neutral, with the negative fixed charge groups of the matrix macromolecules balanced by an excess of mobile cations. Thus,

$$\frac{\rho_m}{F} + \bar{c}_+ - \bar{c}_- = 0, \tag{D.4}$$

where ρ_m is the fixed charge density of the tissue (per unit volume). Solving Equations D.3 and D.4 yields the positive roots

$$\bar{c}_\pm = \mp\frac{\rho_m}{2F} + \sqrt{\left(\frac{\rho_m}{2F}\right)^2 + c_b^2}. \tag{D.5}$$

Using a value of 0.22 M for the molar charge density, ρ_m/F, of normal calf cartilage [67] and a bath concentration of $c_b = 0.15\,M$ (as used in the probe measurements), Equation D.5 yields an intratissue sodium ion concentration of $\bar{c}_{Na} = 0.076\,M$, which is ap-

proximately half the concentration in the bath. The ionic mobilities of sodium and chloride, $\bar{c}_{Na}$ and $\bar{c}_{Cl}$, are approximately 1.8×10^{-4} cm^2/V·s and 2.7×10^{-4} cm^2/V·s, respectively, in human femoral head cartilage equilibrated in Ringer's solution (which has an ionic strength of 0.15 M). Using these values, Equation D.2 yields a conductivity of σ = 0.90 S/m for normal (undigested) calf cartilage. This value is close to the conductivity (1.0 S/m) used in the mathematical simulations presented in Chapters IV and V and is comparable to previously reported values [99,137,158].

Since the fixed charge density of the cartilage matrix is due mainly to the ionized GAG residues of matrix proteoglycans [161], loss of GAG resulting from enzymatic digestion would be expected to decrease the charge density, ρ_m, proportionally; using the adjusted value of ρ_m, the conductivity of degraded tissue can then be computed using Equations D.5 and D.2. For each duration of trypsin digestion, the corresponding electrical conductivity was calculated (with the approximation that the GAG loss was uniform over the degraded region) and expressed as a percentage decrease relative to the initial value of 0.90 S/m (Table D.1). The estimated 25% loss of GAG resulting from two-hour trypsin digestion decreased the conductivity by less than 10%, while complete loss of GAG charge groups would result in a 28% decrease in conductivity. The fixed charge density of human cartilage is lower than that of calf (approximately 0.18 M in femoral head cartilage under physiologic conditions [161]) and thus would have a smaller Donnan osmotic effect on the intratissue ion concentrations. Consequently, the electrical conductivity of human tissue would be even *less* sensitive to changes in GAG content; complete loss of GAG would decrease the conductivity by only 23%. Thus, as is the case with purely mechanical measurements of cartilage material properties [24,66,105,136,175], purely *electrical* parameters such as conductivity would be expected to be less sensitive indicators of GAG loss than electromechanical quantities (such as current-generated stress).

D.1.5 Kinetics of Trypsin Digestion

In order to analyze the kinetics of GAG loss produced by surface trypsin digestion, the GAG data were compared with the predictions of a simple one-dimensional model for diffusion of enzyme into the tissue. For modeling purposes, it was assumed that (1) the reaction rate of trypsin with its substrate was rapid enough, and (2) PG breakdown products were small enough, that diffusion of trypsin into the cartilage plug was the rate-limiting process. The enzyme concentration, $c(z,t)$, within the cartilage is a function of depth into the tissue, z, and time, t, and is assumed to be governed by the one-dimensional diffusion equation [47],

$$\frac{\partial c}{\partial t} = D\frac{\partial^2 c}{\partial z^2}, \tag{D.6}$$

where D is the diffusion coefficient of the enzyme in cartilage. The appropriate boundary conditions are as follows: (1) there is no trypsin in the tissue initially; i.e.,

$$c(z,0) = 0, \tag{D.7}$$

and (2) the concentration at the articular surface ($x = 0$) is maintained at the bath concentration, c_0 (because the bath is well stirred):

$$c(0,t) = c_0. \tag{D.8}$$

For a *semi-infinite* specimen, Equation D.6 can be solved (e.g., by taking the Laplace transform with respect to time) for the concentration within the tissue [47]:

$$c(z,t) = c_0 \operatorname{erfc}\left(\frac{z}{2\sqrt{Dt}}\right), \tag{D.9}$$

where $\operatorname{erfc}(z)$ is the *complementary error function,* defined by the integral

$$\operatorname{erfc}(z) = \frac{2}{\sqrt{\pi}}\int_z^\infty e^{-t^2}\,dt. \tag{D.10}$$

For a cartilage specimen of *finite* thickness, δ, however, with a cartilage-bone interface that is impermeable to the enzyme, the solution consists of an infinite series of "images" [47]:

$$c(z,t) = c_0 \sum_{n=0}^{\infty} (-1)^n \left\{ \operatorname{erfc}\left(\frac{2n\delta + z}{2\sqrt{Dt}}\right) + \operatorname{erfc}\left(\frac{2(n+1)\delta - z}{2\sqrt{Dt}}\right) \right\}. \qquad \text{(D.11)}$$

Using this model, the concentration of enzyme within the tissue was calculated (Figure D.10), where the bath concentration, c_0, was 1 mg/ml, the cartilage thickness was taken to be δ = 6 mm, and a diffusion coefficient of $D = 10^{-6}$ cm^2/sec, a typical value for large solutes in cartilage [159], was assumed. Examination of these curves reveals that the depth at which the enzyme concentration predicted by the model decreases to 0.45 mg/ml (dashed line in Figure D.10) corresponds approximately to the depth at which the GAG content measured in trypsin-digested plugs reaches normal levels (Figure D.7). Thus, the kinetics of GAG loss observed in the surface digestion model are consistent with a diffusion-limited process, with a threshold level of enzyme concentration in the tissue necessary for significant GAG loss to occur.

D.1.6 Collagen Content

A preliminary study was performed to assess the collagen content of normal and trypsin-digested 9.5 mm diameter calf cartilage plugs. The two most superficial 200 μm slices from a 24-hour trypsin-digested plug and the two deepest slices (3.6–4.0 mm into the tissue) from a normal cartilage plug were assayed, following papain digestion, using a colorimetric hydroxyproline assay [227]. The digested samples were acid hydrolyzed in 0.2 ml of 6 *N* HCl at 105° for 24 h, oxidized with chloramine-T (sodium *N*-chloro-*p*-toluenesulfonamide) in a citrate/acetate buffer, and reacted with *p*-dimethylaminobenzaldehyde (DMBA) in perchloric acid to produce a chromophoric product; the optical absorbance at 550 nm was then read using a microplate reader and compared with hydroxyproline standards. The amount of collagen in each disk was determined by multiplying the hydroxyproline content by 10; for each plug, the collagen content (as a percentage of both wet weight and dry

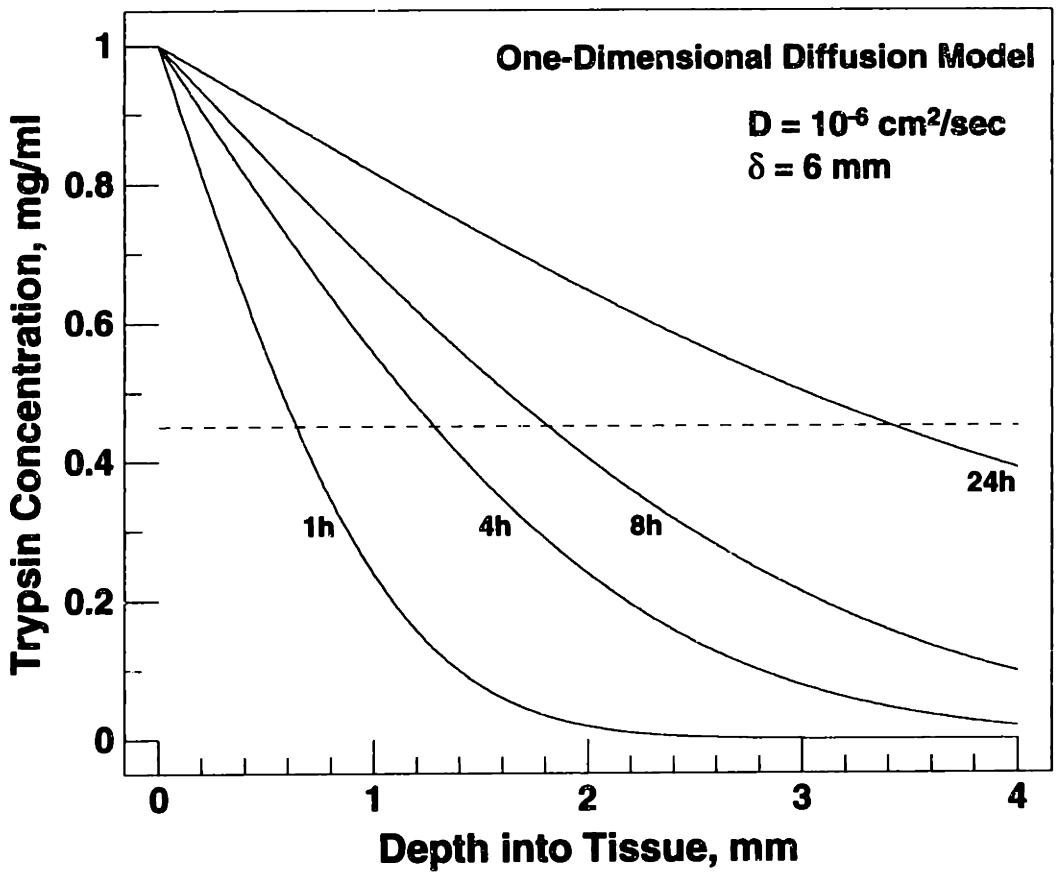

Figure D.10: Trypsin concentration vs. depth into tissue predicted by one-dimensional diffusion model, computed by solving the one-dimensional diffusion equation (Equation D.6) with appropriate boundary conditions (constant enzyme concentration of 1 mg/ml in bath, no trypsin initially in tissue), assuming a diffusion coefficient, D, of 10^{-6} cm^2/sec and an impermeable cartilage-bone interface at a depth of $\delta = 6$ mm. Dashed line is at $c = 0.45$ mg/ml.

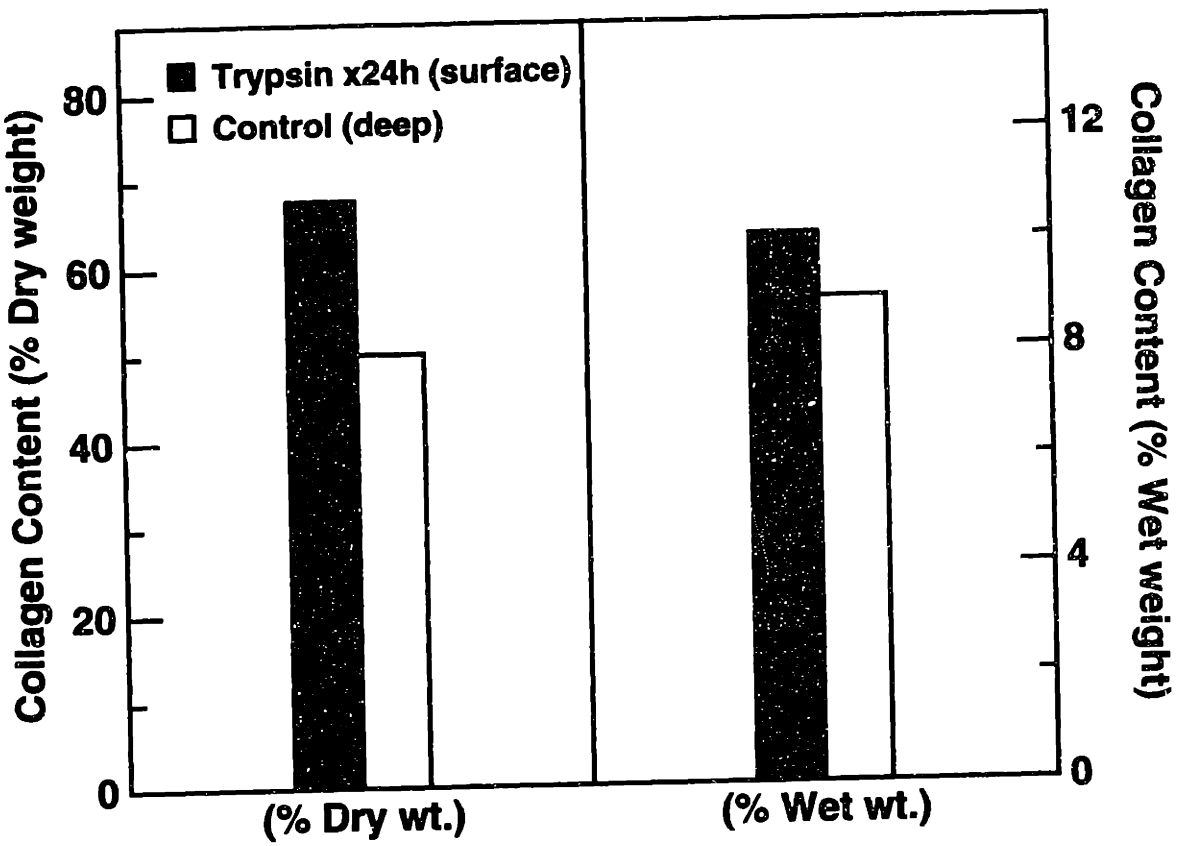

Figure D.11: Collagen content (as percentage of wet weight and dry weight) of superficial region (0-400 μm depth) of a cartilage plug digested with trypsin for 24 h (solid bars) and deep region (3.6–4.0 mm) of a normal plug (open bars), determined by a colorimetric hydroxyproline assay [227].

weight) was then calculated by dividing the *total* collagen in the two disks from each plug by the *total* weight of the two disks (Figure D.11). No hydroxyproline was detected in a control containing trypsin only.

As a percentage of tissue *dry* weight, the trypsin-digested cartilage had a collagen content of 67.70%, as compared to 50.03% in normal tissue. The difference was less pronounced when collagen content was expressed as a percentage of *wet* weight (10.07% in trypsin-digested tissue vs. 8.91% in controls), consistent with the increased hydration of trypsin-digested tissue (Figure D.9). Although these results are preliminary, they are con-

sistent with the hypothesis that trypsin digestion selectively extracts aggrecan from the cartilage matrix while producing minimal or no damage to the collagen network [53,106,133]. Denaturation of type II collagen has been detected (using an immunoassay) in human osteoarthritic cartilage, however [108]. Thus, trypsin digestion may not provide a suitable experimental model for *all* of the biochemical changes which occur in osteoarthritis.

D.2 Multiple-Wavelength Spectroscopy of Cartilage Plugs

D.2.1 Current-Generated Stress, With and Without Intact Articular Surface

Two full-thickness cartilage-bone plugs were tested with the multiple-wavelength probe (long-wavelength configuration only), with the articular surface intact and then tested again after removal of the most superficial 40–100 μm of tissue using a microtome (Figure D.12). At all frequencies (0.025–1.0 Hz), the stress amplitude did not change significantly (as determined by ANOVA) after removal of the articular surface. However, for subsequent experiments using full-thickness plugs, the articular surface was left intact as a more appropriate model for *in vivo* applications. Although the surface of the plugs used was not always completely level, the 50 kPa static stress appeared sufficient to flatten the articular surface against the probe electrodes. An important issue for *in vivo* testing, however, is the question of how curvature of the intact articular surface would affect the contact between the probe electrodes and the tissue (and thus affect the measured stress).

D.2.2 Current-Generated Stress Before and After Trypsin Digestion

In addition to the studies described in Chapter III, in which full-thickness cartilage plugs (9.5 mm diameter, with intact articular surface) were tested with the multiple-wavelength probe before and after 2 h of trypsin digestion, further studies were performed in which plugs exposed to the enzyme for either 1 h (N = 3) or 4 h (N = 3) were tested using the same protocol. The amplitude and phase of the measured stress, both before and after trypsin digestion (including the 2 h data), are shown in Figures D.13–D.18. For each duration of

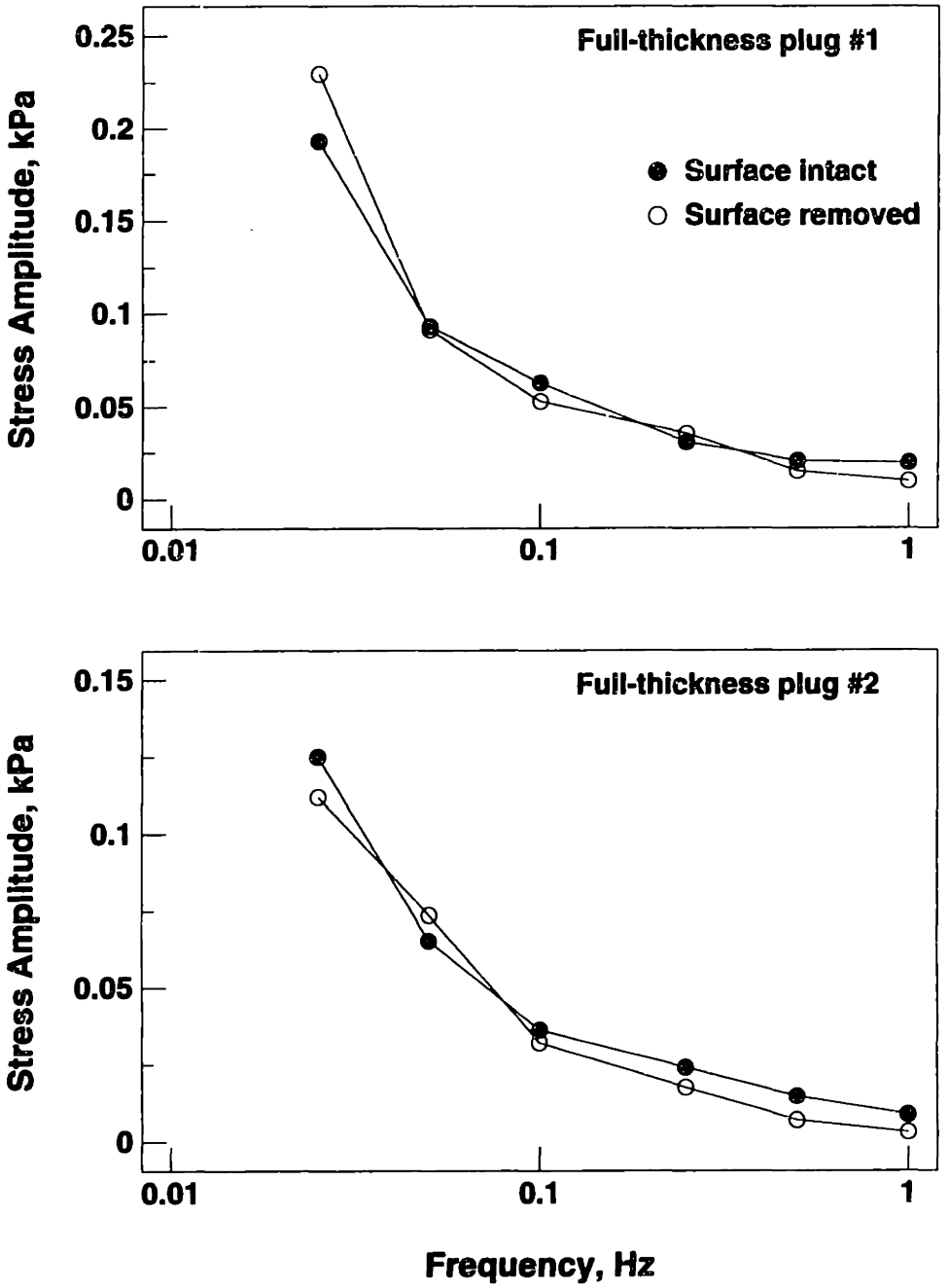

Figure D.12: Current-generated stress amplitude vs. frequency, measured in two 9.5 mm diameter full-thickness calf cartilage plugs using the long-wavelength configuration of the multiple-wavelength probe with an applied current density amplitude of 10 A/m^2, before (solid circles) and after (open circles) removal of the articular surface using the microtome.

enzyme exposure, the ratio of short- to long-wavelength stress response was computed, both before and after trypsin digestion (Figure D.19). Digestion for 1 hour had no detectable effect on the short- to long-wavelength stress ratio (Figure D.19, top). In contrast, enzymatic digestion for 2 hours resulted in a significant decrease in this ratio, with the greatest effect (50%) occurring at low frequencies; there was only a trend toward a difference at 0.5 Hz ($p < 0.1$) and no significant difference at 1 Hz (Figure D.19, middle). Digestion for 4 hours also resulted in a decrease in the short- to long-wavelength ratio (by 40% at 0.025 Hz), although the difference was statistically significant only at some frequencies (Figure D.19, bottom). With 1, 2, or 4 h of trypsin digestion, there were no systematic significant differences (pre-digestion vs. post-digestion) in the *phase* of the current-generated stress or in the amplitude of either the long-wavelength or short-wavelength response alone.

Although a larger sample size might more consistently demonstrate a significant difference, there are several possible reasons why the decrease in ratio with 4-hour digestion is less pronounced than with 2-hour digestion. First, the tissue may become more compressed by the 50 kPa static load during testing after 4 h of digestion (because of the decreased compressive modulus of the digested tissue resulting from PG loss), thus decreasing the thickness of the degraded region of tissue and artificially increasing the fixed charge density in this region. Also, because the degraded region extends further into the tissue after 4 h of digestion, the long-wavelength excitation "senses" a relatively greater region of degraded tissue (as compared with the underlying normal tissue), while with short-wavelength excitation the current remains essentially confined to the same degraded region after either 2 h or 4 h of enzyme exposure. Increasing the duration of surface trypsin digestion would further attenuate the long-wavelength response without further affecting the short-wavelength response, resulting in a less marked decrease in the short- to long-wavelength ratio as compared with normal cartilage. Thus, the change in stress ratio would be most marked when the depth of the degraded region is approximately equal to the short-wavelength current penetration depth. Using a probe which can be configured for more than two wavelengths, the depth of a degraded region could theoretically be inferred by comparing the decrease in

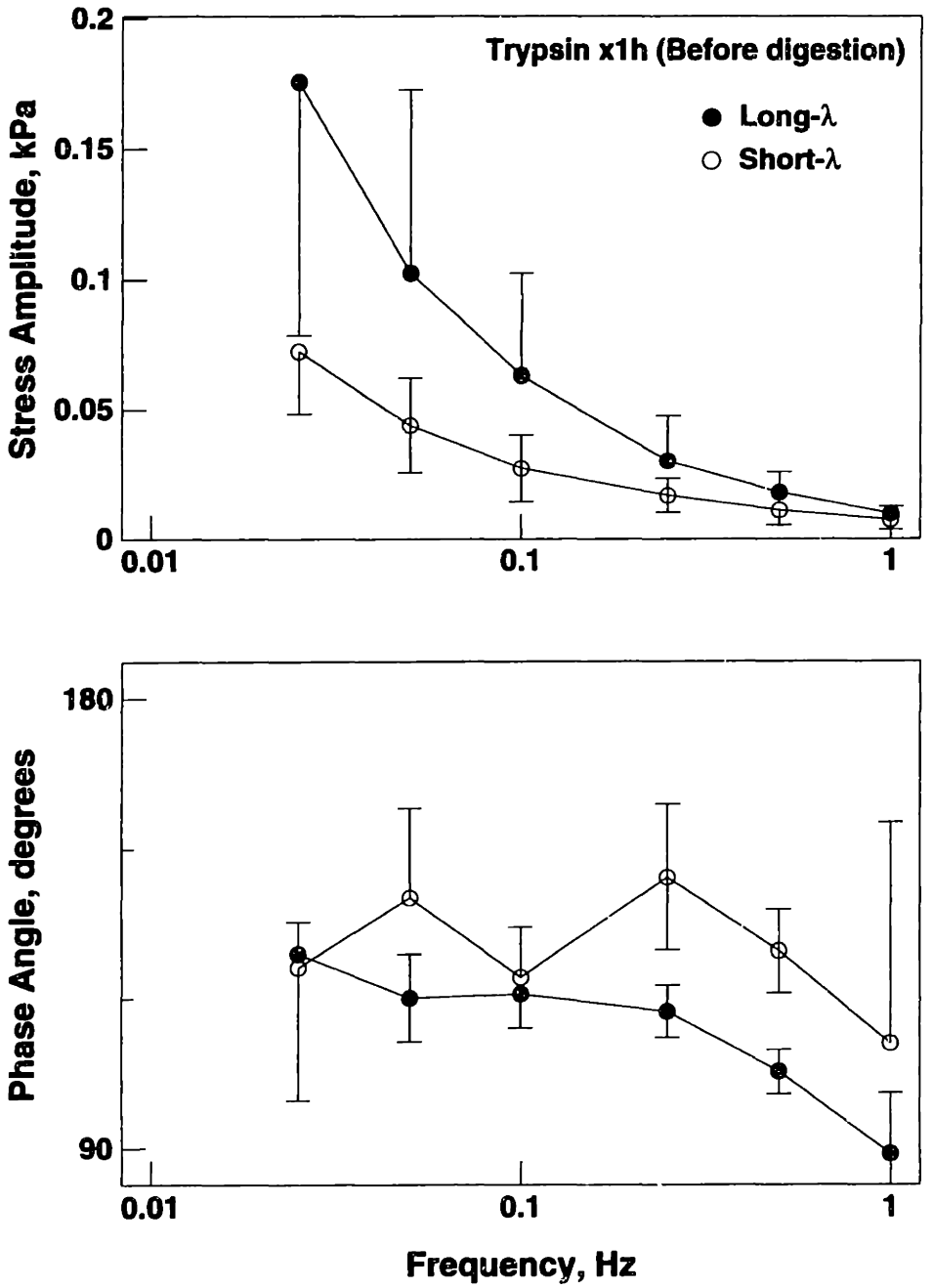

Figure D.13: Current-generated stress (amplitude and phase) versus frequency, measured in 9.5 mm diameter full-thickness calf cartilage plugs (with intact articular surface) using both the long- and short-wavelength configurations of the multiple-wavelength probe with an applied current density amplitude of 10 A/m^2, just prior to surface trypsin digestion for 1 hour. All points are mean ± SEM (N = 3).

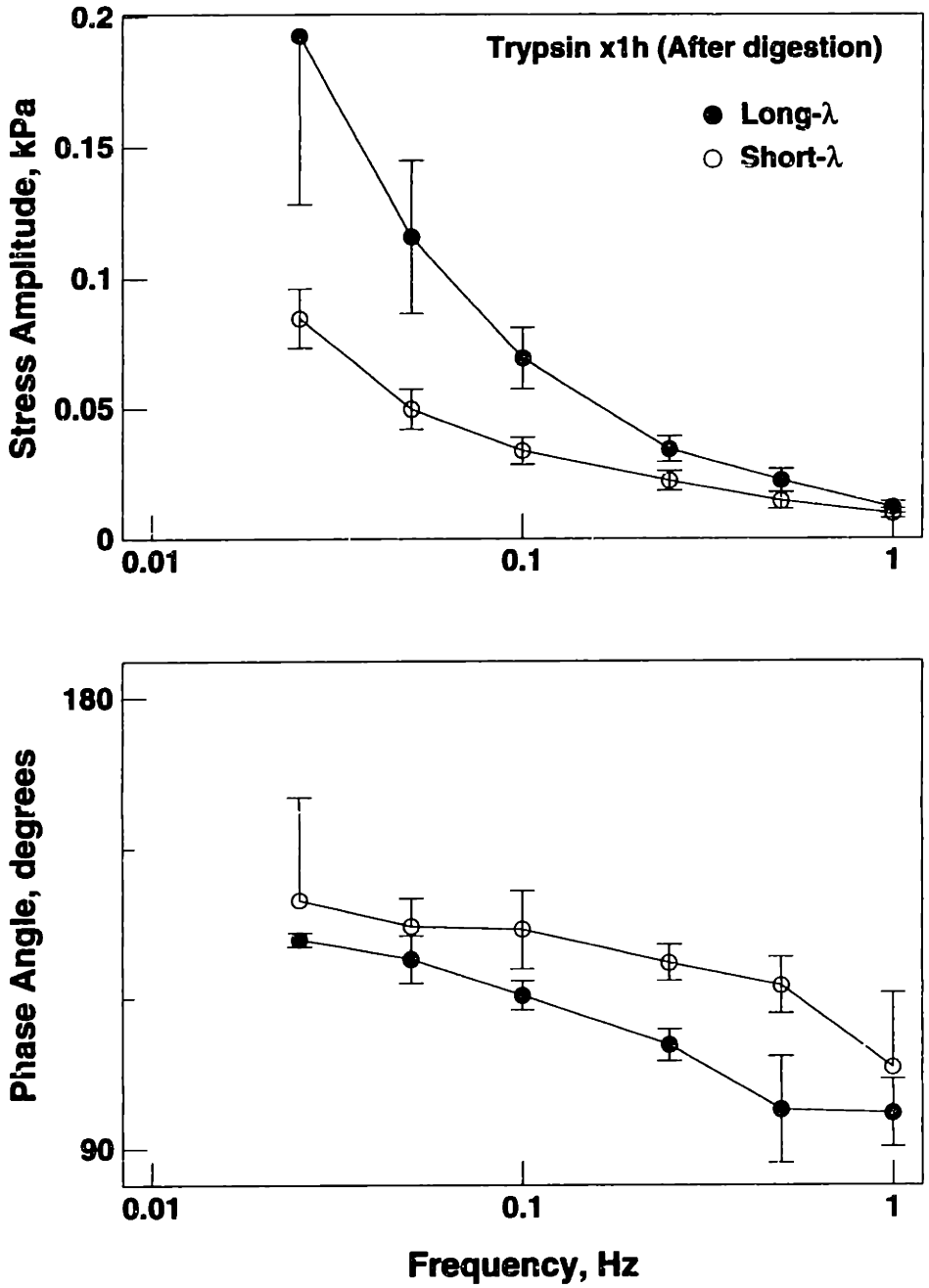

Figure D.14: Current-generated stress (amplitude and phase) versus frequency, measured in 9.5 mm diameter full-thickness calf cartilage plugs (with intact articular surface) using both the long- and short-wavelength configurations of the multiple-wavelength probe with an applied current density amplitude of 10 A/m^2, after surface trypsin digestion for 1 hour. All points are mean ± SEM (N = 3).

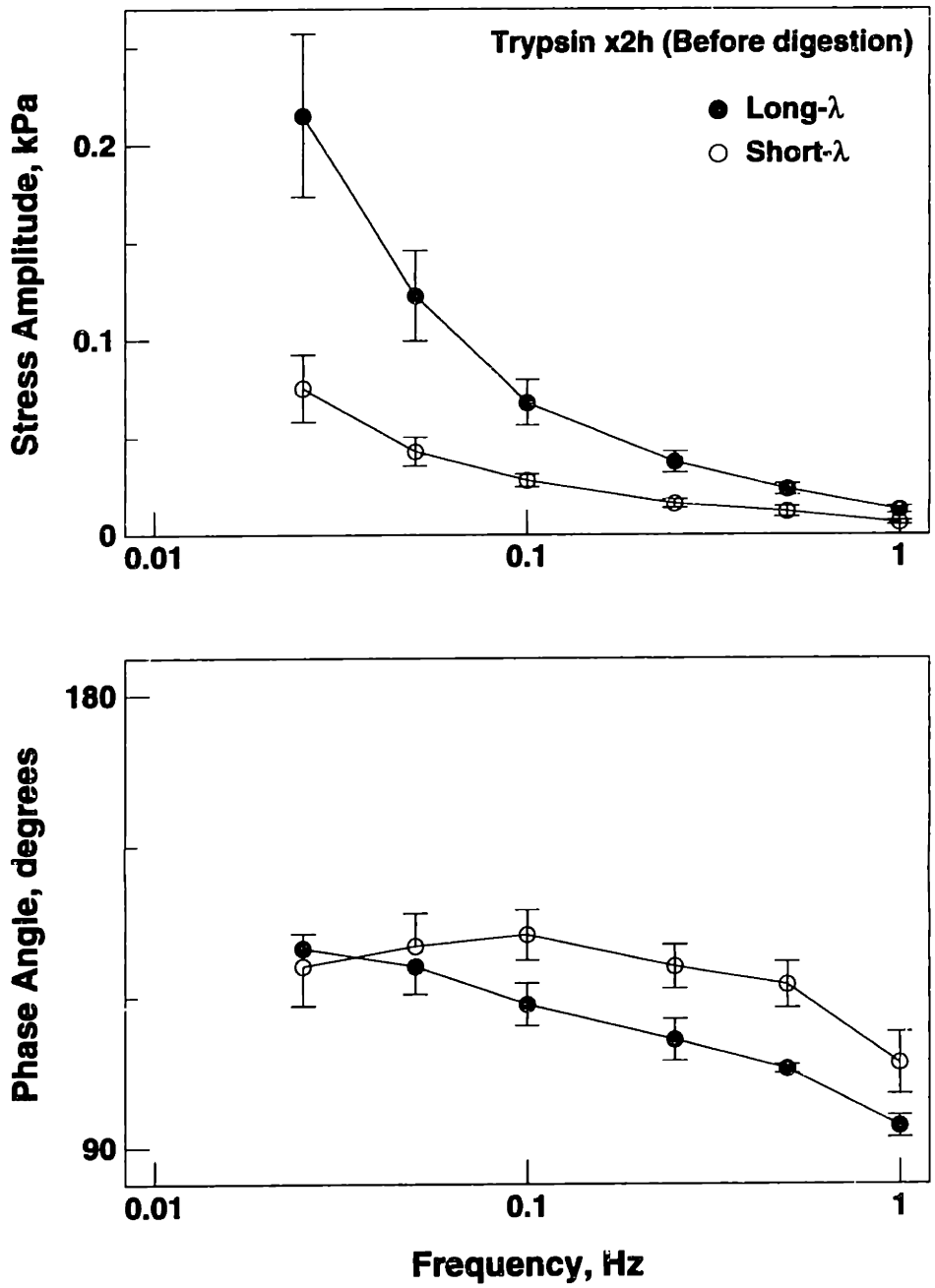

Figure D.15: Current-generated stress (amplitude and phase) versus frequency, measured in 9.5 mm diameter full-thickness calf cartilage plugs (with intact articular surface) using both the long- and short-wavelength configurations of the multiple-wavelength probe with an applied current density amplitude of 10 A/m^2, just prior to surface trypsin digestion for 2 hours. All points are mean ± SEM (N = 4).

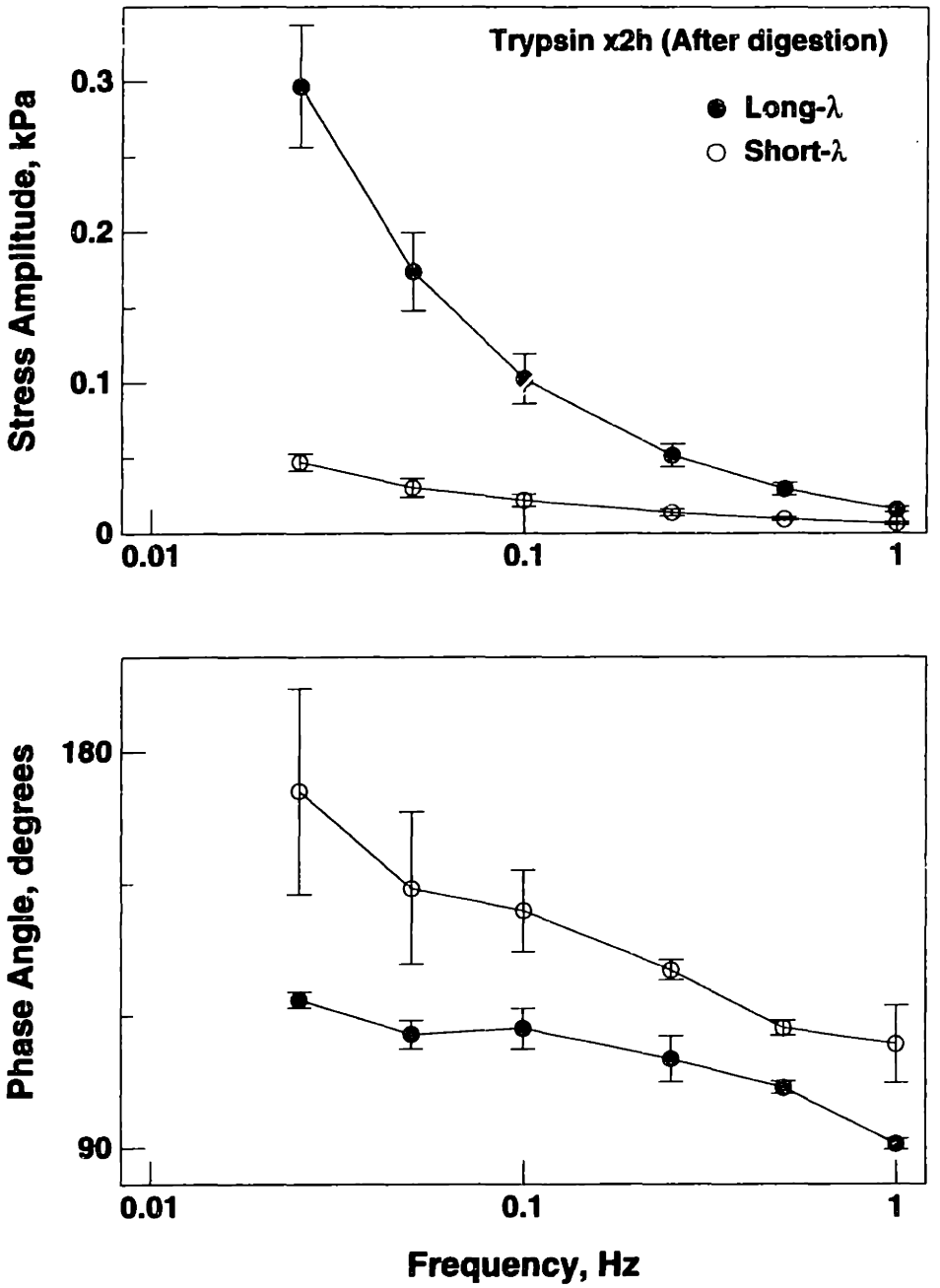

Figure D.16: Current-generated stress (amplitude and phase) versus frequency, measured in 9.5 mm diameter full-thickness calf cartilage plugs (with intact articular surface) using both the long- and short-wavelength configurations of the multiple-wavelength probe with an applied current density amplitude of 10 A/m^2, after surface trypsin digestion for 2 hours. All points are mean ± SEM (N = 4).

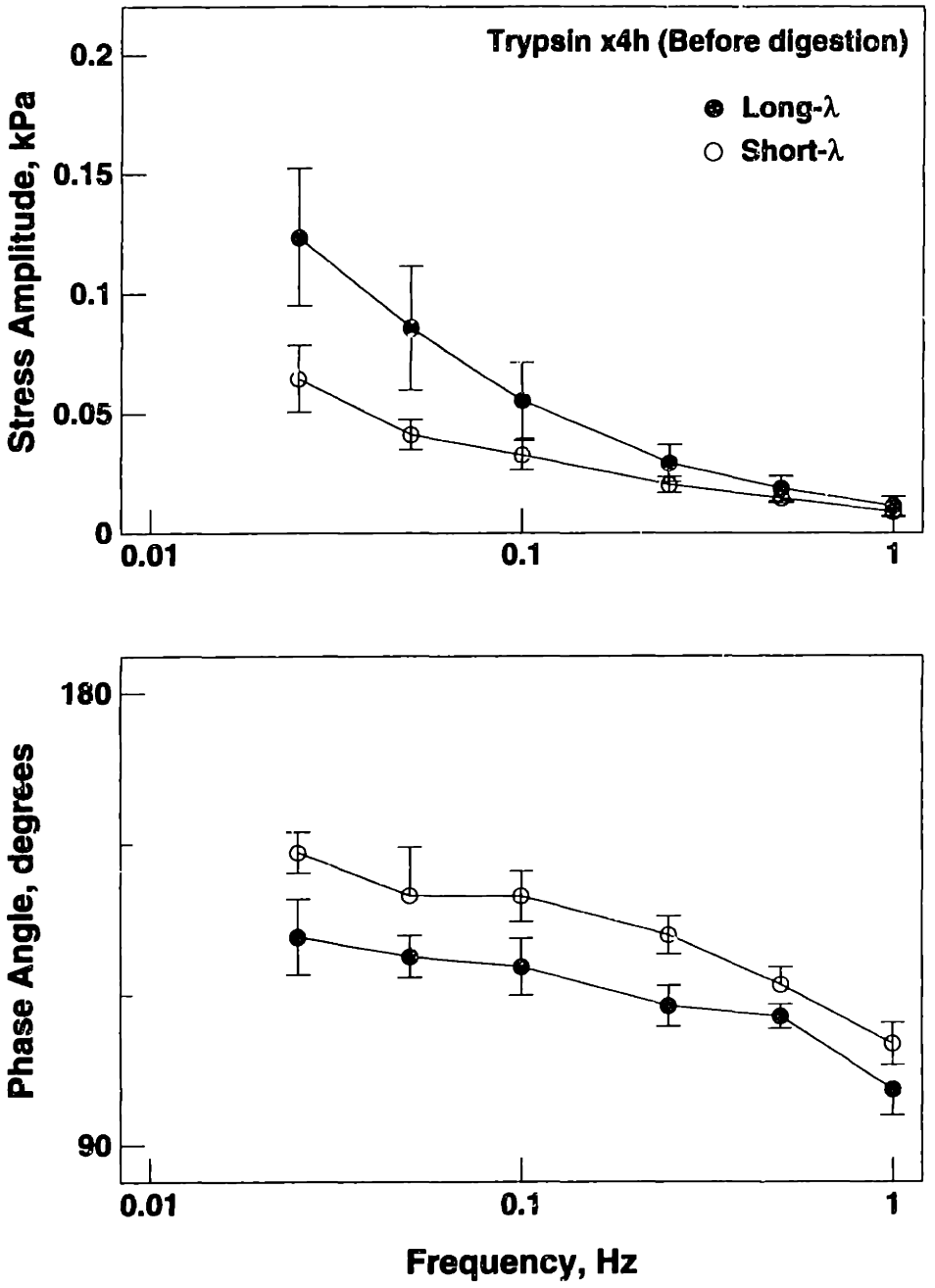

Figure D.17: Current-generated stress (amplitude and phase) versus frequency, measured in 9.5 mm diameter full-thickness calf cartilage plugs (with intact articular surface) using both the long- and short-wavelength configurations of the multiple-wavelength probe with an applied current density amplitude of 10 A/m^2, just prior to surface trypsin digestion for 4 hours. All points are mean ± SEM (N = 3).

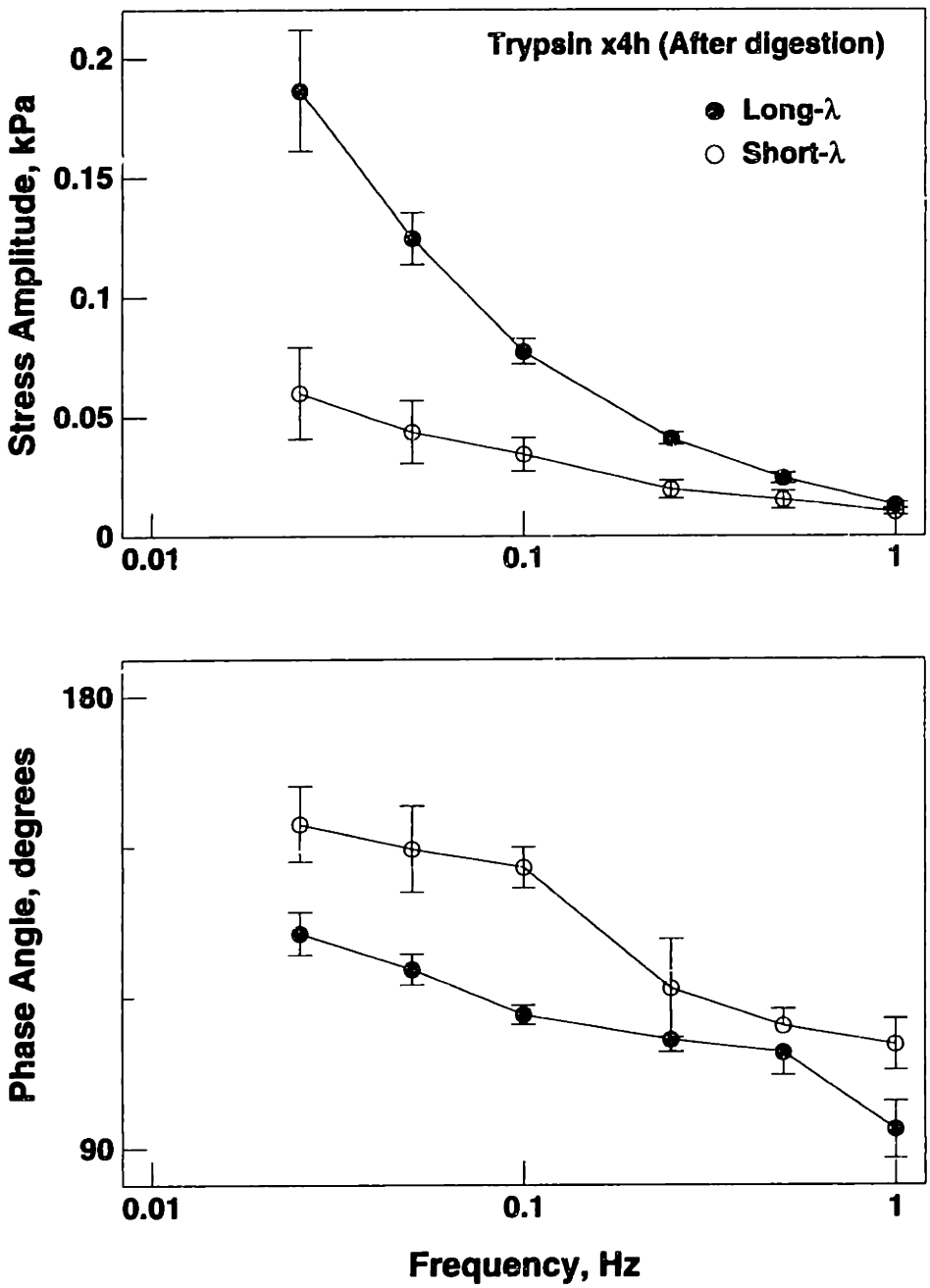

Figure D.18: Current-generated stress (amplitude and phase) versus frequency, measured in 9.5 mm diameter full-thickness calf cartilage plugs (with intact articular surface) using both the long- and short-wavelength configurations of the multiple-wavelength probe with an applied current density amplitude of 10 A/m^2, after surface trypsin digestion for 4 hours. All points are mean ± SEM (N = 3).

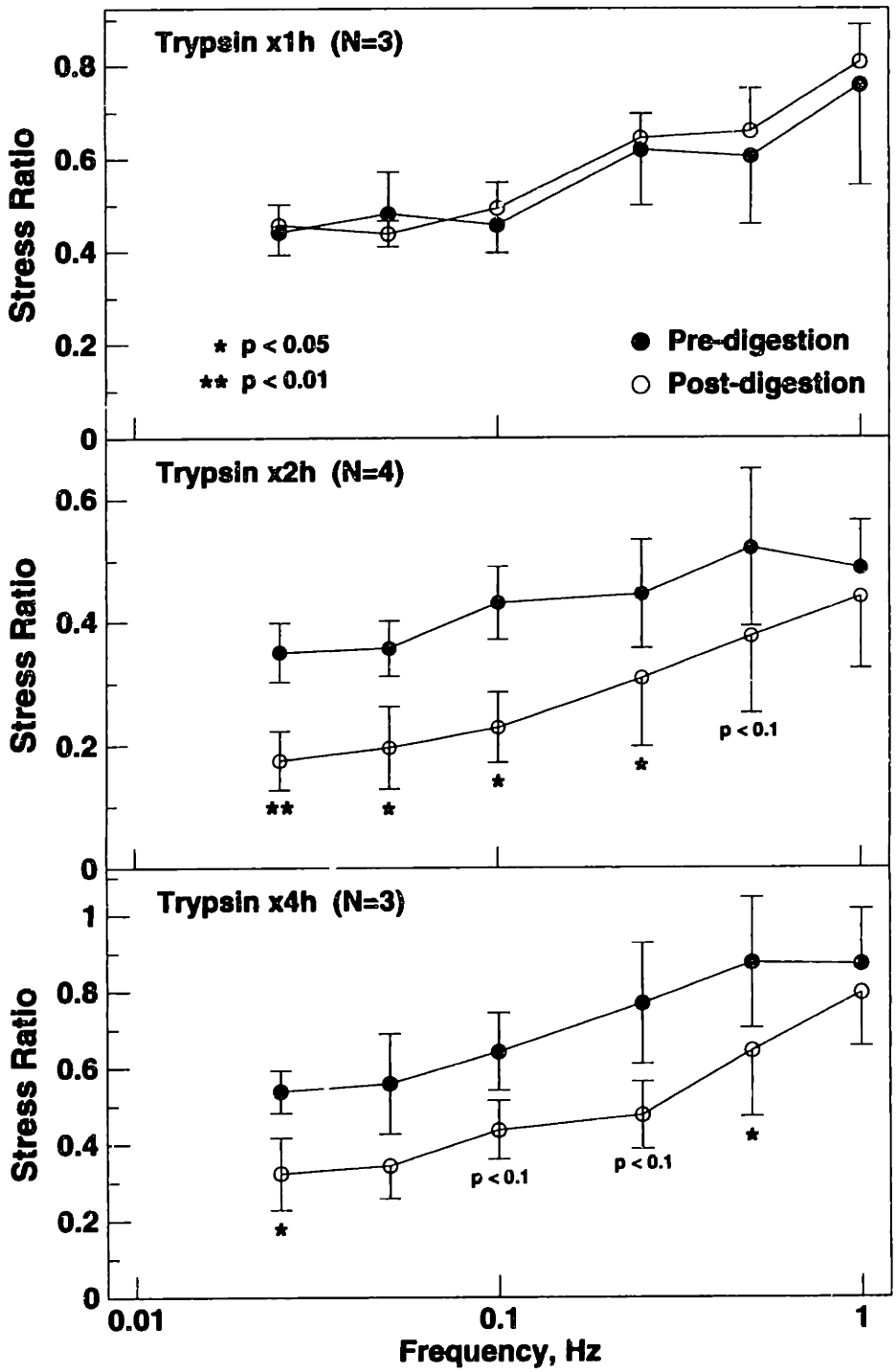

Figure D.19: Ratio of short- to long-wavelength stress response, measured using the multiple-wavelength probe with the same applied current density amplitude at each wavelength, before and after trypsin digestion for 1 h (top), 2 h (middle), and 4 h (bottom). All points are mean ± SEM; p values are for pre- vs. post-digestion, by multivariate analysis of variance (ANOVA).

ratio at each wavelength. Further experiments would be necessary to definitively establish the quantitative relationship between the degree of proteoglycan loss and the change in short- to long-wavelength stress ratio.

Appendix E

Summary of Mathematical Model of Electromechanical Surface Spectroscopy

In this appendix, the theoretical model for surface excitation of an electromechanically coupled poroelastic medium [210,211] is summarized. Although previously solutions have been obtained for the case of an ideal sinusoidal surface excitation, the model has now been extended (by Eliot Frank) to include finite electrode structures.

E.1 Derivation of Governing Equations

Electromechanical transduction in cartilage has been successfully modeled by combining the phenomenological linear equations of non-equilibrium thermodynamics for electrokinetic coupling in isotropic media [49] with the linear biphasic theory [179,180] that relates stress, strain, and fluid flow in poroelastic media. A one-dimensional version of the model has been found to correlate well with experimental measurements of dynamic stiffness, streaming potential and current-generated stress in uniaxial compression [65]. The model has been extended to the case of surface excitation by applying the same equations to a two-dimensional geometry [210,211].

For modeling purposes, certain idealized assumptions are made about the poroelastic medium and the imposed excitation [210,211]. First, the system is assumed to be electroquasistatic, with excitation frequencies low enough that charge relaxation is effectively instantaneous. The imposed wavelengths are assumed to be long enough that a continuum model is applicable. Inertial, acoustical, and chemical reaction effects are assumed to be negligible, and the system is taken to be isothermal. Finally, both the solid and fluid phases of the matrix are assumed to be isotropic, homogeneous, and incompressible; furthermore, the solid matrix is modeled as a linear elastic material, while fluid motion is modeled by Darcy flow (i.e., the fluid is inviscid at macroscopic solid boundaries).

Based on these assumptions, equations for the mechanics and electromechanical interactions can be derived. Conservation of mass takes the form [17,180]

$$\alpha_0 \nabla \cdot \vec{v}_s + \nabla \cdot \vec{v}_f = 0, \tag{E.1}$$

where α_0 is the solid volume fraction and $\vec{v}_s$ and $\vec{v}_f$ are the local velocities of the solid matrix and fluid, respectively. Conservation of momentum can be written

$$\nabla \cdot \vec{\vec{\sigma}} = \vec{0}, \tag{E.2}$$

where $\vec{\vec{\sigma}}$ is the solid stress per total unit area and acoustic and inertial effects are assumed to be negligible. The components of the stress tensor are given by the generalized Hooke's Law plus a pressure term [56,57]:

$$\sigma_{ij} = 2G\epsilon_{ij} + \delta_{ij}\left(\lambda_L \epsilon_{kk} - P\right), \tag{E.3}$$

where G and λ_L are the Lamé elastic coefficients of the solid matrix (G is also the shear modulus), P is the fluid pressure per total unit area (including both hydrostatic and osmotic components), $\vec{\vec{\epsilon}}$ is the small-strain tensor, whose components can be written in terms of the solid matrix displacement, $\vec{u}$, as

$$\epsilon_{ij} = \frac{1}{2}\left(\frac{\partial u_i}{\partial x_j} + \frac{\partial u_j}{\partial x_i}\right), \tag{E.4}$$

and δ_{ij} is the discrete Krönecker delta function, given by

$$\delta_{ij} = \begin{cases} 1, & i = j \\ 0, & i \neq j. \end{cases} \tag{E.5}$$

The double subscript on the ϵ_{kk} term in Equation E.3 implies summation over k.

Electrokinetic coupling is described by the linearized phenomenological equa-

tions [49,125]:

$$\begin{bmatrix} \nabla P \\ \nabla \Phi \end{bmatrix} = \begin{bmatrix} -b_{11} & b_{12} \\ b_{21} & -b_{22} \end{bmatrix} \begin{bmatrix} \vec{U} \\ \vec{J} \end{bmatrix}, \tag{E.6}$$

which can be expressed equivalently as

$$\begin{bmatrix} \vec{U} \\ \vec{J} \end{bmatrix} = \begin{bmatrix} -k_{11} & k_{12} \\ k_{21} & -k_{22} \end{bmatrix} \begin{bmatrix} \nabla P \\ \nabla \Phi \end{bmatrix}, \tag{E.7}$$

where Φ is the electrical potential, $\vec{U} = \vec{v}_f - \vec{v}_s$ is the area-averaged relative fluid velocity, and $\vec{J}$ is the current density. Current flow is assumed to occur only within the bulk of the medium; i.e., there is no surface conduction or shunt. The matrix components, k_{ij}, are interpreted as follows: k_{11} is the short-circuit Darcy hydraulic permeability, k_{22} is the electrical conductivity in the absence of fluid flow, and k_{12} and k_{21} (which are equal by Onsager reciprocity) are electrokinetic coupling coefficients[1]. Taking the curl of both sides of Equation E.6, with the assumption that $\det |k_{ij}| \neq 0$, yields the two relations

$$\nabla \times \vec{U} = \vec{0}, \tag{E.8}$$

$$\nabla \times \vec{J} = \vec{0}. \tag{E.9}$$

Under the assumption of instantaneous charge relaxation, conservation of charge takes the form

$$\nabla \cdot \vec{J} = 0. \tag{E.10}$$

Equations E.9 and E.10, together with the vector identity [171]

$$\nabla \times \left(\nabla \times \vec{A} \right) = \nabla \left(\nabla \cdot \vec{A} \right) - \nabla^2 \vec{A}, \tag{E.11}$$

[1] For the more general case of an *anisotropic* medium, each of the scalar k_{ij} parameters would be replaced by a tensor.

imply that the current density must satisfy the vector form of Laplace's equation,

$$\nabla^2 \vec{J} = \vec{0}. \tag{E.12}$$

The distribution of current density within the bulk of the medium can be determined by solving Equation E.12 with the appropriate boundary conditions.

Assuming the length of the surface electrodes is much greater than their width, these equations may be simplified to the case of two-dimensional rectangular coordinates (where the x- and y-axes lie on the surface of the cartilage and the z-axis is normal to the surface; the x-axis is assumed to lie along the long axis of the electrodes). Conservation of mass then becomes

$$\alpha_0 \left(\frac{\partial^2 u_y}{\partial y \partial t} + \frac{\partial^2 u_z}{\partial z \partial t} \right) + \frac{\partial v_y}{\partial y} + \frac{\partial v_z}{\partial z} = 0, \tag{E.13}$$

where the relation between solid displacement and velocity, $\vec{v}_s = \frac{\partial \vec{u}}{\partial t}$, has been used. Conservation of momentum, substituting the definitions of σ_{ij} and ϵ_{ij}, takes the form

$$(2G + \lambda_L) \nabla^2 u_y + (G + \lambda_L) \left(\frac{\partial^2 u_z}{\partial y \partial z} - \frac{\partial^2 u_y}{\partial z^2} \right) - \frac{\partial P}{\partial y} = 0 \tag{E.14}$$

$$(2G + \lambda_L) \nabla^2 u_z + (G + \lambda_L) \left(\frac{\partial^2 u_y}{\partial y \partial z} - \frac{\partial^2 u_z}{\partial y^2} \right) - \frac{\partial P}{\partial z} = 0. \tag{E.15}$$

Electrokinetic coupling in two dimensions may be rewritten as

$$\begin{bmatrix} U_y \\ J_y \end{bmatrix} = \begin{bmatrix} -k_{11} & k_{12} \\ k_{21} & -k_{22} \end{bmatrix} \frac{\partial}{\partial y} \begin{bmatrix} P \\ \Phi \end{bmatrix} \tag{E.16}$$

and

$$\begin{bmatrix} U_z \\ J_z \end{bmatrix} = \begin{bmatrix} -k_{11} & k_{12} \\ k_{21} & -k_{22} \end{bmatrix} \frac{\partial}{\partial z} \begin{bmatrix} P \\ \Phi \end{bmatrix}. \tag{E.17}$$

Finally, Equation E.8 becomes

$$\frac{\partial U_z}{\partial y} - \frac{\partial U_y}{\partial z} = 0. \tag{E.18}$$

Equations E.13–E.18 constitute 8 linear equations in the 8 unknowns, u_y, u_z, U_y, U_z, P, J_y, J_z, and Φ. Given an appropriate set of boundary conditions, these equations can be solved analytically.

The governing equations have been solved for the case of an imposed current density that is spatially sinusoidal in the y-direction and uniform in the x-direction, with an angular frequency ω. Although the solution is presented in full detail elsewhere [210,211], the method of solution (in somewhat modified form) will be summarized here. The response to excitations that are spatially more complicated, including the case of finite surface electrodes, can be constructed by superposition of an appropriate set of modal solutions, as discussed below.

E.2 Normalization of Variables

To simplify the method of solution, it is convenient to normalize all variables. Spatial dimensions are normalized to an arbitrary characteristic length, ℓ^*:

$$z = z^*/\ell^* \tag{E.19}$$

$$y = y^*/\ell^*. \tag{E.20}$$

All "starred" variables will be considered dimensional quantities, while normalized (and thus dimensionless) quantities will be represented without an asterisk. The cartilage is assumed to have thickness δ^*, which is also normalized:

$$\delta = \delta^*/\ell^*. \tag{E.21}$$

The imposed current is assumed to have an angular frequency, $\omega = 2\pi f$, and spatial wavenumber, $k^* = 2\pi/\lambda$, where λ is the (dimensional) wavelength. The normalized waveneumber is, therefore,

$$k = k^*\ell^*. \tag{E.22}$$

Finally, an additional (arbitrary) normalization length, ξ^*, is defined and is also normalized:

$$\xi = \xi^*/\ell^*. \tag{E.23}$$

(The normalized parameter ξ was used as a scaling factor to verify the numerical solutions, by setting $\xi = 1$ or $\xi = \delta$.)

For a spatially and temporally sinusoidal excitation, with frequency ω and normalized wavenumber k, the solutions take the following forms:

$$\vec{J}^*(y,z) = J_0\vec{J}(z)e^{j(ky-\omega t)} \tag{E.24}$$

$$\vec{u}^*(y,z) = J_0\frac{k_c\xi^{*2}}{k_{21}(G+\lambda_L)}\vec{u}(z)e^{j(ky-\omega t)} \tag{E.25}$$

$$\vec{U}^*(y,z) = J_0\frac{k_{11}}{k_{21}}\vec{U}(z)e^{j(ky-\omega t)} \tag{E.26}$$

$$P^*(y,z) = J_0\frac{\xi^*}{k_{21}}p(z)e^{j(ky-\omega t)} \tag{E.27}$$

$$\Phi^*(y,z) = J_0\frac{\xi^*}{k_{22}}\phi(z)e^{j(ky-\omega t)} \tag{E.28}$$

$$T^*_{zz}(y,z) = J_0\frac{\xi^*}{k_{21}}s_{zz}(z)e^{j(ky-\omega t)} \tag{E.29}$$

$$T^*_{yz}(y,z) = J_0\frac{\xi^*}{k_{21}}s_{yz}(z)e^{j(ky-\omega t)} \tag{E.30}$$

where

$$k_c = k_{12}k_{21}/k_{11}k_{22} \tag{E.31}$$

and the normalized variables represent complex amplitudes.

Substituting the above definitions into Equations E.13–E.15 yields

$$\tau\left(ku_y - ju_z'\right) + \left(jkU_y + U_z\right) = 0 \tag{E.32}$$

$$(1+n)\left(u_y'' - k^2u_y\right) + jku_z' - u_y'' - jkp/\xi = 0 \tag{E.33}$$

$$(1+n)\left(u_z'' - k^2u_z\right) + k^2u_z + jku_y' - p'/\xi = 0, \tag{E.34}$$

where the prime (′) denotes the partial derivative of a variable with respect to z. Similarly, Equations E.16–E.17 transform to

$$U_y = jk\xi\,(-p + k_c\phi) \tag{E.35}$$

$$U_z = \xi\,(-p' + k_c\phi) \tag{E.36}$$

$$J_y = jk\xi\,(p - \phi) \tag{E.37}$$

$$J_z = \xi\,(p' - \phi')\,. \tag{E.38}$$

Finally, Equation E.18 becomes

$$jkU_z - U_y' = 0. \tag{E.39}$$

These relations make use of the following definitions:

$$n = 1 - 2\nu \tag{E.40}$$

$$r = k_s\xi^{*2}(1 + n) \tag{E.41}$$

$$k_s = \frac{\omega b_{11}\,(\alpha_0 + 1)}{2G + \lambda_L} = \frac{\omega b_{11}}{H_A\phi_0}, \tag{E.42}$$

where ν is the Poisson ratio, $H_A = 2G + \lambda_L$ is the equilibrium modulus, and $\phi_0 = 1/(\alpha_0 + 1)$ is the porosity (void fraction) of the tissue. The relations

$$1 + n = 2(1 - \nu) = \frac{H_A}{G + \lambda_L} \tag{E.43}$$

have also been used.

E.3 Modal Solution

The modal solution, corresponding to normalized wavenumber k, for the normalized complex current density, displacement, relative fluid velocity, pressure, potential, and stresses $s_{zz}(z)$ and $s_{yz}(z)$ has been shown to be given by the sum of a particular solution and a

homogeneous solution:

$$
\begin{bmatrix} J_y(z) \\ J_z(z) \\ u_y(z) \\ u_z(z) \\ U_y(z) \\ U_z(z) \\ p(z) \\ \phi(z) \\ s_{zz}(z) \\ s_{yz}(z) \end{bmatrix} = \begin{bmatrix} 1 & -1 \\ 1 & 1 \\ \frac{1+\gamma}{2nk^2\xi^2} & \frac{-1+\gamma}{2nk^2\xi^2} \\ \frac{\gamma}{2nk^2\xi^2} & \frac{-\gamma}{2nk^2\xi^2} \\ 0 & 0 \\ 0 & 0 \\ \frac{1}{k\xi} & \frac{-1}{k\xi} \\ \frac{-1}{k\xi} & \frac{1}{k\xi} \\ \frac{-\gamma}{k\xi} & \frac{-\gamma}{k\xi} \\ \frac{1+\gamma}{k\xi} & \frac{1-\gamma}{k\xi} \end{bmatrix} \begin{bmatrix} c_7 e^{kz} \\ c_8 e^{-kz} \end{bmatrix} + \begin{bmatrix} 0 & 0 \\ 0 & 0 \\ \frac{-k\delta\cosh\gamma}{2nk^2\xi^2} & \frac{k\delta\cosh\gamma}{2nk^2\xi^2} \\ \frac{-k\delta\sinh\gamma}{2nk^2\xi^2} & \frac{k\delta\sinh\gamma}{2nk^2\xi^2} \\ 0 & 0 \\ 0 & 0 \\ 0 & 0 \\ 0 & 0 \\ \frac{-k\delta\cosh\gamma}{k\xi} & \frac{k\delta\cosh\gamma}{k\xi} \\ \frac{-k\delta\sinh\gamma}{k\xi} & \frac{k\delta\sinh\gamma}{k\xi} \end{bmatrix} \begin{bmatrix} c_7/\sinh k\delta \\ c_8/\sinh k\delta \end{bmatrix}
$$

$$
+ \begin{bmatrix} 0 & 0 & 0 & 0 & 0 & 0 \\ 0 & 0 & 0 & 0 & 0 & 0 \\ 1 & -1 & 1/k+z & 1/k-z & 1 & -1 \\ 1 & 1 & z & z & \Lambda & \Lambda \\ 0 & 0 & -2nk\xi^2 & -2nk\xi^2 & jr & -jr \\ 0 & 0 & -2nk\xi^2 & 2nk\xi^2 & jr\Lambda & jr\Lambda \\ 0 & 0 & 2n\xi & 2n\xi & -jr/k\xi & jr/k\xi \\ 0 & 0 & -2nk_c\xi & -2nk_c\xi & jrk_c/k\xi & -jrk_c/k\xi \\ -2nk\xi & 2nk\xi & -2nk\xi z & 2nk\xi z & -2nk\xi & 2nk\xi \\ 2nk\xi & 2nk\xi & n(2kz+1)\xi & n(2kz-1)\xi & 2nk\Lambda\xi & 2nk\Lambda\xi \end{bmatrix} \begin{bmatrix} c_1 e^{kz} \\ c_2 e^{-kz} \\ c_3 e^{kz} \\ c_4 e^{-kz} \\ c_5 e^{\Lambda kz} \\ c_6 e^{-\Lambda kz} \end{bmatrix}
$$

where

$$\gamma = k(\delta + z), \tag{E.44}$$

$$\Lambda = \sqrt{1 - jk_s/k}. \tag{E.45}$$

This solution contains eight constants (denoted $c_1, \ldots, c_8$) which are determined by

the boundary conditions. The particular solution (first two terms on the right-hand side) depends on the constants c_7 and c_8, which are entirely determined by the *electrical* boundary conditions. For example, with an imposed sinusoidal current density at the surface ($z = 0$) and an impermeable lower interface ($z = -\delta$), the boundary conditions are

$$J_z(0) = c_7 + c_8 = 1 \tag{E.46}$$

$$J_z(-1) = c_7 e^{-k\delta} + c_8 e^{k\delta} = 0, \tag{E.47}$$

which yields the following values for the constants:

$$c_7 = \frac{e^{k\delta}}{2\sinh k\delta}, \qquad c_8 = \frac{-e^{-k\delta}}{2\sinh k\delta}. \tag{E.48}$$

The remaining six constants, $c_1, \ldots, c_6$ are determined from the *mechanical* boundary conditions. At the upper surface ($z = 0$), these are assumed to be

$$u_y(0) = u_z(0) = U_z(0) = 0, \tag{E.49}$$

while at the lower surface ($z = -\delta$) it is assumed that

$$u_y(-\delta) = u_z(-\delta) = 0. \tag{E.50}$$

The remaining boundary condition varies according to whether the lower interface is modeled as impermeable to fluid flow or porous. For an impermeable interface, we have

$$U_z(-\delta) = 0, \tag{E.51}$$

while for a porous boundary, the appropriate boundary condition is

$$p(-\delta) = 0. \tag{E.52}$$

Determining these six constants thus requires solving six simultaneous linear equations.

E.4 Mixed Boundary Value Problem

Because the governing equations (E.13–E.18) are linear, the response produced by an imposed array of surface electrodes can be represented as a superposition of modal solutions. Determining the relative weight of each mode requires solving a mixed boundary value problem, since the potential is constrained at each active electrode while the normal component of the current density is constrained to be zero at the surface between the electrodes. For an electrically "floating" electrode, the potential is not explicitly specified; however, the integral of the normal current over the surface of the electrode is constrained to be zero.

For modeling, an array of $2M$ equally spaced electrodes is considered, with polarity antisymmetric about $y = 0$. The electrodes are assumed to be infinite in the x-direction, with finite width, w, and center-to-center spacing, s, between adjacent electrodes. The geometry for the case $M = 1$ is illustrated in Figure E.1. Thus, the mth electrode extends

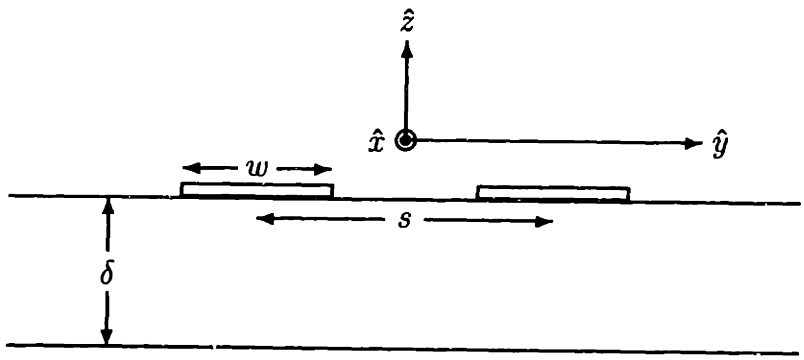

Figure E.1: Coordinate system for mixed boundary value problem, shown for the case of two electrodes

from $y = \left(m - \frac{1}{2}\right) s - \frac{w}{2}$ to $y = \left(m - \frac{1}{2}\right) s + \frac{w}{2}$. To simplify the solution, the system is assumed to be periodic in the y-direction, with a spatial period, Y, that is much greater than the width of the electrode array. Because the electrode array is antisymmetric about $y = 0$,

we need only evaluate the solution in the interval from $y = 0$ to $y = Y$. For a specified number of modes, N, the solution will be evaluated at the set of points

$$y_i = \frac{iY}{N}, \quad i = 1, \ldots, N. \tag{E.53}$$

The problem is approached by first deriving expressions for the current density and potential at the surface. Because the current density, $\vec{J}$, satisfies Laplace's equation (E.12), we must have

$$\vec{J} = -\nabla \Phi_J \tag{E.54}$$

for some potential function, Φ_J. From Equation E.7,

$$\vec{J} = k_{21} \nabla P - k_{22} \nabla \Phi = \nabla (k_{21} P - k_{22} \Phi). \tag{E.55}$$

Thus, the Laplacian potential is given by

$$\Phi_J = k_{21} P - k_{22} \Phi. \tag{E.56}$$

Although Φ_J is Laplacian, the electrical potential, Φ, does *not* satisfy Laplace's equation if electrokinetic coupling is present. Since Φ_J is Laplacian, however, it may be written as a Fourier series expansion:

$$\Phi_J(y, z) = \sum_{n=1}^{N} \frac{J_n}{k_n} \frac{\cosh k_n(\delta + z)}{\cosh k_n \delta} \sinh k_n y, \tag{E.57}$$

where

$$k_n = \frac{2\pi n}{Y} \tag{E.58}$$

is the wavenumber corresponding to the nth mode and J_n are the Fourier coefficients to be

determined. From Equation E.54, it follows that

$$J_y(y,z) = -\sum_{n=1}^{N} J_n \frac{\cosh k_n(\delta+z)}{\cosh k_n\delta} \cos k_n y \tag{E.59}$$

$$J_z(y,z) = -\sum_{n=1}^{N} J_n \frac{\sinh k_n(\delta+z)}{\cosh k_n\delta} \sin k_n y. \tag{E.60}$$

The electrical potential may be written as

$$\Phi(y,z) = \sum_{n=1}^{N} J_n \phi_n(z) \sin k_n y, \tag{E.61}$$

where $\phi_n(z)$ is the nth modal solution.

At the surface, the potential is constrained to be constant at each electrode, while $J_z(0) = 0$ between the electrodes. We define an indicator function, $e(y)$, as follows:

$$e(y) = \begin{cases} \pm 1, & \text{if } \left(m-\frac{1}{2}\right)s - \frac{w}{2} < y < \left(m-\frac{1}{2}\right)s + \frac{w}{2} \text{ for some } m = 1,\ldots,M; \\ 0, & \text{otherwise,} \end{cases} \tag{E.62}$$

where the sign of $e(y)$ is determined by the polarity of the mth electrode. Thus, $e(y) = 1$ if, and only if, y falls within one of the positive electrodes, while $e(y) = -1$ within each negative electrode. With no "floating" electrodes (i.e., with a normalized potential of ± 1 imposed at each electrode), the mixed boundary condition may be expressed mathematically as follows: For each point y_i, either

$$\Phi(y_i,0) = \sum_{n=1}^{N} J_n \phi_n(0) \sin k_n y_i = \pm 1, \quad \text{if} \quad e(y_i) = \pm 1, \tag{E.63}$$

or

$$J_z(y_i,0) = -\sum_{n=1}^{N} J_n \tanh k_n\delta \sin k_n y_i = 0, \quad \text{if} \quad e(y_i) = 0. \tag{E.64}$$

Once $\phi_n(z)$ has been determined for each wavenumber, k_n, these conditions represent N

linear equations in the N unknowns, $J_1, \ldots, J_N$. Thus,

$$\begin{bmatrix} J_1 \\ \vdots \\ J_N \end{bmatrix} = \left[Q_{ij} \right]^{-1} \begin{bmatrix} e(y_1) \\ \vdots \\ e(y_N) \end{bmatrix}, \tag{E.65}$$

where

$$Q_{ij} = \begin{cases} \phi_j(0) \sin k_j y_i, & \text{if } e(y_i) = \pm 1; \\ \tanh k_j \delta \sin k_j y_i, & \text{if } e(y_i) = 0. \end{cases} \tag{E.66}$$

With P pairs of electrically floating electrodes (out of the total of M electrode pairs), the problem is slightly more complicated, as we need to solve for the P unknown electrode potentials, $V_1, \ldots, V_P$, in addition to the N current coefficients, J_i. In this case, for each point y_i lying within the pth floating electrode, the indicator function becomes

$$e(y_i) = V_p, \tag{E.67}$$

while Equation E.63 is replaced by the relation

$$\Phi(y_i, 0) = \sum_{n=1}^{N} J_n \phi_n(0) \sin k_n y_i = V_p. \tag{E.68}$$

An additional P equations are provided by the constraint that there is no net normal current at the surface of each floating electrode; thus,

$$\sum_{n=1}^{N} J_n \left(\int_{y_p - w/2}^{y_p + w/2} \sin k_n y \, dy \right) \tanh k_n \delta = 0, \tag{E.69}$$

where y_p is the y-coordinate of the center of the pth floating electrode. The resulting system of $N + P$ linear equations in $N + P$ unknowns can then be solved by a straightforward extension of Equation E.65.

The method of solution of the mixed boundary value problem is, therefore, as follows:

1. For each wavenumber k_n, determine the constants $c_1, \ldots, c_8$ (and thus the nth modal solution) as described in the previous section.

2. Using $\phi_n(0)$ for each mode, solve Equation E.65 for the Fourier coefficients, $J_1, \ldots, J_N$.

3. The solution is then given by the weighted sum of the N modal solutions, each weighted by the corresponding coefficient, J_n.

Software to solve the mixed boundary value problem in this manner for a specified electrode geometry has been developed by Eliot Frank and was used to generate the simulations presented in Chapter IV.

Appendix F

Supplemental Results: Comparison of Mathematical Theory and Experimental Data

This appendix contains supplemental results pertaining to the mathematical simulations and stress measurements (using the two-electrode and six-electrode fixed-wavelength probes) presented in Chapter IV. The results presented here are divided into (1) simulations of additional mechanical variables (fluid pressure and solid displacement) as a function of depth into the tissue, (2) further analysis of the probe data and comparison of theory and data by frequency and thickness, and (3) comparison of stress measurements made with both permeable and impermeable platens.

F.1 Simulations: Fluid Pressure and Solid Displacement

In addition to relative fluid velocity (Figures 4.3–4.5), theoretical fluid pressure and solid displacement amplitudes were also computed as a function of depth into the tissue, for the case of a two-electrode probe at frequencies of 0.001–1.0 Hz applied to the surface of a 1 mm thick specimen (Figures F.1–F.4). At each depth, the maximum value of the variable over the plane at that depth is plotted.

For each frequency, the theoretical fluid pressure amplitude, P, was highest at the surface and decreased with depth into the tissue, eventually reaching a plateau (Figure F.1). However, at higher frequencies, the pressure decreased more rapidly with increasing depth and reached a lower plateau value (Figure F.1, bottom). For example, at 0.001 Hz, the plateau value, which was approximately 24% of the value at the surface, was not reached until a depth of 0.6 mm. In contrast, at 1.0 Hz, the pressure decreased to 0.78% of its surface value by 0.05 mm into the tissue and reached a lower plateau value (approximately 0.27% of the surface pressure).

The maximum vertical displacement, u_z, decreased in amplitude with increasing

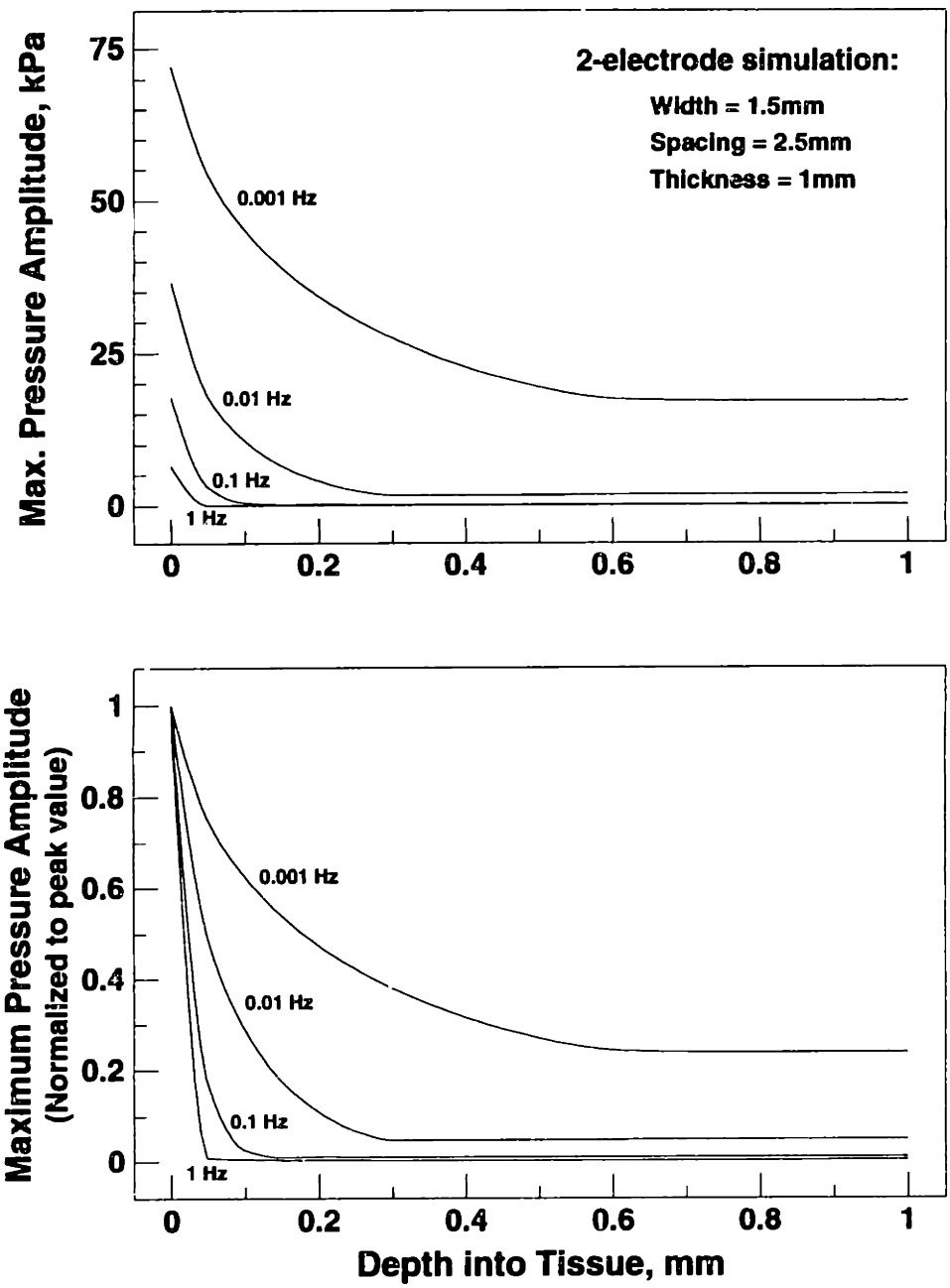

Figure F.1: Theoretical maximum pressure amplitude, P, vs. depth into tissue (1 mm thick) for a two-electrode array, with a current density of 10 A/m^2, computed using the poroelastic model. At each depth, the maximum pressure over the plane at that depth has been plotted. Bottom: Same data normalized to peak value at each frequency.

frequency (Figure F.2, top), ranging from 0.43 μm (0.043% strain) at 0.001 Hz to 2.4 nm (0.00024% strain) at 1.0 Hz. However, the depth into the tissue at which the peak vertical displacement was reached decreased with increasing frequency; while at 0.001 Hz there was a broad peak centered at 0.3 mm, at 1.0 Hz the displacement exhibited a much narrower peak with its maximum value at a depth of only 0.05 mm. Over the range of frequencies used in the probe experiments (0.025–1.0 Hz), the vertical displacement amplitudes predicted by the model were at most approximately 1.3 μm (0.13% strain). Normalizing the vertical fluid velocity by frequency (to yield a characteristic displacement) resulted in a profile that closely resembled the shape of the vertical displacement profile (Figure F.3), with comparable amplitudes. With the total displacement amplitude, $|\vec{u}|$ (Figure F.4), at 0.001 Hz there was a broad peak centered in the middle depths of the tissue, where the horizontal component of displacement, u_y, dominated. However, as the frequency was increased, the peak displacement amplitude shifted toward the surface of the tissue, with a progressively narrower peak (Figure F.4, bottom), dominated by the vertical component.

The shift in peak displacement and relative fluid velocity amplitudes toward the surface with increasing frequency, as well as the narrowing of the pressure, displacement, and velocity profiles, is consistent with a frequency-dependent *mechanical diffusion depth,* which varies as the inverse square root of the frequency (Equation 4.1).

F.2 Comparison of Theory with Data (Fixed-Wavelength Probes)

Because the measured current-generated stress did not vary significantly with cartilage thickness (Figure 4.9), the data from all 15 disks of various thicknesses (0.1–1.8 mm) were pooled for further analysis. At all frequencies, the stress amplitude measured with the six-electrode (λ = 1.68 mm) probe was less than the response with the two-electrode (λ = 5 mm) probe, although the difference was not statistically significant above 0.1 Hz. For the pooled data, the best-fit frequency exponents were -1.01 ± 0.18 for the two-electrode probe and -0.86 ± 0.16 for the six-electrode probe. The *phase* of the stress measured with the two different probes exhibited markedly different behavior with respect to frequency

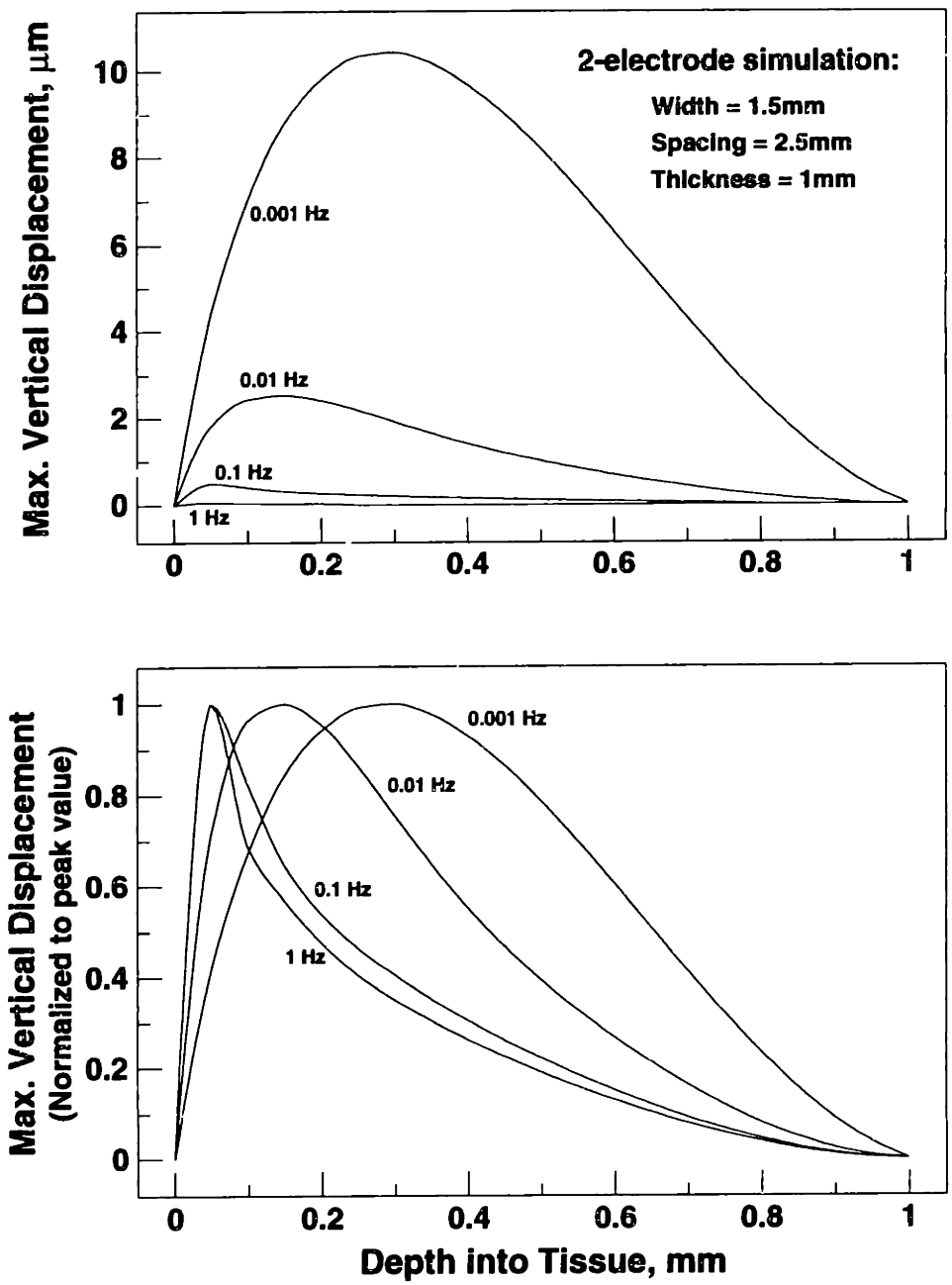

Figure F.2: Theoretical maximum vertical solid displacement amplitude, u_z, vs. depth into tissue for a two-electrode array, with a current density of 10 A/m^2, computed using the poroelastic model. At each depth, the maximum value over the plane at that depth has been plotted. Bottom: Same data normalized to peak value at each frequency.

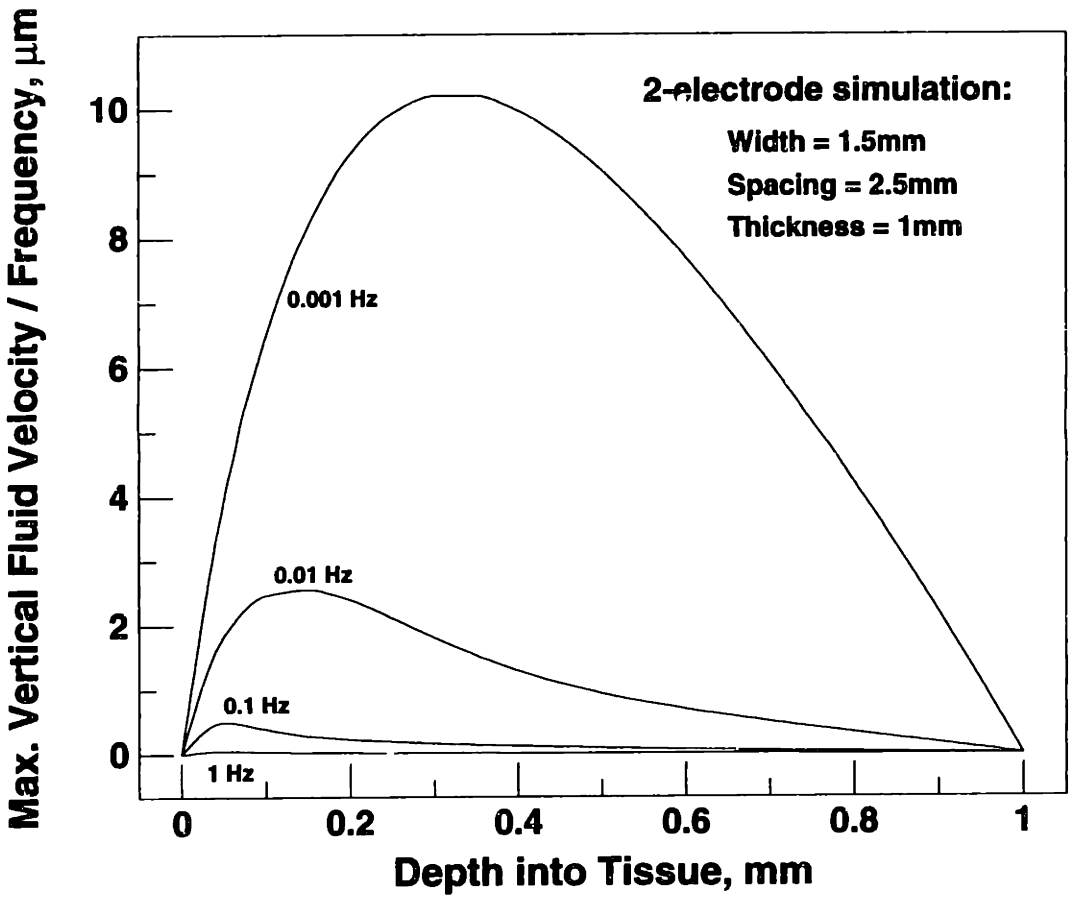

Figure F.3: Theoretical maximum vertical fluid velocity amplitude, normalized to frequency, vs. depth into tissue for a two-electrode array, with a current density of 10 A/m^2, computed using the poroelastic model. At each depth, the maximum value over the plane at that depth has been plotted.

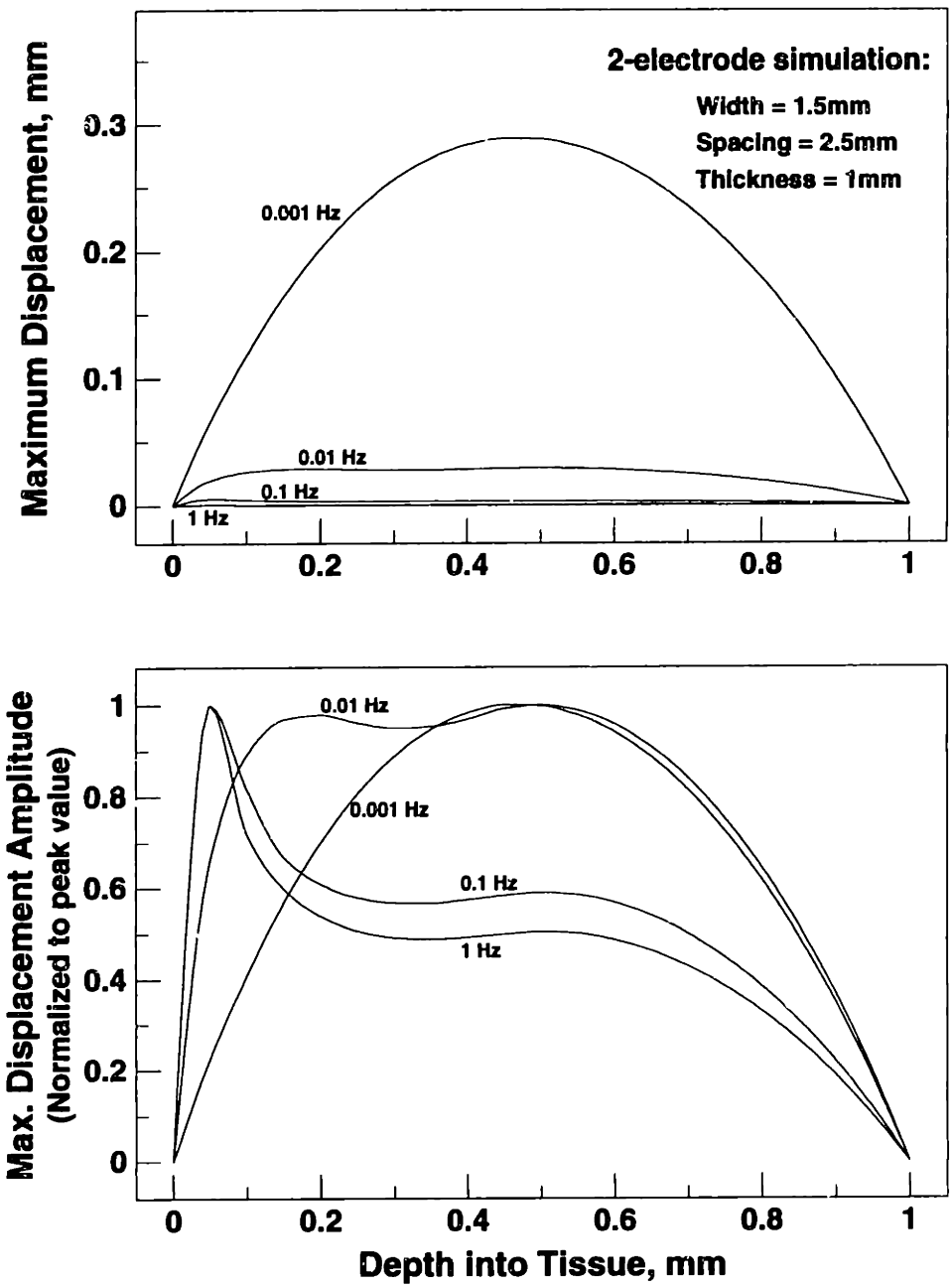

Figure F.4: Theoretical maximum solid displacement amplitude, $|\vec{u}|$ vs. depth into tissue (1 mm thick) for a two-electrode array, with a current density of 10 A/m^2, computed using the poroelastic model. At each depth, the maximum value over the plane at that depth has been plotted. Bottom: Same data normalized to peak value at each frequency.

(Figure F.5, bottom). With long-wavelength excitation, the phase angle remained between 65° and 96° at all frequencies tested. In contrast, with the short-wavelength probe, the phase angle decreased monotonically from 97° at 0.025 Hz to −38° at 1 Hz. Biochemical assay of the disks (not shown) revealed no significant loss of GAG from the tissue during testing.

Comparing the predicted and measured current-generated stress as a function of frequency for each thickness (Figures F.6–F.9) reveals the good agreement between theory and data with respect to frequency dependence, despite the discrepancy by up to three orders of magnitude in the dependence of stress amplitude on cartilage thickness. Furthermore, there is good agreement between the predicted and measured phase angle for the two-electrode probe; with the six-electrode probe, however, the measured phase deviates significantly from the predicted value, particularly at higher frequencies.

F.3 Effect of Platen Type on Current-Generated Stress

In the experiments described in Chapter IV, cartilage disks were placed in the PMMA chamber with one surface in contact with the probe electrodes and the other surface in contact with a 9.5 mm diameter impermeable PMMA platen. However, in preliminary experiments, the response was compared using both a PMMA platen (8.5 mm diameter) and the porous polyethylene platen described in Appendix B and used in previous uniaxial experiments [57]. Current-generated stress (amplitude and phase) was measured via the six-electrode (λ = 1.68 mm) fixed-wavelength probe with 0.1–2 mm thick calf cartilage disks (7 mm diameter) using both platens (Figure F.10). For cartilage thicknesses smaller than the imposed wavelength, both the amplitude and phase of the response were different with the two platen materials. The stress amplitude was *lower* when measured with the PMMA platen, while the phase angle was approximately 0° with the PMMA platen (as compared to 118–128° with the porous platen); this phase behavior was *not* seen in the experiments in which thin cartilage disks were tested using the 9.5 mm diameter PMMA platen (Figure F.6). With thicker cartilage, however, the amplitude and phase of the current-

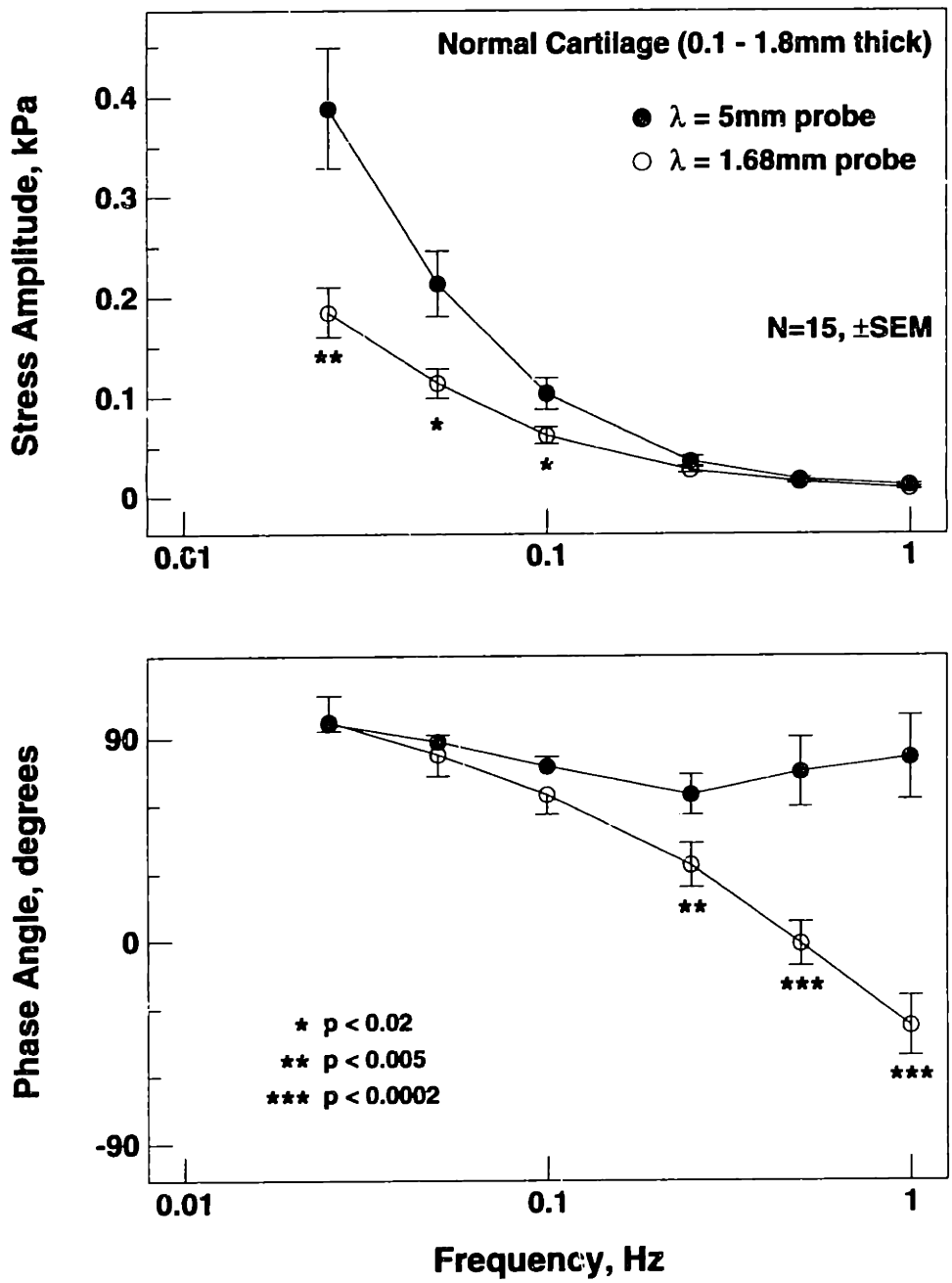

Figure F.5: Current-generated stress (amplitude and phase) measured in calf cartilage disks (pooled data for thicknesses of 0.1–1.8 mm) using both the two-electrode (λ = 5 mm) and six-electrode (λ = 1.68 mm) fixed-wavelength probes with an applied current density amplitude of 10 A/m^2. All data points are mean ± SEM for N = 15 (4 disks each of thickness 0.1, 0.18, and 1.0 mm; 3 disks of thickness 1.8 mm); p values are for long- vs. short-wavelength (by ANOVA).

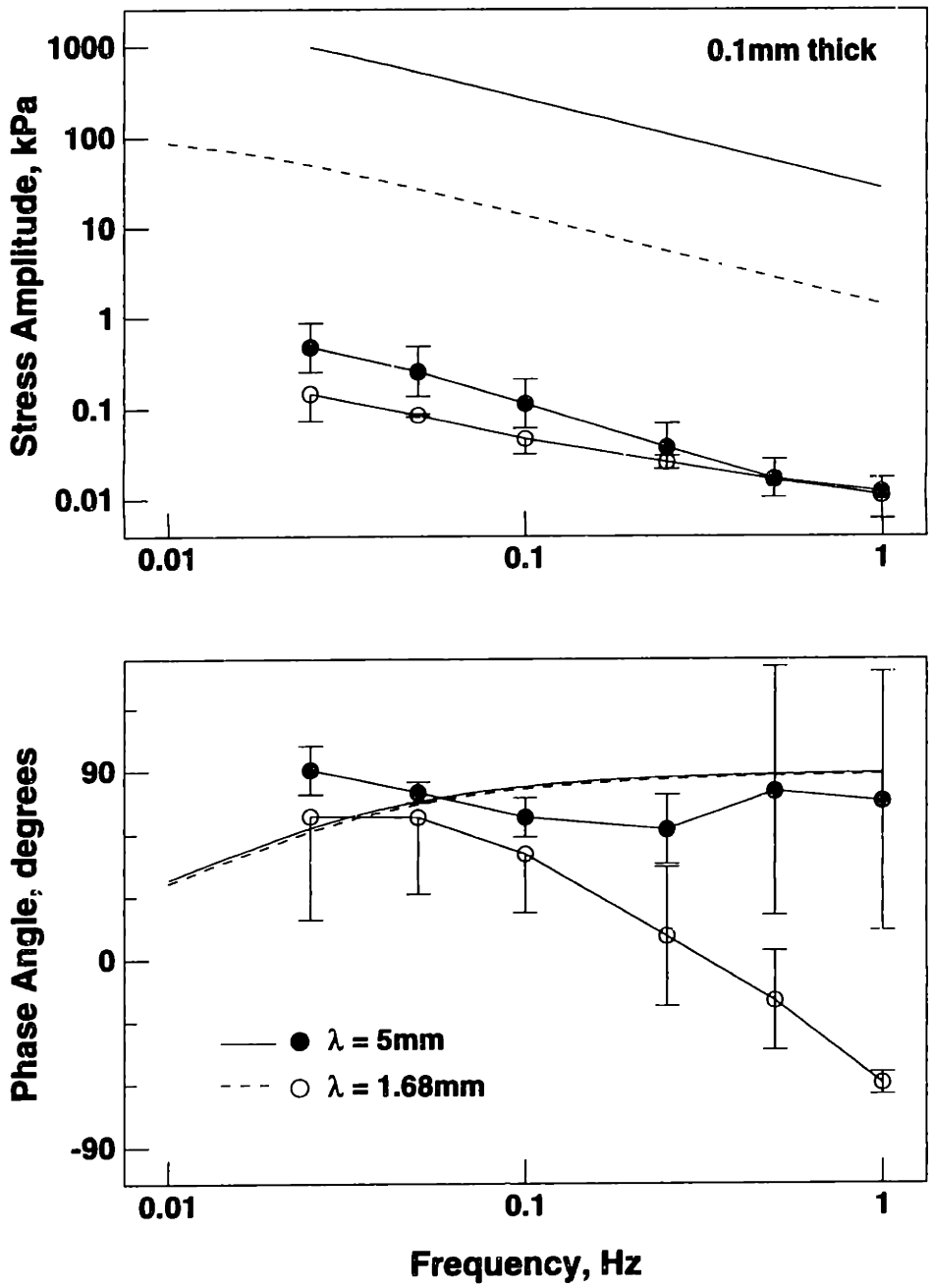

Figure F.6: Comparison of measured current-generated stress (amplitude and phase), using both the two- and six-electrode fixed-wavelength probes (circles) with 0.1 mm thick cartilage, with theoretical normal stress (solid and dashed lines) predicted by poroelastic model.

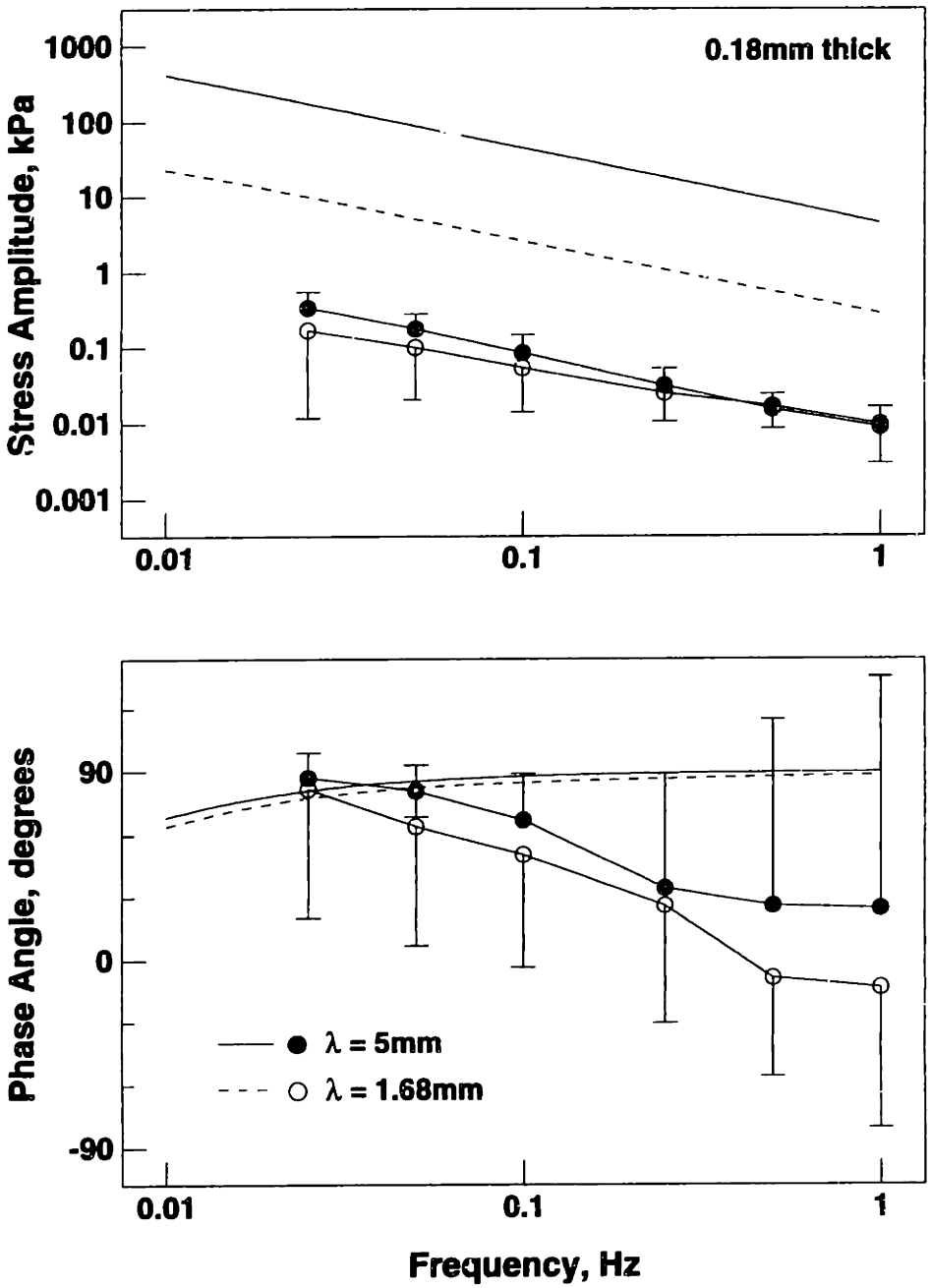

Figure F.7: Comparison of measured current-generated stress (amplitude and phase), using both the two- and six-electrode fixed-wavelength probes (circles) with 0.18 mm thick cartilage, with theoretical normal stress (solid and dashed lines) predicted by poroelastic model.

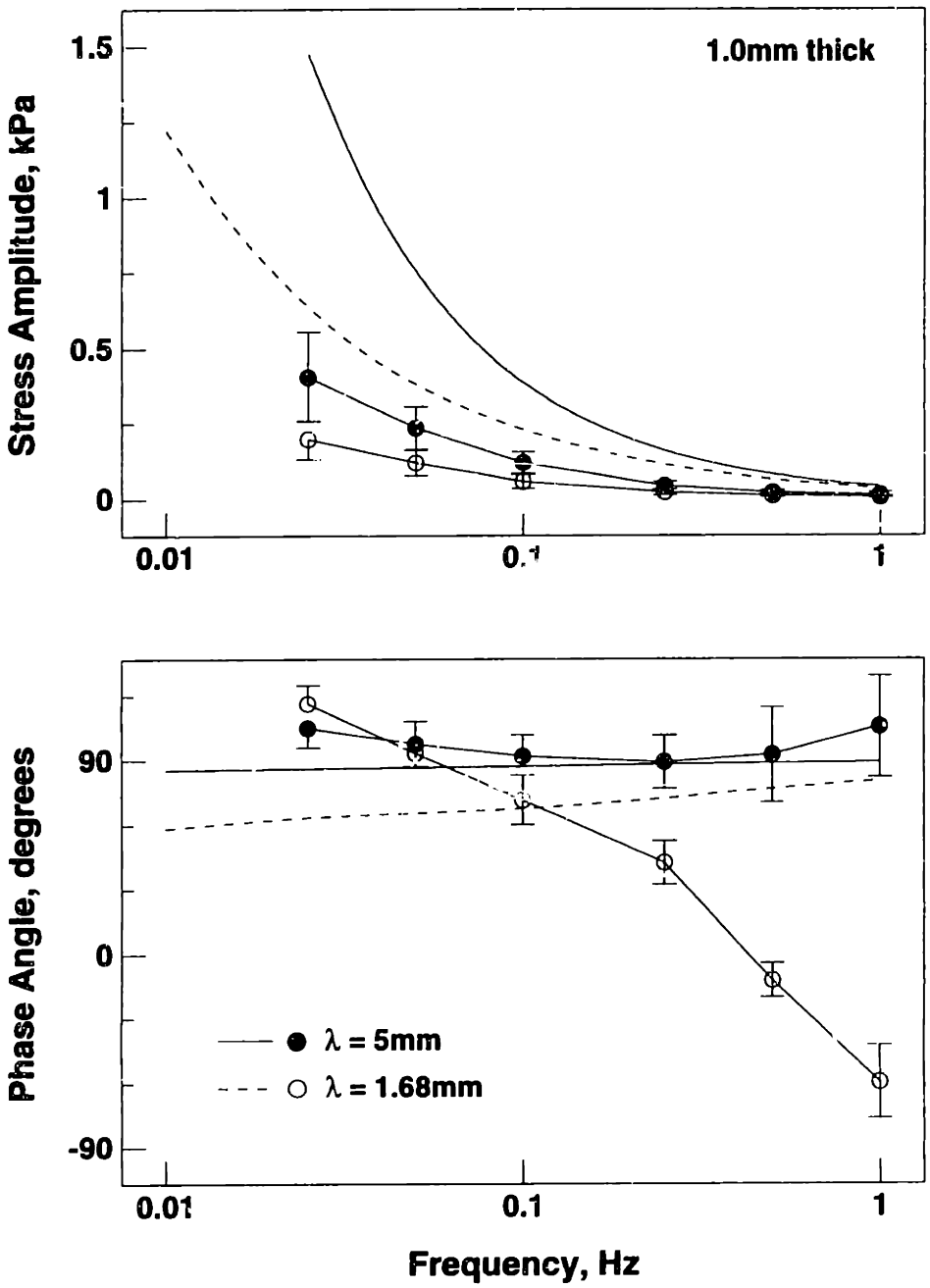

Figure F.8: Comparison of measured current-generated stress (amplitude and phase), using both the two- and six-electrode fixed-wavelength probes (circles) with 1.0 mm thick cartilage, with theoretical normal stress (solid and dashed lines) predicted by poroelastic model.

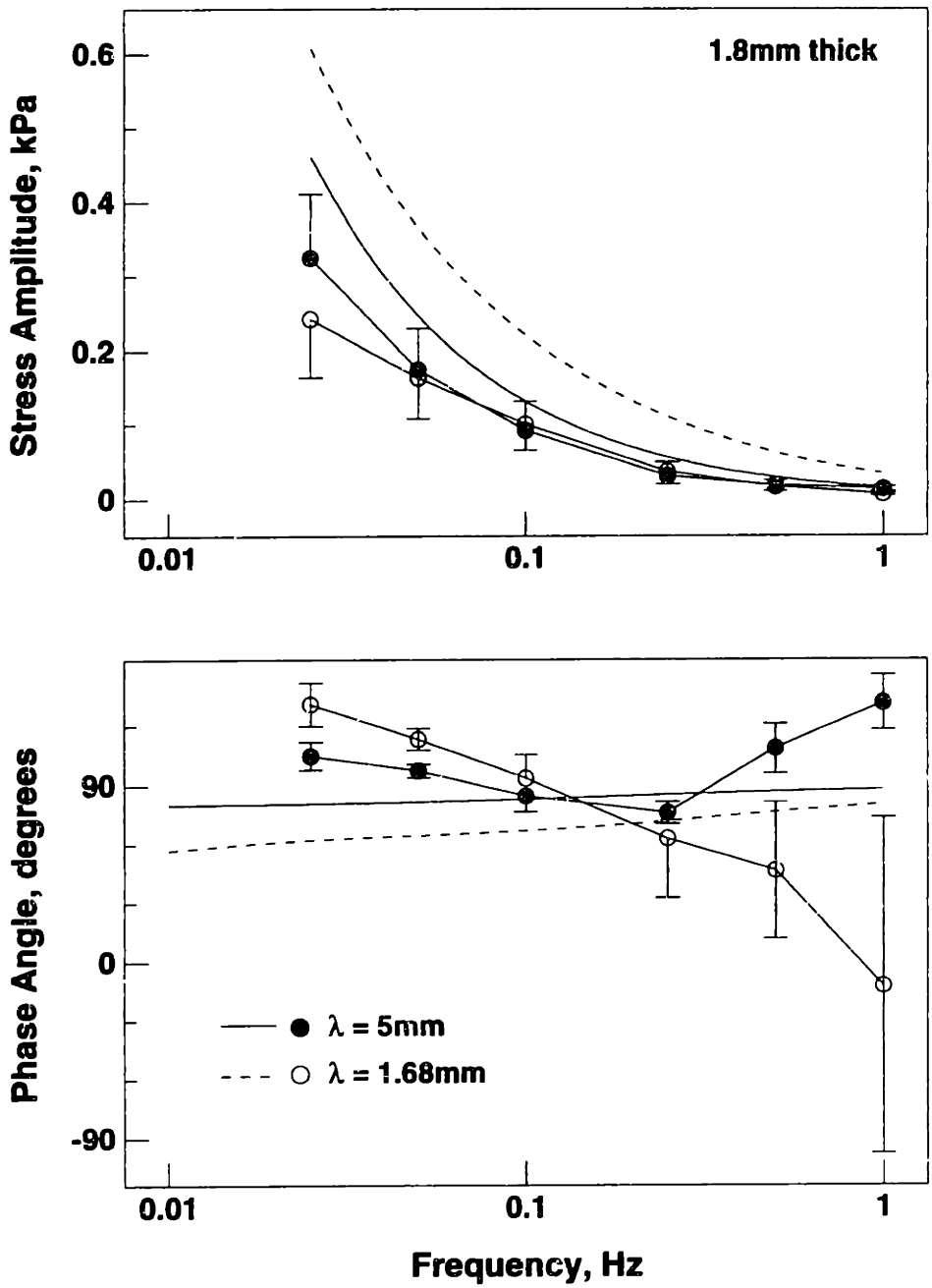

Figure F.9: Comparison of measured current-generated stress (amplitude and phase), using both the two- and six-electrode fixed-wavelength probes (circles) with 1.8 mm thick cartilage, with theoretical normal stress (solid and dashed lines) predicted by poroelastic model.

generated stress did *not* vary with the type of platen used. The difference in response between the two platen types observed in thinner cartilage is consistent with a current penetration depth proportional to the imposed wavelength. Thus, with a thick enough specimen, the properties of the tissue (and the lower cartilage boundary) lying "far" from the articular surface do not influence the developed stress response (because the current does not penetrate into these regions).

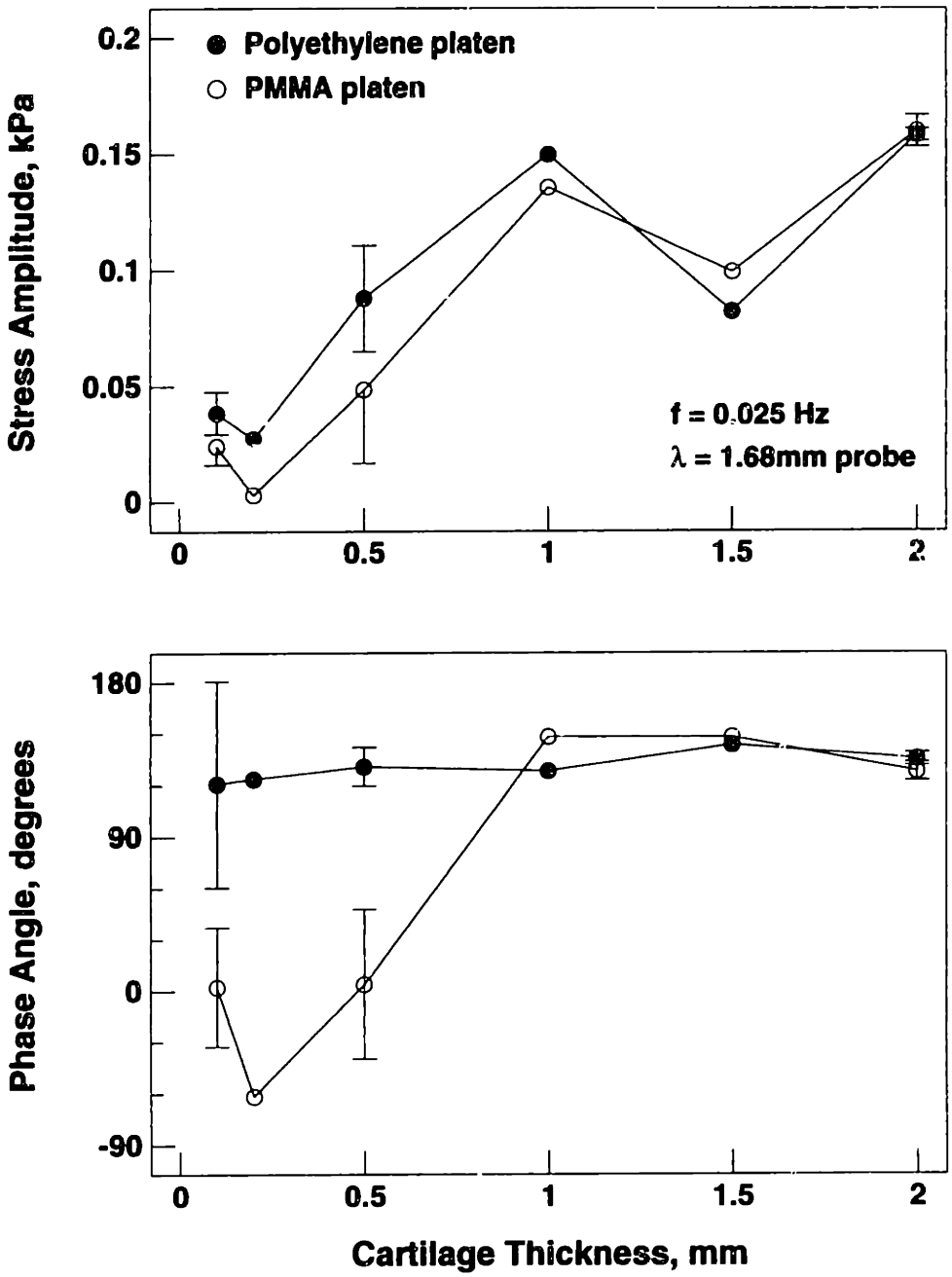

Figure F.10: Current-generated stress (amplitude and phase) versus cartilage thickness, measured using the λ = 1.68 mm probe with both porous polyethylene and impermeable PMMA platens and an applied current density amplitude of 10 A/m^2. Results are shown for a single frequency (0.025 Hz); error bars indicate SD (N = 2). For thicknesses of 0.2, 1.0, and 1.5 mm, only a single disk was tested.

Appendix G

Supplemental Data: Measurement of Cartilage Impedance Using the Surface Probe

This appendix contains supplemental data pertaining to the impedance experiments described in Chapter V. Impedance (at 1 kHz) was measured in calf cartilage disks using both the two- and six-electrode fixed-wavelength probes as well as the multiple-wavelength probe configured for short-, long-, and very long-wavelength excitation (Figure 5.3).

G.1 Fixed-Wavelength Probes

Four cartilage-bone plugs (9.5 mm diameter) were tested with the two-electrode and six-electrode probes, with and without with tape over "non-active" region of the electrodes (i.e., the area not in contact with the cartilage specimen), as described in Chapter V. Disks (9.5 mm diameter) of thickness 0.1, 0.2, 0.5, and 1.0 mm were sequentially cut from each plug; subsequently, a concentric 7 mm disk was cut from each 9.5 mm disk using a metal punch. For each thickness, four combinations of disk and platen diameter were tested: (1) 9.5 mm diameter disk with 9.5 mm diameter PMMA platen, (2) 7 mm disk with 9.5 mm platen, (3) 7 mm disk with 7 mm PMMA platen, and (4) 7 mm disk with 7 mm platen, with the Teflon collar in place around the disk and platen. With the two-electrode probe with tape, only 7 mm diameter disks were tested (using the 7 mm platen).

With both the two-electrode probe and the six-electrode probe (with and without tape over the electrodes), the difference in measured impedance between the 9.5 mm disks and 7 mm disks tested with the 9.5 mm diameter platen was not statistically significant, as determined by ANOVA (Figures G.1, G.3, G.4, top). However, the impedance of 7 mm diameter disks tested with the 7 mm platen was significantly higher when the Teflon collar was in place (Figures G.1–G.4, bottom). When tape was placed over the electrodes, this difference was less pronounced but was still statistically significant.

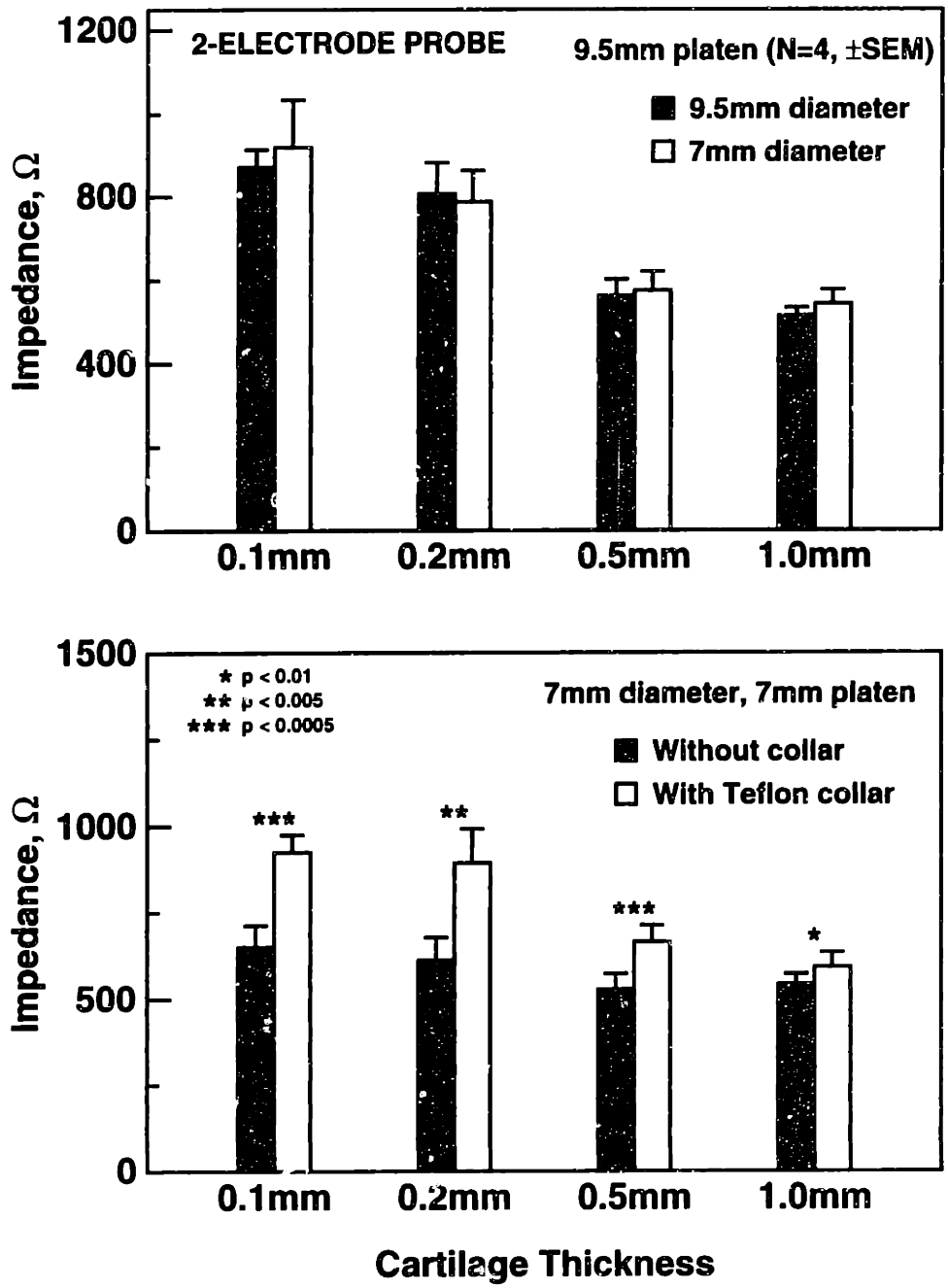

Figure G.1: Electrical impedance measured in 7 mm and 9.5 mm diameter disks (0.1–1.0 mm thick) of calf cartilage using the two-electrode probe. All p-values are for Teflon collar vs. no collar (by ANOVA); differences between the 9.5 mm and 7 mm diameter disks tested with the 9.5 mm platen (top) were not statistically significant. Each bar is mean + SEM for $N = 4$ plugs.

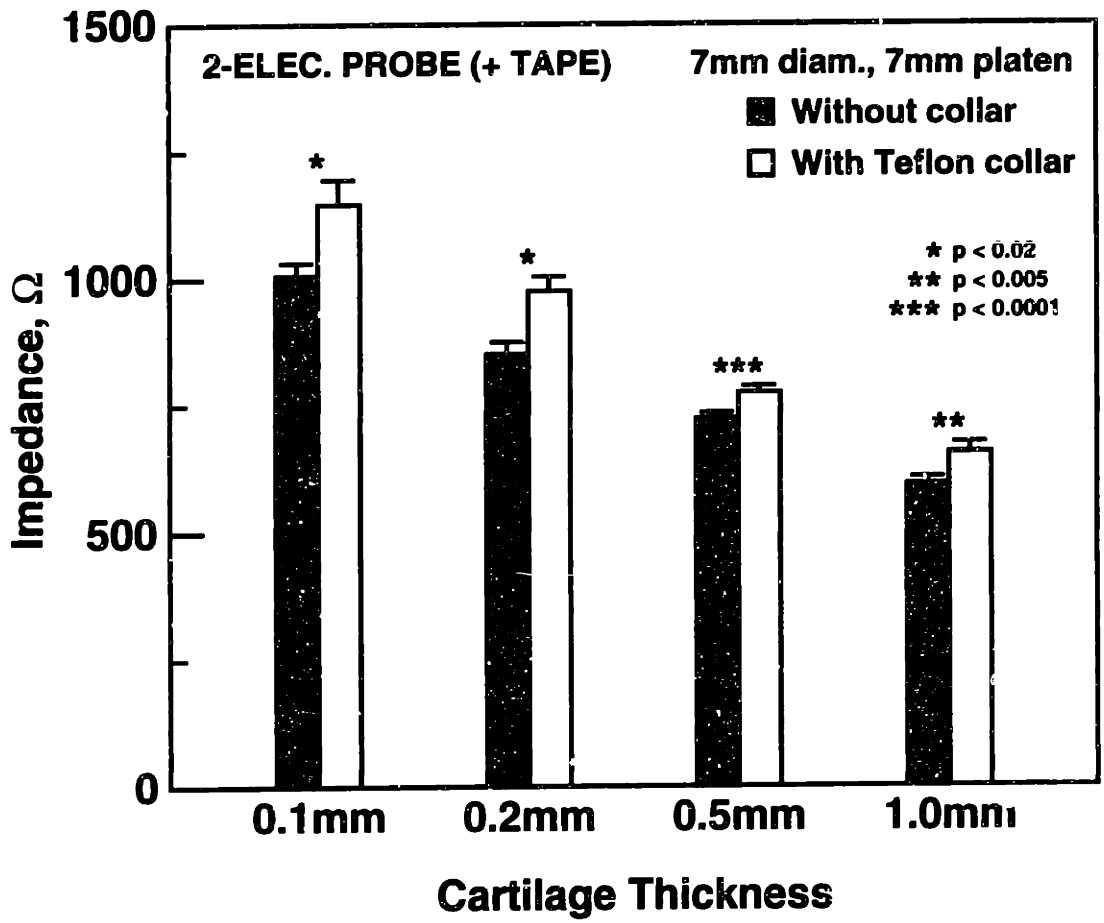

Figure G.2: Electrical impedance measured in 7 mm diameter disks (0.1–1.0 mm thick) of calf cartilage using the two-electrode fixed-wavelength probe with tape over the electrode area not in contact with the cartilage. Each bar is mean + SEM for $N = 4$ plugs; all p-values are for Teflon collar vs. no collar (by ANOVA).

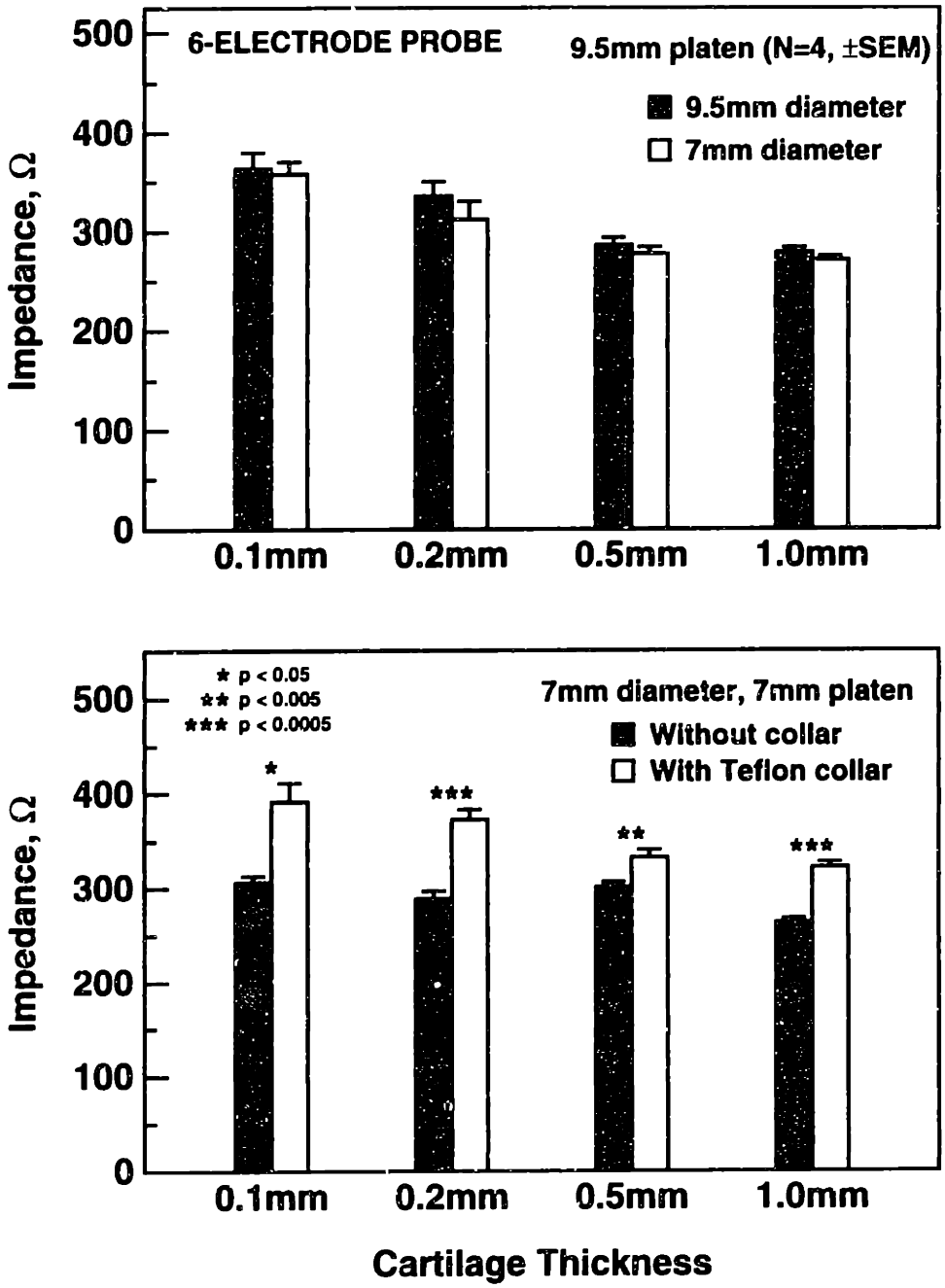

Figure G.3: Electrical impedance measured in 7 mm and 9.5 mm diameter disks (0.1–1.0 mm thick) of calf cartilage using the six-electrode fixed-wavelength probe. All p-values are for Teflon collar vs. no collar (by ANOVA); differences between the 9.5 mm and 7 mm diameter disks tested with the 9.5 mm platen (top) were not statistically significant. Each bar is mean + SEM for $N = 4$ plugs.

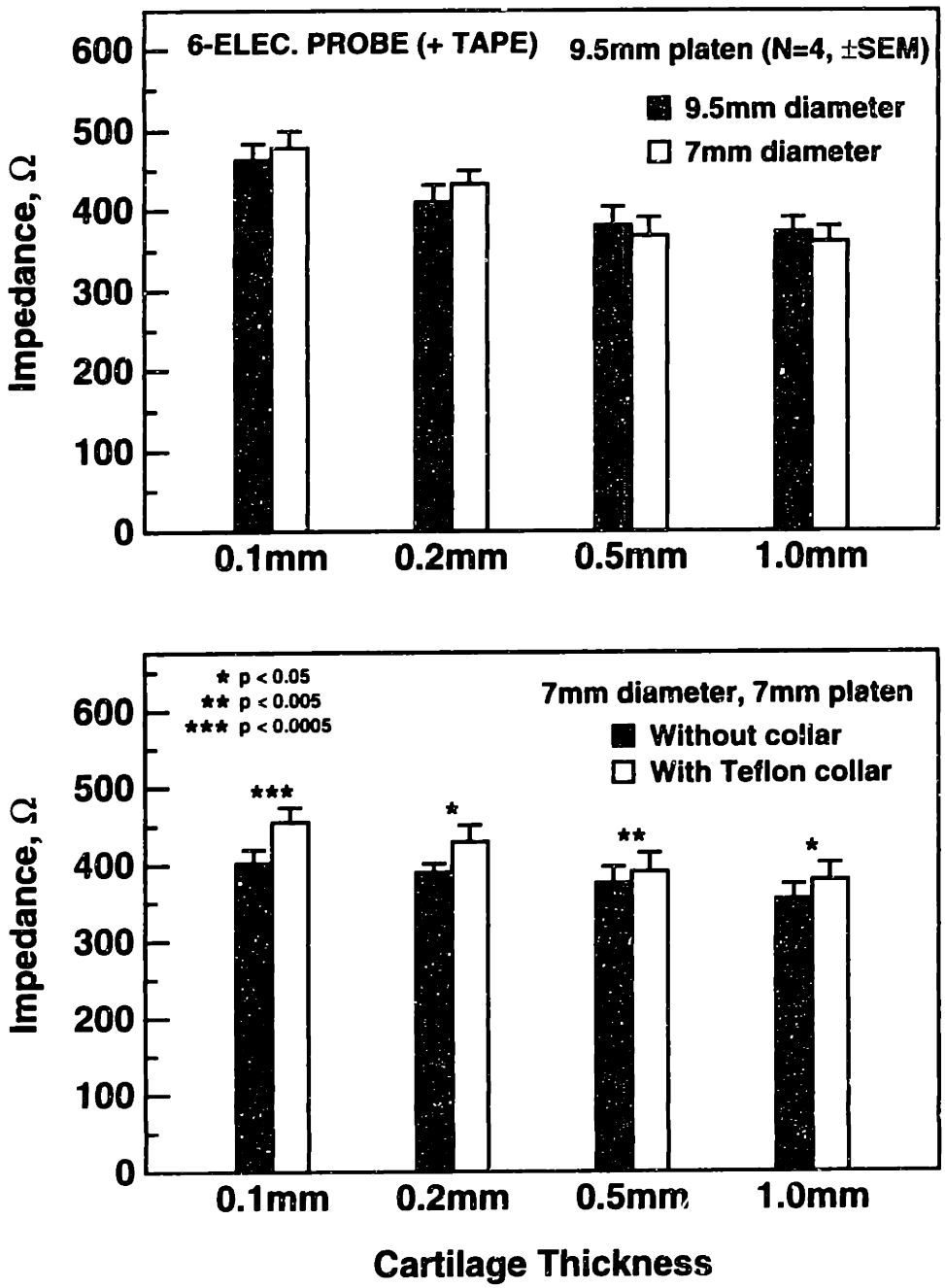

Figure G.4: Electrical impedance measured in 7 mm and 9.5 mm diameter disks (0.1–1.0 mm thick) of calf cartilage using the six-electrode fixed-wavelength probe with tape over the electrode area not in contact with the cartilage. All p-values are for Teflon collar vs. no collar (by ANOVA); differences between the 9.5 mm and 7 mm diameter disks tested with the 9.5 mm platen (top) were not statistically significant. Each bar is mean + SEM for $N = 4$ plugs.

G.2 Multiple-Wavelength Probe

The same protocol as described above for the fixed-wavelength probes was also used with a single multiple-wavelength probe. For each test condition, the probe was sequentially configured for short-, long-, and very long-wavelength excitation (Figure 5.3). With all three configurations, there was no statistically significant difference between the impedance measured in 9.5 mm and 7 mm diameter disks with the 9.5 mm platen (Figures G.5–G.7, top). However, the impedance of 7 mm diameter disks tested with the 7 mm platen was significantly higher when the Teflon collar was in place (Figures G.5–G.7, bottom). This difference was most pronounced with the very long-wavelength configuration tested with thin (0.1–0.2 mm) disks.

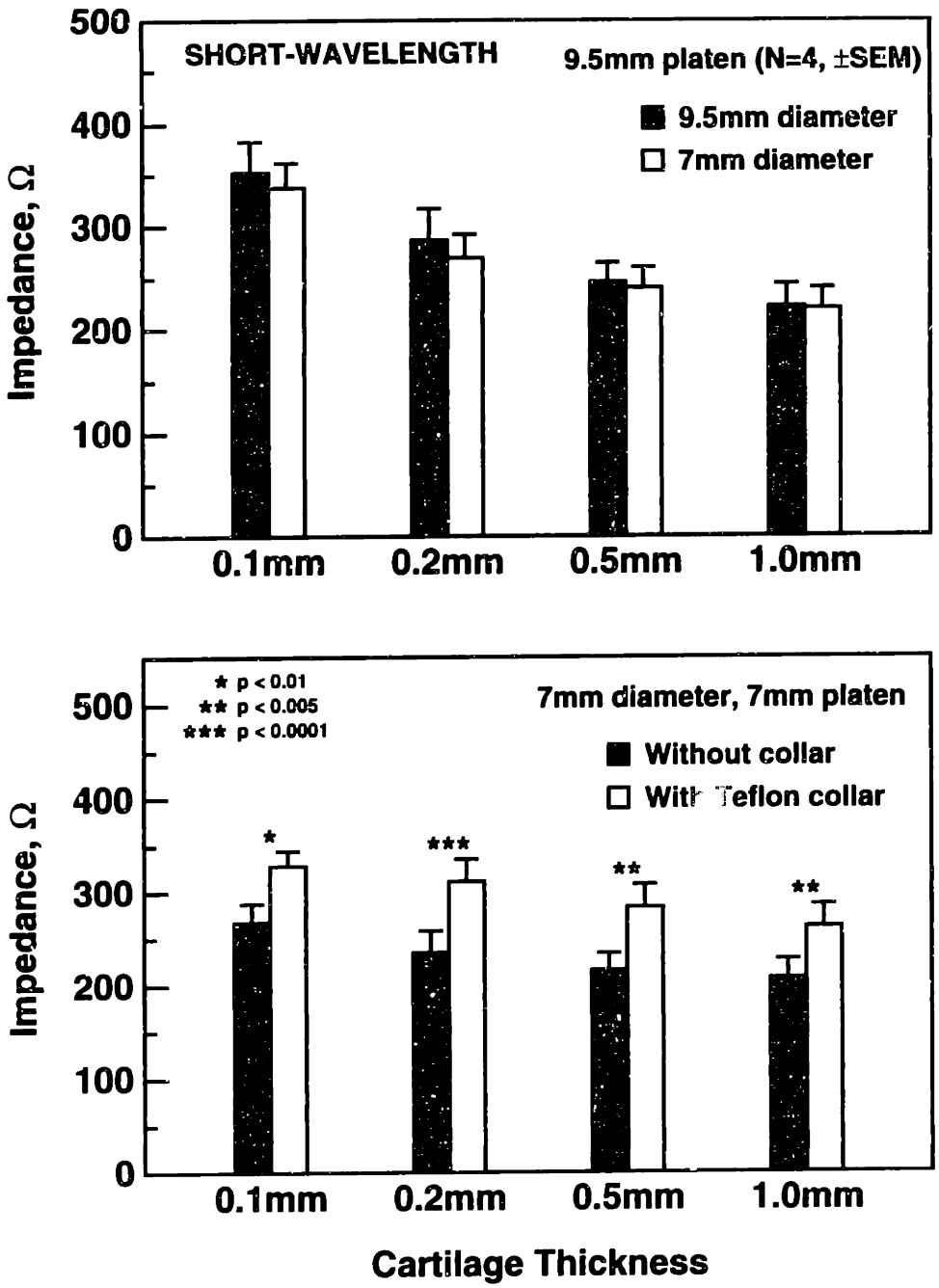

Figure G.5: Electrical impedance measured in 7 mm and 9.5 mm diameter disks (0.1–1.0 mm thick) of calf cartilage using the short-wavelength configuration (Figure 5.3A) of the multiple-wavelength probe. All p-values are for Teflon collar vs. no collar (by ANOVA); differences between the 9.5 mm and 7 mm diameter disks tested with the 9.5 mm platen (top) were not statistically significant. Each bar is mean + SEM for $N = 4$ plugs.

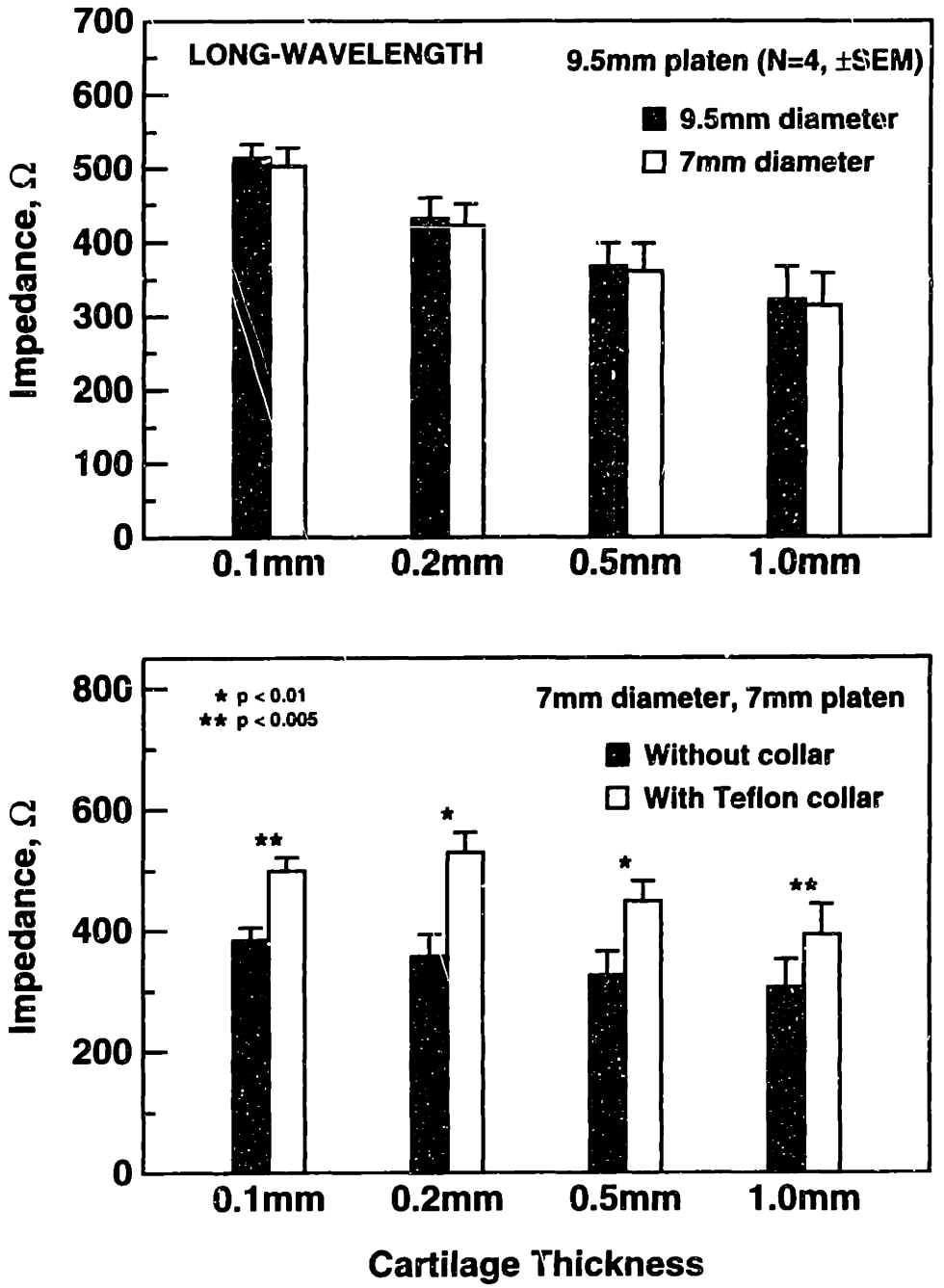

Figure G.6: Electrical impedance measured in 7 mm and 9.5 mm diameter disks (0.1–1.0 mm thick) of calf cartilage using the long-wavelength configuration (Figure 5.3B) of the multiple-wavelength probe. All p-values are for Teflon collar vs. no collar (by ANOVA); differences between the 9.5 mm and 7 mm diameter disks tested with the 9.5 mm platen (top) were not statistically significant. Each bar is mean + SEM for N = 4 plugs.

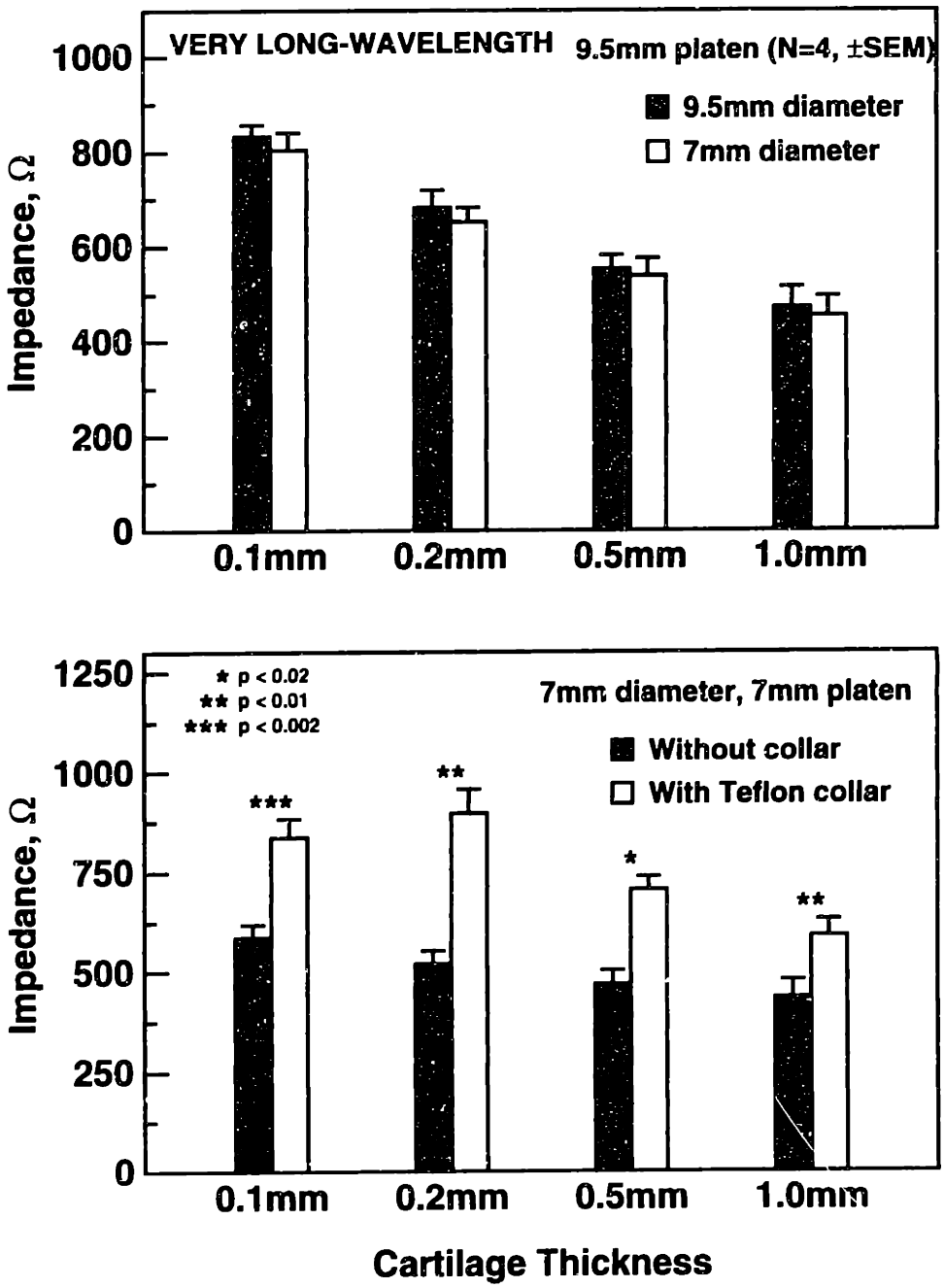

Figure G.7: Electrical impedance measured in 7 mm and 9.5 mm diameter disks (0.1–1.0 mm thick) of calf cartilage using the very long-wavelength configuration (Figure 5.3C) of the multiple-wavelength probe. All p-values are for Teflon collar vs. no collar (by ANOVA); differences between the 9.5 mm and 7 mm diameter disks tested with the 9.5 mm platen (top) were not statistically significant. Each bar is mean + SEM for $N = 4$ plugs.

References

[1] Adams ME, Wallace CJ: Quantitative imaging of osteoarthritis. *Semin Arthritis Rheum*, 6 (Suppl. 2):26–39, 1991

[2] Aisen AM, McCune WJ, MacGuire A, Carson PL, Silver TM, Jafri SZ, Martel W: Sonographic evaluation of the cartilage of the knee. *Radiology*, 153:781–784, 1984

[3] Altman R *et al.*: Development of criteria for the classification and reporting of osteoarthritis: Classification of osteoarthritis of the knee. *Arthritis Rheum*, 29:1039–1049, 1986

[4] Altman RD, Gray R: Diagnostic and therapeutic uses of the arthroscope in rheumatoid arthritis and osteoarthritis. *Am J Med*, 75 (Oct. 31):50–55, 1983

[5] Amstutz HC, Grigoris P, Safran MR, Grecula MJ, Campbell PA, Schmalzreid TP: Precision-fit surface hemiarthroplasty for femoral head osteonecrosis. *J Bone Joint Surg [Br]*, 76-B:423–427, 1994

[6] Anderson JC, Eriksson C: Piezoelectric properties of dry and wet bone. *Nature*, 227:491–492, 1970

[7] Armstrong CG, Mow VC: Variations in the intrinsic mechanical properties of human articular cartilage with age, degeneration, and water content. *J Bone Joint Surg [Am]*, 64-A:88–94, 1982

[8] Bassett CAL, Pawluk RJ: Electrical behavior of cartilage during loading. *Science*, 178:982–983, 1972

[9] Ben-Yishay A, Grande DA, Schwarz RE, Menche D, Pitman MD: Repair of articular cartilage defects with collagen-chondrocyte allografts. *Tissue Eng*, 1:119–133, 1995

[10] Berkenblit SI, Frank EH, Bonassar LJ, Bombard DL, Duffin NJ, Grodzinsky AJ: Electrokinetic methods for arthroscopic detection of cartilage degeneration in synovial joints. In *Proc. 16th International Conference*, pp 746–747. IEEE Engineering in Medicine and Biology Society, 1994

[11] Berkenblit SI, Frank EH, Grodzinsky AJ: Quantitative assessment of cartilage degradation via nondestructive surface electromechanical spectroscopy. *Trans Orthop Res Soc*, 19:214, 1994

[12] Berkenblit SI, Frank EH, Grodzinsky AJ: Spatial localization of cartilage degradation using variable-wavelength surface spectroscopy. *Trans Orthop Res Soc*, 20:98, 1995

[13] Berkenblit SI, Frank EH, Grodzinsky AJ: Spatial localization of cartilage degradation using electromechanical surface spectroscopy with variable wavelength and frequency. *J Orthop Res*, 1996. (Accepted for publication)

[14] Berkenblit SI, Frank EH, Salant EP, Grodzinsky AJ: Nondestructive detection of cartilage degeneration using electromechanical surface spectroscopy. *J Biomech Eng*, 116:384–392, 1994

[15] Berkenblit SI, Quinn TM, Grodzinsky AJ: Molecular electromechanics of cartilaginous tissues and polyelectrolyte gels. *J Electrostatics*, 34:307–330, 1995

[16] Biot MA: General theory of three-dimensional consolidation. *J Appl Phys*, 12:155–164, 1941

[17] Biot MA: Theory of elasticity and consolidation for a porous anisotropic solid. *J Appl Phys*, 26:182–185, 1955

[18] Biot MA: General solutions of the equations of elasticity and consolidation for a porous material. *J Appl Mech*, 23:91–96, 1956

[19] Black D, Duncan A, Robins SP: Quantitative analysis of the pyridinium crosslinks of collagen in urine using ion-paired reversed-phase high-performance liquid chromatography. *Anal Biochem*, 169:197–203, 1988

[20] Bland JH, Cooper SM: Osteoarthritis: A review of the cell biology involved and evidence for reversibility. Management rationally related to known genesis and pathophysiology. *Semin Arthritis Rheum*, 14:106–133, 1984

[21] Bollet AJ, Handy JR, Sturgill BC: Chondroitin sulfate concentration and protein-polysaccharide composition of articular cartilage in osteoarthritis. *J Clin Invest*, 42:853–859, 1963

[22] Bollet AJ, Nance JL: Biochemical findings in normal and osteoarthritic articular cartilage. II. Chondroitin sulfate concentration and chain length, water, and ash content. *J Clin Invest*, 45:1170–1177, 1966

[23] Bombard DL: A surface probe for *in situ* detection of cartilage degradation via electromechanical spectroscopy. Master's thesis, MIT, Cambridge, MA, 1995

[24] Bonassar LJ *et al.*: *In vivo* effects of stromelysin on the composition and physical properties of rabbit articular cartilage in the presence and absence of a synthetic inhibitor. *Arthritis Rheum*, 38:1678–1686, 1995

[25] Bowes JH, Kenten RH: The amino-acid composition and titration curve of collagen. *Biochem J*, 43:358–365, 1948

[26] Brandt KD: Enhanced extractability of articular cartilage proteoglycans in osteoarthrosis. *Biochem J*, 143:475–478, 1974

[27] Brandt KD: A pessimistic view of serologic markers for diagnosis and management of osteoarthritis: Biochemical, immunologic, and clinicopathologic barriers. *J Rheumatol*, 16 (Suppl. 18):39–42, 1989

[28] Brandt KD, Fife RS, Braunstein EM, Katz B: Radiographic grading of the severity of knee osteoarthritis: Relation of the Kellgren and Lawrence grade to a grade based on joint space narrowing, and correlation with arthroscopic evidence of articular cartilage degeneration. *Arthritis Rheum*, 34:1381–1386, 1991

[29] Brandt KD, Palmoski M: Organization of ground substance proteoglycans in normal and osteoarthritic knee cartilage. *Arthritis Rheum*, 19:209–215, 1976

[30] Brittberg M, Lindahl A, Nilsson A, Ohlsson C, Isaksson O, Peterson L: Treatment of deep cartilage defects in the knee with autologous chondrocyte transplantation. *N Engl J Med*, 331:889–895, 1994

[31] Broadhurst MG, Davis GT: Physical basis for piezoelectricity in PVDF. *Ferroelectrics*, 60:3–13, 1984

[32] Broadhurst MG, Davis GT: Piezo- and pyroelectric properties. In Sessler GM, editor, *Electrets*, volume 33 of *Topics in Applied Physics*, pp 285–319. Springer-Verlag, Berlin, 1987

[33] Broom ND, Silyn-Roberts H: Collagen-collagen versus collagen-proteoglycan interactions in the determination of cartilage strength. *Arthritis Rheum*, 33:1512–1517, 1990

[34] Buckwalter J, Hunziker E, Rosenberg L, Coutts R, Adams M, Eyre D: Articular cartilage: Composition and structure. In Woo SLY, Buckwalter JA, editors, *Injury and Repair of the Musculosketal Soft Tissues*, pp 405–425. American Academy of Orthopaedic Surgeons, Park Ridge, IL, 1987

[35] Buckwalter JA, Lohmander S: Operative treatment of osteoarthrosis. *J Bone Joint Surg [Am]*, 76-A:1405–1418, 1994

[36] Burgeson RE, Nimni ME: Collagen types: Molecular structure and tissue distribution. *Clin Orthop*, 282:250–272, 1992

[37] Burks RT: Arthroscopy and degenerative arthritis of the knee: A review of the literature. *Arthroscopy*, 6:43–47, 1990

[38] Butt WP, McIntyre JL: Double-contrast arthrography of the knee. *Radiology*, 92:487–499, 1969

[39] Byers PD, Maroudas A, Oztop F, Stockwell RA, Venn MF: Histological and biochemical studies on cartilage from osteoarthritic femoral heads with special reference to surface characteristics. *Connect Tissue Res*, 5:41–49, 1977

[40] Campion GV, McCrae F, Schnitzer TJ, Lenz ME, Dieppe PA, Thonar EJA: Levels of keratan sulfate in the serum and synovial fluid of patients with osteoarthritis of the knee. *Arthritis Rheum*, 34:1254–1259, 1991

[41] Caterson B, Calabro T, Hardingham TE: Markers of osteoarthritis: Immunological aspects. In Brandt KD, editor, *Cartilage Changes in Osteoarthritis*, pp 89–97. Indiana University School of Medicine, Indianapolis, Indiana, 1990

[42] Chan WP, Lang P, Stevens MP, Sack K, Majumdar S, Stoller DW, Basch C, Genant HK: Osteoarthritis of the knee: Comparison of radiography, CT, and MR imaging to assess extent and severity. *AJR Am J Roentgenol*, 157:799–806, 1991

[43] Chu ML, Gradisar IA, Railey MR, Bowling GF: Detection of knee joint diseases using acoustical pattern recognition technique. *J Biomechanics*, 9:111–114, 1976

[44] Chun LE, Koob TJ, Eyre DR: Sequential enzymic dissection of the proteoglycan complex from articular cartilage. *Trans Orthop Res Soc*, 11:96, 1986

[45] Chwang SB: Electromechanical properties of a piezo film in probe for cartilage degeneration. Bachelor's thesis, MIT, Cambridge, MA, 1990

[46] Coombs CF: *Printed Circuits Handbook*. McGraw-Hill, New York, 3rd edition, 1988

[47] Crank J: *The Mathematics of Diffusion*. Oxford University Press, New York, 2nd edition, 1975

[48] Dashefsky JH: Arthroscopic measurement of chondromalacia of patella cartilage using a microminiature pressure transducer. *Arthroscopy*, 3:80–85, 1987

[49] DeGroot SR, Mazur P: *Nonequilibrium Thermodynamics*. North-Holland, Amsterdam, 1962

[50] Dieppe P, Cushnaghan J, Young P, Kirwan J: Prediction of the progression of joint space narrowing in osteoarthritis of the knee by bone scintigraphy. *Ann Rheum Dis*, 52:557–563, 1993

[51] Doege KJ, Sasaki M, Kimura T, Yamada Y: Complete coding sequence and deduced primary structure of the human cartilage large aggregating proteoglycan, aggrecan. *J Biol Chem*, 266:894–902, 1991

[52] Doyle DV: Tissue calcification and inflammation in osteoarthritis. *J Pathol*, 136:199–216, 1982

[53] Drake MP, Davison PF, Schmitt FO: Action of proteolytic enzymes on tropocollagen and insoluble collagen. *Biochem*, 5:301–312, 1966

[54] Eastman Kodak Co., Rochester, NY: *Photofabrication Methods with Kodak Photoresists*, 1979. (Technical Manual)

[55] Egund N, Frost S, Brismar J, Gustafson T: Radiography and scintigraphy in the assessment of early gonarthrosis. *Acta Radiol*, 29:451–455, 1988

[56] Eisenberg SR, Grodzinsky AJ: Swelling of articular cartilage and other connective tissues: Electromechanochemical forces. *J Orthop Res*, 3:148–159, 1985

[57] Eisenberg SR, Grodzinsky AJ: The kinetics of chemically induced nonequilibrium swelling of articular cartilage and corneal stroma. *J Biomech Eng*, 109:79–89, 1987

[58] Eisenberg SR, Grodzinsky AJ: Electrokinetic micromodel of extracellular matrix and other polyelectrolyte networks. *PhysicoChem Hydrodynamics*, 10:517–539, 1988

[59] Eyre DR, Wu J, Woods P: Cartilage-specific collagens: Structural studies. In Kuettner KE, Schleyerbach R, Peyron JG, Hascall VC, editors, *Articular Cartilage and Osteoarthritis*, pp 119–131. Raven Press, New York, 1992

[60] Farndale RW, Buttle DJ, Barrett AJ: Improved quantitation and discrimination of sulphated glycosaminoglycans by use of dimethylmethylene blue. *Biochim Biophys Acta*, 883:173–177, 1986

[61] Felson DT: Osteoarthritis. *Rheum Dis Clin North Am*, 16:499–512, 1990

[62] Fife RS, Brandt KD, Braunstein EM, Katz BP, Shelbourne KD, Kalasinski LA, Ryan S: Relationship between arthroscopic evidence of cartilage damage and radiographic evidence of joint space narrowing in early osteoarthritis of the knee. *Arthritis Rheum*, 34:377–382, 1991

[63] Frank EH: *Electromechanics of Normal and Degenerated Cartilage: Poroelastic Behavior and Electrokinetic Mechanisms*. PhD thesis, MIT, Cambridge, MA, 1987

[64] Frank EH, Grodzinsky AJ: Cartilage electromechanics I: Electrokinetic transduction and the effects of electrolyte pH and ionic strength. *J Biomechanics*, 20:615–627, 1987

[65] Frank EH, Grodzinsky AJ: Cartilage electromechanics II: A continuum model of cartilage electrokinetics. *J Biomechanics*, 20:629–639, 1987

[66] Frank EH, Grodzinsky AJ, Koob TJ, Eyre DR: Streaming potential: A sensitive index of enzymatic degradation in articular cartilage. *J Orthop Res*, 5:497–508, 1987

[67] Frank EH, Grodzinsky AJ, Phillips SL, Grimshaw PE: Physicochemical and bioelectrical determinants of cartilage material properties. In Mow VC, Ratcliffe A, Woo SL, editors, *Biomechanics of Diarthrodial Joints*, volume I, pp 261–282. Springer-Verlag, New York, 1990

[68] Frank EH, Salant EP, Grodzinsky AJ: Nondestructive surface detection of cartilage degeneration based on electromechanical behavior of extracellular matrix. *Trans Orthop Res Soc*, 16:74, 1991

[69] Frank EH, Salant EP, Grodzinsky AJ. Probe, system, and method for detecting cartilage degeneration. United States Patent number 4,246,013, Sep 1993

[70] Franzén A, Inerot S, Hejderup SO, Heinegard D: Variations in the composition of bovine hip articular cartilage with distance from the articular surface. *Biochem J*, 195:535–543, 1981

[71] Fredlein RA, Damjanovic A, Bockris JO: Differential surface tension measurements at thin solid metal electrodes. *Surface Sci*, 25:261–264, 1971

[72] Freed LE, Grande DA, Lingbin Z, Emmanual J, Marquis JC, Langer R: Joint resurfacing using allograft chondrocytes and synthetic biodegradable polymer scaffolds. *J Biomed Mat Res*, 28:891–899, 1994

[73] Freiberger RH, Killoran PJ, Cardona G: Arthrography of the knee by double contrast method. *AJR Am J Roentgenol*, 97:736–747, 1966

[74] Frenkel J: On the theory of seismic and seismoelectric phenomena in a moist soil. *J Phys [USSR]*, 8:230–241, 1944

[75] Fujioka M, Kusaka Y, Morita Y, Hirasawa Y, Gersonde K: Contrast-enhanced MR imaging of articular cartilage—A new sensitive method for diagnosis of cartilage degeneration. *Trans Orthop Res Soc*, 19:114, 1994

[76] Fukada E, Yasuda I: On the piezoelectric effect of bone. *J Phys Soc Japan*, 12:1158–1162, 1957

[77] Garverick SL, Senturia SD: An MOS device for AC measurement of surface impedance with application to moisture monitoring. *IEEE Trans Electron Devices*, ED-29:90–94, 1982

[78] Geddes LA: *Electrodes and the Measurement of Bioelectric Events*. Wiley-Interscience, New York, 1972

[79] Geddes LA, Baker LE, Moore AG: Optimum electrolytic chloriding of silver electrodes. *Med Biol Eng*, 7:49–56, 1969

[80] Gersing E, Osypka M: EIT using magnitude and phase in an extended frequency range. *Physiol Meas*, 15:A21–A28, 1994

[81] Gimple M, Auld BA: Variable geometry capacitive probes for multipurpose sensing. *Res Nondestr Eval*, 1:111–132, 1989

[82] Goldenberg DL, Egan MS, Cohen AS: Inflammatory synovitis in degenerative joint disease. *J Rheumatol*, 9:204–209, 1982

[83] Goldfine NJ, Washabaugh AP, Dearlove JV, von Guggenberg PA: Imposed ω-k magnetometer and dielectrometer. In Thompson DO, Chimenti DE, editors, *Review of Progress in Quantitative Nondestructive Evaluation*, volume 12, pp 1115–1122. Plenum Press, New York, 1993

[84] Grande DA, Schwartz R, Zhou L, Kwan M: The durability and biomechanical properties of chondrocyte/collagen allografts. *Trans Orthop Res Soc*, 18:731, 1993

[85] Green AE, Naghdi PM: The flow of fluid through an elastic solid. *Acta Mech*, 9:329–340, 1970

[86] Grimshaw PE, Nussbaum JH, Grodzinsky AJ: Kinetics of electrically and chemically induced swelling in polyelectrolyte gels. *J Chem Phys*, 93:4462–4472, 1990

[87] Grodzinsky AJ: Electromechanical and physicochemical properties of connective tissue. *CRC Crit Rev Biomed Eng*, 9:133–199, 1983

[88] Grodzinsky AJ, Eisenberg SR: Double layer mediated energy conversion with a protein membrane using an imposed frequency and wavelength. *J Electrostatics*, 5:33–50, 1978

[89] Grodzinsky AJ, Frank EH: Electromechanical and physicochemical regulation of cartilage strength and metabolism. In Hukins DWL, editor, *Connective Tissue Matrix II*, pp 91–126. MacMillan, London, 1990

[90] Grodzinsky AJ, Lipshitz H, Glimcher MJ: Electromechanical properties of articular cartilage during compression and stress relaxation. *Nature*, 275:448–450, 1978

[91] Grodzinsky AJ, Melcher JR: Electromechanical transduction with charged polyelectrolyte membranes. *IEEE Trans Biomed Eng*, BME-23:421–433, 1976

[92] Gross D, Williams WS: Streaming potential and the electromechanical response of physiologically-moist bone. *J Biomechanics*, 15:277–295, 1982

[93] Grushko G, Schneiderman R, Maroudas A: Some biochemical and biophysical parameters for the study of the pathogenesis of osteoarthritis: A comparison between the processes of ageing and degeneration in human hip cartilage. *Connect Tissue Res*, 19:149–176, 1989

[94] Hardingham TE: The role of link-protein in the structure of cartilage proteoglycan aggregates. *Biochem J*, 177:237–247, 1979

[95] Hardingham TE, Fosang AJ, Dudhia J: Aggrecan, the chondroitin sulfate/keratan sulfate proteoglycan from cartilage. In Kuettner KE, Schleyerbach R, Peyron JG, Hascall VC, editors, *Articular Cartilage and Osteoarthritis*, pp 5–20. Raven Press, New York, 1992

[96] Harris, Jr. ED, Parker PG, Radin EL, Krane SM: Effects of proteolytic enzymes on structural and mechanical properties of cartilage. *Arthritis Rheum*, 15:497–503, 1972

[97] Harris WH, Sledge CB: Total hip and total knee replacement. *N Engl J Med*, 323:801–807, 1990

[98] Hascall VC: Interaction of cartilage proteoglycans with hyaluronic acid. *J Supramolec Struct*, 7:101–120, 1977

[99] Hasegawa I, Kuriki S, Matsuno S, Matsumoto G: Dependence of electrical conductivity on fixed charge density in articular cartilage. *Clin Orthop*, 177:283–288, 1983

[100] Hayes WC, Bodine AJ: Flow-independent viscoelastic properties of articular cartilage matrix. *J Biomechanics*, 11:407–419, 1978

[101] Heinegård D, Oldberg A: Structure and biology of cartilage and bone matrix noncollagenous macromolecules. *FASEB J*, 3:2042–2051, 1989

[102] Hey LA: A cartilage organ culture system for the study of electrical and mechanical stimuli of biosynthesis. Bachelor's thesis, MIT, Cambridge, MA, 1984

[103] Hirsch C: The pathogenesis of chondromalacia of the patella: A physical, histologic, and chemical study. *Acta Chir Scand*, 90 (Suppl. 83):1–106, 1944

[104] Hjertquist S, Lemperg R: Identification and concentration of the glycosaminoglycans of human articular cartilage in relation to age and osteoarthritis. *Calcif Tissue Res*, 10:223–237, 1972

[105] Hoch DH, Grodzinsky AJ, Koob TJ, Albert ML, Eyre DR: Early changes in material properties of rabbit articular cartilage after meniscectomy. *J Orthop Res*, 1:4–12, 1983

[106] Hodge AJ, Highberger JH, Deffner GGJ, Schmitt FO: The effects of proteases on the tropocollagen macromolecule and on its aggregation properties. *Biochem*, 46:197–206, 1960

[107] Holbrook TL, Grazier K, Kelsey JL, Stauffer RN: *The Frequency of Occurence, Impact and Cost of Selected Musculoskeletal Conditions in the United States.* American Academy of Orthopaedic Surgeons, Chicago, IL, 1984

[108] Hollander AP, Heathfield TF, Webber C, Iwata Y, Bourne R, Rorabeck C, Poole AR: Increased damage to type II collagen in osteoarthritic articular cartilage detected by a new immunoassay. *J Clin Invest*, 93:1722–1732, 1994

[109] Hunter W: Of the structures and diseases of articulating cartilages. *Phil Trans*, 42:514–521, 1743

[110] Hunziker EB, Herrmann W, Schenk RK: Improved cartilage fixation by ruthenium hexammine trichloride (RHT). *J Ultrastruct Res*, 81:1–12, 1982

[111] Hunziker EB, Ludi A, Herrmann W: Preservation of cartilage matrix proteoglycans using cationic dyes chemically related to ruthenium hexaammine trichloride. *J Histochem Cytochem*, 40:909–917, 1992

[112] Hutton CW, Higgs ER, Jackson PC, Watt I, Dieppe PA: ^{99m}Tc HMDP bone scanning in generalised nodal osteoarthritis. II. The four hour bone scan image predicts radiographic change. *Ann Rheum Dis*, 45:622–626, 1986

[113] Hutton CW, Vennart W: Osteoarthritis and magnetic resonance imaging: potential and problems. *Ann Rheum Dis*, 54:237–243, 1995

[114] Ike RW, O'Rourke KS: Detection of intraarticular abnormalities in osteoarthritis of the knee: A pilot study comparing needle arthroscopy with standard arthroscopy. *Arthritis Rheum*, 36:1352–1363, 1993

[115] Inerot S, Heinegård D, Audell L, Olsson S: Articular-cartilage proteoglycans in aging and osteoarthritis. *Biochem J*, 169:143–156, 1978

[116] Inerot S, Heinegård D, Olsson S, Telhag H, Audell L: Proteoglycan alterations during developing experimental osteoarthritis in a novel hip joint model. *J Orthop Res*, 9:658–673, 1991

[117] Inkpen S, Brobeck C, Parsons B: Measurement of spatial variations in electrical properties of model ice. *Cold Regions Sci Tech*, 16:201–209, 1989

[118] Ishizue KK, Ehrlich MG, Mankin HJ: Drug-induced inhibition of proteoglycanase activity in the Hulth-Telhag model. *J Orthop Res*, 7:806–811, 1989

[119] Jackson RW: The role of arthroscopy in the management of the arthritic knee. *Clin Orthop*, 101:28–35, 1974

[120] Jackson RW, Abe I: The role of arthroscopy in the management of disorders of the knee: An analysis of 200 consecutive examinations. *J Bone Joint Surg [Am]*, 52-A:310–322, 1972

[121] James GT: Inactivation of the protease inhibitor phenylmethylsulfonyl fluoride in buffers. *Anal Biochem*, 86:574–579, 1978

[122] Janselewitz SJ: A device for characterization of mechanical and electrical properties of cartilage. Bachelor's thesis, MIT, Cambridge, MA, 1992

[123] Johnson MW, Chakkalakal DA, Harper RA, Katz JL: Comparison of the electromechanical effects in wet and dry bone. *J Biomechanics*, 13:437–442, 1980

[124] Karsh RS, McCarthy JD: Archeology and arthritis. *Arch Intern Med*, 105:640–644, 1960

[125] Katchalsky A, Curran PF: *Nonequilibrium Thermodynamics in Biophysics*. Harvard University Press, Cambridge, MA, 1965

[126] Kempson GE: The mechanical properties of articular cartilage. In Sokoloff L, editor, *The Joints and Synovial Fluid*, volume II, pp 177–238. Academic Press, New York, 1980

[127] Kempson GE, Spivey CJ, Swanson SAV, Freeman MAR: Patterns of cartilage stiffness on normal and degenerate human femoral heads. *J Biomechanics*, 4:597–609, 1971

[128] Kempson GE, Tuke MA, Dingle JT, Barrett AJ, Horsfield PH: The effects of proteolytic enzymes on the mechanical properties of adult human articular cartilage. *Biochim Biophys Acta*, 428:741–760, 1976

[129] Kenyon DE: The theory of an incompressible solid-fluid mixture. *Arch Rat Mech Anal*, 62:131–147, 1976

[130] Kiviranta I, Lyyra T, Väätäinen U, Seuri R, Jaroma H, Jurvelin J: Knee joint articular cartilage shows general softening in patients with chondromalacia of the patella. *Trans Orthop Res Soc*, 20:197, 1995

[131] König H, Sauter R, Deimling M, Vogt M: Cartilage disorders: Comparison of spin-echo, CHESS, and FLASH sequence MR images. *Radiology*, 164:753–758, 1987

[132] Krajíčková J, Macek J: Urinary proteoglycan degradation product excretion in patients with rheumatoid arthritis and osteoarthritis. *Ann Rheum Dis*, 47:468–471, 1988

[133] Kühn K, Fietzek P, Kühn J: The action of proteolytic enzymes on collagen. *Biochem Z*, 344:418–434, 1966

[134] Kusaka Y, Gründer W, Rumpel H, Dannhauer KH, Gersonde K: MR microimaging of articular cartilage and contrast enhancement by manganese ions. *Magn Reson Med*, 24:137–148, 1992

[135] Lane JM, Chisena E, Black J: Experimental knee instability: Early mechanical property changes in articular cartilage in a rabbit model. *Clin Orthop*, 140:262–265, 1979

[136] Lee RC, Frank EH, Grodzinsky AJ, Roylance DK: Oscillatory compressional behavior of articular cartilage and its associated electromechanical properties. *J Biomech Eng*, 103:280–292, 1981

[137] Lee RC, Grodzinsky AJ, Glimcher MJ: The electromechanics of normal and chemically modified articular cartilage. In Brighton CT, Black J, Pollack SR, editors, *Electrical Properties of Bone and Cartilage: Experimental Effects and Clinical Applications*, pp 47–56. Grune and Stratton, New York, 1979

[138] Lesperance LM: *Compositional studies of cartilage matrix using NMR spectroscopy.* PhD thesis, MIT, Cambridge, MA, 1993

[139] Lesperance LM, Gray ML, Burstein D: Determination of fixed charge density in cartilage using nuclear magnetic resonance. *J Orthop Res*, 10:1–13, 1992

[140] Levich VG: *Physicochemical Hydrodynamics.* Prentice-Hall, Englewood Cliffs, NJ, 1962

[141] Lindblad S, Hedfors E: Arthroscopic and immunohistologic characterization of knee joint synovitis in osteoarthritis. *Arthritis Rheum*, 30:1081–1088, 1987

[142] Lipshitz H, Etheredge III R, Glimcher MJ: *In vitro* wear of articular cartilage—I. Hydroxyproline, hexosamine, and amino acid composition of bovine articular cartilage as a function of depth from the surface; Hydroxyproline content of the lubricant and the wear debris as a measure of wear. *J Bone Joint Surg [Am]*, 57-A:527–534, 1975

[143] Lipshitz H, Etheredge III R, Glimcher MJ: Changes in the hexosamine content and swelling ratio of articular cartilage as functions of depth from the surface. *J Bone Joint Surg [Am]*, 58-A:1149–1153, 1976

[144] Lohmander LS: Cartilage markers in joint fluid in human osteoarthritis. In Brandt KD, editor, *Cartilage Changes in Osteoarthritis*, pp 98–104. Indiana University School of Medicine, Indianapolis, Indiana, 1990

[145] Lohmander LS, Neame PJ, Sandy JD: The structure of aggrecan fragments in human synovial fluid. *Arthritis Rheum*, 36:1214–1222, 1993

[146] Lotke PA, Black J, Richardson SJ: Electromechanical properties in human articular cartilage. *J Bone Joint Surg [Am]*, 56-A:1040–1046, 1974

[147] Lysholm J, Hamberg P, Gillquist J: The correlation between osteoarthrosis as seen on radiographs and on arthroscopy. *Arthroscopy*, 3:161–165, 1987

[148] Lyyra T, Jurvelin J, Pitkänen P, Väätäinen U, Kiviranta I: Indentation instrument for the measurement of cartilage stiffness under arthroscopic control. *Med Eng Phys*, 17:395–399, 1995

[149] Macdonald JR: Impedance spectroscopy. *Ann Biomed Eng*, 20:289–305, 1992

[150] Mak AF, Lai WM, Mow VC: Biphasic indentation of articular cartilage—I. Theoretical analysis. *J Biomechanics*, 20:703–714, 1987

[151] Manicourt DH, Thonar EJA, Pita JC, Howell DS: Changes in the sedimentation profile of proteoglycan aggregates in early experimental canine osteoarthritis. *Connect Tissue Res*, 23:33–50, 1989

[152] Mankin HJ: The response of articular cartilage to mechanical injury. *J Bone Joint Surg [Am]*, 64-A:460–466, 1982

[153] Mankin HJ, Brandt KD: Biochemistry and metabolism of cartilage in osteoarthritis. In Moskowitz RW, Howell DS, Goldberg VM, Mankin HJ, editors, *Osteoarthritis*, pp 43–79. W. B. Saunders, Philadelphia, 1984

[154] Mankin HJ, Dorman H, Lippiello L, Zarins A: Biochemical and metabolic abnormalities in articular cartilage from osteoarthritic human hips. II. Correlation of morphology with biochemical and metabolic data. *J Bone Joint Surg [Am]*, 53-A:523–537, 1971

[155] Mankin HJ, Thrasher AZ: Water content and binding in normal and osteoarthritic human cartilage. *J Bone Joint Surg [Am]*, 57-A:76–80, 1975

[156] Manouel M, Pearlman HS, Belakhlef A, Brown TD: A miniature piezoelectric polymer transducer for in vitro measurement of the dynamic contact stress distribution. *J Biomechanics*, 25:627–635, 1992

[157] Marcus MA: Ferroelectric polymers and their applications. *Ferroelectrics [GB]*, 1:29–41, 1982

[158] Maroudas A: Distribution and diffusion of solutes in articular cartilage. *Biophys J*, 8:575–595, 1968

[159] Maroudas A: Distribution and diffusion of solutes in articular cartilage. *Biophys J*, 10:365–379, 1968

[160] Maroudas A: Balance between swelling pressure and collagen tension in normal and degenerate cartilage. *Nature*, 260:808–809, 1976

[161] Maroudas A: Physicochemical properties of articular cartilage. In Freeman MAR, editor, *Adult Articular Cartilage*, pp 215–290. Pitman Medical, Kent, England, 2nd edition, 1979

[162] Maroudas A, Venn M: Chemical composition and swelling of normal and osteoarthrotic femoral heac cartilage. II. Swelling. *Ann Rheum Dis*, 36:399–406, 1977

[163] Matthews BF: Composition of articular cartilage in osteoarthritis: Changes in collagen/chondroitin sulphate ratio. *Br Med J*, 2:660–661, 1953

[164] McCarthy C, Cushnaghan J, Dieppe P: The predictive tole of scintigraphy in radiographic osteoarthritis of the hand. *Osteoarthritis and Cartilage*, 2:25–28, 1994

[165] McCoy GF, McCrea JD, Beverland DE, Kernohan WG, Mollan RAB: Vibration arthrography as a diagnostic aid in diseases of the knee. *J Bone Joint Surg [Br]*, 69-B:288–293, 1987

[166] McCune WJ, Dedrick DK, Aisen AM, MacGuire A: Sonographic evaluation of osteoarthritic femoral condylar cartilage: Correlation with operative findings. *Clin Orthop*, 254:230–235, 1987

[167] McCutchen CW: The frictional properties of animal joints. *Wear*, 5:1–17, 1962

[168] McCutchen CW: Cartilage is poroelastic, not viscoelastic (including an exact theorem about strain energy and viscous loss, and an order of magnitude relation for equilibration time). *J Biomechanics*, 15:325–327, 1982

[169] McDevitt CA, Muir HJ: Biochemical changes in the cartilage of the knee in experimental and natural osteoarthritis in the dog. *J Bone Joint Surg [Br]*, 58-B:94–101, 1976

[170] Meachim G, Ghadially FN, Collins DH: Regressive changes in the superficial layer of human articular cartilage. *Ann Rheum Dis*, 24:23–30, 1965

[171] Melcher JR: *Continuum Electromechanics*. MIT Press, Cambridge, MA, 1981

[172] Melcher JR. Apparatus and methods for measuring permeability and conductivity in materials using multiple wavenumber magnetic interrogations. United States Patent number 5,015,951, May 1991

[173] Melcher JR, Zaretsky MC. Apparatus and methods for measuring permittivity in materials. United States Patent number 4,814,690, Mar 1989

[174] Messner K, Gillquist J: Synthetic implants for the repair of osteochondral defects of the medial femoral condyle: a biomechanical and histological evaluation in the rabbit knee. *Biomaterials*, 14:513–521, 1993

[175] Morgenthaler AW: Electromechanical response of articular cartilage subject to enzymatic degradation. Master's thesis, MIT, Cambridge, MA, 1987

[176] Moskowitz RW, Goldberg VM: Osteoarthritis. In Schumacher HR, editor, *Primer on the Rheumatic Diseases*, chapter 38, pp 171–177. Arthritis Foundation, Atlanta, GA, 9th edition, 1988

[177] Moskowitz RW, Howell DS, Goldberg VM, Muiz O, Pita JC: Cartilage proteoglycan alterations in an experimentally induced model of rabbit osteoarthritis. *Arthritis Rheum*, 22:155–163, 1979

[178] Moussavi ZMK, Rangayyan RM, Bell GD, Frank CB, Ladly KO, Zhang Y: Screening of vibroarthrographic signals via adaptive segmentation and linear prediction modeling. *IEEE Trans Biomed Eng*, 43:15–23, 1996

[179] Mow VC, Holmes MH, Lai WM: Fluid transport and mechanical properties of articular cartilage: A review. *J Biomechanics*, 17:377–394, 1984

[180] Mow VC, Kuei SC, Lai WM, Armstrong CG: Biphasic creep and stress relaxation of articular cartilage in compression: Theory and experiments. *J Biomech Eng*, 102:73–84, 1980

[181] Myers S, Dines K, Albrecht M, Wu E, Brandt K: Assessment by high frequency ultrasound (HFU) of the thickness and subsurface characteristics of normal and osteoarthritic human cartilage. *Trans Orthop Res Soc*, 19:215, 1994

[182] Myers SL, Brandt KD, Eilam O: Even low-grade synovitis significantly accelerates the clearance of protein from the canine knee. *Arthritis Rheum*, 38:1085–1091, 1995

[183] Obeid EMH, Adams MA, Newman JH: Mechanical properties of articular cartilage in knees with unicompartmental osteoarthritis. *J Bone Joint Surg [Br]*, 76-B:315–319, 1994

[184] O'Driscoll SW, Keeley FW, Salter RB: The chondrogenic potential of free autogenous periosteal grafts for biological resurfacing of major full-thickness defects in joint surfaces under the influence of continuous passive motion. An experimental investigation in the rabbit. *J Bone Joint Surg [Am]*, 68-A:1017–1035, 1986

[185] Otter M, Shoenung J, Williams WS: Evidence for different sources of stress-generated potentials in wet and dry bone. *J Orthop Res*, 3:321–324, 1985

[186] Outerbridge RE: The etiology of chondromalacia patellae. *J Bone Joint Surg [Br]*, 43-B:752–757, 1961

[187] Overbeek JTG: Electrokinetic phenomena. In Kruyt HR, editor, *Colloid Science*, volume 1, pp 194–244. Elsevier Publishing Co., Amsterdam, 1952

[188] Paguio CG: Effects of enzymatic degradation on articular cartilage: Relevance to osteoarthritis. Bachelor's thesis, MIT, Cambridge, MA, 1992

[189] Palmoski MJ, Brandt KD: Proteoglycan depletion, rather than fibrillation, determines the effects of salicylate and indomethacin on osteoarthritic cartilage. *Arthritis Rheum*, 28:548–553, 1985

[190] Parsons JR, Black J: The viscoelastic shear behavior of normal rabbit articular cartilage. *J Biomechanics*, 10:21–29, 1977

[191] Paul PK, O'Byrne E, Blancuzzi V, Wilson D, Gunson D, Douglas FL, Wang JZ, Mezrich RS: Magnetic resonance imaging reflects cartilage proteoglycan degradation in the rabbit knee. *Skeletal Radiol*, 20:31–36, 1991

[192] Pearson JP, Mason RM: The stability of bovine nasal cartilage proteoglycans during isolation and storage. *Biochim Biophys Acta*, 498:176–188, 1977

[193] Pennwalt Corp., Valley Forge, PA: *Kynar Piezo Film*, 1987. Technical Manual

[194] Pienkowski D, Pollack SR: The origin of stress-generated potentials in fluid-saturated bone. *J Orthop Res*, 1:30–41, 1983

[195] Pita JC, Manicourt DH, Muller FJ, Howell DS: Studies on the potential reversibility of osteoarthritis in some experimental animal models. In Kuettner KE, Schleyerbach R, Hascall VC, editors, *Articular Cartilage Biochemistry*, pp 349–364. Raven Press, New York, 1986

[196] Poole AR: The relationship between toluidine blue staining and hexuronic acid content of cartilage matrix. *Histochem J*, 2:425–430, 1970

[197] Poole AR: Enzymatic degradation: Cartilage destruction. In Brandt KD, editor, *Cartilage Changes in Osteoarthritis*, pp 63–72. Indiana University School of Medicine, Indianapolis, Indiana, 1990

[198] Praemer A, Furner S, Rice DP: *Musculoskeletal Conditions in the United States*. American Academy of Orthopaedic Surgeons, Park Ridge, IL, 1992

[199] Press WH, Flannery BP, Teukolsky SA, Vetterling WT: *Numerical Recipes in C*. Cambridge University Press, New York, 1988

[200] Pugh J: Biomechanical aspects of osteoarthritic joints: Mechanisms and noninvasive detection. In Ghista DN, editor, *Osteoarthromechanics*, pp 161–191. McGraw-Hill, New York, 1982

[201] Rand JA: Role of arthroscopy in osteoarthritis of the knee. *Arthroscopy*, 7:358–363, 1991

[202] Ratcliffe A, Fryer PR, Hardingham TE: The distribution of aggregating proteoglycans in articular cartilage: Comparison of quantitative immunoelectron microscopy with radioimmunoassay and biochemical analysis. *J Histochem Cytochem*, 32:193–201, 1984

[203] Reddy NP, Rothschild BM, Mandal M, Gupta V, Suryanarayanan S: Noninvasive acceleration measurements to characterize knee arthritis and chondromalacia. *Ann Biomed Eng*, 23:78–84, 1995

[204] Revell PA, Mayston V, Lalor P, Mapp P: The synovial membrane in osteoarthritis: a histological study including the characterisation of the cellular infiltrate present in inflammatory osteoarthritis using monoclonal antibodies. *Ann Rheum Dis*, 47:300–307, 1988

[205] Rice JR, Cleary MP: Some basic stress diffusion solutions for fluid-saturated elastic porous media with compressible components. *Rev Geophys Space Phys*, 14:227–241, 1976

[206] Rigaud B, Hamzaoui L, Chauveau N, Granié M, Di Rinaldi JS, Morucci J: Tissue characterization by impedance: a multifrequency approach. *Physiol Meas*, 15:A13–A20, 1994

[207] Ritsalä VA *et al.*: Periosteal and perichondral grafting in reconstructive surgery. *Clin Orthop*, 302:259–265, 1994

[208] Roberts S, Weightman B, Urban J, Chappell D: Mechanical and biochemical properties of human articular cartilage in osteoarthritic femoral heads and in autopsy specimens. *J Bone Joint Surg [Br]*, 68-B:278–288, 1986

[209] Sabiston CP, Adams ME, Li DKB: Magnetic resonance imaging of osteoarthritis: Correlation with gross pathology using an experimental model. *J Orthop Res*, 5:164–172, 1987

[210] Sachs JR: *A Mathematical Model of an Electromechanically Coupled Poroelastic Medium*. PhD thesis, MIT, Cambridge, MA, 1987

[211] Sachs JR, Grodzinsky AJ: An electromechanically coupled poroelastic medium driven by an applied electric current: Surface detection of bulk material properties. *PhysicoChem Hydrodynamics*, 11:585–614, 1989

[212] Sachs JR, Grodzinsky AJ: Electromechanical spectroscopy of cartilage using a surface probe with applied mechanical displacement. *J Biomechanics*, 28:963–976, 1995

[213] Salant EP: Surface probe for electrokinetic detection of cartilage degeneration. MD thesis, Harvard-MIT Division of Health Sciences and Technology, Cambridge, MA, 1991

[214] Salzstein RA, Pollack SR: Electromechanical potentials in cortical bone—II. Experimental analysis. *J Biomechanics*, 20:271–280, 1987

[215] Salzstein RA, Pollack SR, Mak AFT, Petrov N: Electromechanical potentials in cortical bone—I. A continuum approach. *J Biomechanics*, 20:261–270, 1987

[216] Sandy JD, Flannery CR, Neame PJ, Lohmander LS: The structure of aggrecan fragments in human synovial fluid. *J Clin Invest*, 89:1512–1516, 1992

[217] Schmidt MB, Mow VC, Chun LE, Eyre DR: Effects of proteoglycan extraction on the tensile behavior of articular cartilage. *J Orthop Res*, 8:353–363, 1990

[218] Scott GC, Korostoff E: Oscillatory and step response electromechanical phenomena in human and bovine bone. *J Biomechanics*, 23:127–143, 1990

[219] Seibel MJ, Duncan A, Robins SP: Urinary hydroxy-pyridinium crosslinks provide indices of cartilage and bone involvement in arthritic diseases. *J Rheumatol*, 16:964–970, 1989

[220] Senturia SD, Garverick SL. Methods and apparatus for microdielectrometry. United States Patent number 4,423,371, Dec 1983

[221] Senturia SD, Sheppard, Jr. NF, Lee HL, Day DR: *In-situ* measurement of the properties of curing systems with microdielectrometry. *J Adhesion*, 15:69–90, 1982

[222] Setton LA, Mow VC, Müller FJ, Pita JC, Howell DS: Mechanical properties of canine articular cartilage are significantly altered following transection of the anterior cruciate ligament. *J Orthop Res*, 12:451–463, 1994

[223] Shapiro FS, Glimcher MJ: Induction of osteoarthrosis in the rabbit knee joint: Histologic changes following meniscectomy and meniscal lesions. *Clin Orthop*, 147:287–295, 1980

[224] Sheppard NF, Day DR, Lee HL, Senturia SD: Microdielectrometry. *Sensors and Actuators*, 2:263–274, 1982

[225] Shinmei M, Ito K, Matsuyama S, Yoshihara Y, Matsuzawa K: Joint fluid carboxy-terminal type II procollagen peptide as a marker of cartilage collagen biosynthesis. *Osteoarthritis and Cartilage*, 1:121–128, 1993

[226] Stahurski TM, Armstrong CG, Mow VC: Variation of the intrinsic aggregate modulus and permeability of articular cartilage with trypsin digestion. In *1981 Biomechanics Symposium*, pp 137–140. ASME, 1981

[227] Stegmann H, Stalder K: Determination of hydroxyproline. *Clin Chim Acta*, 18:267–273, 1967

[228] Stockwell RA, Scott JE: Distribution of acid glycosaminoglycans in human articular cartilage. *Nature*, 215:1376–1378, 1967

[229] Strawich E, Nimni ME: Properties of a collagen molecule containing three identical components extracted from bovine articular cartilage. *Biochem*, 10:3905–3911, 1971

[230] Strobel M, Stedtfeld H: *Diagnostic Evaluation of the Knee*, pp 276–316. Springer-Verlag, New York, 1990

[231] Stryer L: *Biochemistry*. W.H. Freeman, New York, 3rd edition, 1988

[232] Swartz RG, Plummer JD: Integrated silicon-PVF_2 acoustic transducer arrays. *IEEE Trans Electron Devices*, ED-26:1921–1931, 1979

[233] Sweet MBE, Thonar EJA, Immelman AR, Solomon L: Biochemical changes in progressive osteoarthrosis. *Ann Rheum Dis*, 36:387–398, 1977

[234] Theiler R, Ghosh P, Brooks P: Clinical, biochemical, and imaging methods of assessing osteoarthritis and clinical trials with agents claiming 'chondromodulating' activity. *Osteoarthritis and Cartilage*, 2:1–23, 1994

[235] Thomas RH, Resnick D, Alazraki NP, Daniel D, Greenfield R: Compartmental evaluation of osteoarthritis of the knee: A comparative study of available diagnostic modalities. *Radiology*, 116:585–594, 1975

[236] Thonar EJA *et al.*: Serum keratan sulfate: A measure of cartilage proteoglycan metabolism. In Kuettner KE, Schleyerbach R, Peyron JG, Hascall VC, editors, *Articular Cartilage and Osteoarthritis*, pp 429–445. Raven Press, New York, 1992

[237] Troyer H: Experimental models of osteoarthritis: A review. *Semin Arthritis Rheum*, 11:362–374, 1982

[238] Uebelhart D, Thonar EJA, Pietryla DW, Williams JM: Elevation in urinary levels of pyridinium cross-links of collagen following chymopapain-induced degradation of articular cartilage in the rabbit knee provides evidence of metabolic changes in bone. *Osteoarthritis and Cartilage*, 1:185–192, 1993

[239] Urban JPG, Maroudas A, Bayliss MT, Dillon J: Swelling pressures of proteoglycans at the concentrations found in cartilaginous tissues. *Biorheology*, 16:447–464, 1979

[240] Vasan N: Proteoglycans in normal and severely osteoarthritic human cartilage. *Biochem J*, 187:781–787, 1980

[241] Venn M, Maroudas A: Chemical composition and swelling of normal and osteoarthrotic femoral head cartilage. I. Chemical composition. *Ann Rheum Dis*, 36:121–129, 1977

[242] Venn MF: Variation of chemical composition with age in human femoral head cartilage. *Ann Rheum Dis*, 37:168–174, 1978

[243] Vignon E, Arlot M: Macroscopically normal cartilage from the human osteoarthritic femoral head. I. Histological evaluation. *J Rheumatol*, 8:440–446, 1981

[244] Vincenti MP, Clark IM, Brinckerhoff CE: Using inhibitors of metalloproteinases to treat arthritis. *Arthritis Rheum*, 37:1115–1126, 1994

[245] von Guggenberg PA, Melcher JR: A three-wavelength flexible sensor for monitoring the moisture content of transformer pressboard. In *3rd International Conference on Properties and Applications of Dielectric Materials*, pp 1262–1265. IEEE, 1991

[246] von Guggenberg PA, Zaretsky MC: Estimation of one-dimensional complex-permittivity profiles: A feasibility study. *J Electrostatics*, 34:263–277, 1995

[247] Weast RC, Astle MJ, Beyer WH, editors: *CRC Handbook of Chemistry and Physics*. CRC Press, Inc., Boca Raton, FL, 66th edition, 1985

[248] Williams JM, Ongchi DR, Thonar EJA: Repair of articular cartilage injury following intra-articular chymopapain-induced matrix proteoglycan loss. *J Orthop Res*, 11:705–716, 1993

[249] Woessner, Jr. JF: Matrix metalloproteinases and their inhibitors in connective tissue remodeling. *FASEB J*, 5:2145–2154, 1991

[250] Yannas IV, Grodzinsky AJ: Electromechanical energy conversion with collagen fibers in an aqueous medium. *J Mechanochem Cell Motility*, 2:113–125, 1973

[251] Yu WKS, Shaw SM, Bartlett JM, van Sickle DC, Mock BH: The biodistribution of [^{75}Se] bis[β-(N, N, N-trimethylamino)ethyl]selenide diiodide in adult guinea pigs. *Nucl Med Biol*, 16:255–259, 1989

[252] Zaretsky MC, Li P, Melcher JR: Estimation of thickness, complex bulk permittivity and surface conductivity using interdigital dielectrometry. *IEEE Trans Electr Insul*, 24:1159–1166, 1989

[253] Zaretsky MC, Melcher JR, Cooke CM: Moisture sensing in transformer oil using thin film microdielectrometry. In *IEEE International Symposium on Electrical Insulation*, pp 12–17. IEEE, 1988

[254] Zaretsky MC, Mouayad L, Melcher JR: Continuum properties from interdigitated electrode dielectrometry. *IEEE Trans Electr Insul*, 23:897–917, 1988

[255] Zuercher JC, Melcher JR: Double-layer transduction at a mercury-electrolyte interface with imposed temporal and spatial periodicity. *J Electrostatics*, 5:21–31, 1978

Endnote

". . . all things must have a usefulness; that is certain. Since electricity must have a usefulness, and we have seen that it cannot be looked for either in theology or in jurisprudence, there is obviously nothing left but medicine."
—*Johann Gottlob Krüger* (1743)